

University of Kentucky

UKnowledge

Theses and Dissertations--Electrical and
Computer Engineering

Electrical and Computer Engineering

2014

Machine-human Cooperative Control of Welding Process

Weijie Zhang

University of Kentucky, weijie.zhang@live.com

[Right click to open a feedback form in a new tab to let us know how this document benefits you.](#)

Recommended Citation

Zhang, Weijie, "Machine-human Cooperative Control of Welding Process" (2014). *Theses and Dissertations--Electrical and Computer Engineering*. 45.

https://uknowledge.uky.edu/ece_etds/45

This Doctoral Dissertation is brought to you for free and open access by the Electrical and Computer Engineering at UKnowledge. It has been accepted for inclusion in Theses and Dissertations--Electrical and Computer Engineering by an authorized administrator of UKnowledge. For more information, please contact UKnowledge@lsv.uky.edu.

STUDENT AGREEMENT:

I represent that my thesis or dissertation and abstract are my original work. Proper attribution has been given to all outside sources. I understand that I am solely responsible for obtaining any needed copyright permissions. I have obtained needed written permission statement(s) from the owner(s) of each third-party copyrighted matter to be included in my work, allowing electronic distribution (if such use is not permitted by the fair use doctrine) which will be submitted to UKnowledge as Additional File.

I hereby grant to The University of Kentucky and its agents the irrevocable, non-exclusive, and royalty-free license to archive and make accessible my work in whole or in part in all forms of media, now or hereafter known. I agree that the document mentioned above may be made available immediately for worldwide access unless an embargo applies.

I retain all other ownership rights to the copyright of my work. I also retain the right to use in future works (such as articles or books) all or part of my work. I understand that I am free to register the copyright to my work.

REVIEW, APPROVAL AND ACCEPTANCE

The document mentioned above has been reviewed and accepted by the student's advisor, on behalf of the advisory committee, and by the Director of Graduate Studies (DGS), on behalf of the program; we verify that this is the final, approved version of the student's thesis including all changes required by the advisory committee. The undersigned agree to abide by the statements above.

Weijie Zhang, Student

Dr. Yu-Ming Zhang, Major Professor

Dr. CaiCheng Lu, Director of Graduate Studies

MACHINE-HUMAN COOPERATIVE CONTROL OF WELDING PROCESS

DISSERTATION

A dissertation submitted in partial
fulfillment of the requirements for the
degree of Doctor of Philosophy in the
College of Engineering at the
University of Kentucky

By
WeiJie Zhang
Lexington, Kentucky

Director: YuMing Zhang, Ph.D., Professor of Electrical and Computer Engineering
Lexington, Kentucky

2014

Copyright© WeiJie Zhang 2014

ABSTRACT OF DISSERTATION

MACHINE-HUMAN COOPERATIVE CONTROL OF WELDING PROCESS

An innovative auxiliary control system is developed to cooperate with a unskilled welder in a manual GTAW in order to obtain a consistent welding performance. In the proposed system, a novel mobile sensing system is developed to non-intrusively monitor a manual GTAW by measuring three-dimensional (3D) weld pool surface. Specifically, a miniature structured-light laser mounted on torch projects a dot matrix pattern on weld pool surface during the process; Reflected by the weld pool surface, the laser pattern is intercepted by and imaged on the helmet glass, and recorded by a compact camera on it. Deformed reflection pattern contains the geometry information of weld pool, thus is utilized to reconstruct its 3D surface. An innovative image processing algorithm and a reconstruction scheme have been developed for (3D) reconstruction.

The real-time spatial relations of the torch and the helmet is formulated during welding. Two miniature wireless inertial measurement units (WIMU) are mounted on the torch and the helmet, respectively, to detect their rotation rates and accelerations. A quaternion based unscented Kalman filter (UKF) has been designed to estimate the helmet/torch orientations based on the data from the WIMUs. The distance between the torch and the helmet is measured using an extra structure-light low power laser pattern.

Furthermore, human welder's behavior in welding performance has been studied, e.g., a welder's adjustments on welding current were modeled as response to characteristic parameters of the three-dimensional weld pool surface. This response model as a controller is implemented both automatic and manual gas tungsten arc welding process to maintain a consistent full penetration.

KEYWORDS: Manual GTAW, Weld Pool Mobile Sensing, Real-time Reconstruction, Human Welder Response

Author's signature: _____ WeiJie Zhang

Date: _____ June 24, 2014

MACHINE-HUMAN COOPERATIVE CONTROL OF WELDING PROCESS

By

WeiJie Zhang

YuMing Zhang, Ph.D.

Director of Dissertation

CaiCheng Lu, Ph.D.

Director of Graduate Studies

June 24, 2014

Date

ACKNOWLEDGEMENTS

The research work in this dissertation is funded by the National Science Foundation Project under grant CMMI-0927707.

Firstly I would like to sincerely thank my advisor Dr. YuMing Zhang for his invaluable guidance, continuous encouragement and constructive instructions. I am also grateful to Drs. Alan T. Male, Jingshan Li, Yuan Liao, and Larry Holloway for their helpful insight and supervision. I want to thank all of my colleagues in the Welding Research Lab: Jinsong Chen, YuKang Liu, Kun Qian, Jun Xiao, Xiaopei Liu, Yu Shi, Yi Huang, Zhenzhou Wang, Xiangrong Li, Yan Shao, and Xiaoji Ma, Yao Hu for their helpful suggestions for my work.

In addition, I want to give my thanks to my parents for their endless love and support throughout all my life. Lastly I'd like to express my great appreciation to my wife, YuQi Zhang, my daughter, Grace Zhang and my parents, for bringing me and sharing with me so many wonderful things in my life.

Contents

Acknowledgements	iii
Contents	iv
List of Tables	vii
List of Figures	viii
1 Introduction	1
1.1 Background	1
1.2 Objective and Approach	2
1.3 Organization	4
2 Literature Review	7
2.1 Overview	7
2.2 Sensing Techniques of Welding	8
2.2.1 Vision-based Techniques	9
2.2.2 Other Techniques	15
2.3 Control of Welding Process	16
3 Mobile Sensing System Design	18
3.1 System Design	18
3.1.1 Configuration of the mobile sensing system	18
3.1.2 Manual welding process with the proposed sensing system	20
3.2 System Analysis and Simulation	22
3.2.1 System Analysis	22
3.2.2 System Simulation	32
3.3 Observation Results	35

3.3.1	Experimental Setup	35
3.3.2	Acquired Images	37
3.4	Summary	37
4	Processing of Acquired Images	40
4.1	System Calibration	40
4.2	Image Processing	42
4.2.1	Features of dot matrix reflection pattern	44
4.2.2	Image processing of dot matrix reflection	46
4.2.3	Real-time verification for identification of dot matrix reflection pattern	57
4.3	Summary	65
5	Orientation Estimation of Sensing System	67
5.1	Introduction and related works	67
5.2	Representation of Torch Orientation	70
5.3	Sensor Modeling	72
5.4	Auto-nulling Algorithm	74
5.5	Unscent Kalman Filter (UKF) design	75
5.6	Verifications Simulation and Experiments	78
5.6.1	Experimental equipment	78
5.6.2	Simulations procedure	79
5.6.3	Experimental Validation	80
5.7	Results and discussion	81
5.7.1	Results	81
5.7.2	Discussion	85
5.8	Summary	89
6	Weld Pool Reconstruction Scheme	91
6.1	Spatial Relations of the Sensing System	91
6.2	3D Weld Pool Surface Reconstruction	95
6.2.1	Modeling of 2D weld pool boundary	95
6.2.2	3D weld pool reconstruction	96
6.3	Reconstruction Example	100

6.4	Simulation and results analysis	103
6.4.1	Helmet rotation-category A	103
6.4.2	Torch rotation-category B	104
6.5	Summary	106
7	Modeling of Human Welder Behavior	112
7.1	Background and Purpose	112
7.2	Principle of Human Welder Behavior	114
7.3	Weld Pool Characterization	115
7.3.1	Estimation of weld penetration with characteristic parameters	117
7.4	Modeling Experiments	121
7.4.1	Experiment set-up	121
7.4.2	Dynamic experiment design	122
7.5	Experimental Results and Analysis	124
7.5.1	Dynamic experiments and modeling results	124
7.5.2	Model verification	128
7.6	Summary	128
8	Human Machine Cooperative Welding Process	130
8.1	Automatic GTAW Process Using Human Welder Behavior Model	130
8.1.1	Experiment configuration and approach	130
8.1.2	human welder response model control	131
8.1.3	Improvement of human welder response model	133
8.1.4	Robustness experiment results and analysis	134
8.2	Manual GTAW Process Using Human Welder Behavior Model	139
8.2.1	Experiment configuration and approach	140
8.2.2	Experiment results	140
8.3	Summary	142
9	Conclusion and Future Work	143
9.1	Conclusion	143
9.2	Future Work	144
	Bibliography	146
	Vita	156

List of Tables

3.1	Parameters for the sensing system simulation	32
4.1	Parameters of the sensing system for image processing	42
4.2	Robustness experiments with different conditions	58
4.3	Major experimental conditions	59
5.1	Major Welding Conditions For the GTAW Experiments	80
5.2	Initializations of the UKF parameters for Method A and B	81
5.3	Orientation estimation ($RMSE_{\theta}$), in the form of mean \pm standard deviation, obtained by the different estimation methods in the course of the monte carlo performance trials. Additional distance of gyro and acceleration were artificially introduced in data set D_{4+n}^s	82
5.4	Orientation estimation ($RMSEs$ ($^{\circ}$)), in the form of mean \pm standard deviation, obtained by the different estimation methods in course of six repeated trials for each simulation.	82
5.5	Dynamic Orientation estimation [$RMSE_{\theta}$]($^{\circ}$), in the form of mean \pm standard deviation, obtained by Method A. The angular rate is larger than 5°	85
5.6	Orientation estimation [$RMSE_{\theta}$]($^{\circ}$), produced by different data sets using Method A with a sampling rate $f_s = 128$ Hz. The four types of welding account for those in Figure.5.1 (for data set D_1^e and D_{1+n}^e), and in Figure. 5.2(for data set D_2^e and D_{2+n}^e).	85
7.1	Characteristic parameters estimation results	119
7.2	Resultant dynamic models of human welder's behavior	127
8.1	Welding parameters in experiments with different initial currents	131
8.2	Welding parameters for initial current robustness experiments	134
8.3	Welding parameters for arc length robustness experiments	135
8.4	Welding parameters for arc length robustness experiments	138

List of Figures

1.1	Illustration of Gas tungsten arc welding	1
1.2	Organization of the dissertation	4
2.1	Different penetration statuses in welding process[81]	7
2.2	Experiment setup and the captured image [72]	9
2.3	Experiment setup, captured and resultant images [16]	10
2.4	Experiment setup and the captured images [43]	10
2.5	Experiment setup, captured and resultant images [53]	11
2.6	Experiment setup, captured image and the geometrical model [143]	11
2.7	Resultant image using model-based weld pool reconstruction [143]	12
2.8	Captured image and resultant image of stereo-vision measurement [89] . .	12
2.9	Biprism diagram and captured images[30]	13
2.10	Shape from shape weld pool reconstruction, diagram, captured and resultant images[162]	13
2.11	Experiment setup and resultant image of weld pool reconstruction[71] . .	14
2.12	Diagram of the laser grating sensing system, captured image and reconstructed weld pool [136]	14
2.13	Diagram of the sensing system, captured image and reconstructed weld pool [114]	15
3.1	Proposed mobile machine vision system	19
3.2	Illustration of weld actions	21
3.3	Initial setup of the sensing system	23
3.4	Projection and reflection of dot matrix pattern	24
3.5	Example of projection and reflection patterns. (A) 7×7 Projection pattern example; (B) The corresponding reflection pattern on the imaging plane .	25
3.6	Illustration of two kinds of correspondences	25
3.7	The configuration of the moving shield glass and the fixed torch	26

3.8	Illustration of the pattern L_2 in the auxiliary coordinate system $(xyz)_{L_2}$	28
3.9	Illustration of the pattern L_1 and its reflection in the shield glass	29
3.10	The configuration of the flexible torch and the fixed shield glass	31
3.11	The convex spherical weld pool simulation	33
3.12	The two patterns on the shield glass at initial position	33
3.13	The translations of the helmet to boundary positions where $D_{mh} =$ (a) [36.20, 125, 20] mm, (b) [-36.20, 125, 20] mm, (c) [0, 139.90, 20] mm and (d) [0, 93.50, 20] mm, (e) [0, 125, 36.02] mm, (f)[0, 125, -0.20] mm.	34
3.14	The rotations of the helmet to boundary positions where $\Theta_{mh} =$ (a) [30°, 0°, 0°], (b) [-3.51°, 0°, 0°], (c) [0°, 21.5°, 0°] and (d) [0°, -21.5°, 0°], (e) [0°, 0°, 33.8°], (f)[0°, 0°, -33.8°].	35
3.15	The boundary positions for the torch's rotation where $\Theta_{mt} =$ (a) [12.65°, 0°, 0°], (b) [-3.20°, 0°, 0°], (c) [0°, 19.91°, 0°] and (d) [0°, -19.91°, 0°], (e) [0°, 0°, 17.46°], (f)[0°, 0°, -17.46°].	36
3.16	The experiment set-up	36
3.17	The acquired image as the sensing system in initial position in using the experiment setup	37
3.18	Captured image of reflection pattern in helmet rotation where the helmet is at the boundary positions of: A) Positive x-axis direction; B) Negative x-axis direction; C) Positive y-axis direction; D) Negative y-axis direction; E) Positive z-axis direction; and F) Negative z-axis direction.	38
3.19	Captured image of reflection pattern in torch rotation where the torch is at the boundary positions of: A) Positive x-axis direction; B) Negative x-axis direction; C) Positive y-axis direction; D) Negative y-axis direction; E) Positive z-axis direction; and F) Negative z-axis direction.	39
4.1	The A) radial and B) tangential distortion of the camera used in this study	42
4.2	Results of camera and imaging plane calibration: A) The original image of the chessboard; B) Result of camera distortion correction; C) Result of frontal parallel view for the chessboard; and D) The conversion to the $(xyz)_{A_2}$ coordinate system.	43
4.3	The original captured image and the calibrated image in A) and B) respectively	44
4.4	Results of grid pattern identification: A) The example image; B) Result of Hugh Transformation; C)The grid pattern	45
4.5	Captured image of dot matrix reflection. A) Original image; B) Brightness-enhanced image.	45
4.6	Flowchart for the proposed recognition procedure	46

4.7	Results of the image processing. (A) resultant image of wavelet noise reduction, brightness of the image is deliberately enhanced for readability purposes; (B) resultant image of top-hat operation and gray stretch; (C) histogram of the image in Figure. 4.7b; (D) resultant image after the binary segmentation, the unit of both axes is pixel.	48
4.8	Histogram of dot size	50
4.9	Identification of reflection pattern. (A) dots in the captured image before the proposed adaptive thresholding, those dots includes both the reflected laser dots and the fake dots; (B) identified reflected laser dots.	51
4.10	Illustration of fitted curves of the rows	52
4.11	The illustration of a 3-dimension discrete parameter space. $[(i_1)_{\min}, (i_1)_{\max}]$, $[(i_2)_{\min}, (i_2)_{\max}]$ and $[(i_3)_{\min}, (i_3)_{\max}]$ are the ranges of the three coefficients i_1, i_2 and i_3 , which are divided into n, m and k segments, respectively.	53
4.12	The row cluster selection algorithm	54
4.13	Results of pattern recognition. (A) results of row identification; (B) reflected dots in different rows; (C) reflected rows matching with the corresponding incident rows in the dot matrix. The numbers represent the incident rows in the dot matrix that the reflected rows match respectively; (D) column recognition with fitted line.	56
4.14	The results of the proposed image processing and pattern recognition	57
4.15	Image captured in the first experiment	60
4.16	Results of pattern recognition in the first experiment	61
4.17	The resultant pattern recognition rate in the first experiment	62
4.18	Noise reduction rate in the first experiment	62
4.19	Thresholding error rate in the first experiment	63
4.20	Noise reduction rate for the robustness experiments from (a) category 1; (b) category 2; and (c) category 3	63
4.21	Thresholding error rate for the robustness experiments from (a) category 1; (b) category 2; (c) and category 3	64
4.22	Pattern recognition rate for the robustness experiments from (a) category 1; (b) category 2; (c) and category 3	64
5.1	Torch orientations for different welds types in GTAW process: (A) butt welds; (B) lap joint; (C) T-joint; and (D) Corner joint.	68
5.2	Torch orientations for different welds types in non and low alloyed steel GMAW process: (A) 2F/PB-horizontal-vertical fillet; (B) 3G \uparrow /PF-vertical up root pass and (C) fill passes; and (D) 4G/PE-overhead.	69
5.3	The illustration of torch and IMU which is rigidly amounted on the torch handle by a hard plastic fixture. ${}^t(XYZ)$ and ${}^s(XYZ)$ denote the 3-D Cartesian coordinate system for the torch and the WIMU, respectively.	71

5.4	Estimated and reference orientation (in Euler angle) at sampling rate of $f_s = 128$ Hz for A) x -axis using data set D_1^s . B) y -axis using data set D_2^s , and C) z -axis using data set D_3^s	83
5.5	RMSEs of orientation in Euler angle at sample rate of $f_s = 51.2$ Hz for A) $RMSE_x$, B) $RMSE_y$, and C) $RMSE_z$ using data set D_4^s	84
5.6	The obtained unit-norm quaternion of rotation from data set D_4^s using Method A at sampling rate $f_s = 51.2$ Hz. The quaternion components are dimensionless.	84
5.7	Orientation estimations in (A) x -axis, (B) y -axis and (C) z -axis, and D) the unit-norm quaternion components in a GTAW experiment using the proposed estimation algorithm, i.e., Method A. The used data set is D_1^e . The weld type is lap joint correspond to Figure. 5.1b	86
5.8	Orientation estimations in (A) x -axis, (B) y -axis and (C) z -axis, and D) the unit-norm quaternion components in a GMAW experiment using the proposed estimation algorithm, i.e., Method A. The used data set is D_2^e . The weld type is horizontal vertical fillet correspond to Figure. 5.2a	87
5.9	Orientation estimations in (A) x -axis, (B) y -axis and (C) z -axis, and D) the unit-norm quaternion components in one GMAW experiment using the proposed estimation algorithm, i.e., Method A. The used data set is D_2^e . The weld type is vertical up root pass correspond to Figure. 5.2b	88
5.10	Orientation estimations in (A) x -axis, (B) y -axis and (C) z -axis, and D) the unit-norm quaternion components in a GMAW experiment using the proposed estimation algorithm, i.e., Method A. The used data set is D_2^e . The weld type is vertical up root pass correspond to Figure. 5.2c	89
6.1	Illustration of coordinate systems (CS) : Universal fixed CS $((xyz) _U)$, A_1 internal CS $((xyz) _{A_1})$, A_2 internal CS $((xyz) _{A_2})$, and weld pool moving CS $((xyz) _w)$	92
6.2	Illustration of the shield glass plane in the auxiliary coordinate system. Grid patten is imaged in the plane.	94
6.3	Illustration of the weld pool boundary model	96
6.4	Illustration of the projection and reflection dot matrix patterns	96
6.5	Illustration of the projected laser dot in ζ^{th} row (an arbitrary row) of pattern L_1 . Along the x_{p_ζ} -axis, the short dash lines are the row slopes at the dots projected on the pipe surface. The dash curve below the axis is the desired curve of the row that satisfies the row slopes at each new dot along the curve.	98
6.6	Flowchart of the reconstruction algorithm. K_{row} is the number of the rows in the matrix pattern reflected by the weld pool surface.	101
6.7	Results of weld pool reconstruction	102

6.8	Corresponding results of image processing for images where helmet rotates to the boundary positions of: A) Positive x-axis direction; B) Negative x-axis direction; C) Positive y-axis direction; D) Negative y-axis direction; E) Positive z-axis direction; and F) Negative z-axis direction.	104
6.9	The reconstruction results of the spherical convex mirror as the helmet rotates from the initial positions to the boundary points along: A) Positive x-axis direction; B) Negative x-axis direction; C) Positive y-axis direction; D) Negative y-axis direction; E) Positive z-axis direction; and F) Negative z-axis direction.	105
6.10	Orientation of the helmet where helmet rotates from the initial positions to the boundary positions of: A) Positive x-axis direction; B) Negative x-axis direction; C) Positive y-axis direction; D) Negative y-axis direction; E) Positive z-axis direction; and F) Negative z-axis direction.	106
6.11	M_c , ARE and MRE of weld pool reconstruction as the helmet rotates to the boundary points along: A) Positive x-axis direction; B) Negative x-axis direction; C) Positive y-axis direction; D) Negative y-axis direction; E) Positive z-axis direction; and F) Negative z-axis direction.	107
6.12	Corresponding results of image processing for images where torch rotates to the boundary positions of: A) Positive x-axis direction; B) Negative x-axis direction; C) Positive y-axis direction; D) Negative y-axis direction; E) Positive z-axis direction; and F) Negative z-axis direction.	108
6.13	The reconstruction results of the spherical convex mirror as the torch rotates from the initial positions to the boundary points along: A) Positive x-axis direction; B) Negative x-axis direction; C) Positive y-axis direction; D) Negative y-axis direction; E) Positive z-axis direction; and F) Negative z-axis direction.	109
6.14	Orientation of the helmet where torch rotates from the initial positions to the boundary positions of: A) Positive x-axis direction; B) Negative x-axis direction; C) Positive y-axis direction; D) Negative y-axis direction; E) Positive z-axis direction; and F) Negative z-axis direction.	110
6.15	M_c , ARE and MRE of weld pool reconstruction as the torch rotates to the boundary points along: A) Positive x-axis direction; B) Negative x-axis direction; C) Positive y-axis direction; D) Negative y-axis direction; E) Positive z-axis direction; and F) Negative z-axis direction.	111
7.1	Illustration of an interpretation of human welders' behavior	114
7.2	Illustration of the weld pool boundary model	116
7.3	Schematic of the cross section of weld pool in the oyz plane	117
7.4	Measured 3D weld pool surface parameters from 36 experiments. The values of the convexity and area have been adjusted for illustration purpose . . .	117
7.5	Cross-section of full-penetration weld, the current is 56 A, arc length is 4 mm, and welding speed is 1 mm/s	118

7.6	3-parameter model estimation of backside weld bead using the width, length, and convexity	119
7.7	Demonstration of a manual control system of GTAW process	122
7.8	The random speed period in the identification experiment. (a) current and speed; (b) length; (c) width; (d) convexity. The range for each variable is given in each plot and corresponds to $[0, 1]$ in the normalized scale.	125
7.9	Comparison of estimated current and current adjustment using the two models in Table 7.2. (a) and (b) shows the estimation results using the Model 1, and the estimation results of Model 2 are shown in (c) and (d).	126
7.10	Step responses of the human welder model which are step responses for (a) the width, (b) the length and (c) the convexity	127
7.11	Results of the verification experiments at different arc length, (a) Standard deviation; (b) Correlation coefficients. The square and error bar for the experiments at each arc length are the average value and the range of the two values from the verification experiments conducted at this particular arc length.	128
8.1	Demonstration of experimental set-up.	131
8.2	Results from experiment with initial current 50 A. a) the current and voltage; b) the backside weld bead width; c) the backside weld bead (the unit of x and y axis is pixel)	132
8.3	Results from experiment with initial current 54 A. a) the current and voltage b) the backside weld bead width c) the backside weld bead (the unit of x and y axis is pixel)	132
8.4	Diagram of control system of the human welder response model with additional low-pass filter	133
8.5	Current and voltage of the experiments with initial current (a) 50 A, (b) 54 A, (c) 58 A and (d) 62 A	135
8.6	The backside appearance of the weld bead with initial current (a) 50 A, (b) 54 A, (c) 58 A and (d) 62 A	135
8.7	The backside width of weld beads with different initial current	136
8.8	Current and voltage from arc length robustness experiments with arc length (a) 2 mm, (b) 3 mm, (c) 4 mm, and (d) 5 mm.	136
8.9	The backside weld beads from arc length robustness experiments with arc length (a) 2 mm, (b) 3 mm, (c) 4 mm, and (d) 5 mm.	137
8.10	The backside width of weld beads from arc length robustness experiments	137
8.11	Front side of the weld joint before experiment for joint gap robustness experiments. (a) 0 nominal joint gap; (b) 2 mm nominal joint gap; (c) nominal joint gap increases from 0 to 5 mm (0.21 inch); (d) close review of the wide gap for marked area in (c).	138

8.12	Current and voltage from joint gap robustness experiments. (a) 0 nominal joint gap; (b) 2 mm nominal joint gap; (c) nominal joint gap increases from 0 mm to 5 mm.	138
8.13	The backside appearance of the weld beads from joint gap robustness experiments.(a) 0 nominal joint gap; (b) 2 mm nominal joint gap; (c) nominal joint gap increases from 0 mm to 5 mm.	139
8.14	The backside width of weld beads from joint gap robustness experiments.	139
8.15	The experimental setup for manual GTAW process	140
8.16	M_c , ARE and MRE of weld pool reconstruction as the helmet translates to the boundary points along: A) x-axis; B) y-axis; C) z-axis	141
8.17	M_c , ARE and MRE of weld pool reconstruction as the helmet rotates to the boundary points along: A) x-axis; B) y-axis; C) z-axis	141
8.18	M_c , ARE and MRE of weld pool reconstruction as the torch rotates to the boundary points along: A) x-axis; B) y-axis; C) z-axis	141
8.19	The backside weld bead width for the 9 experiments for human-machine cooperative control in A) helmet translation; B) helmet rotation; and C) torch rotation	142

Chapter 1

Introduction

1.1 Background

Gas tungsten arc welding (GTAW), as shown in Figure. 1.1, is the primary process used by human welders for applications where precision joining is critical for the services [92]. In the figure, an arc is established between the non-consumable tungsten electrode and base metal. The base metal is melted by the arc forming a liquid weld pool that joins the two pieces of base metal together after solidification. An optional filler metal (not shown in the figure) can be added if necessary.

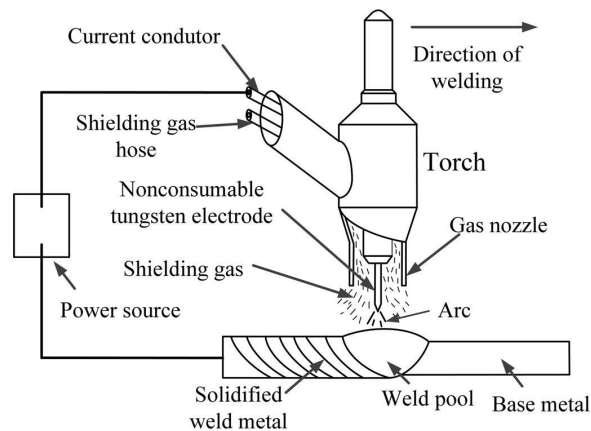


Figure 1.1: Illustration of Gas tungsten arc welding

Because GTAW is primarily used in applications where appropriate degree of full penetration (if and how much the liquid metal has fully penetrated the entire thickness of the base metal) is critical for the service, the process should be mechanized or automated as long as it can be justified for production cycle, cost, and quality. However, there are a number of issues which adversely affect the automation significantly. The first one is the accessibility. That is, in many applications there is no sufficient space to allow a mechanized system's torch head to access. Second, mechanized systems require significant amount of time for on-site installation and joints be prepared with great precision. The production cycle in many applications is adversely affected substantially. The third issue is the assurance of

the weld quality. In manual arc welding, skill welders can appraise the state of weld joint penetration through their observation on the weld pool and intelligently adjust the welding parameters (e.g., current, welding speed, arc length and torch orientation) accordingly to control the welding process for the desired state of weld joint penetration.

However, critical welding operations require welders to concentrate consistently in order to react rapidly and accurately. Fatigue and stress build up quickly so that welders' capabilities degrade rapidly. The welding quality might not be assured then. On the other hand, in mechanized welding, no welder has the capability to interference with the system; they are not required or allowed in robotic welding to observe the welding process with the similar level of concentration as in manual operation. Mechanized/automated systems rely on precision control of joint fit-up and welding conditions and tedious programming of welding parameters to produce repeatable results. However, precision control of joints and welding conditions is very costly and not always guaranteed. Up to date, there are no satisfactory sensors/ways that can be conveniently carried by the torch to automatically monitor the penetration depth (how far the liquid metal penetrates along the thickness of the base metal) or the degree of the full penetration like a skilled welder.

There are major differences between robotic and manual welding in sensing techniques and control strategies. It takes countless hours of practice to train a human welder to acquire accurate and enough quality related information using his/her sophisticated sensing system. In the scope of the author's limited searching capability, there is no literature addressing on what the information they are exactly, let alone adapting these sensory inputs to robotic welding control. For automatic welding applications, involving through-the-arc sensing technique have been extensively studied, and employed into commercial use and in manufacturing industry ([3],[24], [84]). Since a weld pool contains abundant information of the weld quality, a number efforts have been devoted to sensing weld pool related parameters using a few methods including vision technology, pool oscillation, acoustic emission, ultrasonic, X-ray radiation, and etc.([13],[116],[19],[138],[91], [111]).

For the control of a robotic welding process, conventional quantitative techniques of system analysis through the use of difference, differential, and integral equations to model and control the mechanized aspects of welding. The implementation of a automatic welding control require physically weld understood mechanistic approaches and mathematically feasible sensors and control algorithms. The ability of a skilled human welder to control the welding process is not due to a fundamental understanding of the laws of physics, but based on the feedback sensory information which might be imprecise or partial truths.

1.2 Objective and Approach

As mentioned in the last section, both robotic and manual welding process have their advantages and limits, i.e., human welders are versatile with sufficient experience and skill for critical applications, while they have their physical limitation. Robotic welding is suitable for precision and repeated, massive production applications, but it is not easy to set up. This study tries to combine the flexibility and experience from welders with accurate machine supervision. To this end, as a part of NSF project "Machine-Human Cooperative Control of Welding Process", the objective of this study is to build a so-called cooperative control system in which by using vision feedback a machine algorithm determines the

adjustment to human welder operated process based on model prediction of human and process responses. Specifically, the tasks of this study are

1. To take advantage of human welder's natural movement to facilitate an automatic process monitoring;
2. To model how a human welder responds to the welding process;
3. To model how the welding process responds to human welder actions;
4. To formulate a so-called machine-human cooperative control scheme;
5. To demonstrate the effectiveness of the cooperative control using full circumferential pipe welding as a case study.

The proposed machine vision system should be able to "see" the weld pool in the way as a human welder observes the welding process in real-time. Thus a scheme of weld pool reconstruction is required. The major difficulties for weld pool monitoring is the bright arc and specular weld pool surface. The approach to observe weld pool surfaces is extend from previous work. In the proposed machine vision system, a structured light laser pattern (dot matrix) produced by a low-power illumination laser diode is projected onto the weld pool surface and the corresponding specular reflection is observed on a imaging plane which is captured by a camera. Because the arc radiation decays very fast with the travel distance while the reflection of the projected laser almost remains its intensity, it is possible that the reflection of the projected laser can be clearly imaged on the imaging (interception) plane. The dynamic changes of the weld pool surface can be implicitly observed the reflection's formation. The shape of the reflection is determined by the weld pool surface. Therefore the reflection is utilized for weld pool reconstruction in this study.

For our specific machine vision system which should move along with the torch, the spatial relations amid the components (dot matrix laser pattern, weld pool and the imaging plane) of the system are also required for the accurate weld pool reconstruction. In the proposed system, the pattern is mounted on the torch, the camera is attached on top of the helmet. The helmet's shield glass is the imaging plane. In addition to the mobility of the vision system, one extra structured light pattern (grid pattern) and two inertia measurement units (IMU) are applied to calculate the spatial positions and orientations.

To this end, the main approach to reach objective in this dissertation including following steps:

1. Design the mobile machine vision system and analyze the feasibility of the proposed system;
2. Apply machine vision techniques to extract useful information from the captured reflected images;
3. Detect the positions and orientations for the torch and helmet using a Kalman-based estimation algorithm;

4. Develop reconstruction scheme to effectively rebuild the three-dimensional weld pool surface based on the reflection patterns from the acquired images and the orientations of the torch and the helmet;
5. Develop the models for human welder behavior in response to the weld pool variation.
6. Formulate the cooperative control process and demonstrate the machine vision system and the control process in the pipe GTAW processes.

1.3 Organization

In this dissertation, a cooperative control process with a mobile machine vision system is developed to assist a human welder to perform quality weld in manual GTAW process. The main research steps and results are discussed sequentially in the following chapters. The relationships among the chapters are shown in Figure 1.2.

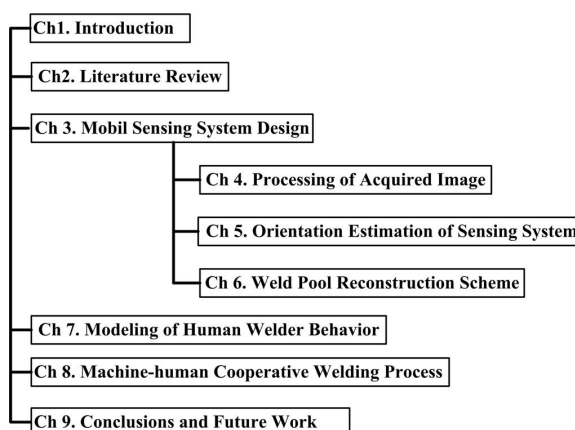


Figure 1.2: Organization of the dissertation

Chapter 1: Introduction

The background and motivation of this dissertation are illustrated, as well as the the objectives of this study.

Chapter 2: Literature Review

In this section, the sensing techniques of welding process are introduced, including the vision-based techniques and other techniques such as the infrared radiation, ultrasonic, acoustic emission sensing, and so on. Furthermore, control schemes of welding process are also introduced.

Chapter 3–6 present the design of a mobile machine vision system, as well as the associated image process algorithm and weld pool reconstruction algorithm.

Chapter 3: Mobile Sensing System Design

An innovative mobile machine vision sensing system is proposed, which consists of a dot matrix laser pattern, a grid pattern, a compact camera, a torch, a helmet, and two inertia measurement units. In this system, the dot matrix pattern attached on the torch is projected onto the molten specular weld pool surface, and the reflection is intercepted by the shield glass of the helmet. At the same time, the reflected image is captured by the camera mounted on the helmet. The grid pattern and the two IMUs are applied to detect the spatial relations amid the torch, weld pool and the helmet. In this chapter, the system configuration is described. The analysis and simulation are detailed to verify the feasibility of the proposed system. At last the reflection images are captured using the vision system.

Chapter 4: Processing of Acquired Images

The proposed vision system is calibrated in details in this chapter. An imaging processing algorithm is then developed to extract the dot matrix reflection and other useful information. The corresponding pattern recognition is proposed accordingly.

Chapter 5: Orientation Estimation of Sensing System

A kalman-based orientation estimation algorithm is developed in this chapter to detect the orientation for both the torch and the helmet. The IMU is used to provide the acceleration and the angular rate of the torch/helmet. Using both the measurements, a new Unscented Kalman Filter (UKF) algorithm to detect the orientation of the torch/helmet which is formulated in a new formation.

Chapter 6: Weld Pool Reconstruction Scheme

Based on the achieved information, a weld pool reconstruction scheme is discussed in details. First of all, the spatial relations of torch, helmet and the weld pool surface is mathematically formulated. The reconstruction algorithm is derived based on the slopes of the projected dots on the weld pool surface. The process is performed row by row of the reflection pattern. To demonstrate the accuracy of the proposed algorithm, an example of reconstruction is detailed later in this chapter.

Chapter 7: Modeling of Human Welder Behavior

The models of a novice human welder's adjustment on current in response to the weld pool variation are developed and analyzed in this chapter. The weld pool surface is characterized first in order to find out what kind of information a welder obtains from observation of weld pool. The length, width and convexity of the weld pool are found to be an optimal set of parameters to characterize the weld pool. Second, experiments are designed and performed to develop models of human welder behavior. The models are further verified for accuracy

and robustness.

Chapter 8: Human-machine Cooperative Welding Process

In this chapter, the model obtained in Chapter 7 is applied to a robotic GTAW process to control the process to a desired and consistent penetration status. To verify the effectiveness of the model, the welding process is set up with different initial current, arc length, and other disturbances. Furthermore, the obtained model is applied in manual GTAW process to formulate a cooperative welding process. Experiments are designed and conducted to verify the cooperative welding process.

Chapter 9: Conclusions and Future Work

The main findings and contributions are concluded and the future research work to improve this study is also introduced.

Chapter 2

Literature Review

2.1 Overview

Welding process has been widely applied in manufacturing industries, such as automotive assembly, aircraft production, micro-electric components joining, and etc. Intelligent and accurate control of a welding process is the becoming the trend for next generation welding machine. The major challenge in both industry and academic communities is to monitor and control the welding quality fast, reliably and cost-effectively. Therefore, on-line sensing and control systems have been developed with various techniques.

Gas Tungsten Arc Welding (GTAW) is one primary manual welding process used to produce high-quality weld due to its capability in precision control of the process [119]. In GTAW a non-consumable tungsten electrode to strike an arc between work piece and the electrode. The weld area is protected by an inert shielding gas, usually argon or helium, from atmospheric contamination. A welding power supply produces energy which is conducted across the arc through a column of highly ionized gas and metal vapors. GTAW is most commonly used to weld thin sections of stainless steel and non-ferrous metal such as aluminum, magnesium, and copper alloys [137].

Among the parameters to decide the quality of the welding process, the penetration depth is the most important criterion which can be further measured and deduced by the back-side bead width during welding process [71, 100]. There are three different penetration statuses in welding process from the profile view, shown in Figure. 2.1.

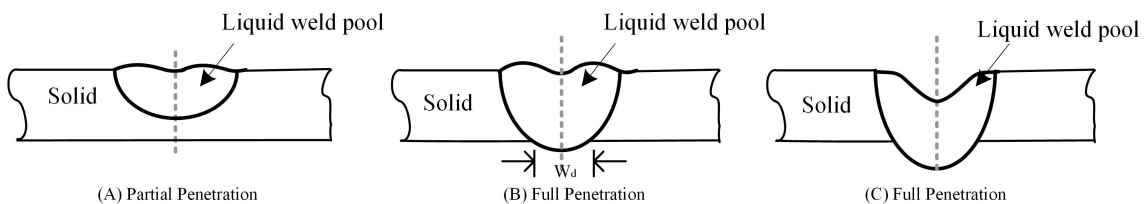


Figure 2.1: Different penetration statuses in welding process[81]

The full penetration is generally desired for some critical applications due to its high quality in terms of the weld's mechanical properties, appearance, and micro-structure features.

However the welding process of full penetration is also every different to establish. Closed control strategies might be applied for welding robots with full penetration requirements. A human welder must acquire sufficient skills and experience to conduct a full penetration welding process. Partial penetration status is comparatively easy to accomplish for both robotic and manual welding. It is commonly used for components with less critical requirements. Over penetration, on the other hand, should be avoided since it does not meet most of the quality standards due its concave appearance and its damages to the material properties.

The penetration statuses are the outcomes of different welding situations, which are depends on metal properties, surface conditions, welding parameters. In manual welding, human welders are the complex vision sensor and welding parameters' controller. In this chapter, some vision-based weld pool observation techniques are introduced first. Then other different methods used for sensing the welding process, such as ultrasonic, acoustic sensors are reviewed. Then the control strategies of welding process are finally introduced.

It should be noted that those sensing methods are applied robotic gas tungsten arc welding, gas metal arc welding (GMAW) and plasma arc welding (PAW). None of them are so far used in manual welding.

2.2 Sensing Techniques of Welding

Monitoring and measuring of the welding process is the core of the development for next generation intelligent welding robots. The difficulty of weld pool sensing is primarily due to the invisibility of the liquid metal *bottom surface* underneath the weld pool and the extreme brightness of the arc and various methods have been studied, including pool oscillation, ultrasound, infrared sensor, etc. The pioneering work in pool oscillation was conducted by Richardson [97], Hardt [141] and their co-workers. den Ouden found an abrupt change in the oscillation frequency of the pool during the transition from partial to full penetration ([140, 13]).

Although the two-dimensional (2D) weld pool geometry has been obtained with different techniques ([16], [43],[53]), the convexity/deformation of the weld pool is not yet fully explored. Early researches have found that important information such as weld defects and penetration are contained in the surface deformation of the weld pool ([80, 103]). A recent study suggests that compared with the 2D weld pool geometry, the three-dimensional (3D) geometry can better predict the weld penetration which is measured by the backside weld bead width [146]. Therefore, numerous methods have been developed to reconstruct the 3D weld pool surface.

The measurement of 3D surface has been recently studied extensively with techniques which can be roughly categorized into three branches: 1) reflectometry/deflectometry with fringe reflection technique ([122], [163], [59]); 2) phase shifted digital fringe projection technique for diffuse objects ([145, 144]); 3) shape from shading technique [17]. Unfortunately, the dynamic and specular nature of the weld pool and the interference from the strong arc radiation complicate the observation and deteriorate the effectiveness of most of those methods.

In this section, the vision-based sensing techniques and other method are introduced, respectively.

2.2.1 Vision-based Techniques

In welding process, vision-based sensors are applied to determine the state of the weld pool. Although some vision sensors are used for weld seam tracking, these are not in the scope of discussion in this thesis. Generally, vision sensors are mimics of human welder's eyes, i.e., to acquire the image of the weld pool, and the image processing is done that to identify the shape of the weld pool. Then the related control algorithms will be applied to adjust the welding process for specific quality-related requirements. Usually, the vision sensors can be sorted into two categories: two-dimensional and three-dimensional.

Two-dimensional weld pool sensing

Two-dimensional (2D) shape of the weld pool has been studied by many methods. By using one or multiple cameras, the images of the front side weld pool profile are captured [108]. The weld pool 2D geometric parameters, e.g., length, width, area, are extracted and used as certain metrics to predict the penetration status.

The pioneer work of 2D weld pool profile sensing was done by Dr. Kovacevic and Dr. YuMing Zhang in the University of Kentucky [72], the experiment setup is shown in Figure. 2.2. The sensing system includes a high-power pulse laser, a high-speed camera and a system mobility controller. The wavelength of the laser is 337.1 nm. Attached by an optical filter in wavelength 330-340 nm, the camera is used to observe the weld pool profile with an angle to the welding direction. The laser is synchronized with the shuttle of the camera such that it can suppress the welding arc radiation when the camera is capturing the image of weld pool, which can be seen in Figure. 2.2. On-line weld pool edge detection is performed based on the grayness difference and its directional gradient among the weld pool, the heat affected zone (HAZ) and the base metal. Furthermore, the weld pool are was controlled by using an adaptive algorithm.

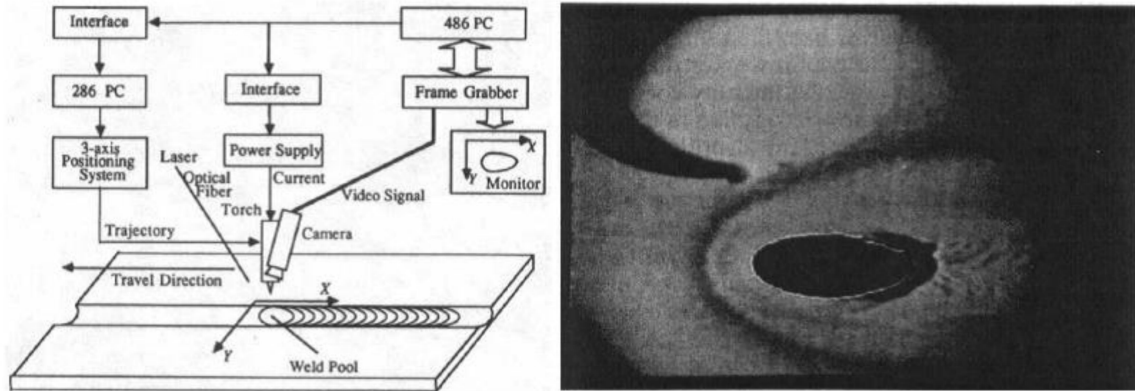


Figure 2.2: Experiment setup and the captured image [72]

Another important early work for 2D weld pool boundary detection is the co-axial viewing of the weld pool, proposed by Dr. Richardson et al [99]. In the study, the electrode is used to block the arc so that the weld pool boundary can be clearly detected using specific camera and image processing algorithm.

The co-axial viewing method has been extensively studied. One typical recent research is conducted by Dr. Balfour in 2006 [16]. The weld pool width is identified based on the grayness difference between weld pool and the base metal by an adaptive edge detection method. Figure 2.3 shows the experiment setup and the captured images. Furthermore, closed-loop process control is conducted using the obtained weld pool width as the feedback.

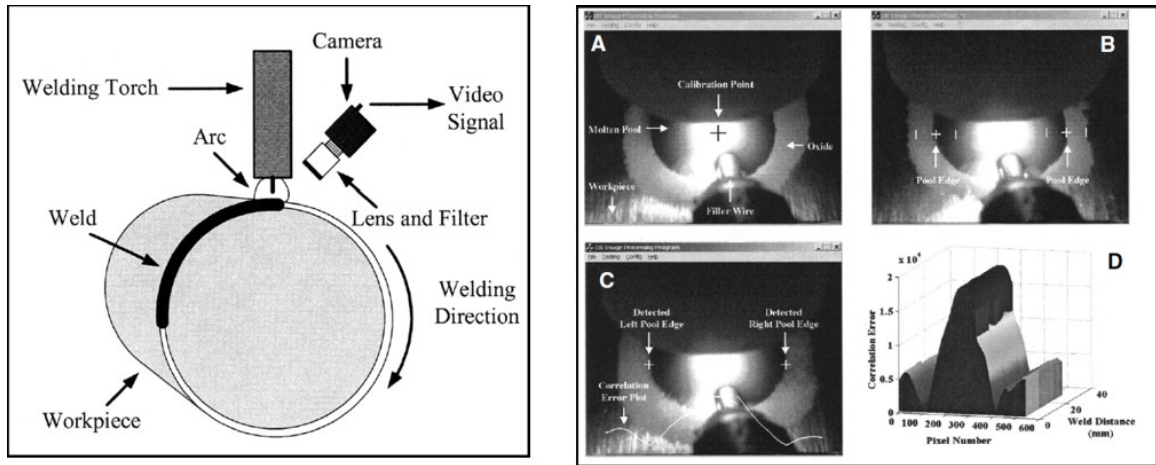


Figure 2.3: Experiment setup, captured and resultant images [16]

Multiple cameras are employed in the study conducted by Dr. Fan et al. in 2009 [43]. The front topside and back topside of a weld pool, as well as the back side weld pool are captured simultaneously using a three-routes optical sensing system, as shown in Figure 2.4.

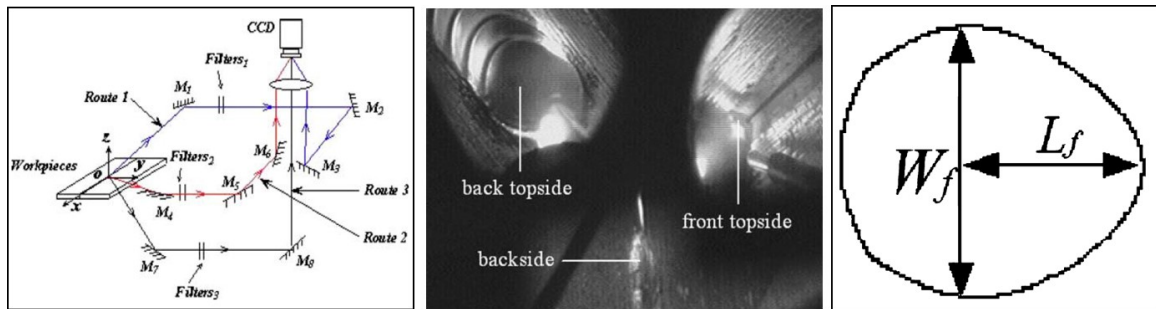


Figure 2.4: Experiment setup and the captured images [43]

With the complex sensing system, the whole boundary of the front side weld pool and the width of the back side weld pool can be obtained in real-time. A neuro-fuzzy adaptive process control algorithm was then proposed accordingly for a consistent penetration (back side weld pool width).

Similar work has been performed by Dr. Ma in 2010 [53], in which two cameras capture the head and tail part of the front side weld pool simultaneously. As shown in Figure. 2.5, two images that captured at the same time are processed to render the weld pool boundary.

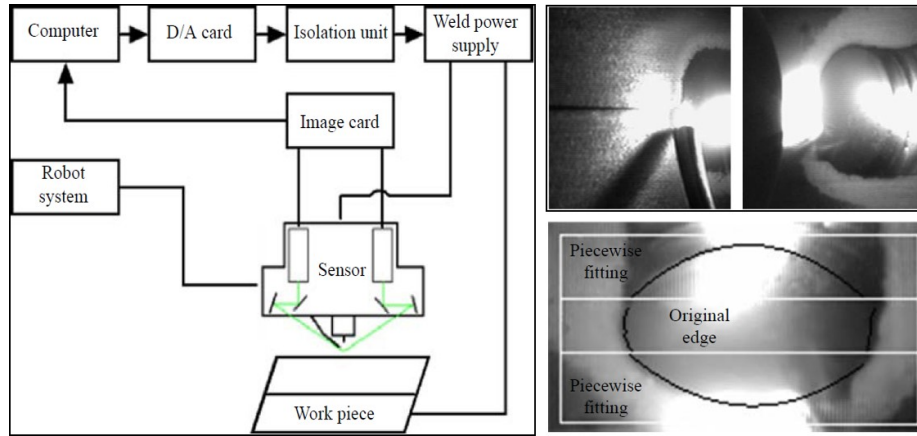


Figure 2.5: Experiment setup, captured and resultant images [53]

Three-dimensional weld pool sensing

The most popular techniques currently being studied for 3D weld pool measurement can be divided into four categories:

1. Model-based reconstruction

The 3D weld pool surface is partially reconstructed based on a simple model proposed in [143]. The experiment setup, 3D weld pool geometric model are shown in Figure. 2.6.

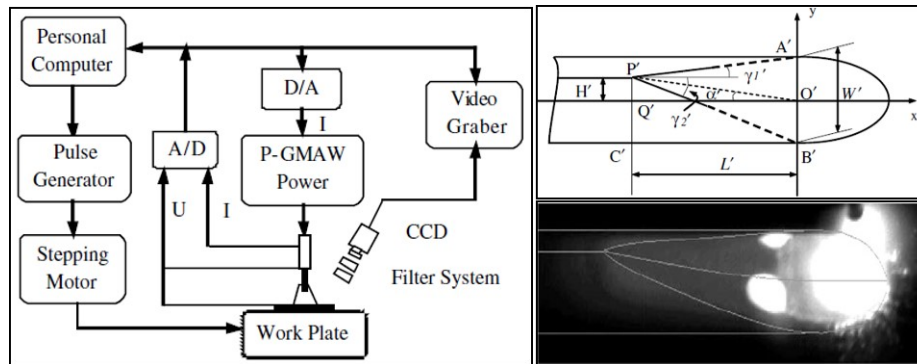


Figure 2.6: Experiment setup, captured image and the geometrical model [143]

The 2D weld pool images are captured under the base-current period in GMAW. The proposed model then uses the capturing angle of the camera and the 2D weld pool profile to calculate the weld pool width, the length of the pool tail, the height of the rear of the pool, etc. The resultant image is shown in Figure. 2.7.

The reconstruction algorithm is further applied in [139] for the weld shape control. Although the model-based reconstruction algorithm is simple and fast, it can only measure the height of the weld bead that is solidifying or already solidified at the rear of the weld pool. The 3D geometry of head of the weld pool cannot be acquired using this method. Further, the mode-based reconstruction algorithm only suits for thin work piece welding application.

2. Stereo-vision measurement

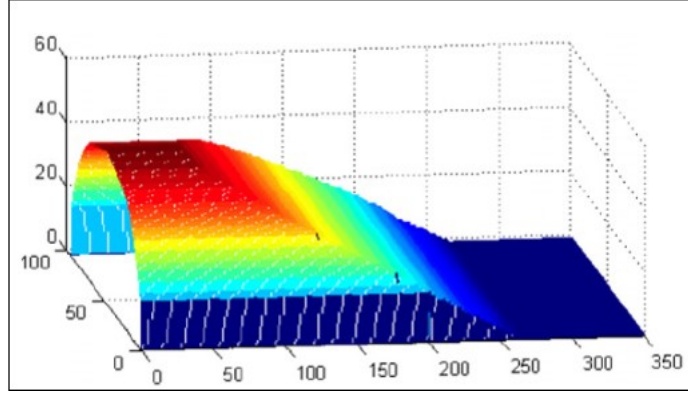


Figure 2.7: Resultant image using model-based weld pool reconstruction [143]

In [89], two cameras are synchronized to capture the two images of weld pool surface simultaneously in the short circuit period during the Surface Tension Transfer (STT) process. Based on specific calibration, the 3D weld pool surface can be reconstructed using the two images. The captured and resultant images are shown in Figure. 2.8.

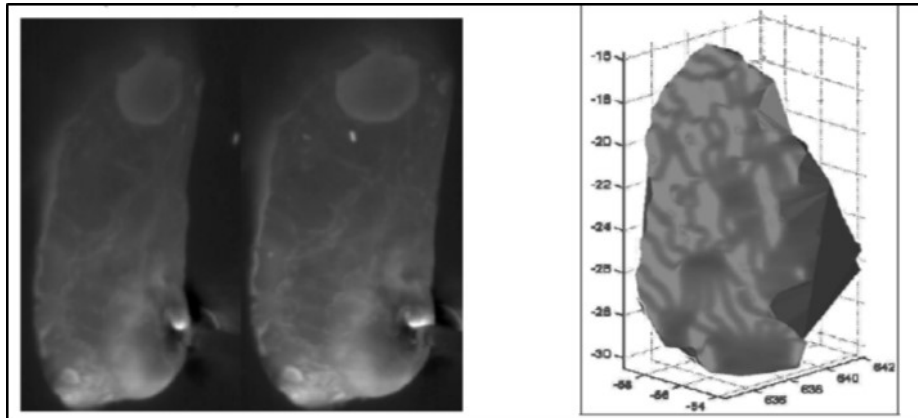


Figure 2.8: Captured image and resultant image of stereo-vision measurement [89]

A closed-loop control system is developed using the technique for robot welding process [117]. However, the shape of the bright part in the head of the weld pool cannot be acquired by using this method. The accurate reconstruction of the weld pool requires both precise synchronization of the two cameras and high quality of the captured images.

To avoid the synchronization problem, the biprism stereo vision sensing is proposed in which one camera is used with a biprism attached on its head [30], as shown in Figure. 2.9.

Only the height of the weld pool boundary is extracted in real-time, the 3D geometry inside the weld pool is missed. Furthermore, the reconstruction accuracy might be an issue since the visual differences are comparatively small between the two simultaneously captured images. A similar reconstruction algorithm has been utilized in a stereo sensing system using single camera with a stereo adapter developed to reconstruct the 3D weld pool for tracking particle flow on the weld pool surface [161].

3. Shape from shading reconstruction

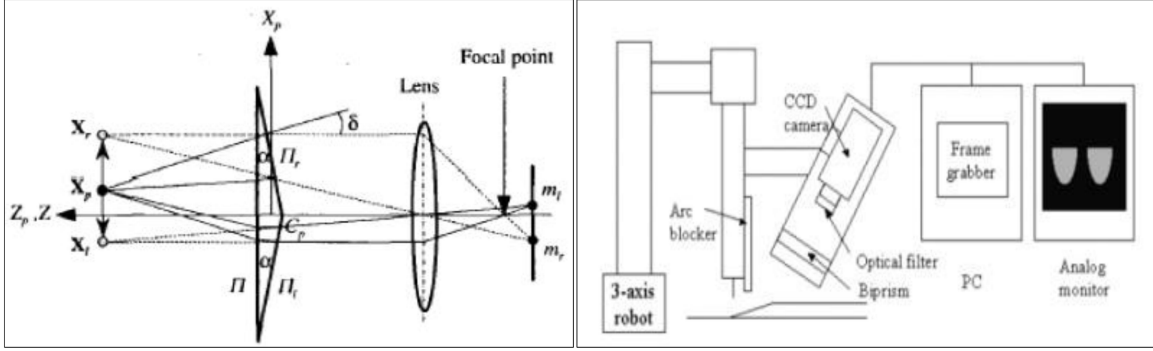


Figure 2.9: Biprism diagram and captured images[30]

3D weld pool reconstruction algorithms have also been proposed based on shape from shading method ([38], [132], [133], [78]).

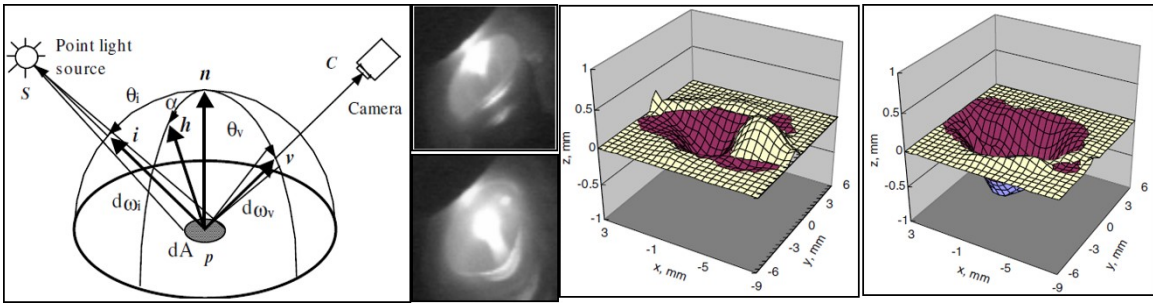


Figure 2.10: Shape from shape weld pool reconstruction, diagram, captured and resultant images[162]

The algorithms are usually complex and thus used for off-line reconstruction of the 3D weld pool surface. Furthermore, the reconstruction algorithms using shape from shading are based on two assumptions: 1) The object surface is a Lambertian surface which reflects light with equal intensity in all directions; 2) The camera and the light source are at the infinite far distance from the object surface. However, the weld pool is a specular surface which is not a Lambertian surface. The camera and light source in the experiment systems are not far enough from the weld pool to qualify the infinite far position assumption. Therefore, the 3D weld pool reconstruction using shape from shading might not be an ideal solution.

4. Structured-light based sensing

A structured-light vision system is developed in [71] projecting a pulsed laser on the weld pool surface through a special grid. A high shutter-speed camera is used to capture the laser stripe pattern reflected by the weld pool surface. An iterative algorithm is proposed to reconstruct the 3D weld pool surface without knowing the slopes of the surface. The experiment setup and resultant image are shown in Figure. 2.11.

The time cost of the reconstruction is about 1s. Also, the boundary of the weld pool is hard to extract using this sensing method. Follow-up study [107] provides a measurement system based on a mathematical model of weld pool surface. The captured image from [71] is applied as an example in the study. Although this work does not propose a new reconstruction algorithm, it provides some novel insights of 3D weld pool surface measurement.

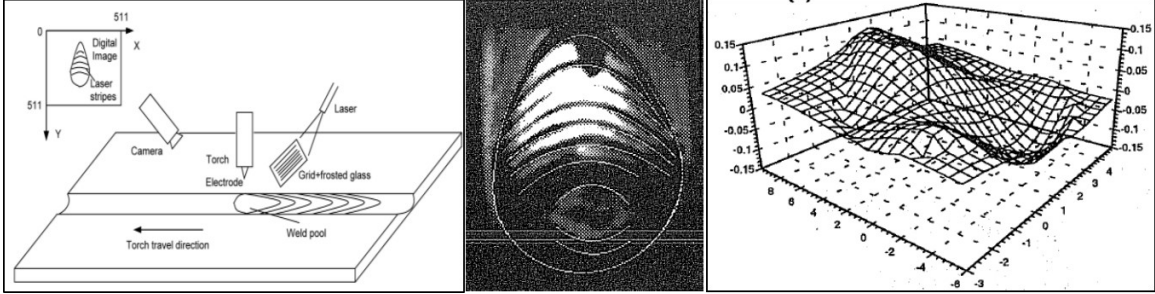


Figure 2.11: Experiment setup and resultant image of weld pool reconstruction[71]

A laser grating sensing technique is proposed in [10]. The reflected grating is captured by a two-lens system. The depth of weld pool is determined based on the phase changes of the deformed grating image [136], as shown in Figure. 2.12. However, using this method the boundary of the weld pool is hard to be determined. Further, it is only a primarily study since there is no detailed quantitative analysis of the reconstruction.

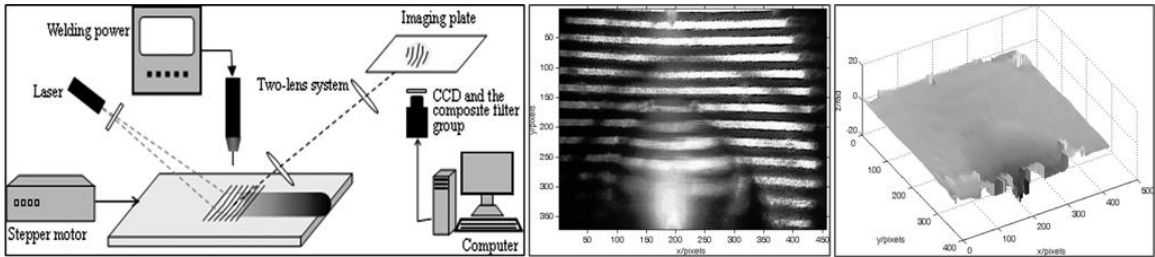


Figure 2.12: Diagram of the laser grating sensing system, captured image and reconstructed weld pool [136]

A novel reconstruction algorithm using the slope field and point tracking of the dot matrix has been proposed in [106]. Although the height reconstruction error is small, the point tracking procedure is complex such that the point matching for each frame requires to process three consecutive frames. It is thus only suitable for off-line reconstruction of 3D weld pool surface. Also, the boundary information of the weld pool in the reconstruction is not addressed.

In the University of Kentucky, a laser pattern reflected from the weld pool surface has been intercepted/imaged by/on a diffusive imaging plane placed with a distance from the weld pool [114]. The diagram of the sensing system is shown in Figure. 2.13.

The camera aims at the imaging plane (rather than the weld pool illuminated by the extremely strong arc) to acquire the reflected laser pattern. Its uniqueness lies in its simultaneous use of the distance and specular nature of the weld pool surface to significantly decay the arc radiation but not the intensity of the laser reflection from the specular weld pool surface despite the distance. To compute the weld pool surface from the reflected patterns, an iterative algorithm has been proposed using the slope field of the projected dot matrix. The slope differences between the neighborhood laser dots are used to find the estimated height of the weld pool surface. This slope error based algorithm requires numerous iterative loops till the estimated surface approaches the actual weld pool surface resulting in relatively large reconstruction errors. Similarly, this imaging method and reconstruction

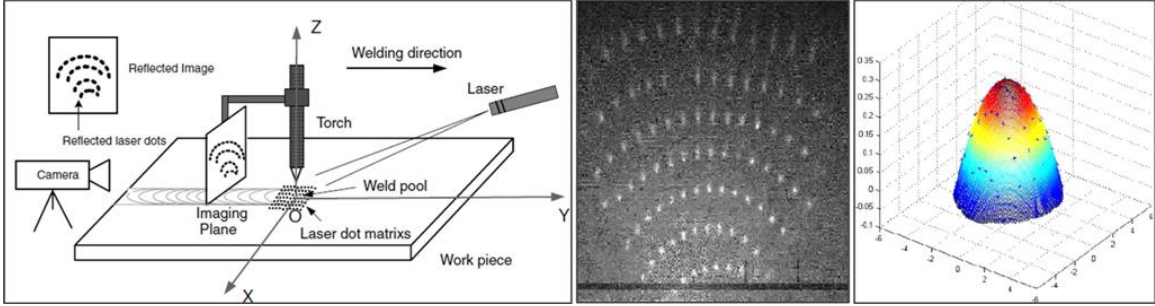


Figure 2.13: Diagram of the sensing system, captured image and reconstructed weld pool [114]

algorithm have been used to image and reconstruct the weld pool surface in gas metal arc welding (GMAW) using a five line laser pattern [83].

2.2.2 Other Techniques

Besides the vision-based sensing technologies, some other methods are also applied for the observation of weld pool surface, which are introduced from different areas. Here are some of the typical techniques:

1. Ultrasonic technique

Ultrasonic waves were applied to measure the depth of the penetration of a weld pool by locating the fusion interface between the weld pool and the work piece [113]. The ultrasonic wave is generation by an angled piezoelectric transducer in contact with the surface. The total wave path is shorter as the weld pool depth grows deeper.

For effective application of ultrasonic techniques, there are requirements to be met: 1) the work piece must have a simple, uniform surface with minimum irregularities to ensure good coupling between the work piece and the transducer; 2) Since the transducers must track the weld pool, the component vibration or unexpected probe movement must be prevented during the process; 3) Specific calibrations must be performed before used for practical applications.

2. Acoustic emission sensing method

Acoustic emissions can be generated by the stress upon on the weld pool surface in welding process, due to the thermal gradient and the change of the liquid metal volume. The acoustic emissions travel throughout the work piece and can be detected. The frequency spectrum of the acoustic emission can be found out an abrupt change as penetration status changes from partial to full penetration. In the acoustic emission sensing method [51], a stationary acoustic transducer remote from the weld can be used to measure the emission.

Although acoustic emission methods are extensively studied, there is a major issue in practical application, i.e, the relationship between the acoustic emissions and the weld penetration depth is not fully understood and some micro-structural features may also influence the performance. So acoustic emission monitoring is an instructive trial in this area, which can function independently of welding position, process and joint type.

3. X-ray radiation method

An early work using X-ray radiation (radiography) to detect the penetration status of the weld pool Dr. Rokhlin and Guu at the Ohio State University [103]. It was found that the radiation of the received of X-ray increases as the depth of the weld pool depression grows. Thus, the depression depth measured by the x-ray radiation can be considered as a metric for penetration status detection. However, the principle behind this method is to measure the material thickness. For full penetration where backside pool surface deformation occurs, the pool surface shape will be difficult to extract.

4. Thermal sensing technique

The thermal sensing technique takes the advantage of the difference in temperature of various penetration status, i.e., the penetration status is still leads to constant thermal gradient. In this method the temperature may be measured using a contact thermocouple or an infrared pyrometer or a camera [42].

Thermal sensing is the most widely applied technology in practical use and can also provide seam tracking. However, the thermal cameras require to be specifically calibrated before use for practical applications. these systems are particularly sensitive to variations in the surface condition and the emissivity of the material. The accuracy of camera-based systems is reduced by contributions from the arc light and this can be greatly overcome by the use of filters.

5. Weld pool oscillation sensing

Since arc press upon of the weld pool surface is proportional to welding current, the surface of the pool can be observed vibration in pulsed welding processes. Furthermore, the vibration frequency is dependent on the weld pool size, and can be found an abrupt reduction as the weld pool grows from partial penetration to full penetration. The oscillation frequency can be further monitored by measuring the fluctuations of either the arc voltage or the arc light reflection. Thus the weld pool oscillation sensing method was proposed [43].

Oscillation sensing technique's accuracy is degraded by the increases of the traveling speed, electricity power source ripple, sag, and the weld contamination, such as dirt, slag and oxide in the pool. Therefore, the application for this method is constricted.

2.3 Control of Welding Process

Arc welding process is tightly coupled system which is composed of the power sources, the arc, and possible wire feeder as well as any positioning system, other consumables, and the work piece. Several welding parameters used in most control systems are current, voltage, traveling speed, wire feed rate, electrode extension and torch angle. These parameters indirectly determine the attributes of weld quality, such as fusion zone geometry, residual stresses and distortion, mechanical properties, internal discontinuities, metallurgical structure, and etc.

An extensive amount of research has studied the control of welding process for years. However, large portion of the control techniques developed has not been applied in commercial applications, in which the control of one, or at most two, parameters of welding process

are mostly employed with classical feedback control, based on the assumptions of linear and time-invariant behavior of the controlled systems. This section will discuss some of the research and development that attempt to extend the commercial, state-of-the-art welding process controllers.

1. Adaptive control

Welding process is a complex, highly coupled, multivariable process. The highly non-linear relationship requires a feedback control system with self-tuning capabilities, such as adaptive control. An adaptive controller provides the robustness to maintain stable control process over the entire (linear and non-linear) operating range. Adaptive control algorithms have been developed for the non-linear operating regions of the arc-voltage arc length relationship [69].

2. Intelligent control Researchers working in the field of intelligent control typically derive a method to solveing a control application that is inspired by the decision-making process of humans. There are four intelligent control approaches most commonly used : fuzzy logic, neural networks, expert system, and generic algorithms.

Neural networks and genetic algorithms operate on unstructured data in the form of numbers, usually normalized between 0 and 1. Expert systems excel through the use of rules which operate on structured data in the form of words of symbols. Fuzzy logic can work well with both structured and unstructured data in the form of both symbols and numbers. Weld penetration is a typically target for the intelligent control. A single-input, single-output fuzzy controller was developed in [55] to capture the non-linear, time-varying thermal relation of the arc welding process.

Chapter 3

Mobile Sensing System Design

The assurance of the weld quality mainly relies on welders' skill and experience, i.e., welders have to consistently concentrate on the weld pool surface to react rapidly and accurately. However, human welders have physical restrictions such as fatigue and stress. Those limitations might degrade the welders' capabilities in daily operations; cause long-term health risks; and adversely affect the assurance of the weld quality and the production cycle of manufacturing. Therefore, it is critical to evaluate the weld quality and welders' performance during the weld.

Successful evaluation of a manual welding process requires a non-intrusion, portable, and real-time sensing system. Furthermore, the corresponding measurement scheme should be robust enough to guard the measurement accuracy against the disturbances caused by welders' operations. In robotic welding system, the augmentation of sensing components/systems is comparatively easy. Thus, numerous sensing techniques, as introduced in the last chapter, have been developed and applied in mechanized/automated welding to acquire weld quality information from the observation of weld pool. However, those aforementioned sensing techniques have been only proved valid for robotic welding process, few can be utilized to conveniently and automatically monitor the weld pool in manual welding. This chapter a mobile, non-intrusive sensing system is developed to measure the weld pool in manual welding for pipe application.

3.1 System Design

3.1.1 Configuration of the mobile sensing system

The configuration of the proposed sensing system is shown in Fig. 3.1. The structured lighted laser patterns, L_1 and L_2 , are mounted properly on the torch. The camera is attached on the helmet. Two inertia measurement units are attached on the shield glass and the torch, respectively. A 19×19 laser dot matrix pattern (L_1) is projected under the torch electrode and covers the whole possible weld pool region. Reflected by the weld pool surface, the laser pattern is intercepted by the shield glass in the welder's helmet. A camera mounted on the helmet captures images of the reflection pattern in the shield glass. Reflection from grid pattern L_2 , and data from IMUs A_1 , A_2 are utilized to determine the

spatial geometric relation amid the weld pool, torch and the helmet. Dot matrix reflection pattern along the spatial relation can reconstruct the profile of 3D weld pool surface.

The origin of the 3D Cartesian coordinate system $(xyz)_w$ is O_w , i.e., the center of the weld pool. It is defined as the interception for the extension of the torch and the pipe surface. Thus, the coordinate system slides around the pipe following the torch's rotation movement. The positive z -direction coincides with the normal direction at the center of the weld pool. The x_w -axis coincides with the pipe's axis (Γ_p) in directions.

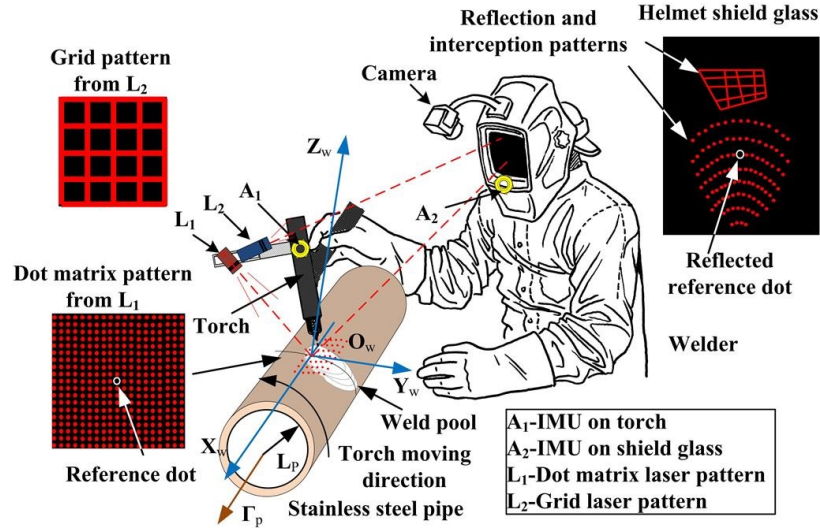


Figure 3.1: Proposed mobile machine vision system

Dot matrix laser pattern L_1

Structured-light laser pattern L_1 (Coherent SNF-519X-0.77-685-50, 95.1 (Length) \times 18.64mm (Diameter)) is mounted in the fixture which is perpendicularly connected to the torch. It projects a 19×19 dot matrix laser pattern covering the weld pool region. Since the liquid weld pool has a mirror-like surface while the surface of the solid pipe is not specular, only the pattern projected on the weld pool is thus specularly reflected in GTAW ([146], [147], [114]). With the torch hold by the welder as shown in Fig. 3.1, L_1 and the helmet are in different sides of the weld pool. The reflection pattern of L_1 is thus expected to be intercepted by and imaged on the shield glass in the helmet despite reasonable torch or head position adjustments. The range of the adjustment within which the reflection pattern can be successfully captured is detailed in section 3.2.2.

A 3D weld pool deforms the pipe surface, and the formation of reflection pattern varies accordingly. Therefore, it contains the geometry information of the 3D weld pool surface, and thus can be used for surface reconstruction.

Since arc light intensity decays significantly as it travels over distance while the intensity of laser remain almost the same, the sensing system thus takes advantage of this propagation difference such that clear images of the reflection pattern can be captured in the shield glass.

Grid laser pattern L_2

Structured-light laser pattern L_2 (Coherent SNF-504G-2.44-685-50, 95.1 (Length) \times 18.64mm (Diameter)) projects a 4×4 grid which is also intercepted by and imaged on the shield glass. The formation of the interception pattern is dominated by the the distance between the torch and the shield glass as well as their relative orientations. Therefore, it is used to determine the spatial geometry relations among the torch, weld pool and the shield glass. The formulation of the geometry relation, using the grid reflection pattern, as well as data obtained from IMU A_1 and A_2 , is detailed in Chapter 6.

Sensory helmet

The shield glass in the helmet is designed to intercept the two patterns (L_1 and L_2) such that 1) laser light from the two patterns is blocked from the welder's eyes and 2) the two patterns are clearly imaged on the glass. The camera (Flea 3 FL3-FW-03S1C-C) with a dimension of $29 \times 29 \times 30$ mm is mounted on the helmet which covers the whole view of shield glass so that the images on the glass can be captured. The camera captures the images of the reflected pattern from the imaging plane. The captured image is 8-bit monochrome with a resolution of 640×480 or 480×640 . A band-pass filter of 20 nm band-width centered at a wavelength of 685 nm is attached to the camera. A computer connects with the camera using a 9-pin 1394b interface. With a maximal frame rate of 200 fps (frame per second), the high transfer rate from the camera to PC (maximum rate 800Mbit/s) makes possible the real-time monitoring and measurement of the 3D weld pool surface in GTAW.

A welder would always try to find the best perspective to observe weld pool, this innovative sensing system takes advantage of welders' intelligent tracking capability to facilitate the sensing of the weld pool at (semi-)optimal locations.

IMU A_1 and A_2

Two IMUs (Shimmer kinetic sensors) are used in the sensing system as shown in Fig. 3.1: A_1 is mounted on the torch; A_2 is attached on the shield glass. The size of the IMUs is about $53 \times 32 \times 19$ mm. It is an IMU with wireless capability which is composed of a tri-axial accelerometer (Freescale MMA7260Q) , a tri-axial gyro sensor (InvenSense 500 series), a microprocessor (MSP430F1611), and a Bluetooth unit. The accelerometer is endowed with one filter capacitor in each axis. The gyro sensor contains three vibrating elements. The angular rate at each axis is obtained by measuring the Coriolis acceleration of the corresponding vibrating elements. The microprocessor captures the sensor data using a 12 bit analog-to-digital converter (ADC) at a pre-defined frequency. The Bluetooth unit transmits the data from the WIMU to a desktop.

The calibration procedure for the two IMUs is performed according to literature [45]. Using the IMUs, a Kalman-based algorithm is proposed in [152] to provide an accurate estimation of the orientations of the torch and shield glass.

3.1.2 Manual welding process with the proposed sensing system

In manual GTAW, a welder might adjust the orientation of the torch; In the meantime, he/she might also constantly change the spatial location and orientation of his/her head for a better view of the weld pool; Further, the weld pool slides on the pipe following the torch rotates around the pipe, hold by the welder, with millimeters away from the weld pool surface.

The manual welding process with the proposed sensing system is shown in Fig. 3.2. An arbitrary spatial relation for the torch, and helmet is illustrated in the figure. In particular, the coordinate system $(xyz)_w$ rotates around the pipe surface indicating the movement of the weld pool. The position and orientation adjustments of the torch and the helmet can be represented by the translation and rotation of the IMUs' internal coordinate systems, $(xyz)_{A_1}$ and $(xyz)_{A_2}$, respectively. P_{shield} is the plane of shield glass in the sensory helmet.

The movement of helmet in/around the three axes of $(xyz)_{A_2}$ is independent. Since the arc length is not as significant as the welding current or the traveling speed in assurance of weld quality, it is rarely a primary control variable during manual welding. Therefore, in this study the welder is assumed to maintain the arc length within a small variation margin. In this sense, the translation and rotation of $(xyz)_{A_1}$ are restrained.

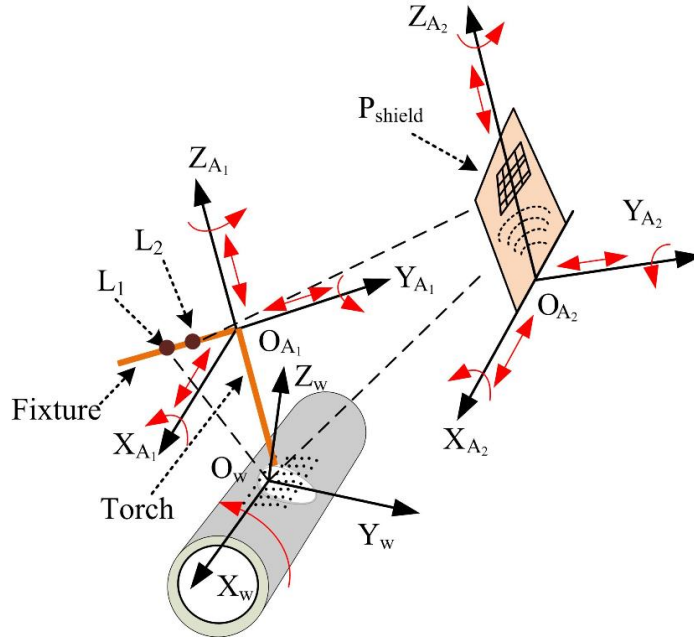


Figure 3.2: Illustration of weld actions

A welder might also adjust the welding current using a remote controller such as a foot pedal or a knob on the torch [149]. The variation of current changes the dimension of a weld pool. Yet, adjusting welding current would not affect the geometric relations of the components in the proposed sensing system.

It should be noted that accurate measurements of weld pool using proposed sensing system based on three prerequisites: 1) The qualified image of reflection pattern is captured; 2) and the reflection pattern is successful extracted through image processing; 3) the spatial geometric relation among the weld pool, torch and helmet is accurately estimated using the grid reflection pattern, and the data obtained from the two IMUs, i.e., A_1 and A_2 . The three issues are addressed in Section 3.2, Chapter 4, and 6, respectively.

3.2 System Analysis and Simulation

The welder's torch and helmet movements must ensure the complete interception of the two laser patterns on the shield glass such that a successful measurement of weld pool surface can be guaranteed. In this section, the boundaries of their spatial movements are mathematically formulated by locating the two laser patterns on the shield glass. In particular, the movement restrictions of the helmet is studied first while assuming the position of the torch is stationary. Then considered that the helmet is fixed, the limitations of torch's variation is analyzed.

It should be noted that in real manual welding process, the spatial positions of the torch and the helmet might vary simultaneously. The overall effect might increase or decrease their movement boundaries for effectiveness sensing. This subsection provides an evaluation for the moderate variations of the sensing system.

3.2.1 System Analysis

Initial Setup

An initial setup for the proposed sensing system is defined in Fig. 3.3. The origin of the universal coordinate system $(xyz)_U$ is at the top of the pipe. The pipe's normal direction at origin point is the positive direction of z_U -axis, and x_U -axis coincides with the pipe's axis. The torch is hold vertically such that its direction coincides with z_U -axis, and the two laser generators are in $(oyz)_U$ plane. The axes directions of the internal coordinate systems $(xyz)_{A_1}$ and $(xyz)_{A_2}$ coincide with that of the three corresponding axes in $(xyz)_U$. Origin O_{A_1} is in z_U -axis, The shield glass is in $(oyz)_U$ plane. The rectangular shield glass is in plane $(oxz)_{A_2}$ with its lower edge coinciding with x_{A_2} -axis. The origin O_{A_2} , i.e., the position of the IMU A_2 , is the middle point of the lower edge. The initial setup serves to facilitate the further analysis in the rest of this section.

The initial positions of the two IMUs in $(xyz)_U$ are:

$$D_{A_1}|_{initial} = [d_{A_1}^x, d_{A_1}^y, d_{A_1}^z]|_{initial} = [0, 0, d_{torch}] \quad (3.1)$$

$$D_{A_2}|_{initial} = [d_{A_2}^x, d_{A_2}^y, d_{A_2}^z]|_{initial} = [0, L_{A_2}^y, L_{A_2}^z] \quad (3.2)$$

where d_{torch} is the distance from the weld pool to the fixture bar:

$$d_{torch} = L_{torch} + L_{arc} \quad (3.3)$$

The IMUs' position in initial setup can be easily measured. In manual GTAW, based on data obtained from the IMUs, i.e., the acceleration and angular rate of the two sensors, accurate orientations of the IMUs can be obtained in real-time using the Kalman-based algorithm in [152]. The obtained orientations are denoted as G_{A_1} , and G_{A_2} , respectively. Further, the distance from the torch to helmet can be calculated online based on the grid

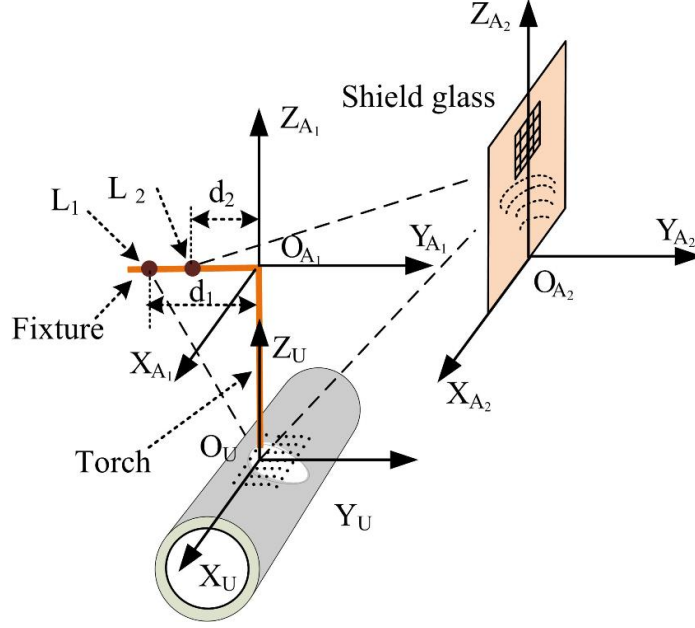


Figure 3.3: Initial setup of the sensing system

reflection pattern. The position of the IMUs in coordinate system $(xyz)_w$ can thus be determined in real-time.

The position vectors of the two laser patterns in $(xyz)_U$ are:

$$D_{L_1}|_{initial} = [0, -d_1, d_{torch}] \quad (3.4)$$

$$D_{L_2}|_{initial} = [0, -d_2, d_{torch}] \quad (3.5)$$

where d_1 and d_2 are the distances from the tips of the two patterns to the torch, respectively.

The initial projection vector $(\Psi_{L_1}|_{initial})$ of laser L_1 in $(xyz)_U$ is

$$\Psi_{L_1}|_{initial} = [0, \sin(\theta_{TL_1}), -\cos(\theta_{TL_1})] \quad (3.6)$$

where θ_{TL_1} is the angle which the torch makes to the extension of the laser.

In the initial set-up, the projection angle is carefully calibrated such that the interception for the extension of the torch and the projection direction is the weld pool center, i.e., the reference dot of the pattern coincides with the weld pool center. Since a welder might hold the torch with a small variation of the arc length (L_{arc}) in welding process, the reference dot might slightly deviate from the weld pool center.

The projection vector $(\Psi_{L_2}|_U)$ of laser L_2 in $(xyz)_U$ is

$$\Psi_{L_2}|_{initial} = [0, \sin(\theta_{TL_2}), \cos(\theta_{TL_2})] \quad (3.7)$$

The shield glass plane function in $(xyz)_U$ is:

$$y = L_{A_2}^y \quad (3.8)$$

Projection and Reflection of Dot Matrix Pattern

The projection pattern, the dot matrix, is shown in Figure. 3.4a. Typical reflection patterns at the solution 480×640 and 640×480 , captured in the initial setup of the sensing system during GTAW process, are presented in Figure. 3.4b and 3.4c, respectively. The brightness of the two reflection images are deliberately reinforced for the readability purpose. The marker in Figure. 3.4b are the coordinate frame drawn on the imaging plane also for the readability purpose.

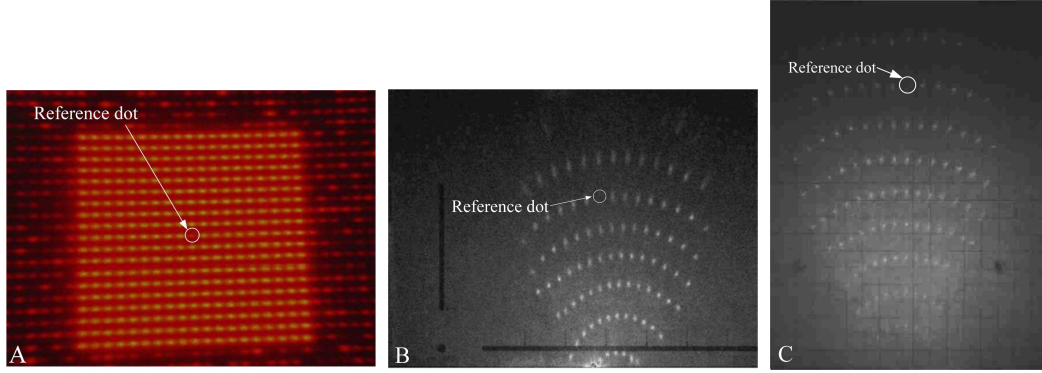


Figure 3.4: Projection and reflection of dot matrix pattern

The reference dot, i.e., the center ray of the dot matrix is intentionally missed. Please note that the brightness of reflected patterns in the captured images are intentionally enhanced for readability. The original images captured from welding process are much darker than the presented ones. During the welding process, the arc presses the liquid weld pool and deforms its surface. If the arc pressure is strong enough (usually happens when the welding current is about over 80 A according to our observation), the weld pool surface tends to be concave. Otherwise, it is convex. The dot matrix reflection pattern is thus deformed by the 3D convex/concave weld pool surface accordingly.

As can be seen from Figure. 3.4b and 3.4c, the similarity of the reflected dots in the captured image makes it difficult to identify which incident rays in the dot matrix they come from. The distortion of the reflection pattern is caused by the weld pool, and its surface geometry (size and shape) determines the correspondence between the projected and reflected laser dots. The detailed analysis finding the possible correspondences is presented in [114]. The analysis is briefed here for the integrity of this chapter. Fig. 3.5 is an example of 7×7 dot matrix including the projection pattern and the reflection pattern. The point position can be recognized by its row and column numbers not only for the projection pattern but also for the reflection pattern. In Fig. 3.5a, $p_{i,j}$ ($1 \leq i, j \leq 7$) represents the projected dot in the i^{th} row and j^{th} column. The reflect pattern with a possible correspondence is shown in Fig. 3.5b. $r_{i,j}$ represents the reflected dot in the i^{th} row and j^{th} column.

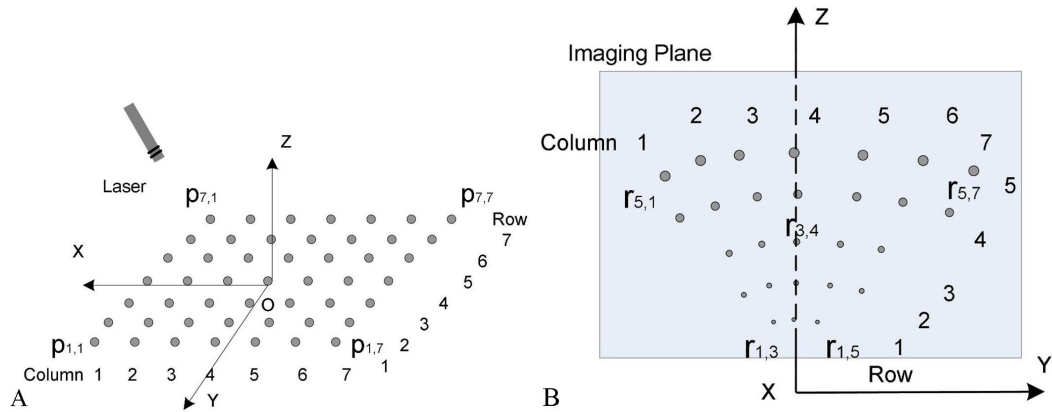


Figure 3.5: Example of projection and reflection patterns. (A) 7×7 Projection pattern example; (B) The corresponding reflection pattern on the imaging plane

In Figure. 3.6 illustrates two kinds of corresponding relationships in the dot matrix. One is column correspondence, which represents the column relationship of dots in a projected row and its reflected row. The other is the row correspondence, which indicates the row relationship of dots in a projected row and its reflected column. Both of them have three types of correspondences: sequential, inverse and disordered. In Figure. 3.6a, the dots in the k^{th} row of the projected dot matrix are investigated and the dashed line indicate the column correspondence. In Fig. 3.6b, three types of column correspondences are shown. Based on the assumption of small deformation in the smooth weld pool surface, a part of a sphere is tested as a concave/convex weld pool surface in the simulation [115]. In this study, moderate welding parameter (current, arc length and welding speed) is utilized, therefore the weld pool surface is convex. Both of the correspondences for the row and column of the weld pool obtained during the welding process are sequential.

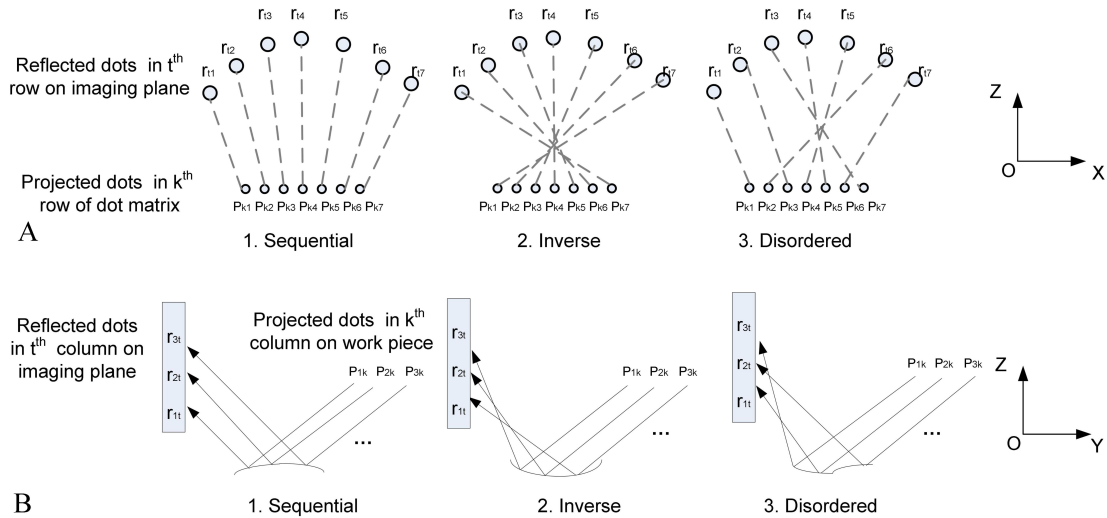


Figure 3.6: Illustration of two kinds of correspondences

However, with the knowledge of the correspondence between the projection and reflection

pattern, the individual mapping between the projected dots and reflected dots is still unclear. At least one pair of dots in the two patterns is to be determined first, then the mapping of other dot pairs can be derived using the known correspondence. To this end, it can be observed in Fig. 3.4a that the center dot of dot-matrix located at 10^{th} row and 10^{th} column is intentionally missed in the design. It provides a reference to help determine the row and column of each reflected laser dot in the captured image shown in Figure. 3.4b and 3.4c. A dot matrix laser pattern is chosen because it helps facilitate the extraction of the weld pool boundary during 3D weld pool reconstruction by clearly indicating the part of the dot matrix reflected by the weld pool. Every dot in the matrix also brings independent 3D geometric information of the weld pool surface.

Helmet movement

The configuration of the moving helmet and the stationary torch is shown in Figure. 3.7. Coordinate system $(xyz)_{mh}$ is identical to $(xyz)_{A_2}$ in Figure. 3.3, while using different subscript merely emphasizes the flexible feature of the helmet. The position of the fixed torch is same as it is in the initial setup in Figure. 3.3.

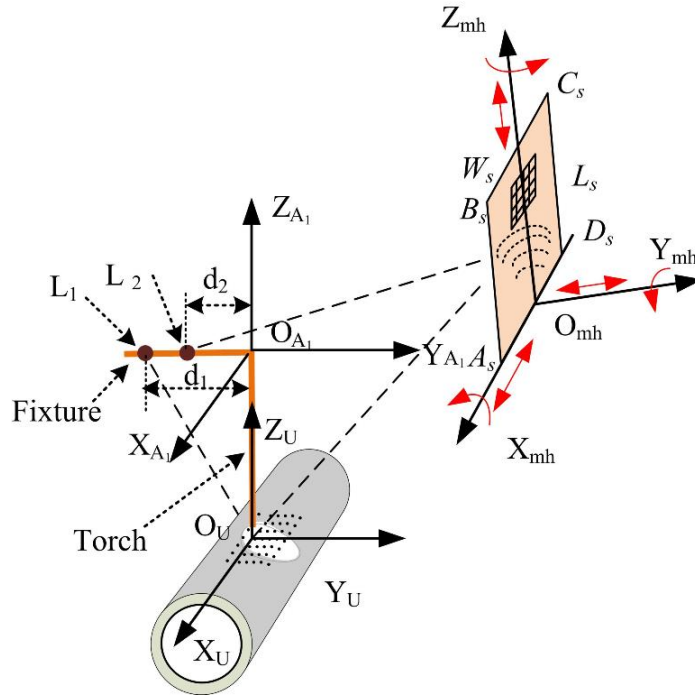


Figure 3.7: The configuration of the moving shield glass and the fixed torch

After the helmet/shield glass translates in $(xyz)_U$ with an arbitrary location deviance from its initial setup, denoted as $D_{mh} = [d_{mh}^x, d_{mh}^y, d_{mh}^z]$, and rotates with an arbitrary angles, denoted as $\Theta_{mh} = [\theta_{mh}^x, \theta_{mh}^y, \theta_{mh}^z]$, its normal vector, $\Psi_{mh} = [\psi_{mh}^x, \psi_{mh}^y, \psi_{mh}^z]$ is:

$$[\Psi_{mh}, 1] = [0, 1, 0, 1] \mathbf{R}(\Theta_{mh}) \quad (3.9)$$

where $\mathbf{R}(\cdot)$ is the rotation transformation matrix from one coordinate system to another:

$$\mathbf{R}(\Theta_{mh}) = R^x(\theta_{mh}^x)R^y(\theta_{mh}^y)R^z(\theta_{mh}^z) \quad (3.10)$$

and R^x , R^y and R^z are the rotation transformation matrices for the rotation around the x , y and z axis, respectively.

$$R^x(\alpha) = \begin{bmatrix} 1 & 0 & 0 & 0 \\ 0 & \cos(\alpha) & \sin(\alpha) & 0 \\ 0 & -\sin(\alpha) & \cos(\alpha) & 0 \\ 0 & 0 & 0 & 1 \end{bmatrix} \quad (3.11)$$

$$R^y(\beta) = \begin{bmatrix} \cos(\beta) & 0 & -\sin(\beta) & 0 \\ 0 & 1 & 0 & 0 \\ \sin(\beta) & 0 & \cos(\beta) & 0 \\ 0 & 0 & 0 & 1 \end{bmatrix} \quad (3.12)$$

$$R^z(\gamma) = \begin{bmatrix} \cos(\gamma) & \sin(\gamma) & 0 & 0 \\ -\sin(\gamma) & \cos(\gamma) & 0 & 0 \\ 0 & 0 & 1 & 0 \\ 0 & 0 & 0 & 1 \end{bmatrix} \quad (3.13)$$

α , β and γ are the rotation angles of the three axes, their positive directions are shown in Figure. 3.7.

The shield glass plane function in $(oxyz)_U$ can be written as

$$\Psi_{mh}([x, y, z] - D_{mh})^T = 0 \quad (3.14)$$

where $(\cdot)^T$ is the transposition of the vector.

The positions of four corners of the shield glass in $(oxyz)_{mh}$ are: $D_{A_s} = [W_s/2, 0, 0]$, $D_{B_s} = [W_s/2, 0, L_s]$, $D_{C_s} = [-W_s/2, 0, L_s]$, and $D_{D_s} = [-W_s/2, 0, 0]$. In coordinate system $(oxyz)_U$, their positions are:

$$[D_\eta|_U, 1] = [D_\eta, 1]\mathbf{R}(\Theta_{mh})T_{mh \rightarrow U} \quad (3.15)$$

where $\eta = A_s, B_s, C_s$, or D_s , and

$$T_{mh \rightarrow U} = \begin{bmatrix} 1 & 0 & 0 & 0 \\ 0 & 1 & 0 & 0 \\ 0 & 0 & 1 & 0 \\ d_{mh}^x & d_{mh}^y & d_{mh}^z & 1 \end{bmatrix} \quad (3.16)$$

For the convenience to obtain the size of reflection pattern of L_2 in the shield glass, an auxiliary coordinate system $(oxyz)_{L_2}$ is developed using the following steps: 1) translate

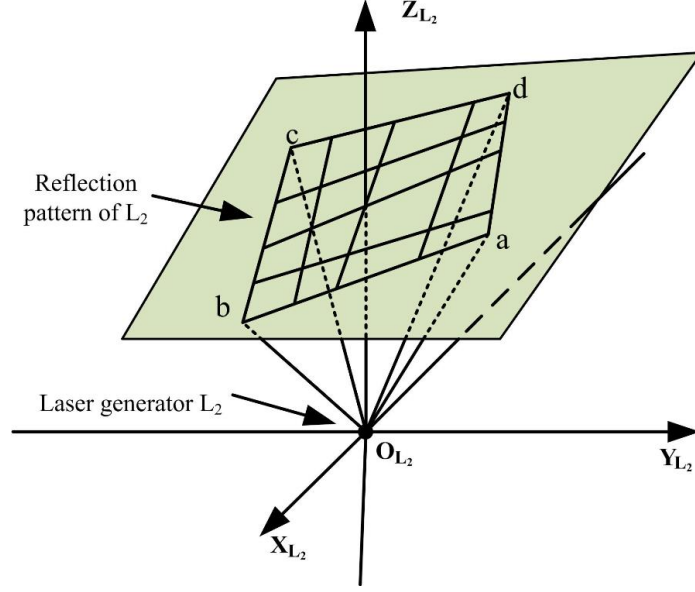


Figure 3.8: Illustration of the pattern L_2 in the auxiliary coordinate system $(xyz)_{L_2}$

origin O_U to the tip of L_2 and 2) rotate $(xyz)_U$ clockwise around x_U -axis for θ_{TL_2} such that the projection vector of L_2 coincides with z_U -axis.

In this new coordinate system $(xyz)_{L_2}$, the projection of pattern L_2 is shown in Figure. 3.8 . The direction vectors for projection rays of the four corner points ($a-d$) are $\Psi_\xi|_{L_2} = [\psi_\xi^x, \psi_\xi^y, \psi_\xi^z]$, $\xi = a, b, c, d$ which can be written as:

$$[\Psi_a|_{L_2}, 1] = [0, 0, 1, 1]\mathbf{R}([-2\theta_{in_2}, 2\theta_{in_2}, 0]) \quad (3.17)$$

$$[\Psi_b|_{L_2}, 1] = [0, 0, 1, 1]\mathbf{R}([2\theta_{in_2}, 2\theta_{in_2}, 0]) \quad (3.18)$$

$$[\Psi_c|_{L_2}, 1] = [0, 0, 1, 1]\mathbf{R}([2\theta_{in_2}, -2\theta_{in_2}, 0]) \quad (3.19)$$

$$[\Psi_d|_{L_2}, 1] = [0, 0, 1, 1]\mathbf{R}([-2\theta_{in_2}, -2\theta_{in_2}, 0]) \quad (3.20)$$

The functions for the four projection rays in $(xyz)_U$ are:

$$[x, y, z] = D_{L_2}|_{initial} + t\Psi_\xi \quad (3.21)$$

where t is an unknown variable, and

$$[\Psi_\xi, 1] = [\Psi_\xi|_{L_2}, 1]R^x(-\theta_{TL_2}) \quad (3.22)$$

With Equation. 3.14, and Equation. 3.21, the positions of four corner points in the grid pattern, D_ξ , can be located in $(oxyz)_U$:

$$D_\xi = D_{L_2}|_{initial} + \frac{\Psi_{mh}(D_{mh} - D_{L_2}|_{initial})^T}{\Psi_{mh}\Psi_\xi^T}\Psi_\xi \quad (3.23)$$

where $\xi = a, b, c, d$.

It is reasonable to assume that the dot matrix pattern's reflection at the weld pool boundary is not distorted by the liquid weld pool. Hence, the laser dots at the boundary can be considered as the interception points of the projection rays and the work piece (pipe). Figure 3.9 illustrates the projection and reflection of L_1 with an arbitrary size weld pool. Only a certain part of pattern L_1 's projection is reflected by the weld pool.

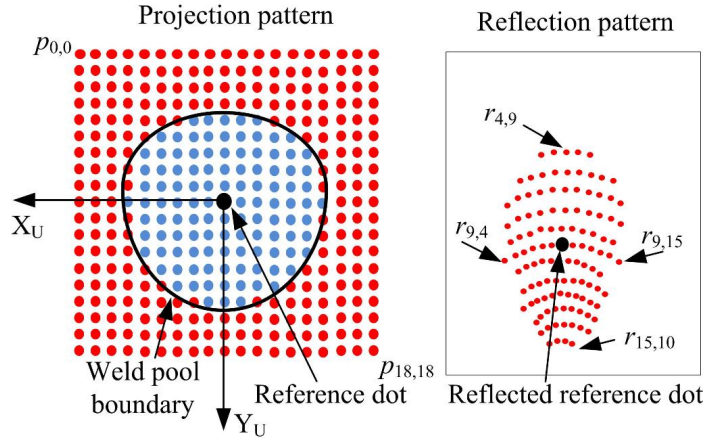


Figure 3.9: Illustration of the pattern L_1 and its reflection in the shield glass

With the similar procedure as building $(oxyz)_{L_2}$, an auxiliary coordinate system $(oxyz)_{L_1}$ is developed 1) translate origin O_U to the tip of L_1 and 2) rotate $(oxyz)_U$ clockwise around x_U -axis for θ_{TL_1} such that the projection vector of L_1 coincides with z_U -axis. The projection vectors for all the laser rays in the dot matrix in the new coordinate system are

$$[\Psi_{p_{i,j}}|_{L_1}, 1] = [0, 0, 1, 1]\mathbf{R}([(i-9)\theta_{in_1}, (j-9)\theta_{in_1}, 0]) \quad (3.24)$$

where $i, j = 0, \dots, 18$.

The projection rays in the universal coordinate system are

$$[x, y, z] = D_{L_1}|_{initial} + t\Psi_{p_{i,j}} \quad (3.25)$$

where

$$[\Psi_{p_{i,j}}, 1] = [\Psi_{p_{i,j}}|_{L_1}, 1]R^x(\pi + \theta_{TL_1}) \quad (3.26)$$

The pipe function is easily obtained in $(oxyz)_U$:

$$y^2 + (z + L_P)^2 = L_P^2 \quad (3.27)$$

where L_P is the radius of the pipe. The positions of projection boundary points, as shown in the left figure of Figure. 3.9, can be calculated using Equation. 3.25 and Equation. 3.27, denoted as $D_{p_{i,j}} = [d_{p_{i,j}}^x, d_{p_{i,j}}^y, d_{p_{i,j}}^z]$ where $d_{p_{i,j}}^z > -L_P$.

From Equation. 3.27, the normals ($\Psi_{np_{i,j}}$) of the pipe at the boundary points are:

$$\Psi_{np_{i,j}} = \frac{1}{\|[0, 2d_{p_{i,j}}^y, 2(d_{p_{i,j}}^z + L_P)]\|_2} [0, 2d_{p_{i,j}}^y, 2(d_{p_{i,j}}^z + L_P)] \quad (3.28)$$

Based on the law of specular reflection [reference ??], the reflection vectors ($\Psi_{rp_{i,j}}$) are obtained:

$$\Psi_{rp_{i,j}} = 2(-\Psi_{p_{i,j}} \Psi_{np_{i,j}}^T) \Psi_{np_{i,j}} + \Psi_{p_{i,j}} \quad (3.29)$$

Hence, the reflection rays from the boundary points are:

$$[x, y, z] = D_{p_{i,j}} + t\Psi_{rp_{i,j}} \quad (3.30)$$

Using Equation. 3.14 and Equation. 3.30, the boundary points reflections on the shield glass, $D_{r_{i,j}}$ can be calculated:

$$D_{r_{i,j}} = D_{p_{i,j}} + \frac{\Psi_{mh}(D_{mh} - D_{p_{i,j}})^T}{\Psi_{mh} \Psi_{rp_{i,j}}^T} \Psi_{rp_{i,j}} \quad (3.31)$$

Compared Equation. 3.15 and Equation. 3.31 with Equation. 3.23, the movement of helmet/shield glass, i.e., the variations of Θ_{mh} and D_{mh} should assure both D_ξ and $D_{rp_{i,j}}$ to be inside the quadrangle with D_η as its corners. The detailed numerical analysis will be in following subsection.

Torch movement

With a fixed helmet/shield glass and a flexible torch as shown in Figure. 3.10, the translations and rotations of the coordinate system $(oxyz)_{mt}$ in the universal coordinate system represents the movement of the torch. The origin O_{mt} 's position is denoted by $D_{mt} = [d_{mt}^x, d_{mt}^y, d_{mt}^z]$ and the rotation of $(oxyz)_{mt}$ is $\Theta_{mt} = [\theta_{mt}^x, \theta_{mt}^y, \theta_{mt}^z]$.

Coordinate system $(oxyz)_{mt}$ is identical to $(oxyz)_{A_1}$ in Figure. 3.3, while using different subscript merely emphasizes the flexible feature of the torch. The position of the fixed helmet is same as it is in the initial setup in Figure. 3.3.

Since the origin O_{mt} 's position can be represented as

$$[D_{mt}, 1] = [0, 0, d_{torch}, 1] \mathbf{R}(\Theta_{mt}) \quad (3.32)$$

the movement of torch is thus determined by Θ_{mt} .

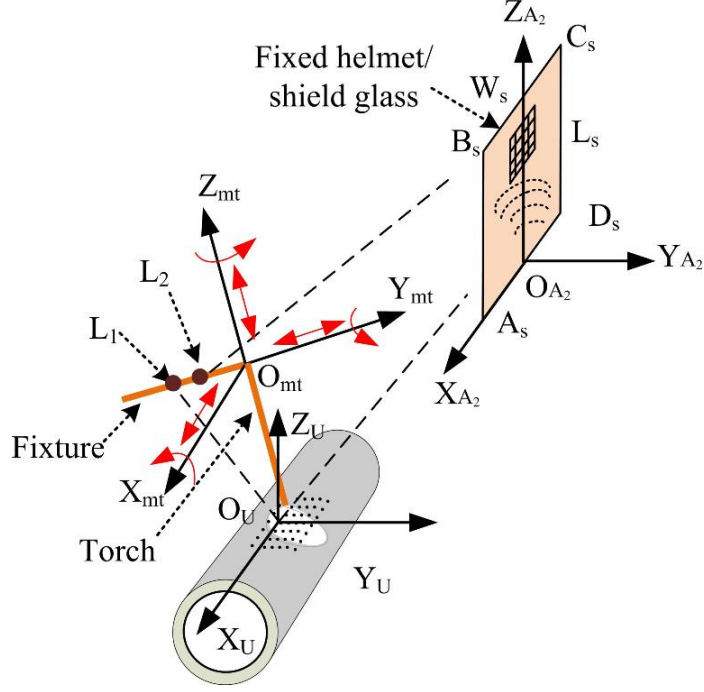


Figure 3.10: The configuration of the flexible torch and the fixed shield glass

The positions of four corners of the shield glass in $(oxyz)_U$ are: $D_{A_s} = [W_s/2, L_{A_2}^y, L_{A_2}^z]$, $D_{B_s} = [W_s/2, L_{A_2}^y, L_s + L_{A_2}^z]$, $D_{C_s} = [-W_s/2, L_{A_2}^y, L_s + L_{A_2}^z]$, and $D_{D_s} = [-W_s/2, L_{A_2}^y, L_{A_2}^z]$. The position of L_2 is

$$[D_{L_2}, 1] = [D_{L_2}|_{initial}, 1] \mathbf{R}(\Theta_{mt}) \quad (3.33)$$

Thus, the projection rays of the four corners in L_2 (a , b , c and d) in $(oxyz)_U$ are:

$$[x, y, z] = D_{L_2} + t\Psi_\xi \quad (3.34)$$

where $\xi = a, b, c$, and d , t is an unknown variable, and

$$[\Psi_\xi, 1] = [\Psi_\xi|_{L_2}, 1] R^x(-\theta_{TL_2}) \mathbf{R}(\Theta_{mt}) \quad (3.35)$$

where $\Psi_\xi|_{L_2}$ can be calculated using Equation. 3.17 to Equation. 3.20. With Equation. 3.8 and Equation. 3.34, the four grid pattern corners can be obtained:

$$D_\xi = D_{L_2} + \frac{L_{A_2}^y - d_{L_2}^y}{\psi_\xi^y} \Psi_\xi \quad (3.36)$$

The position of pattern L_1 in the universal coordinate system is

$$[D_{L_1}, 1] = [D_{L_1}|_{initial}, 1] \mathbf{R}(\Theta_{mt}) \quad (3.37)$$

and the projection rays of the laser dots in the pattern are

$$[x, y, z] = D_{L_1} + t\Psi_{P_{i,j}} \quad (3.38)$$

where

$$[\Psi_{P_{i,j}}, 1] = [\Psi_{P_{i,j}}|_{L_1}, 1]R^x(\pi + \theta_{TL_1})\mathbf{R}(\Theta_{mt}) \quad (3.39)$$

$\Psi_{P_{i,j}}|_{L_1}$ can be obtained using Equation. 3.24. Using the Equation. 3.27 to Equation. 3.29, the boundary points reflection in Figure. 3.9 can be calculated:

$$D_{r_{i,j}} = D_{P_{i,j}} + \frac{L_{A_2}^y - d_{P_{i,j}}^y}{\psi_{r_{P_{i,j}}}^y} \Psi_{r_{P_{i,j}}} \quad (3.40)$$

Similar with the movement of helmet/shield glass, the torch movement Θ_{mt} should be constrained in a certain range such that both D_ξ and $D_{r_{P_{i,j}}}$ to be inside the quadrangle with D_η as its corners. The detailed numerical analysis will be in the following subsection.

Since the shape of a weld pool surface is practical unknown in mathematically form during a GTAW process, then dot matrix reflection within the weld pool is thus unable to calculated in real-time. However, if the geometry of the weld pool is known, e.g., in a simulation, then the whole dot matrix reflection can be easily obtained besides the boundary points' reflection.

3.2.2 System Simulation

The major parameters for the numerical simulation are presented in Table 3.1. In a typical manual welding, a welder might performs welding while observing the weld pool at the distance approximately from 100 mm to 180 mm. The initial settings are thus: $\Theta_{mh} = [0^\circ, 0^\circ, 0^\circ]$, and $D_{A_2}|_{initial} = [0, 125\text{mm}, 20\text{mm}]$. The boundaries of the helmet and the torch movement are discussed based on the initial definitions.

Table 3.1: Parameters for the sensing system simulation

Parameter	Conditions	Parameter	Conditions
L_{torch} (mm)	$L_1 : 25.67, L_2 : 103.18$	L_{arc} (mm)	4
d_1 (mm)	34.50	d_2 (mm)	18.85
L_s (mm)	180	W_s (mm)	147
θ_{TL_1} ($^\circ$)	47.0	θ_{TL_2} ($^\circ$)	83.5
θ_{in_1} ($^\circ$)	0.77	θ_{in_2} ($^\circ$)	2.44

The geometry of the simulated weld pool in the numerical analysis is illustrated in Figure. 3.11. Its nominal radius is 12 mm, Since the chamfer angle on the edge of the mirror surface is not specular, the diameter of specular surface of the convex mirror is 11.2 mm. The edge thickness is 1.76 mm, and the center thickness is 2.5 mm. With known geometry, all the reflection dots of the dot matrix can be calculated using similar procedure aforementioned which is to obtain the boundary points of dot matrix reflection.

With the initial settings and the known geometry of the weld pool simulation, the reflections of the two patterns on the shield glass are shown in Figure. 3.12. The black quadrangle

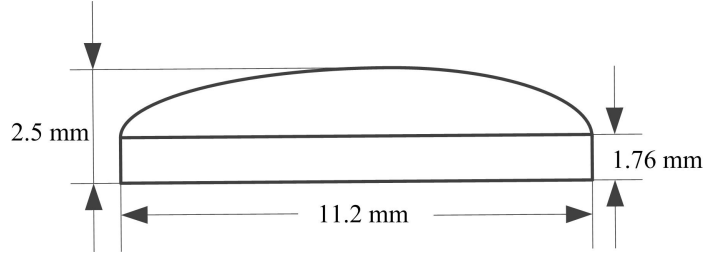


Figure 3.11: The convex spherical weld pool simulation

with triangle-shape corners is the shield glass; The blue dots are from pattern L_1 reflected by the weld pool simulation; The red quadrangle is the interception of the grid pattern L_2 . The star-shape dot is the reference dot.

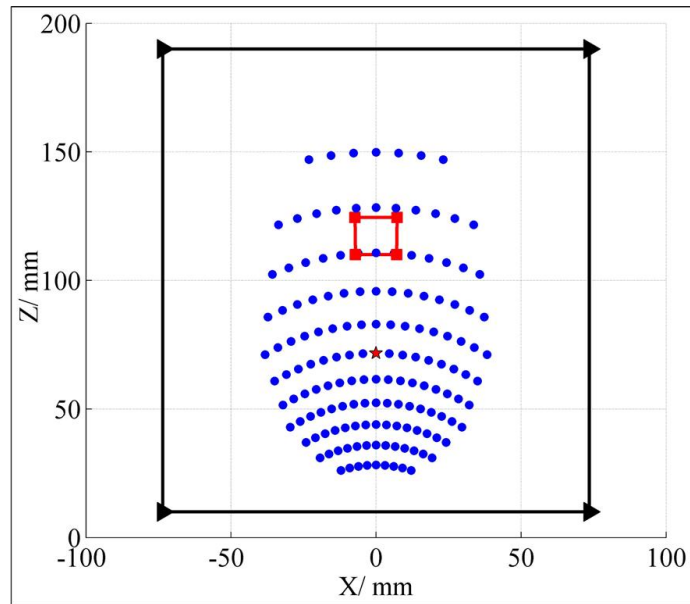


Figure 3.12: The two patterns on the shield glass at initial position

1. *Simulation for movement of sensory helmet*

Using the parameters in Table 3.1, only part of L_1 reflected by the weld pool simulation. The translations boundaries of the helmet in the universal coordinate system are shown in Figure. 3.13. In the figure, the black quadrangle with triangle-shape corners is the shield glass; The red quadrangles is the grid pattern on the shield glass; The dots are from the dot matrix pattern reflected by the weld pool simulation. Figure. 3.13a and 3.13b show the range the helmet translations in x_U -axis directions, Figure. 3.13c and 3.13d illustrate the helmet translations in y_U -axis directions, and Figure. 3.13e and 3.13f are the boundary positions of the helmet in z_U -axis directions. The range of the helmet translations in the three axes directions are $[-36.20, 36.20]$ mm, $[93.50, 139.90]$ mm and $[-0.2, 36.02]$ mm, respectively. At those extreme positions one of the corner point for two the patterns approaches the edge of the shield glass. Therefore, as shown in Figure. 3.13, the two patterns can be successfully intercepted by the shield glass within the range of the translations.

While the position of the helmet is hold at the initial setting, i. e., $D_{mh} = [0, 125\text{mm}]$,

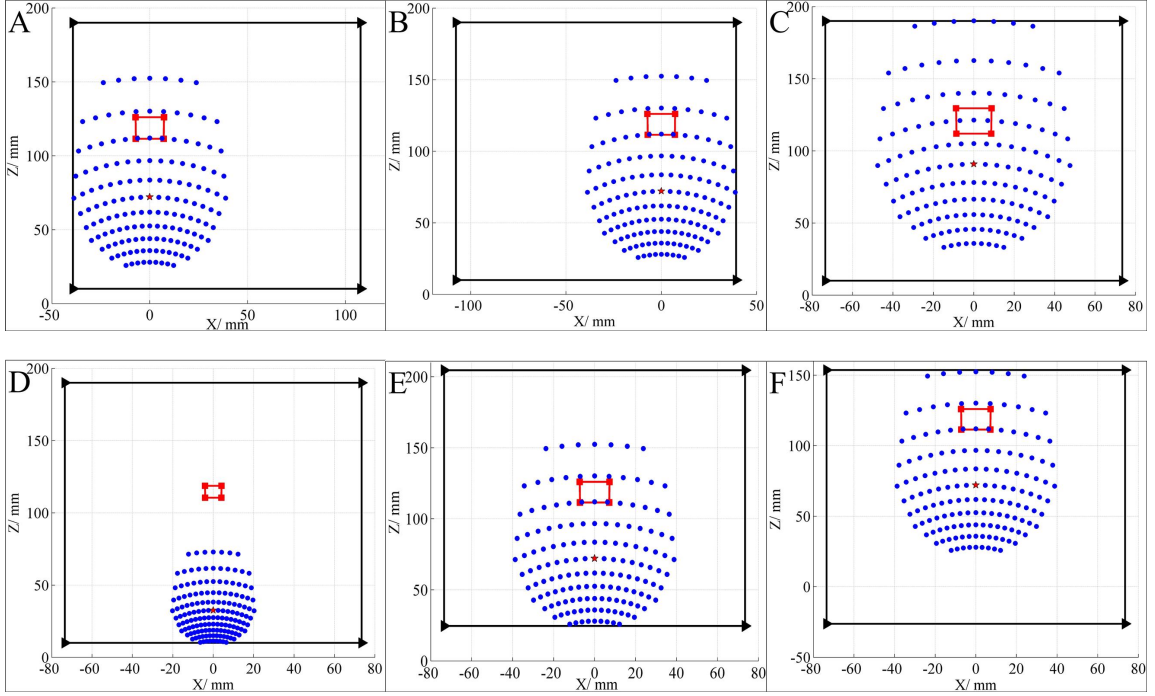


Figure 3.13: The translations of the helmet to boundary positions where $D_{mh} =$ (a) $[36.20, 125, 20]$ mm, (b) $[-36.20, 125, 20]$ mm, (c) $[0, 139.90, 20]$ mm and (d) $[0, 93.50, 20]$ mm, (e) $[0, 125, 36.02]$ mm, (f) $[0, 125, -0.20]$ mm.

20mm], the ranges of helmet's rotation in the universal coordinate system are illustrated in Figure. 3.14. The positive rotation directions are shown in Figure. 3.7. The ranges for the helmet rotations around the three axes of $(xyz)_{mh}$ are $[-3.51^\circ, 30^\circ]$, $[-21.5^\circ, 21.5^\circ]$ and $[-33.8^\circ, 33.8^\circ]$, respectively. As one can observe that the two patterns are able to be fully intercepted by the shield glass as it rotates within this ranges.

It should be noted that the upper limit of rotation along x_U -axis should be large than 30° . However, with larger rotation angle, the two patterns on the smaller on the shield glass which would lead the image processing more difficult to extract these patterns. Also, the physical accessibility might be an issue for the welder to bend the head over for that large degree ($> 30^\circ$).

2. Simulation for movement of projective torch The simulation of the flexible torch using the same parameters in Table 3.1. The shield glass is fixed in the simulation in which $\Theta_{mh} = [0^\circ, 0^\circ, 0^\circ]$, and $D_{A_2}|_{initial} = [0, 125\text{mm}, 20\text{mm}]$. The variations of Θ_{mt} , i.e., the movements of the torch, are calculated and the boundary positions are shown in Figure. 3.15. The positive rotation directions are shown in Fig. 3.7.

It can be observed in Figure. 3.15, the ranges of the torch rotation around the three axes of $(xyz)_{mt}$ are $[-3.20^\circ, 12.65^\circ]$, $[-19.91^\circ, 19.91^\circ]$ and $[-17.46^\circ, 17.46^\circ]$, respectively. The rotation for the torch around x_{mt} -axis is smaller than the rotation ranges around the other axes. However, it can be considered acceptable during a manual welding process.

It can be found from the simulations for the helmet/shield glass and torch movement, the proposed mobile sensing system can successfully captured the images of the two patterns

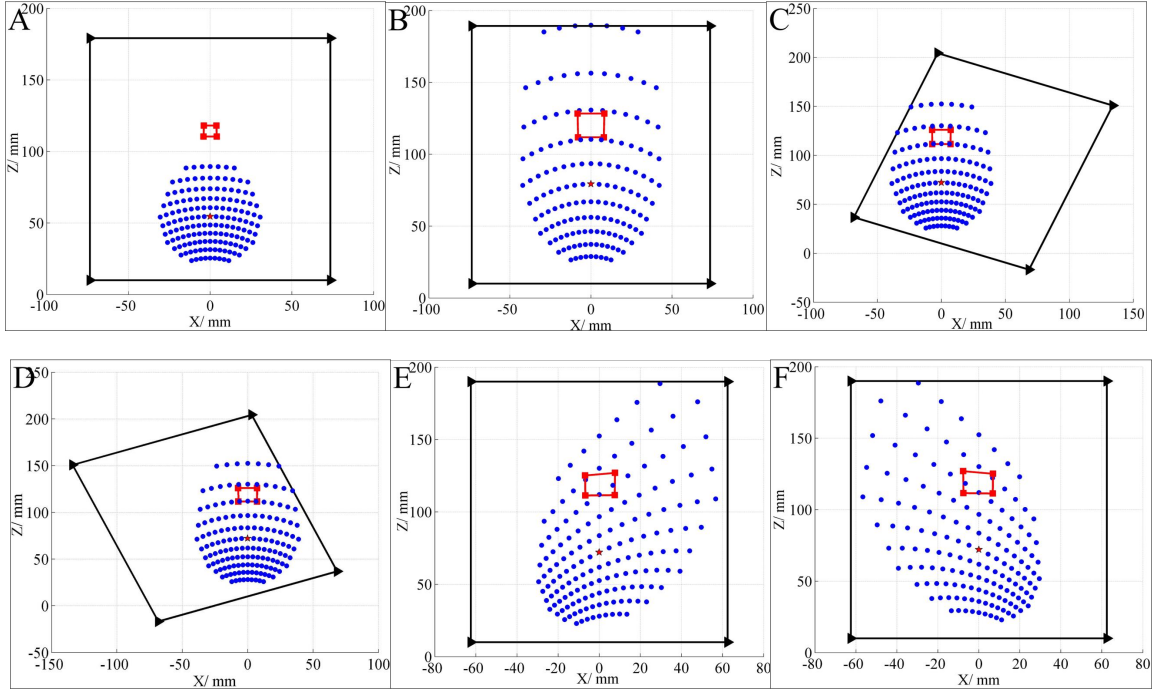


Figure 3.14: The rotations of the helmet to boundary positions where $\Theta_{mh} =$ (a) $[30^\circ, 0^\circ, 0^\circ]$, (b) $[-3.51^\circ, 0^\circ, 0^\circ]$, (c) $[0^\circ, 21.5^\circ, 0^\circ]$ and (d) $[0^\circ, -21.5^\circ, 0^\circ]$, (e) $[0^\circ, 0^\circ, 33.8^\circ]$, (f) $[0^\circ, 0^\circ, -33.8^\circ]$.

on the shield glass despite the wide range of the torch and helmet movements.

3.3 Observation Results

Upon the design of the machine vision system, an experimental platform for the system is developed. Images are captured as the torch and helmet are in the boundary positions using the experimental setup.

3.3.1 Experimental Setup

In order to verify the effectiveness of the proposed sensing system, an experiment setup is shown in Figure. 3.16. In the configuration, the welder's head is replaced by a tripod head (Manfrotto 808RC4) with 6 degree-of-freedom which is sufficient to imitate welder's head movements. A piece of glass with a sheet of paper attached is adopted here to simulate the helmet shield glass. The sensory helmet is referred as the combination of the helmet and the camera. Two patterns together with the torch are referred as the projective torch. The distance between the camera and the shield glass is adjustable. The torch is hold by a flexible post (PanaVise) capable of mimicking a welder's arm movements. The two laser patterns are mounted on the torch. Their positions on torch are changeable such that the distances between the patterns and weld pool can be appropriately adjusted.

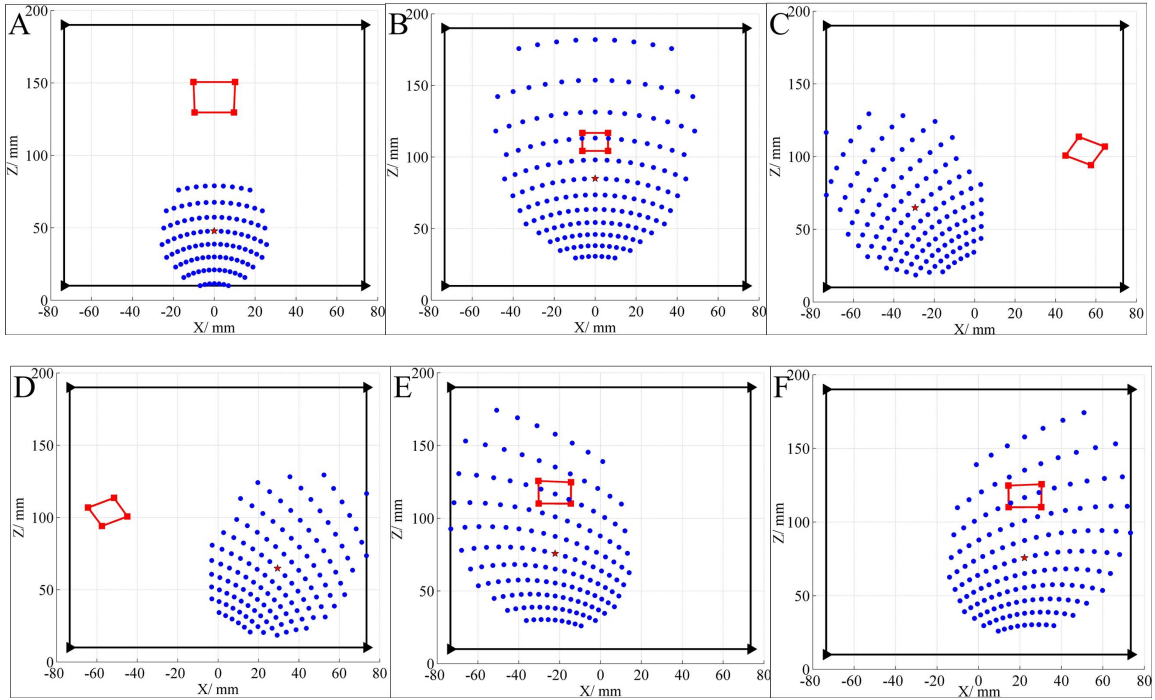


Figure 3.15: The boundary positions for the torch's rotation where $\Theta_{mt} =$ (a) $[12.65^\circ, 0^\circ, 0^\circ]$, (b) $[-3.20^\circ, 0^\circ, 0^\circ]$, (c) $[0^\circ, 19.91^\circ, 0^\circ]$ and (d) $[0^\circ, -19.91^\circ, 0^\circ]$, (e) $[0^\circ, 0^\circ, 17.46^\circ]$, (f) $[0^\circ, 0^\circ, -17.46^\circ]$.

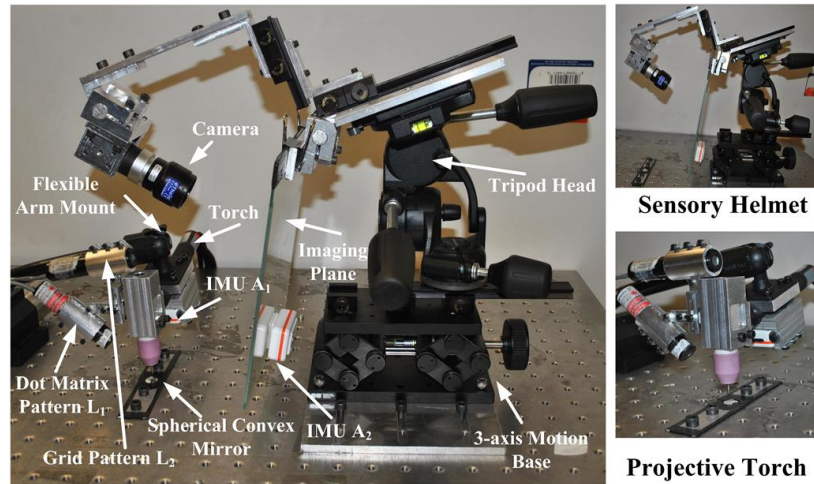


Figure 3.16: The experiment set-up

A convex spherical mirror (Edmund optics NT64-057) is used to simulate a real weld pool. The geometry of the mirror is illustrated in Figure. 3.11. The mirror's nominal diameter is 6 mm. However, since the chamfer angle on the edge of the mirror surface is not specular, the diameter of the specular surface of the convex mirror is 5.6 mm.

In the experiment configuration, the two structured light patterns are attached to the torch. Reflected by the mirror, the matrix pattern is imaged on the shield glass. The grid pattern

is directly projected on the shield glass.

3.3.2 Acquired Images

Using the configuration of the experimental setup detailed in Table 3.1, the acquired image as the sensing system is at the initial position is shown in Fig 3.17.

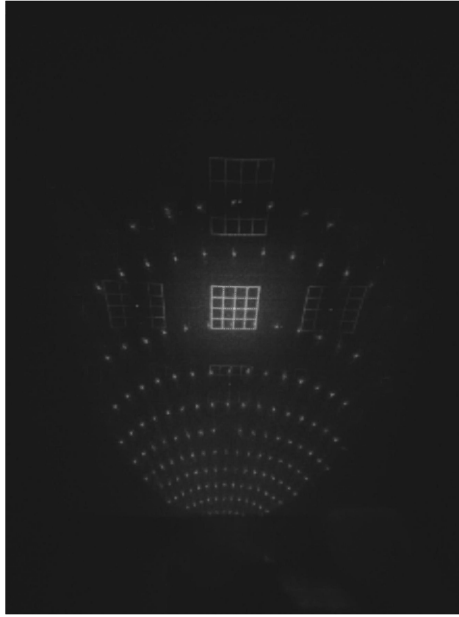


Figure 3.17: The acquired image as the sensing system in initial position in using the experiment setup

The images acquired when the sensing system is at the forementioned boundary positions are shown in Fig 3.18 and Fig 3.19. From the images, one can find 1) the images are twisted since the camera is not aiming to the normal direction of the imaging plane. This causes an additional distorted of the acquired image, which is restored in the next chapter using the proposed image processing algorithm; 2) The acquired images are identical to the corresponding pictures obtained in the numerical simulations. That verifies the effectiveness of the sensing system.

Fig 3.18 C and D, the whole image of the laser reflections are tilted, which are not identical with the corresponding images in Fig. 3.14, where the image plane are titled. That is because when the helmet rotates, the camera rotates accordingly with the helmet. So, in the cameras view the laser reflections are tilted, rather than the image plane. Rotating the Fig. 3.18 C and D with angle which the helmet has rotated towards the opposite direct, the two corresponding pairs of images between Fig. 3.18 and Fig. 3.14 will be identical.

3.4 Summary

An innovative mobile sensing system is developed to non-intrusively monitor the manual (GTAW) process in pipe applications by real-time measuring the three-dimensional (3D)

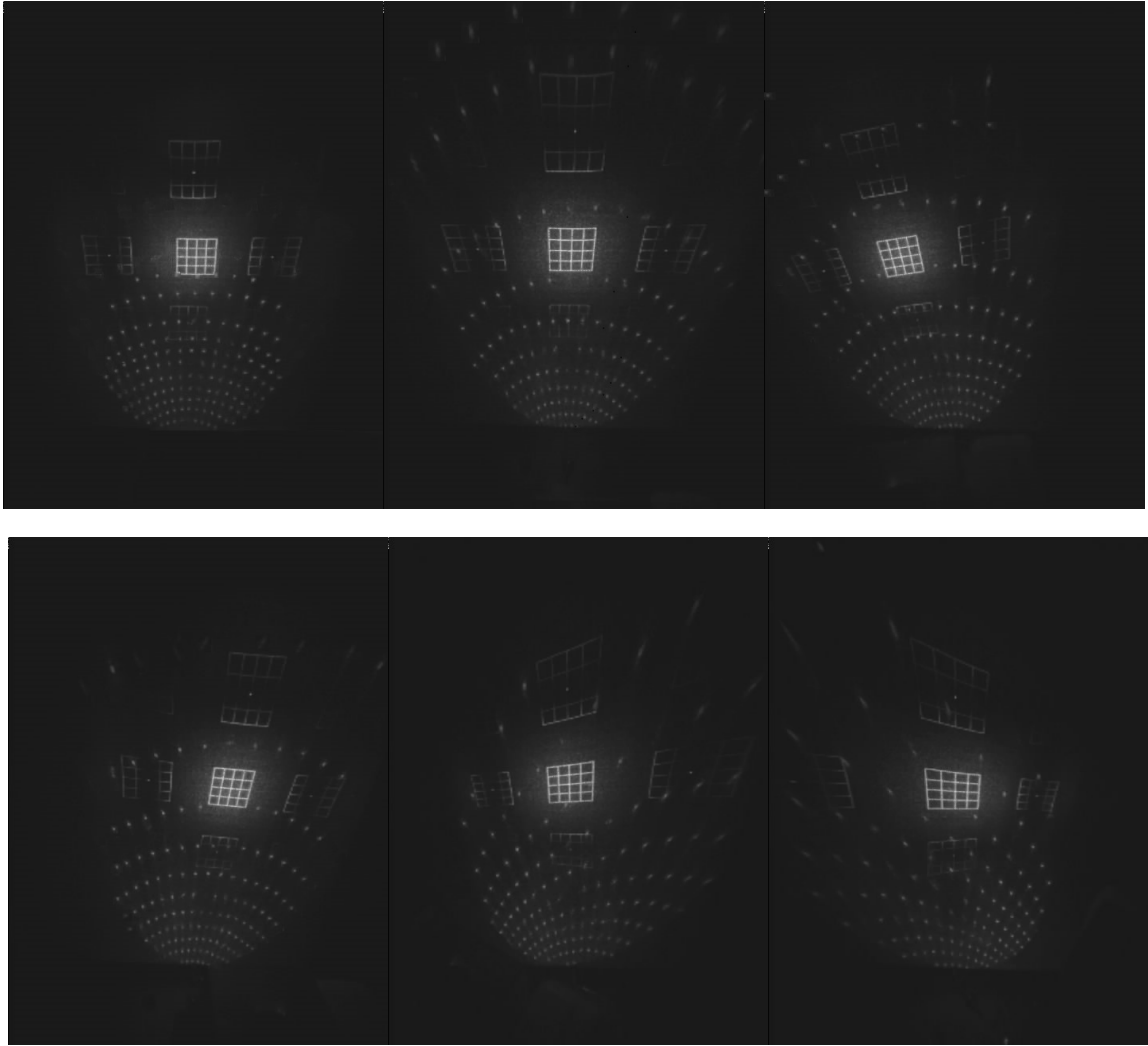


Figure 3.18: Captured image of reflection pattern in helmet rotation where the helmet is at the boundary positions of: A) Positive x-axis direction; B) Negative x-axis direction; C) Positive y-axis direction; D) Negative y-axis direction; E) Positive z-axis direction; and F) Negative z-axis direction.

weld pool surface. The mobile sensing system is developed and analyzed by numerical simulations in which the spatial boundaries for effective sensing have been determined. It is further evaluated using a simulation platform in which the movement of the helmet/welder's head is mimicked by a tripod head with 6 degrees of freedom (DOF), and a convex spherical mirror with a comparable size of a typical weld pool in GTAW is applied to as a weld pool substitute. The effectiveness of the proposed system is validated by successfully capturing laser reflections from the mirror without much constraints of a welder's movements for the torch and the helmet.

The proposed sensory helmet provides a flexible and innovative method to measure the 3D weld pool surface in manual GTAW. By taking advantage of welder's intelligent tracking capability, the sensory helmet can capture the reflection pattern of the structure light

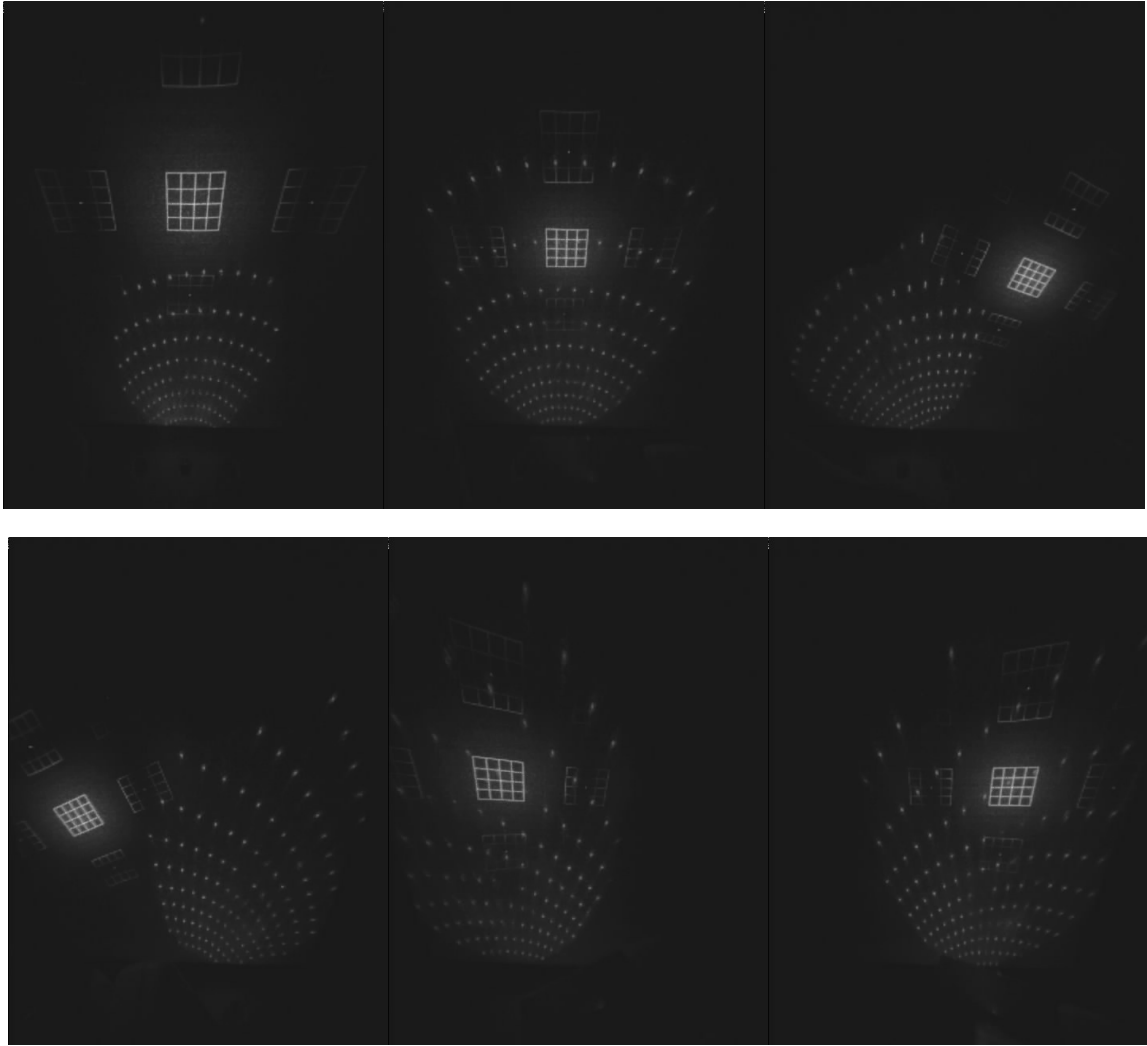


Figure 3.19: Captured image of reflection pattern in torch rotation where the torch is at the boundary positions of: A) Positive x-axis direction; B) Negative x-axis direction; C) Positive y-axis direction; D) Negative y-axis direction; E) Positive z-axis direction; and F) Negative z-axis direction.

reflected by the specular weld pool surface.

Chapter 4

Processing of Acquired Images

The feasibility evaluation of the proposed sensing system is analyzed based on the assumption that the pattern reflections are successfully extracted from the captured images. A robust image processing algorithm is proposed in this section to extract the reflection patterns.

4.1 System Calibration

The calibration in this paper is in addition to the HongSheng's paper. including the chapter and the appendix.

An appropriate system calibration is necessary for the accurate reconstruction in this study. In the experiment set-up as shown in Figure 3.16, there are mainly three categories of system errors:

- Set-up errors for the sensory helmet and the projective torch, which might leads to static errors for the weld pool reconstruction;
- Accuracy error of the gyro sensors which might result to the position/orientation measurement errors;
- Camera distortion may cause the deformation of the captured images/reflection patterns.

Static errors can be neutralized using numerical methods [147]. The IMUs are used in this study to detect the orientation of the torch and helmet. The calibration of the IMUs are performed according to literature [45]. The calibration process is conducted in three steps:

1. Correct the camera distortion with a camera internal model;
2. Calibrate the deformation caused by the tilted camera position from the shield glass using a perspective matrix [56];
3. Convert the reflection pattern in pixel unit to coordinate system $(xyz)_{A_2}$.

The camera internal model in [56] is adopted which includes the following internal parameters:

- Focal length 2×1 vector f_c : The focal length in pixels of the camera;
- Principal point 2×1 vector c_c : The principal point coordinates in the camera frame;
- Skew coefficient α_c : The skew coefficient defining the angle between the x and y pixel axes;
- Distortions 5×1 vector k_c : The image distortion coefficients (radial and tangential distortions) ([23, 46]).

The focal length, principal point and the skew coefficient consist of the intrinsic matrix of the camera:

$$H_{intr} = \begin{bmatrix} f_{c_x} & \alpha_c * f_{c_x} & c_{c_x} \\ 0 & f_{c_y} & c_{c_y} \\ 0 & 0 & 1 \end{bmatrix} \quad (4.1)$$

where $f_c = [f_{c_x}, f_{c_y}]$, and $c_c = [c_{c_x}, c_{c_y}]$.

The method of calibration is to target the camera on a known structure, a chessboard, that has many individual and identifiable points. By viewing this structure from a variety of angles, it is possible to compute the (relative) location and orientation of the camera at the time of each image and the internal parameter of the camera [118]. In this study, the chessboard is made by a chessboard paper attached on the imaging plane, as shown in Figure. 4.2a.

Using the calibration process detailed in ([159, 160]), the distortions including the radial distortion and tangential distortion are obtained and illustrated in Figure. 4.1. The intrinsic matrix H_{intr} and the distortion vector k_c are shown in Equation. 4.2 and Equation. 4.3. The result of distortion correction is shown in Figure. 4.2b.

$$H_{intr} = \begin{bmatrix} 297.5577 & 0 & 250.5846 \\ 0 & 297.5577 & 341.4556 \\ 0 & 0 & 1 \end{bmatrix} \quad (4.2)$$

$$k_c = [-0.0077, -0.0053, 0.0002, 0.0011, 0.0061] \quad (4.3)$$

Given the intrinsic matrix and the distortion vector, the position and orientation of the chessboard in each image can be calculated. Hence a perspective transformation matrix H_{per} can be obtained to convert the tilted position, as shown in Figure. 4.2b, to a frontal parallel view. The result is shown in Figure. 4.2c. Given the known position of gyro sensor A_2 in the imaging plane, the coordinate system $(oxyz)_{A_2}$ can be established, as shown in Figure. 4.2d. The pixel-to-mm ratio is 3.1

$$H_{per} = \begin{bmatrix} 31.6444 & 8.2752 & 142.1832 \\ 0.3089 & 41.5341 & 207.8942 \\ -0.0004 & 0.0378 & 26 \end{bmatrix} \quad (4.4)$$

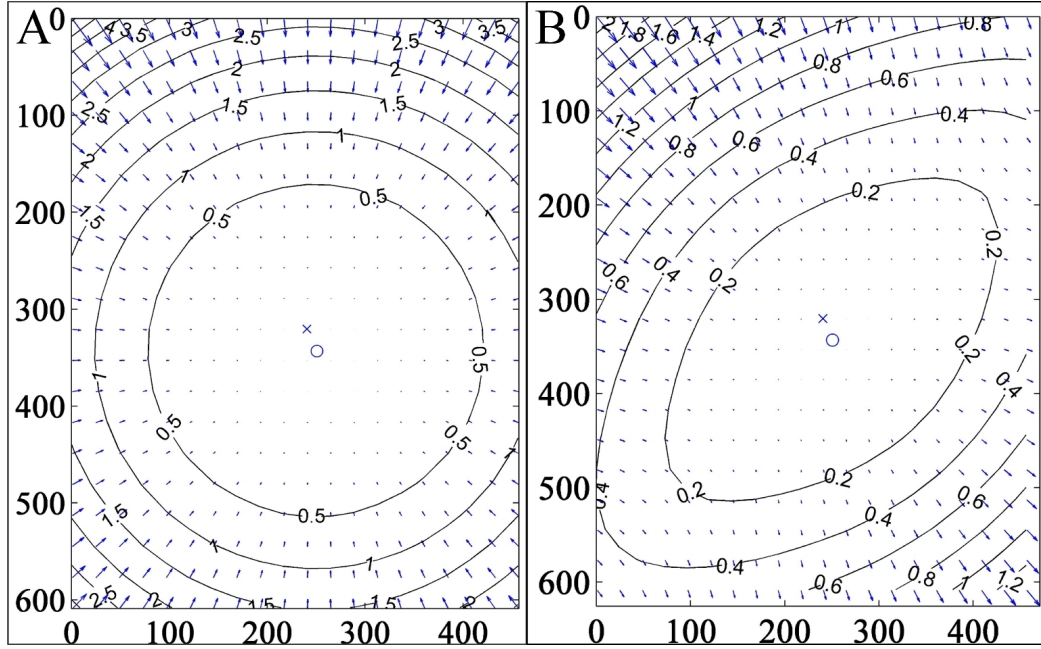


Figure 4.1: The A) radial and B) tangential distortion of the camera used in this study

With experiment configuration shown in Fig. 3.16 and the corresponding geometry settings detailed in Table 4.1, an image of the two patterns is captured by the sensing system, and shown in Fig. 4.3a. Spatial positions and orientations of the torch and the helmet in the universal system corresponding to the captured image are $D_{mh} = [20, 125\text{mm}, 20\text{mm}]$, $\Theta_{mh} = [0^\circ, 0^\circ, 0^\circ]$, $\Theta_{mt} = [0^\circ, -5^\circ, 0^\circ]$.

Table 4.1: Parameters of the sensing system for image processing

Parameter	Conditions	Parameter	Conditions
L_{torch} (mm)	$L_1 : 34.2, L_2 : 96.4$	L_{arc} (mm)	4
d_1 (mm)	26.7	d_2 (mm)	38.85
L_s (mm)	180	W_s (mm)	147
θ_{TL_1} ($^\circ$)	35.7	θ_{TL_2} ($^\circ$)	80.2
θ_{in_1} ($^\circ$)	0.77	θ_{in_2} ($^\circ$)	2.44

First, as one can find in Fig. 3.16 that the camera is not in the normal direction of the shield glass, which arguments an extra distortion of the reflection patterns in the captured images. For the calibration of the sensing system, the first step of the proposed processing is to correct this distortion by using a perspective matrix to perform a back projection, such that an image can be rendered, as captured in the normal direction [56]. The resultant of the calibration process is shown in Fig. 4.4a.

4.2 Image Processing

In this section, the grid pattern and the dot matrix are extracted using proposed image processing algorithms. Since the extraction of the grid pattern is relatively simpler than

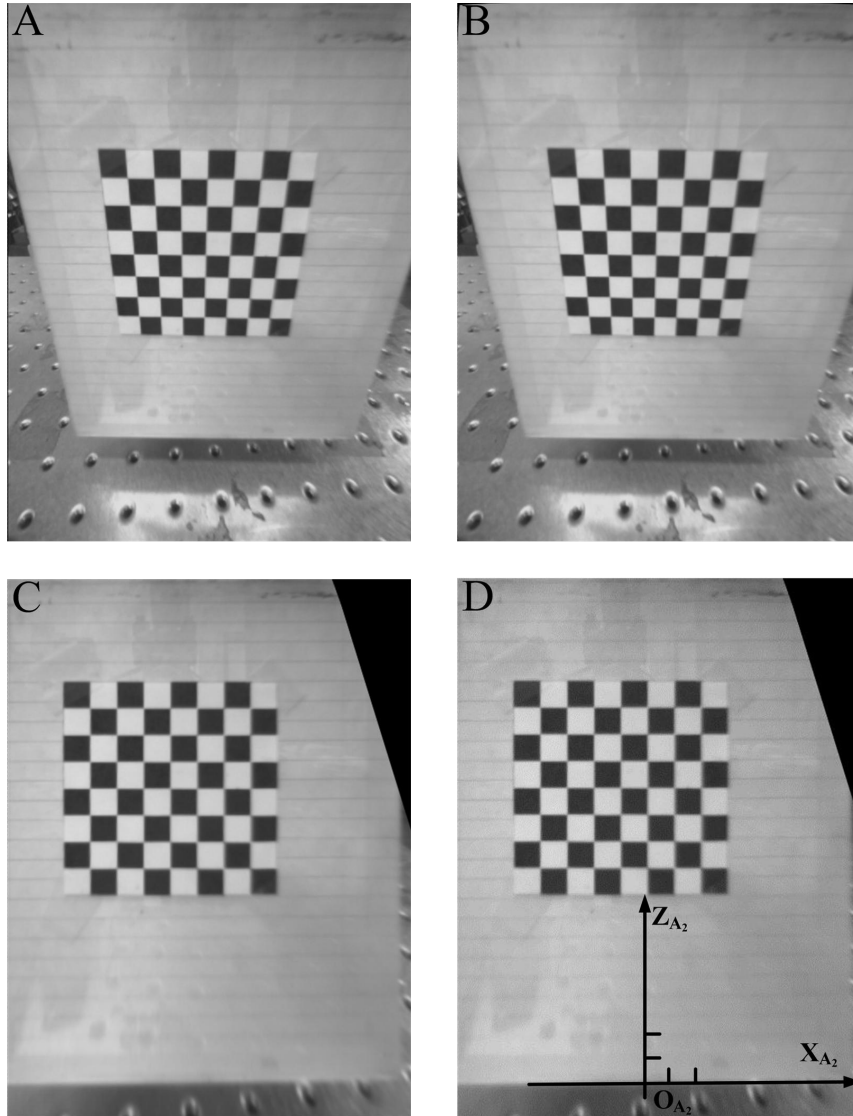


Figure 4.2: Results of camera and imaging plane calibration: A) The original image of the chessboard; B) Result of camera distortion correction; C) Result of frontal parallel view for the chessboard; and D) The conversion to the $(xyz)_{A_2}$ coordinate system.

the identification of the dot matrix, the chapter is main focused on pattern recognition of the dot matrix reflection.

The image processing is required to be robust enough to successfully identify two patterns despite the interference from the strong arc radiation. During an arc welding process, the quality of acquired images is degraded in terms of the brightness contrast between the reflection patterns and the background of images. Due to the power difference of the lasers (50 mW of grid pattern and 20 mW of dot matrix pattern), the deterioration of the two patterns thus varies. Specifically, the grid pattern reflection is bright enough to guard against the arc radiation interference, i.e., the images of grid pattern captured from the practical welding process and by the experimental setup (Figure 3.16) are no huge difference

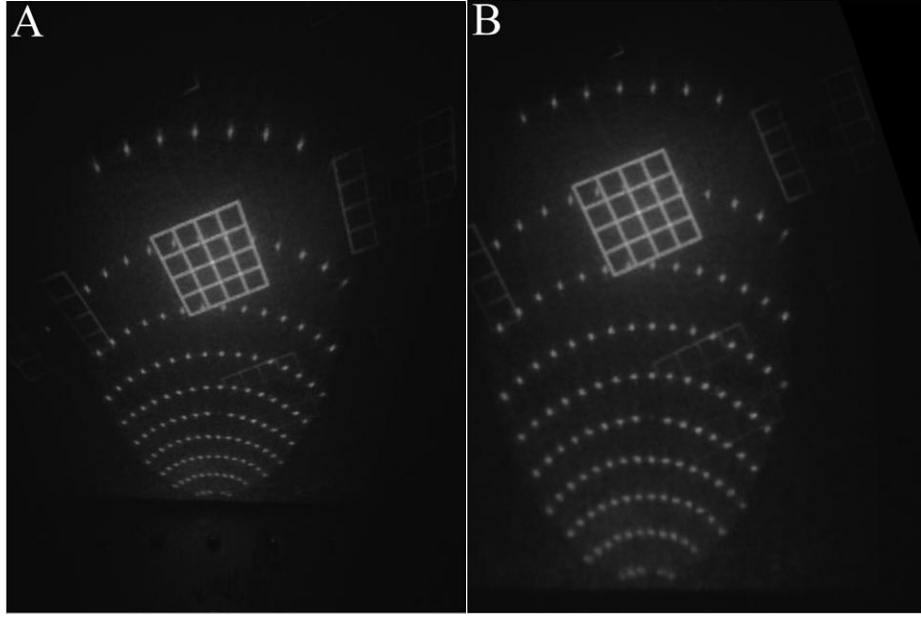


Figure 4.3: The original captured image and the calibrated image in A) and B) respectively

in brightness contrast, while the dot matrix reflection is severely degraded by the noise from the radiation. To this end, the example image to demonstrate to grid pattern identification is captured by the experimental setup, as shown in Figure 4.4a, while the image for dot matrix reflection recognition is captured from practical welding process, as shown in Figure 3.4b.

The grid pattern can be easily identified using the Hugh Transformation algorithm ([49, 58]), which is to find the straight line that contains most number of non-zero grey value points in the image. The lines in the pattern are thus identified one by one. The results of grid pattern identification is show in Figure 4.4. The transformation is illustrated in Figure 4.4b. The result of grid pattern is shown Figure 4.4c. Dots in different rows in the reflected pattern are marked with different shapes and colors. It should be noted that the two patterns on the shield glass are not necessarily separated from the each other. Because of the huge difference of the two in shape, they can be easily distinguished by proposed image processing algorithm even they are overlapped.

4.2.1 Features of dot matrix reflection pattern

The dot matrix reflection shown in the figure is deliberately enhanced in brightness such that the range of grey level in the image is linearly normalized to scale [0, 255] as presented in Equation. 4.5.

$$g^N(x, y) = \frac{255}{g_{max} - g_{min}}(g(x, y) - g_{min}) \quad (4.5)$$

where $g(x, y)$ and $g^N(x, y)$ are grey level at position (x, y) before and after normalization respectively, and g_{max} , g_{min} are the maximum and minimum grey level of the image before

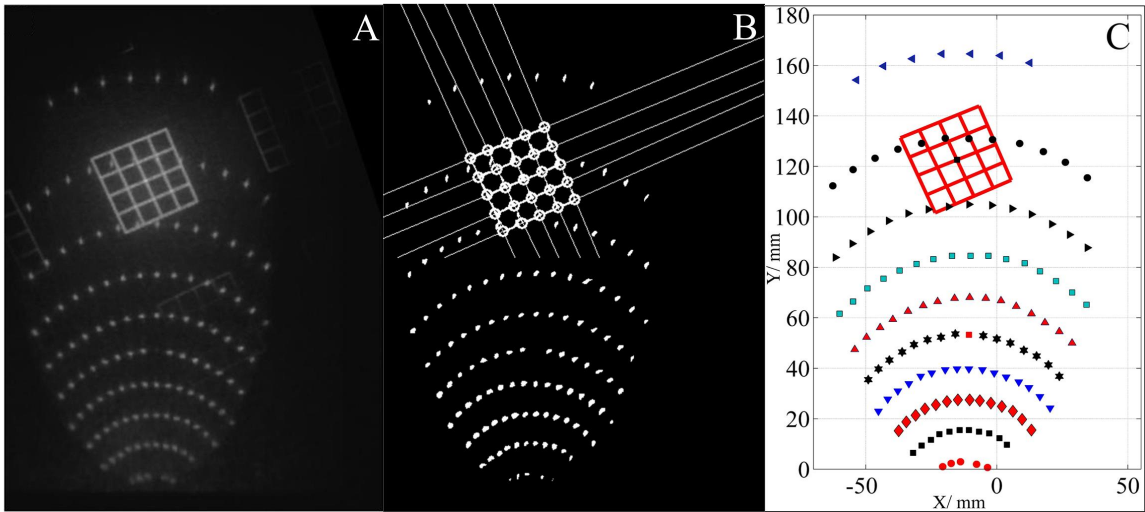


Figure 4.4: Results of grid pattern identification: A) The example image; B) Result of Hugh Transformation; C)The grid pattern

normalization. The original captured image corresponding to Figure. 3.4b is shown in Figure. 4.5a. Figure. 3.4b is also presented in Figure. 4.5b for a comparison. Please note that the brightness enhance is only for readability purposes. In this section, Figure. 4.5a is taken as an example to demonstrate the development of the proposed recognition procedure.

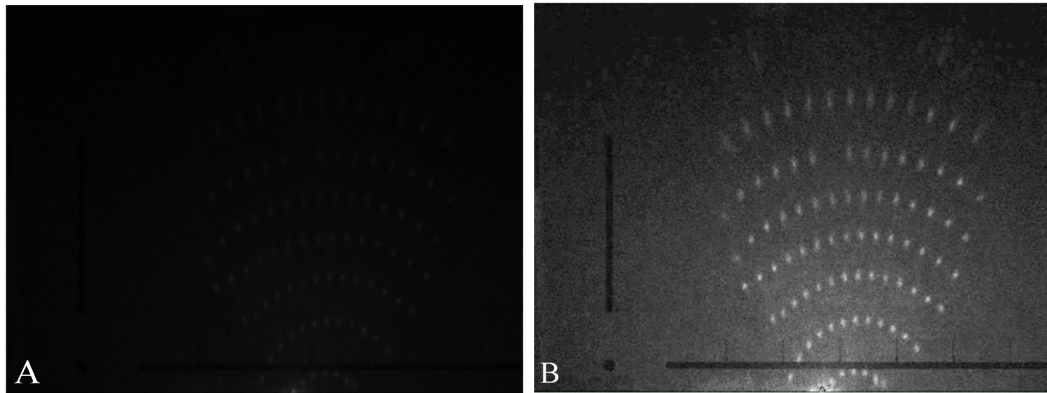


Figure 4.5: Captured image of dot matrix reflection. A) Original image; B) Brightness-enhanced image.

The following observations can be found in Figure. 4.5.

- The reflected laser dots, especially those in the upper part of the image are highly alike in appearance with the impulse noises in the image.
- The reflection pattern has a comparatively low contrast to the background i.e., the part other than the reflection pattern in the captured image.

- Because of the difference in travel distance for the arc radiation in the sensing system, the background in the lower part of the image is much brighter than that in the upper part.

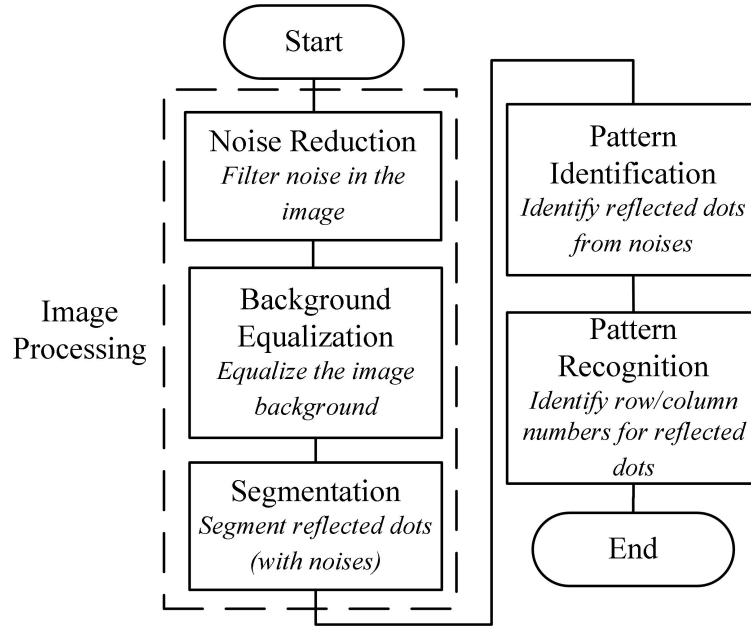


Figure 4.6: Flowchart for the proposed recognition procedure

Images with different patterns' grey levels might be captured due to different welding conditions, i.e, the welding current, travel speed, etc. Yet, because of the inherent nature of the sensing system, the aforementioned observations can always be found in every captured image during the welding experiments.

To avoid the interference noise to the recognition procedure, a noise reduction algorithm is required to remove the noise in the image. Also, it is necessary to balance the brightness of the background before segmentation otherwise irrelevant information from the background would be extracted in addition to the reflection pattern. To this end, the pattern recognition procedure is proposed as shown in Figure. 4.6. The effectiveness and robustness of the proposed procedure will be demonstrated in the following two section and verified in next sections.

4.2.2 Image processing of dot matrix reflection

Image processing

The image processing in the proposed procedure includes three operations: 1) noise reduction to smooth the image to assure the effectiveness of subsequent operations; 2) background equalization to unify the background brightness of the captured image ; and 3) segmentation to extract the reflection pattern.

1 **Noise Reduction** The laser reflection pattern can be considered as a set of subjective speckle pattern [127], which needs to be reduced in circumstances such as medical imaging

([167, 52]) and radar imaging [77]. In this research, the reflection pattern is the feature required to identified against the noise mainly introduced by the arc radiation. In the proposed procedure, the wavelet soft thresholding method is employed in the procedure [37].

Wavelet noise reduction procedures rely on the recurrent fast wavelet transform (FWT) algorithm proposed by Mallet[85]. Denote signal

$$\tilde{x} = x + \tilde{n} \quad (4.6)$$

where x is the noise-free signal and \tilde{n} is the noise. Then the principle of a wavelet-based noise reduction can be described as

$$\hat{x} = FW^{-1}T_{\lambda}FW(\tilde{x}) \quad (4.7)$$

where \hat{x} is an estimation of x , $T_{\lambda}(\cdot)$ is the thresholding operation, $FW(\cdot)$ and $FW^{-1}(\cdot)$ are the forward and inverse FWT respectively. In order to present lose of useful information in the captured image, a soft thresholding is applied [37]:

$$T_{\lambda}(w) = \text{sgn}(w) \times \max(0, |w| - \lambda) \quad (4.8)$$

where w is the wavelet coefficient in the thresholding and the threshold λ is defined as

$$\lambda = \sqrt{2 \ln(N)} \times \sigma \quad (4.9)$$

where N is the signal length, and σ is the standard deviation of the noise.

A 8th Symlet Wavelet with 3 levels is used for the fast wavelet transformation (FWT) [34]. The Symlet wavelet with even number of wavelets is a good tradeoff for noise reduction performance and computation complexity in soft thresholding [27]. The resultant image is shown in Figure. 4.7a.

2 Background Equalization Due to the uneven background in the image which would adversely affects an effective segmentation, an equalization operation is thus adopted in the proposed procedure. Because of the comparatively low contrast of the reflection pattern in the captured image, a traditional histogram equalization would enhance irrelevant information in the background which would lead to the reflection pattern even harder to be identified [49]. To this end, a Top-hat transformation is adopted equalize the grey level of the background equalization while preserving the reflection pattern [49]. A morphological top-hat operation is performed which is defined:

$$h = f - (f \circ b) \quad (4.10)$$

where f and h are the image before and after the top-hat operation respectively, b is the structuring element, and $(f \circ b)$ is the opening operation.

The dimension of the structuring element should be selected carefully here to guarantee that on one side the whole peak area of every reflected dot is preserved, and on the other side the noise around those peak areas are included in the structuring element (the noise should be reduced or erased if not included in the structuring element). According to observation

during welding process, the size of the reflected dot almost remains the same in the process. Hereby a flat 7-by-7 element is used here. Due to different welding conditions, the grey level scales in different images might vary. Grey level normalization as shown in Equation. 4.5, is further applied. The resultant image is shown in Figure. 4.7b.

3 Segmentation In order to extract the reflected laser dots from the background in the image, an appropriate segmentation is required which can be determined by analyzing the histogram of the image, as shown in Figure. 4.7c. It can be observed that most pixels are concentrated in two levels: 0 and 12, the first non-zero gray level. Most of those pixels can be considered as the background and possibly part of the noise. In this sense, the second smallest nonzero gray level in the histogram is chosen as the threshold for a binary segmentation. In the demonstration case, the threshold value is 23. The result is shown in Fig. 4.7d.

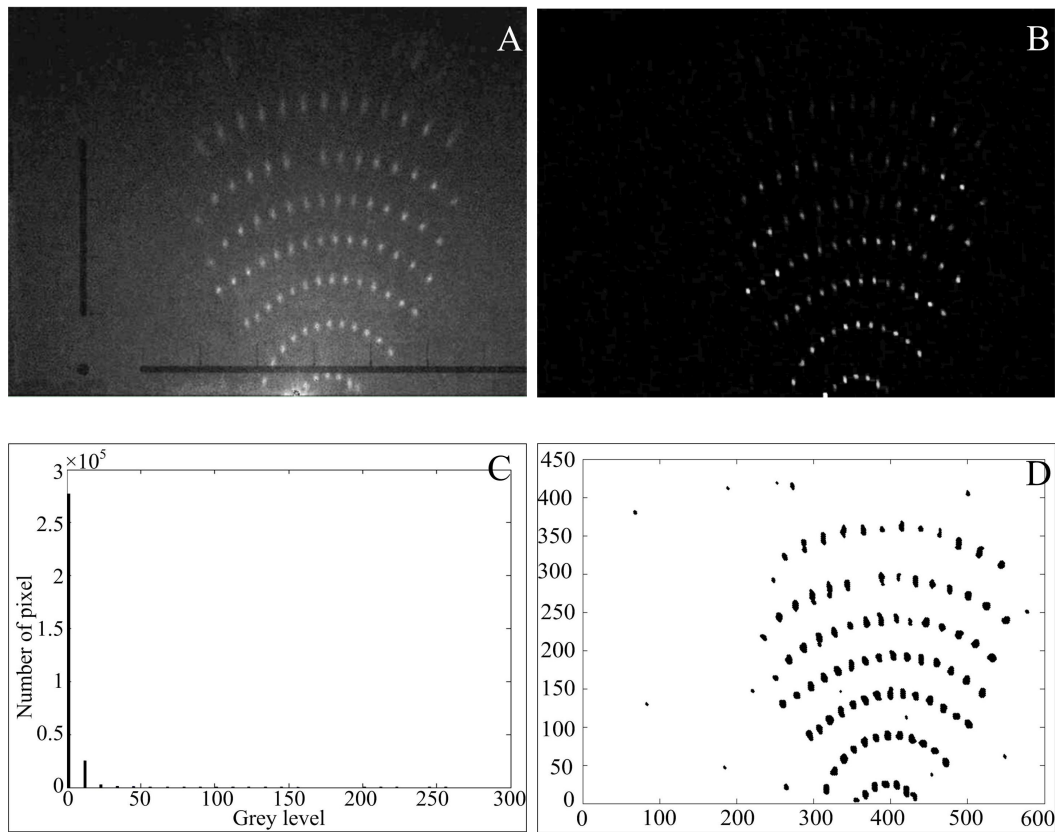


Figure 4.7: Results of the image processing. (A) resultant image of wavelet noise reduction, brightness of the image is deliberately enhanced for readability purposes; (B) resultant image of top-hat operation and gray stretch; (C) histogram of the image in Figure. 4.7b; (D) resultant image after the binary segmentation, the unit of both axes is pixel.

The simple binary segmentation can effectively identify all the reflected laser dots. However, it nevertheless can be found that some noises, referred as the “fake dots”, are mistakenly identified as well in the resultant image. Since the binary segmentation is not an adaptive thresholding algorithm, it might either lost uncertain numbers of reflected laser dots or retain some fake dots. For the former situation, the lost laser dots might not able to be

retrieved. To this end, in the proposed procedure the second smallest nonzero gray level is chosen as the threshold to preserve as many as reflected dots as possible. For the fake dots, an robust identification algorithm is required which is capable of distinguishing the laser dots from fake dots in different experiment conditions. Further, a recognition rate has been defined later in the paper to evaluate the unsuccessful recognition or loss of the reflected dots.

As can be appreciated from in Figure. 4.7d, each dot, including both fake dots and reflected laser dots, refers to a region of connected dark pixels. In the 8-bit gray image, the gray level of the background is 255 and the dots' gray level is 0. Denote I be all the pixels in the image. The set of all dark pixels D can be defined as $D = \{g(x, y) = 0 | (x, y) \in I\}$. For each dot $D_i, i = 1, 2, \dots, N$, where N is number of dots, it has the following properties:

1. $\bigcup_{i=1}^N D_i = D$
2. $D_i \cap D_j = \phi, \forall i, j \in 1, 2, \dots, N$

where ϕ is a null set.

Hereby, a recursive search algorithm based on seeded region growing (SRG) [9] is employed to find the size of each dot in the image. The size histogram for all the dots thus can be calculated, as shown in Figure. 4.8. It can be found that fake dots' size is small, thus they are concentrated in area F . The laser dots' size is comparatively large, therefore they are clustered in area R . Therefore, a bimodal histogram is presented in Figure. 4.8. The size difference between reflected dots and the fake dots indicates that the laser light (reflection pattern) is brighter than the arc radiation (noise) in the imaging plane. This is the uniqueness of the sensing system, i.e., keep the imaging plane a certain distance from the electrode such that arc radiation significantly decays in the propagation while the laser light's intensity remains almost the same. The arc radiation is roughly proportional to the welding current applied in the process. Since in this research a moderate range of current is used, the intensity of the arc radiation is thus not as sufficiently strong as that of the laser dots in the imaging plane. Therefore, the size difference/bimodal histogram can always hold in our study although it can not be ground proved.

To distinguish the reflected laser dots from fake dots an optimal threshold is required. Moreover, the required threshold should be adaptive and robust against different welding conditions in order to effectively identify the reflection pattern, since the reflection pattern during different welding experiments might not be the same.

The size-level histogram and the probability mass function (PMF) of the dots are respectively denoted by $h(s)$ and $p(s)$, $s = 1, \dots, S$, where S is is the maximum size of the dots in the image. The cumulative probability function is defined as:

$$P(S) = \sum_{i=1}^s p(i) \quad (4.11)$$

where $p(i) = \frac{n_i}{N}$, N is the total number of the dots, n_i presents the number of the dots whose size is i . An arbitrary threshold $T \in (1, S]$ divides the dots into two groups, fake

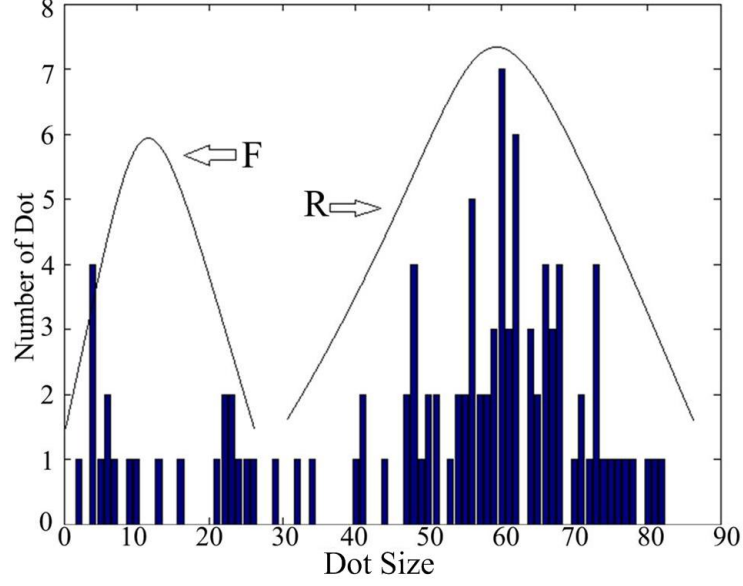


Figure 4.8: Histogram of dot size

dot group and reflected dot group whose PMFs are defined as $p_f(s), 1 \leq s \leq T - 1$ and $p_r(s), T \leq s \leq S$. Their probabilities are calculated as follows:

$$P_f(T) = \sum_{s=1}^{T-1} p(s) = P(T), \quad P_r(T) = 1 - P(T) \quad (4.12)$$

The mean for each group is a function of the threshold T :

$$\mu_f(T) = \sum_{s=1}^{T-1} \frac{s \cdot p(s)}{P(T)}, \quad \mu_r(T) = \sum_{s=T}^S \frac{s \cdot p(s)}{1 - P(T)} \quad (4.13)$$

In order to evaluate the threshold, an objective function is introduced which is defined in the following equation [47].

$$J(T) = \sigma_B^2(T)/\sigma^2 \quad (4.14)$$

where

$$\sigma_B^2(T) = P(T)[1 - P(T)][\mu_r(T) - \mu_f(T)]^2 \quad (4.15)$$

$$\sigma^2 = \sum_{s=1}^S (s - \mu)^2 p(s) \quad (4.16)$$

are the between-class variance and the variance of sizes for all (reflected laser and fake) dots respectively, and μ is the mean of the sizes for all dots. Then, an optimal threshold is T^* what maximizes the objective function:

$$J(T^*) = \max (\sigma_B^2(T)/\sigma^2) \quad (4.17)$$

Taking the dots in Figure. 4.7d into calculation, the resultant T^* is 23. Using this threshold, the reflected laser dots are identified, and their the positions are shown in Figure. 4.9b. Figure. 4.9a shows all the dots in the captured image before the thresholding operation.

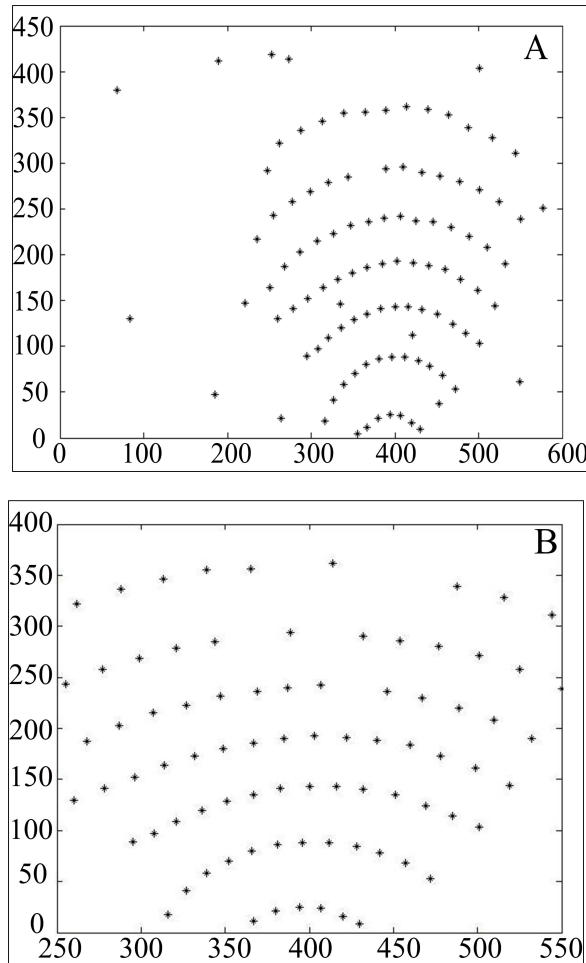


Figure 4.9: Identification of reflection pattern. (A) dots in the captured image before the proposed adaptive thresholding, those dots includes both the reflected laser dots and the fake dots; (B) identified reflected laser dots.

Compared between Figure. 4.9b and Figure. 4.9a, one can find all the fake dots are filtered out after the thresholding, while majority of the reflected dots is identified. The proposed optimal thresholding can adaptively calculate the threshold value for each individual captured image. In different images, the dynamically calculated threshold is expected to be different such that the laser dots can be effectively distinguished from those fake dots.

However, it can also be observed that a few reflected laser dots, 5 out of 86 dots which is about 5.81% of the error rate in this case, are misjudged as fake dots. Although a small portion of reflected dots are temporally miscategorized, they can be retrieved which will be detailed in the next section. Furthermore, the adaptive thresholding facilitates the recognition of the reflection pattern by avoiding the possible interference from the fake dots.

Pattern recognition process

In this section, a recognition process is developed to correlate the reflection pattern to the projection pattern, i.e., to match each reflected dot to its corresponding incident ray. The recognition of the row and column number for each reflected dot is detailed in following next two sections.

1 *Row recognition of the reflection pattern*

The row recognition can be considered as a two-step process:

- cluster selection process which is to identify the row numbers for each reflected dot in the reflection pattern as illustrated in Figure. 4.10; The curves
- mapping process in which the resultant row numbers in the reflection pattern are matched to the projection pattern (dot matrix).

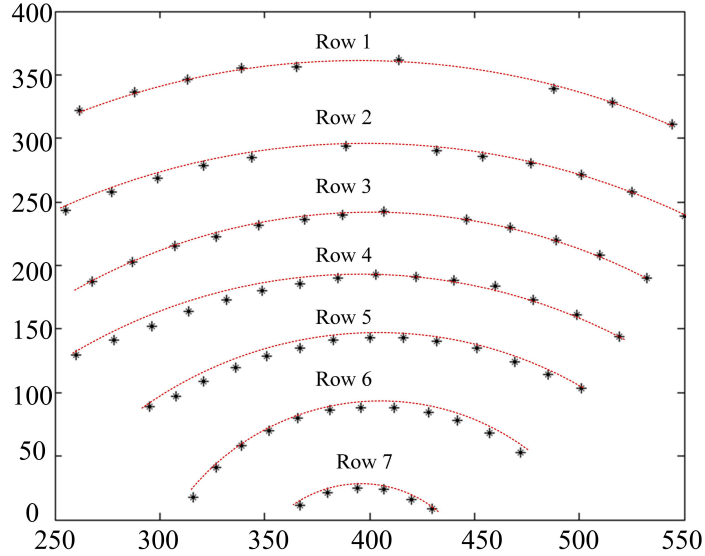


Figure 4.10: Illustration of fitted curves of the rows

In Figure. 4.10, the reflected dots are well distributed in several smooth convex curves which can be denoted by different curve equations with finite orders. For an arbitrary row r_α in the reflection pattern, its corresponding equation can be written as

$$y = r_\alpha(i_{N_\alpha}^{(\alpha)}, \dots, i_1^{(\alpha)}) = i_{N_\alpha}^{(\alpha)} x^{N_\alpha-1} + \dots + i_2^{(\alpha)} x + i_1^{(\alpha)} \quad (4.18)$$

where $i_{N_\alpha}^{(\alpha)}, \dots, i_1^{(\alpha)}$ are the coefficients of the curve equation for row r_α , and $\alpha = 1, \dots, R$, where R is the number of the rows in the reflection pattern, in the case shown in Fig. 4.10, $R = 7$.

It should be noted that the rotations of the torch and the helmet (R_{mt} or R_{mh}) twist the formation of the reflection curves. However, with a corresponding reverse rotation transformation, the curves can be presented using Equation 4.18.

This reflection pattern is determined by the dynamics of the arc welding process. With a moderate current applied in the process, the arc pressure employed upon the weld pool is not enough to change convex smooth weld pool surface to concave. Therefore, the reflection pattern presents a cluster of smooth convex rows. Since there is no filler metal to the weld pool in this study, the convexity of the weld pool is comparatively small such that the curvatures of the reflection rows in the reflection pattern are close to each other. Without abrupt change of current (arc pressure), the curvatures of the rows are expected to vary slightly during the welding process. Therefore, the rows can be denoted by equations with the same order, e.g., $r_\alpha(i_N^{(\alpha)}, \dots, i_1^{(\alpha)})$

It should be noted the intention of the curve equations, the finite-order polynomials, is to find the discrete reflected dots close enough to certain curves such that they can be clustered to the particular rows other than to exactly fit the rows. To this end, a threshold δ is required for the cluster selection.

Let P be the number of the reflected dots in the reflection pattern, then the row number of an arbitrary reflected dot (x_k, y_k) is α if

$$\hat{y}_k - y_k \in [-\delta, \delta] \quad (4.19)$$

where $\hat{y}_k = r_\alpha(i_N^{(\alpha)}, \dots, i_1^{(\alpha)})$, and $k = 1, \dots, P$. δ is the threshold in pixel.

Row r_α can be considered a unique point in the N -dimension parameter space expanded by the N linearly independent variables, i.e., i_N, \dots, i_1 . If an arbitrary reflected dot fits Equation. 4.18, any curves that pass through the dot in the captured image cross the point $r_\alpha(i_N^{(\alpha)}, \dots, i_1^{(\alpha)})$ in the parameter space. Because of the discrete distribution of the rows in the reflection pattern, the parameter space can be discretized along each dimension to finite number of bins. Figure. 4.11 shows an illustration of a 3-dimension discrete parameter space.

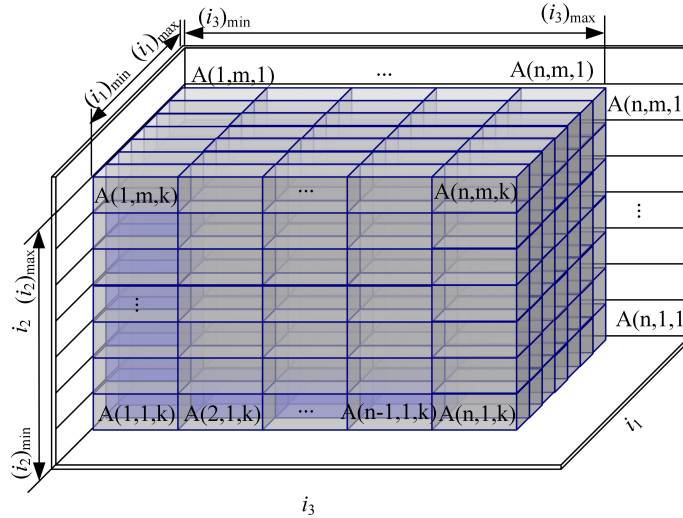


Figure 4.11: The illustration of a 3-dimension discrete parameter space. $[(i_1)_{\min}, (i_1)_{\max}]$, $[(i_2)_{\min}, (i_2)_{\max}]$ and $[(i_3)_{\min}, (i_3)_{\max}]$ are the ranges of the three coefficients i_1, i_2 and i_3 , which are divided into n, m and k segments, respectively.

In Figure. 4.11, each bin in the space corresponds to a possible row candidate $\xi(g, h, l)$ where $g = 1, \dots, n$, $h = 1, \dots, m$ and $l = 1, \dots, k$. Further, associated to each row candidate there is an accumulator $A(g, h, l)$ recording the number of reflected dots that are in the row $\xi(g, h, l)$. In this sense, with careful selection for the scale of the row coefficients, the row candidate that holds the most reflected dots in its associated accumulator must be one of the qualified row. Therefore, the algorithm for the row cluster selection is developed as shown in flowchart in Figure. 4.12.

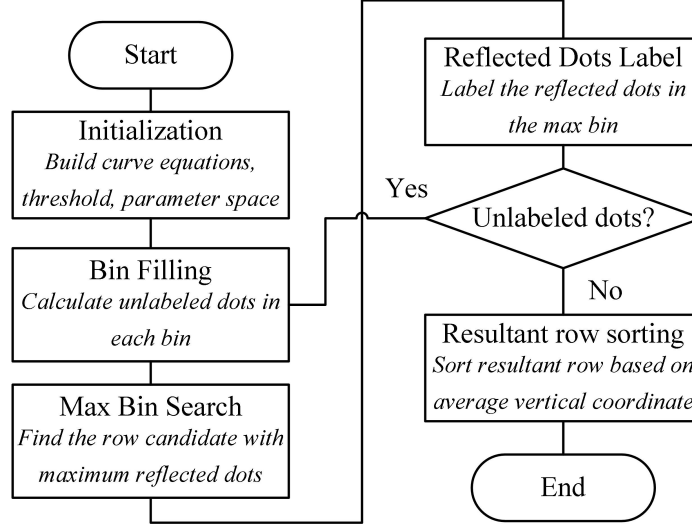


Figure 4.12: The row cluster selection algorithm

After sorting the resultant rows based on the average vertical coordinate of the reflected dots in each rows, i.e., the y values, the cluster selection process result is illustrated in Figure. 4.10.

In this study, the equation used to fit the row of reflected dots, i.e., Equation. 4.18, is a 2-order polynomial as shown in Equation. 4.20,

$$y = a(x - b)^2 + c \quad (4.20)$$

where a , b and c are the three coefficients. Hence, the parameter space for the cluster selection is three-dimensional.

The scales for the coefficients should be carefully determined. In the experiments conducted in this study, the variation of a is small, the range of a falls in $[-0.005, -0.001]$. The scale of b is $[x_c - \sigma, x_c + \sigma]$ where x_c is the mean value of the x coordinates of all the reflected dots, i.e., $x_c = \frac{\sum_{k=1}^P x_k}{P}$, and σ is a pre-defined offset. Parameter c is in the range $[y_{min}, y_{max}]$ where y_{min} and y_{max} are the minimum and maximum y coordinates of all the reflected dots, i.e., $y_{min} = \min(y_1, \dots, y_p)$ and $y_{max} = \max(y_1, \dots, y_p)$. According to Figure. 4.11, the length of step for a is 0.0005, thus $n = 11$. Offset for b , σ , is set 20, and the length of step for b is 5, thus $m = 19$. The length of step for c is set 10, which means the $k = \lceil \frac{y_{max} - y_{min}}{10} \rceil$.

The resultant rows, as shown in Figure. 4.13a, are effectively identified using the proposed procedure. The curves present the identified row. It can be found some of the reflected dots are missed in some of the rows. That is because those reflected dots are mistakenly judged

as impulse noise. After all the rows are extracted, those reflected dots can be retrieved. For one specific row, abnormal large distances, 1.8 times large than the mean distance in this study, between neighbor dots are found, if any, where reflected dots are considered missed among the distances; then starting from the largest size, all the filtered out dots (including the fake dots, i.e., the noise) are visited to find the fittest to fill in the positions. The result is shown in Figure. 4.13b. Reflected dots are marked with different shapes in different rows. Compared with Figure. 4.13a and Figure. 4.13b, the misjudged reflected dots are identified and retrieved.

It should be noted the row equation for the cluster selection, i.e., Equation. 4.18 does not have to be 2-order polynomial. For more accuracy to describe the row, curve equations with higher orders might be selected. However, higher orders bring more coefficients which leads to a great increase of computation for the Bin Filling in Figure. 4.12. Further, the resultant accurate matches of reflection pattern recognition in turn confirm the reasonableness of the selection for the 2-order polynomial.

The distortion of the reflection pattern is caused by the weld pool, and its surface geometry (size and shape) determines the correspondence between the projected and reflected laser dots. In this study, moderate welding parameters (current, arc length and welding speed) are utilized, therefore the weld pool surface is convex and both of the correspondences for the row and column of the weld pool obtained during the welding process are sequential[114].

With the knowledge of the correspondence between the projection and reflection pattern, the individual mapping between the projected dots and reflected dots is still unclear. At least one pair of dots in the two patterns is required to be determined first, then the mapping of other dot pairs can be derived using the known correspondence.

It can be found in Figure. 4.13b that there is one point missed in the second row of reflected dots from the top of the reflection image. That intentionally absent dot is the center dot (in 10th row and 10th column of the 19 × 19 dot matrix). It serves as the reference dot to facilitate the row/column identification and the corresponding match between reflected dots and incident rays. To this end, the row pattern recognition can be accomplished. The result is shown in Figure. 4.13c. The numbers in the image indicate the corresponding row match between the row in the reflection image and the incident rows in the dot matrix.

2 Column recognition of the reflection pattern

Since the correspondence between the projection and reflection pattern is sequential, the column number for each dot in the row can be easily identified, after the reference dot is found in one row in the reflection image. The result is shown in Figure. 4.13d. The distortion of the laser pattern in the vertical direction is much less severe than that in the horizontal direction. Therefore, a center line $y = kx + b$ is fitted using the reference dot together with its nearest adjacent dots in the neighbor rows. For any row r_α , the 10th dot is the one nearest to the fitted line:

$$(x_\alpha^{10}, y_\alpha^{10}) = \{(x_\alpha^i, y_\alpha^i) | \min(y_\alpha^i - (kx_\alpha^i + b))\} \quad (4.21)$$

where $i = 1, \dots, S_\alpha$, (x_α^i, y_α^i) is one of the S_α dots in row r_α . The center line is tilted other than being vertical to the horizontal axis. It is because the center dots in each row are not always projected on the line formed by interception between smooth symmetric weld pool surface and yoz plane during experiments. There also might be some deviation of the center line projection due to the fluctuation of the weld pool.

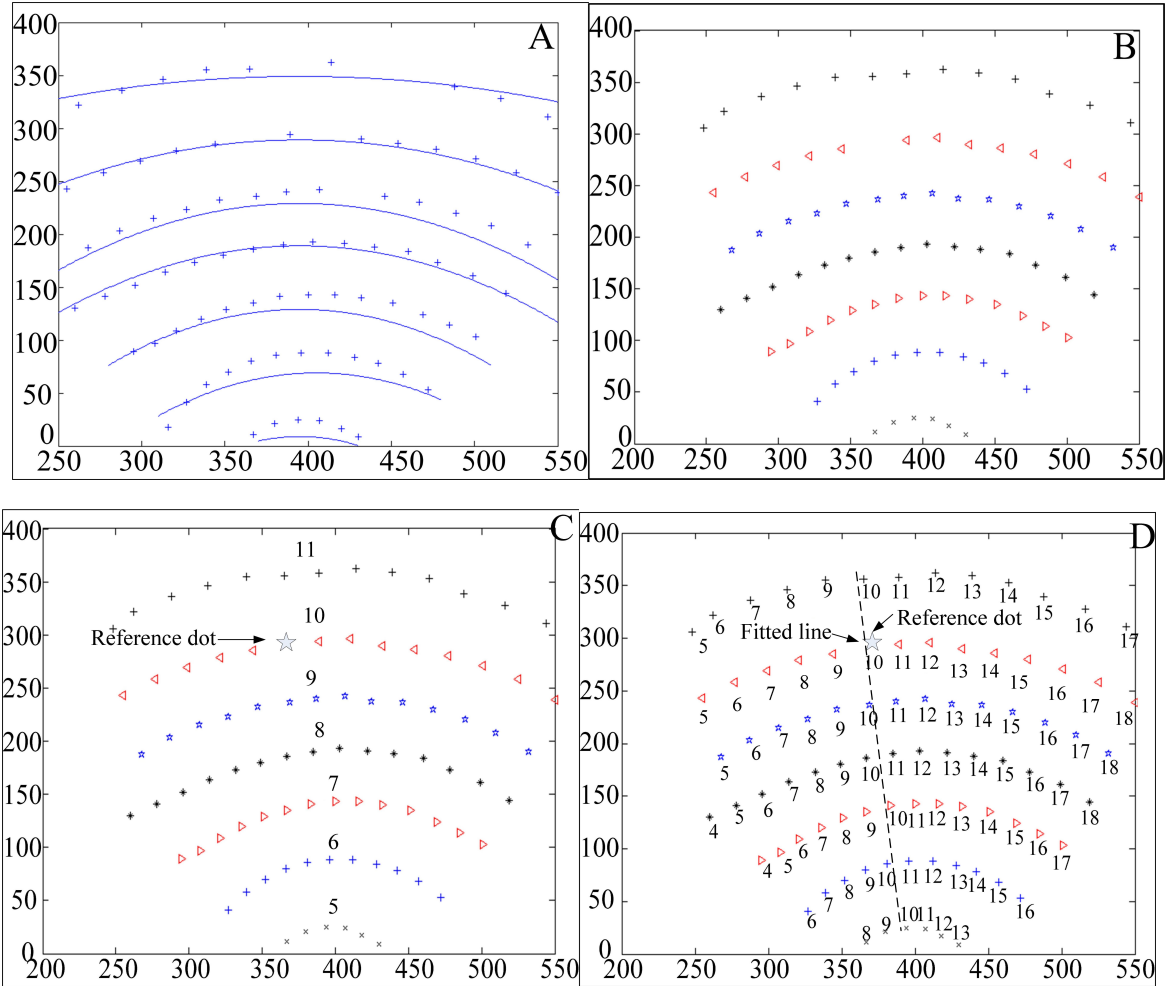


Figure 4.13: Results of pattern recognition. (A) results of row identification; (B) reflected dots in different rows; (C) reflected rows matching with the corresponding incident rows in the dot matrix. The numbers represent the incident rows in the dot matrix that the reflected rows match respectively; (D) column recognition with fitted line.

Verification of the image processing algorithms

The proposed image processing and pattern recognition algorithms are verified using an image example with both grid and dot matrix reflection patterns, Figure. 4.3a. The results are shown in Figure. 4.14, i.e., Figure. 4.14a is the originally captured image using the mobile sensing system illustrated in Figure. 3.1. The calibration result is shown in Figure. 4.14b. Figure. 4.14c is the resultant image of noise reduction and background equalization. Based on the resultant image, Hugh Transformation is applied to identify the reflection grid pattern, as shown in Figure. 4.14e. With implementing the proposed pattern recognition, the dot matrix reflection pattern is successfully identified shown in Figure. 4.14f.

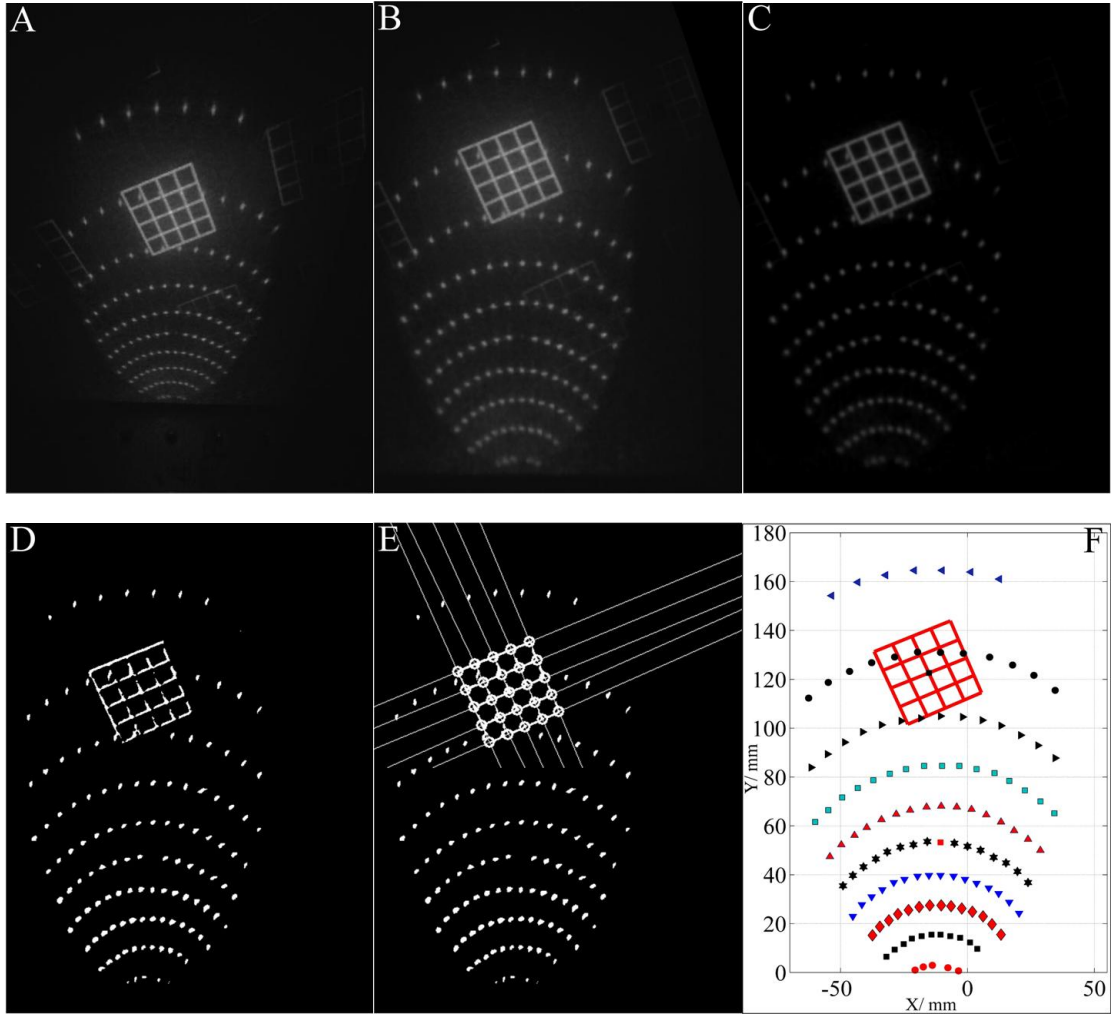


Figure 4.14: The results of the proposed image processing and pattern recognition

4.2.3 Real-time verification for identification of dot matrix reflection pattern

In this section, the image processing and pattern recognition algorithms proposed to identify the reflection pattern of dot matrix are verified by a series of welding experiments.

1 *Experiment conditions and designs*

To evaluate the robustness of the proposed pattern recognition procedure, and the effectiveness of the steps in the procedure, three single-value metrics are defined as the following:

1. **Noise Reduction (NR) rate** The NR rate (R_{NR}) is defined in Equation. 4.22:

$$R_{NR} = N_{nonNR}/N_{NR} \quad (4.22)$$

where N_{nonNR} and N_{NR} are the numbers of extracted dots (including both reflected dots and fakes dots) after segmentation without and with the noise reduction operation, respectively. With the same reflected dots contained in both N_{nonNR} and N_{NR} ,

NR rate counts for the difference of the reduction of the fake dots, i.e., the effectiveness of the noise reduction.

2. **Thresholding Error (TE) rate** The definition of TE rate is in Equation. 4.23:

$$R_{TE} = N_{mTE}/N_{TE} \times 100\% \quad (4.23)$$

where N_{mTE} is the number of reflected dots misjudged as fake dots in the pattern identification, and N_{TE} is the number of identified reflected dots in the pattern identification step.

3. **Pattern Recognition (PR) rate** The PR rate is defined in Equation. 4.24:

$$R_{PR} = N_{iPR}/N_{PR} \times 100\% \quad (4.24)$$

where N_{PR} is the actual number of the reflected dots in the captured image, while N_{iPR} is the corresponding dots identified by the proposed procedure.

It should be noted that some of the metrics (N_{mTE} , N_{PR} and etc.) in Equation. 4.22 to Equation. 4.24 need to be manually counted frame by frame. Hence, the captured images with one second interval are evaluated by the three metrics during the welding experiments.

To evaluate the robustness of the proposed procedure, experiments with different conditions should be conducted. The major interference for the pattern recognition is the arc radiation which is mostly determined by three parameters: 1) welding current which is approximately proportional to the radiation; 2) shield glass to electrode distance which affects the propagation decay of the arc light; and 3) arc length that determines the amount of radiation blocked by the torch. To this end, three categories of experiments are conducted as shown in Table 4.2. For each set of the three parameters in the categories, same welding experiments are repeatedly conducted for five times. The results from those experiments are analyzed in the following section.

Table 4.2: Robustness experiments with different conditions

Category	Parameters	Conditions
1	Welding Current (A)	56 61 66 71 76
	Tungsten Tip-To-Work Distance (arc length) [mm]	3
	Shield Glass to Electrode (SGE) Distance (mm)	95
2	Welding Current (A)	61
	Tungsten Tip-To-Work Distance (arc length) [mm]	2 3 4 5
	Shield Glass to Electrode (SGE) Distance (mm)	95
3	Welding Current (A)	61
	Tungsten Tip-To-Work Distance (arc length) [mm]	3
	Shield Glass to Electrode (SGE) Distance (mm)	105 115 125 135

The experimental set-up is shown in Figure. 3.1. The welding process is based on direct current electrode negative (DCEN) GTAW. To implement the aforementioned experiments, modifications of the set-up are necessary, i.e., replacing the human welder such that parameters in Table 4.2 can be control accurately: The projective torch is hold by a fixture

and stationary during the experiments; the sensory helmet is also stationary, amounted on a camera tripod, such that the projection angles of the two patterns, SGE distance can be controlled accurately. The pipe is stainless steel T-304/304L schedule 5 [1]. It rotates during the welding, the rotation speed and the arc length are controlled by a computer.

Major parameters selected to conduct the welding experiments and acquire images are shown in Table 4.3. The full penetration, i.e., the liquid weld pool extends from the front to the back face of the work piece, can be produced on the work piece with those welding parameters.

Table 4.3: Major experimental conditions

Welding Parameter	Conditions
Pipe Rotation Speed [mm/s]	1
Tungsten Tip-To-Work Distance (arc length) [mm]	2 ~ 5
Electrode Extension (mm)	3
Electrode Type	EWCe-2
Electrode Diameter (mm)	2.38
Shielding Gas	Argon 100%
Flow rate of Shielding Gas L/min	11.8
Monitoring Parameters	Conditions
Pattern Projection Angle [°]	36
Laser to Electrode Distance (mm)	25
Camera Parameters	Conditions
Shutter Speed (ms)	2 ~ 6
Frame rate (FPS)	30

2 *Experiments and results analysis*

To evaluate the effectiveness of the proposed pattern recognition procedure, an experiment is conducted in which the welding current is 61 A; arc length is 3 mm; and the SGE distance is 105 mm. Other parameters are listed in Table 4.3. A set of captured image with 1 second interval starting from 3 second after the weld pool starts to form is presented in Figure. 4.15. The number in the left upper corner of each image refers the time the image is captured during the experiment. The brightness and the contrast of the images are intentionally enhanced for readability. Using proposed pattern recognition procedure, the resultant pattern in each image is shown in Figure. 4.16. In the figures, the units for x and y axis are both pixel. The stars are the reference dots.

The pattern recognition rate R_{PR} corresponding to Figure. 4.16 is shown in Figure. 4.17. It can be observed in Figure. 4.15 and Figure. 4.16 that only a small portion of dot matrix is reflected by the specular weld pool surface since the weld pool is comparatively small at the beginning of the welding process. Accordingly, the interference of the arc radiation is also weak, therefore the reflection pattern can be easily identified.

As the weld pool keeps growing, more laser dots are reflected. In particular, from 3 second to 8 second the reflection pattern grows from 4 rows to 7 rows indicating the growth in longitudinal direction of the the weld pool, while increase of columns from 9 to 13 showing the extension of the weld pool in transversal direction. More arc light is then reflected which

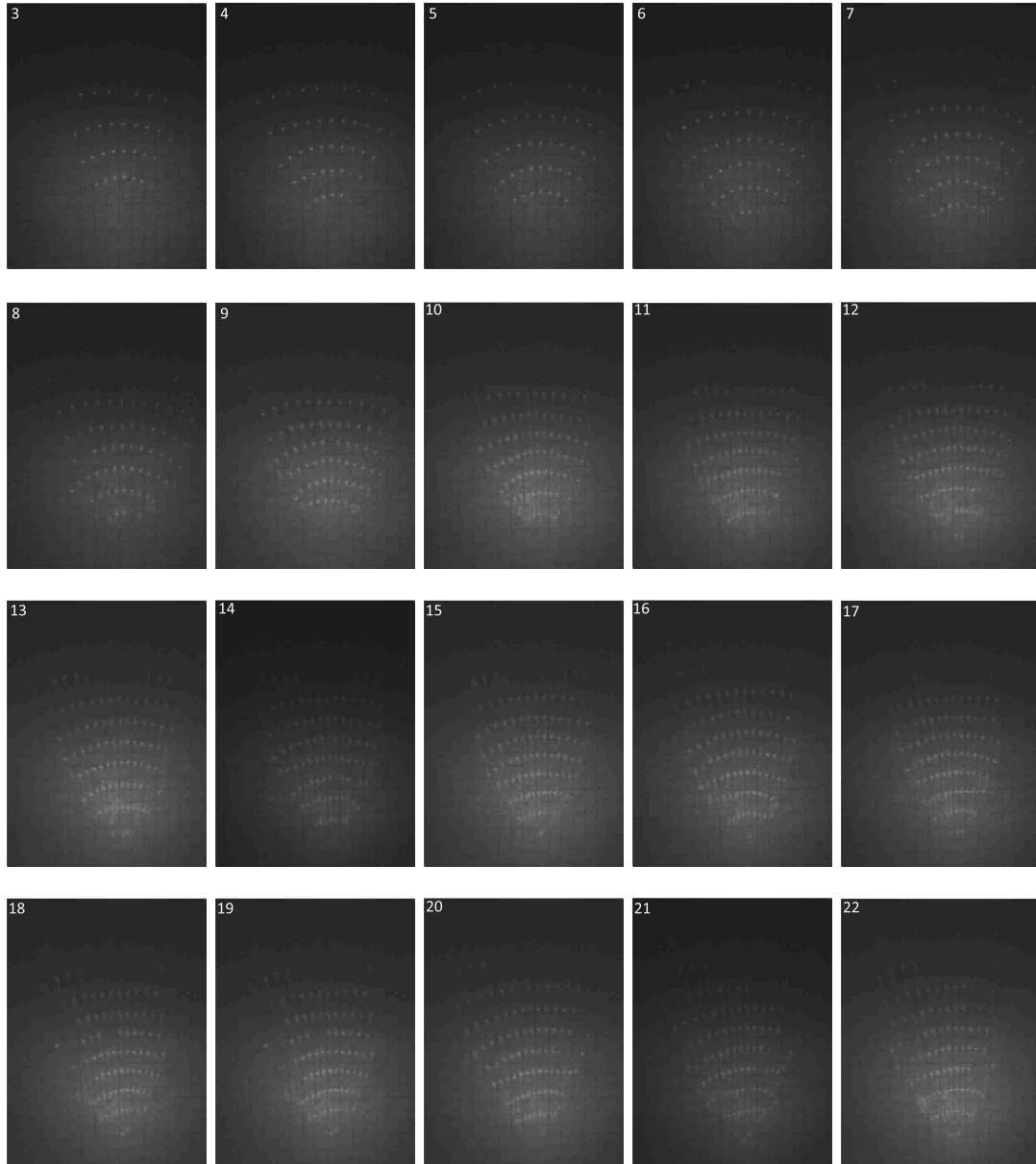


Figure 4.15: Image captured in the first experiment

leads to more radiation interference during the pattern recognition. The arc radiation deteriorates the proposed procedure mainly because the strong radiation comparatively lower the contrast for the reflection pattern to the background, especially, the upper part of the pattern. Therefore, few amount of laser dots, most likely in the upper part of the captured image show no difference in grey level with noise. They are thus considered as noises in the noise reduction operation and would not show in the resultant image after the segmentation. To this end, R_{PR} varies from 100% to 97.8% during this period as shown Figure. 4.17, that means 1 or 2 reflected dots are missed in few frames using the proposed pattern recognition procedure.

It should be noted the purpose of the reflection pattern identification is to reconstruct

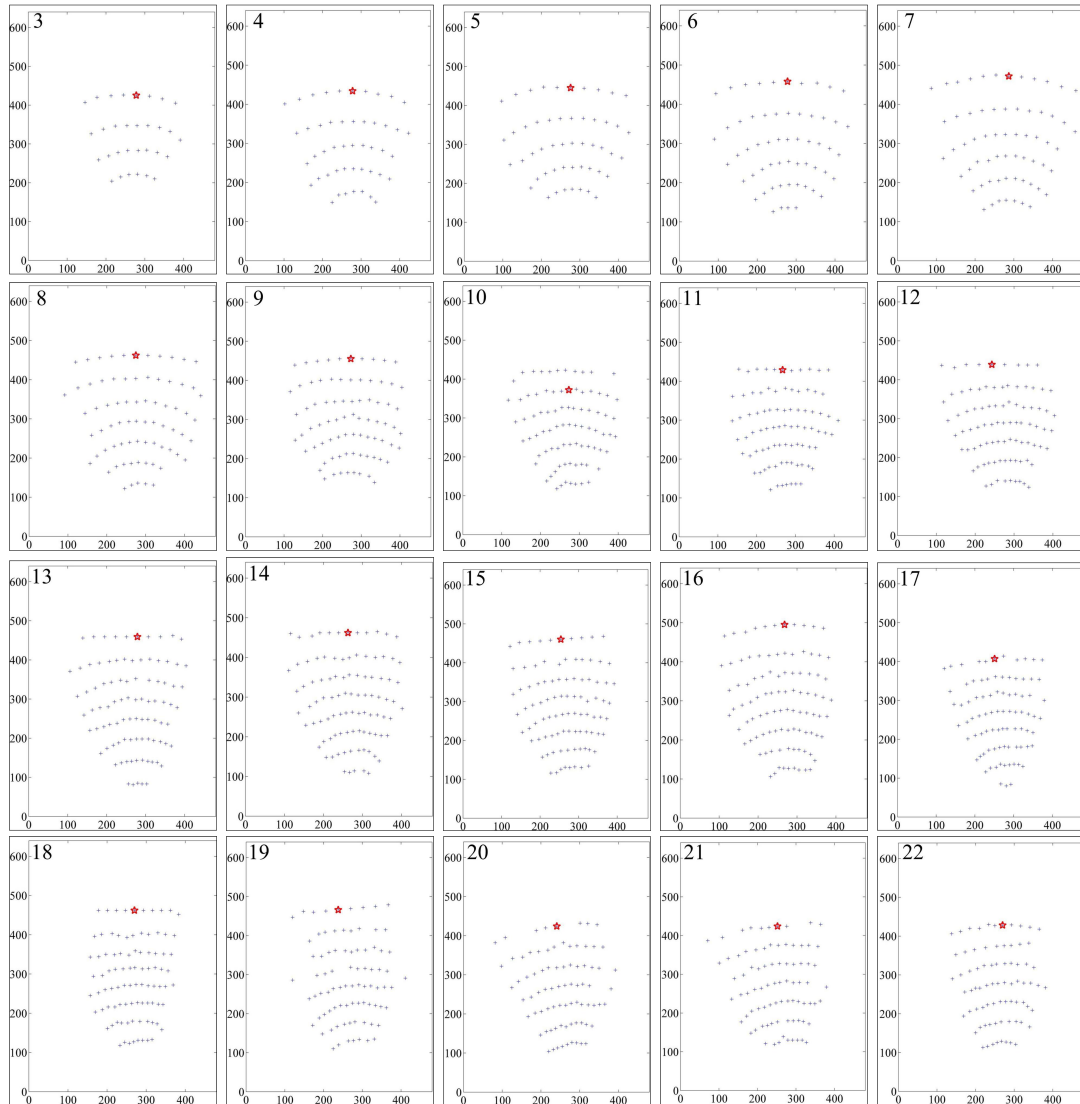


Figure 4.16: Results of pattern recognition in the first experiment

the profile of the weld pool surface. Even in case certain reflected laser dots are missed, the three-dimensional weld pool surface can also be reconstructed using reduced samples. For GTAW process with moderate experiment conditions detailed in Table 4.3, the weld pool surface is relatively smooth and a surface reconstruction using reduced samples is acceptable. In case greater accuracy is needed, the density of the projected laser dots on the weld pool surface can be increased through upgrading the laser dot matrix. In that case, the reflection pattern is expected to be much clearer despite the arc radiation in the captured images.

From 9 second to 22 second, the area of the reflection pattern in the captured image becomes smaller, i.e., the distribution of laser dots in the reflection pattern becomes denser. It is because the weld pool reaches full penetration as the process continues, the weld pool tends to be concave because of the growing gravity force from the liquid metal in the pool. That leads to a smaller size of the reflection pattern in the captured image. The PR rate keeps

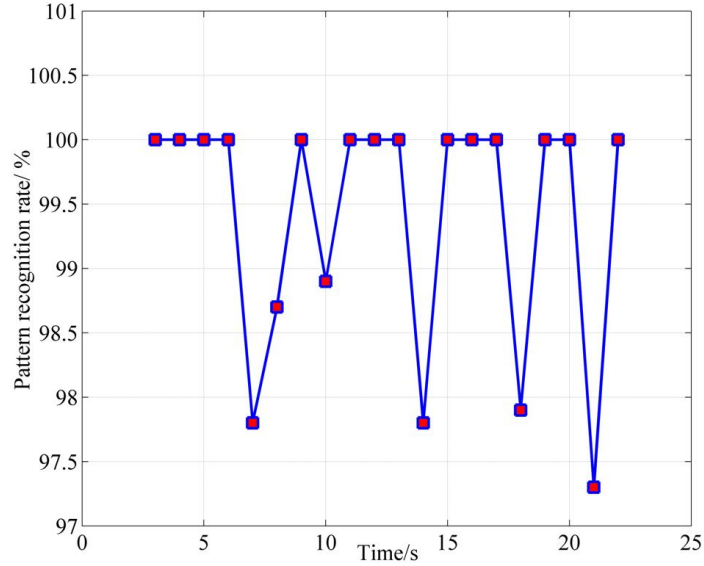


Figure 4.17: The resultant pattern recognition rate in the first experiment

above 97.3% in the whole welding process which verifies the effectiveness proposed pattern recognition procedure.

To demonstrate effectiveness of noise reduction proposed in this study, the NR rate corresponding the processed frames in Figure. 4.16 are shown in Figure. 4.18. As mentioned before, the arc radiation interference at the beginning of the process is weak. Hence, only a few amount of fake dots (noise) are shown in the captured image. Therefore, NR rate is close to 1. With increasingly strong arc radiation, the fake dots would grow greatly without noise reduction. However, the increase of R_{NR} indicates that a significant amount of noise is effectively filtered using the proposed noise reduction algorithm.

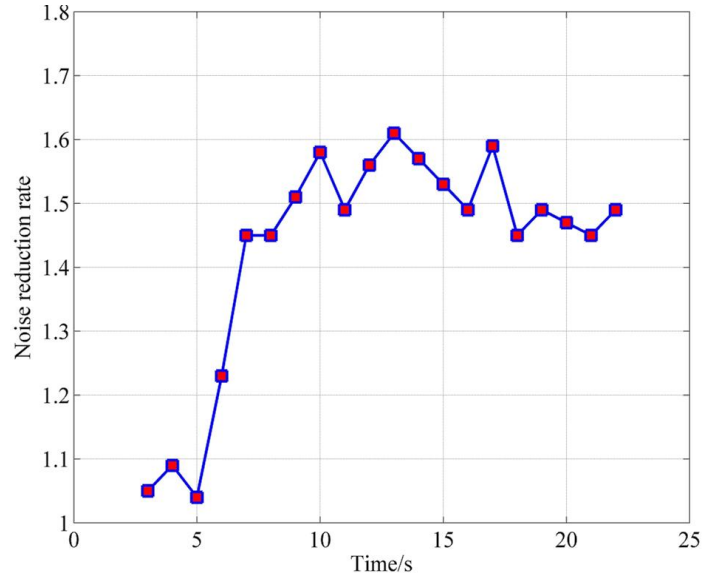


Figure 4.18: Noise reduction rate in the first experiment

To further verify the effectiveness of the adaptive thresholding algorithm, the corresponding thresholding error (TE) rate is shown in Figure. 4.19. With less radiation interference, the error rate tends to be lower. And it increases as the arc radiation grows stronger. Nevertheless, it can be found that the proposed thresholding algorithm keeps the error rate under 6.8% during the experiment. Furthermore, as can be observed in Figure. 4.16 those misjudged reflected dots are successfully retrieved.

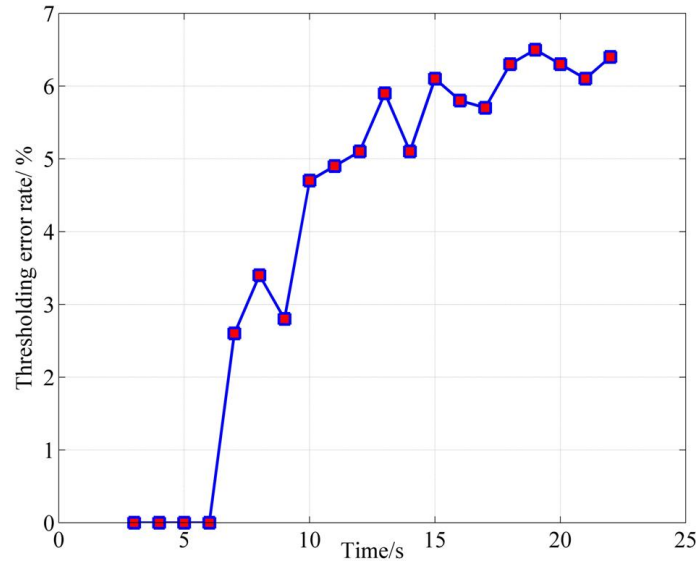


Figure 4.19: Thresholding error rate in the first experiment

To demonstrate the robustness of the proposed procedure, the experiments listed in Table 4.2 are conducted. The noise reduction rate, thresholding error rate and the pattern recognition rate are shown in the Figure. 4.20 to Figure. 4.22. As mentioned in the last subsection, for each parameter set same experiments are repeatedly conducted five times. The square for each parameter set in the figures shows the mean value of the rate in the five experiments, while the error bar indicates the corresponding minimum and maximum rate.

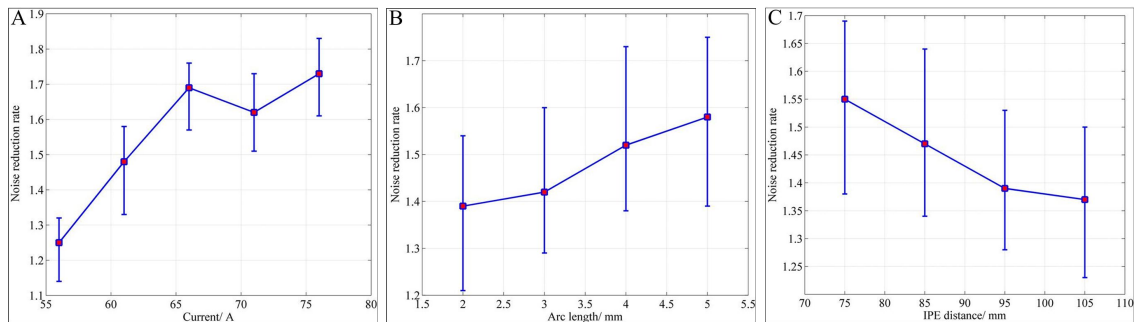


Figure 4.20: Noise reduction rate for the robustness experiments from (a) category 1; (b) category 2; and (c) category 3

It can be observed from Figure. 4.20, the mean NR rate increases from 1.25 to 1.74 as the current varies from 56 A to 76. Also, by increasing the arc length and the SGE distance, the rate slightly augments and decreases respectively. An increase of current leads to the raise of

the arc radiation density which indicates more impulse noise appears in the captured images. Further, by decreasing the arc length the welding torch blocks more arc radiation which would otherwise adversely affect the success of reflection pattern recognition. Moreover, by increasing the SGE distance the captured images are less interfered by the arc radiation. With proposed noise reduction algorithm, the fake dots (noise) have been significantly reduced. Therefore, the NR rate increases as the rise of the current, decreases along with the reduce of the arc length and augmentation of the SGE distance. Comparatively, significance of arc length and SGE distance in affecting the arc radiation interference is less that of the welding current.

The interference from the arc radiation also affects the thresholding error rate. Because of the aforementioned significance differences for the three parameters, the increase of TE rate caused by current augmentation is comparatively larger than that caused by the rise of the arc length or decrease of the SGE distance. The similar tendency is also shown in Figure. 4.22 for the pattern recognition rate.

It should be noted that theoretically, there is another possible error which can be caused by the proposed adaptive thresholding algorithm, i.e, certain number of fake dots are misjudged as the reflected dots. However, that does not happen in our conducted experiments. It might be expected when the arc radiation interference grows strong as the welding conditions go extreme , such as large current, short SGE distance, and etc.

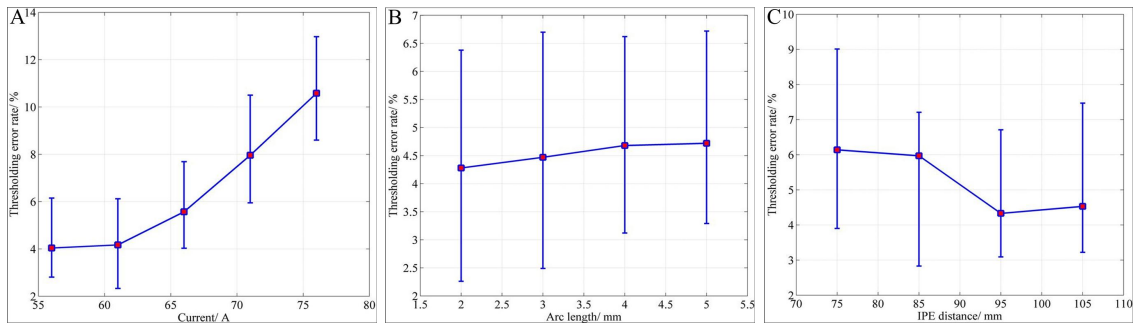


Figure 4.21: Thresholding error rate for the robustness experiments from (a) category 1; (b) category 2; (c) and category 3

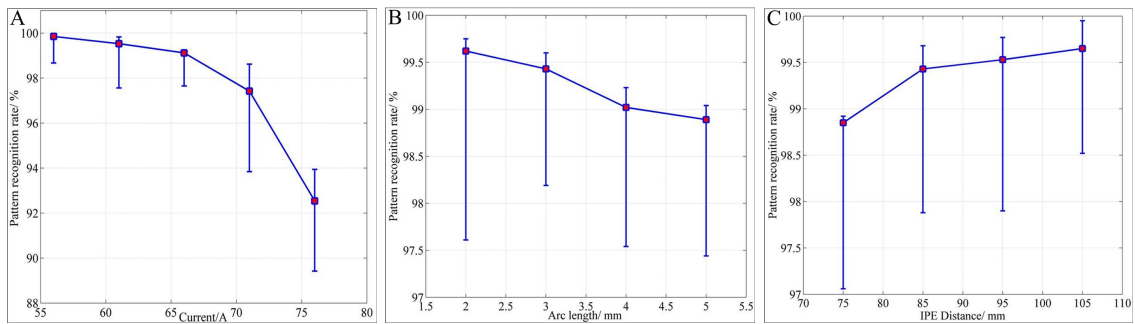


Figure 4.22: Pattern recognition rate for the robustness experiments from (a) category 1; (b) category 2; (c) and category 3

With more arc radiation interference caused by the increase of the current, or the arc length, or decrease of the SGE distance, the fake dots obtained during the proposed procedure

increase not only in number but also in size. Therefore, the bimodal histogram as shown in Figure. 4.8 varies accordingly such that the F area slightly approaches to the R area. That leads to an increase of the TE rate for the proposed adaptive thresholding algorithm, and a corresponding decrease of the pattern recognition rate. However, within all the experiments conducted, the TE rate is less than 12.95 % and the PR rate is higher than 89.32 %. The robustness of the proposed procedure is thus verified.

It should be also noted for a higher accuracy of pattern recognition, the laser generator should be updated with more power density. Then the reflection pattern in the captured image would be clearer, and be identified with higher accuracy.

To test the time complexity, the proposed image processing algorithms and the surface reconstruction procedure have been implemented using Visual Studio 2010 in a desktop with Intel Core 2 T9600 2.8 GHz processor and 4 GB RAM. The images are 640x480 or 480x640 pixels as mentioned earlier and acquired at 30 fps(frame per second). Tests show the proposed image processing procedure/algorithms and the surface reconstruction can be completed in real-time, i.e., at 30 fps, from image capture to the computation of the weld pool surface [151]. The proposed image processing algorithms can be finished in less than 19 ms. The real-time image processing and three-dimensional weld pool surface measurement are thus achieved. For GTAW process that only requires to be controlled a few times per second [100], this real-time speed provided is sufficient.

4.3 Summary

Observing the weld pool surface and measuring its geometrical parameters is a key to develop intelligent welding machines. The observation system used in this study can capture the image of reflection pattern of dot matrix which can be used to reconstruct the 3D weld pool surface. A recognition procedure has been proposed to identify the reflection pattern. In particular, an robust pattern identification algorithm has been proposed to identify the reflected laser dots from the noise in the captured image. Further, an pattern recognition algorithm has been developed to match the the row and column numbers for the reflection pattern to the projection matrix.

Experiments have been conducted in this paper to verify the proposed procedure and the following are concluded:

1. The proposed image processing method can effectively reduce the noise in the captured image and unify the brightness of the image background;
2. The pattern identification algorithm is able to adaptively generate an optimal threshold such that an overall majority of the reflected laser dots are distinguished from the impulse noises;
3. The row and column numbers of the reflected pattern are effectively acquired using the proposed pattern recognition algorithm. The foundation of reconstruction of 3D weld pool surface in GTAW is established;
4. Verification experiments under different conditions confirmed the effectiveness and robustness of the proposed pattern recognition procedure;

5. The proposed procedure can be accomplished within 19 ms which meets the requirements for real-time monitoring and control of weld pool surface in GTAW.

Chapter 5

Orientation Estimation of Sensing System

5.1 Introduction and related works

The measurement of the GTAW process, i.e., reconstruction of the 3D weld pool surface, using the proposed mobile sensing system requires detection of orientation for the torch and helmet in real-time. In this section, the orientation of the projective torch, as an example, is estimated using a kalman-based detection algorithm.

The torch orientation is defined as the torch posture throughout a welding process. It is one of the most important welding parameters, and is directly contingent upon the weld quality and appearance. Optimal quality welds can only be guaranteed if the torch orientation is well adjusted. Inappropriate torch manipulations cause various weld defects/discontinuities, such as poor penetration, undercut, porosity, and different types of cracks ([95],[96],[90]). Thereby, detailed torch orientations for almost every welding process have been specified/recommended by both standardization organizations such as American Welding Society (AWS) ([5], [7]) and by different welding-related companies ([4], [42], [6]).

Different welding processes may have various parameters, such as welding current, voltage, torch traveling speed, wire feed speed if applicable, number of weld pass/layer. The recommended torch orientation manipulations can be different accordingly. Typical recommended torch postures are shown in Figure. 5.1 and Figure. 5.2 for the two welding processes: Gas Tungsten Arc Welding (GTAW) [32] and Gas Metal Arc Welding (GMAW) [42], respectively. Four different fit-up types for each process are illustrated in the two figures. Moreover, four different torch swing patterns are adopted for the four fit-up types in Figure. 5.2, respectively, besides the diversities in torch orientation.

Mastering the torch manipulation is challenging in manual arc welding process. To ensure the weld quality, a human welder is required to maintain a recommended torch posture while moving the torch smoothly along the weld bead, possibly with one particular swing patterns. Due to various disturbances in welding field, the torch is required to be adjusted accordingly to guard against the effect of the disturbances to the weld quality. The capability of proper torch orientation manipulation depends on the welder's skill level and his/her physiological conditions [137].

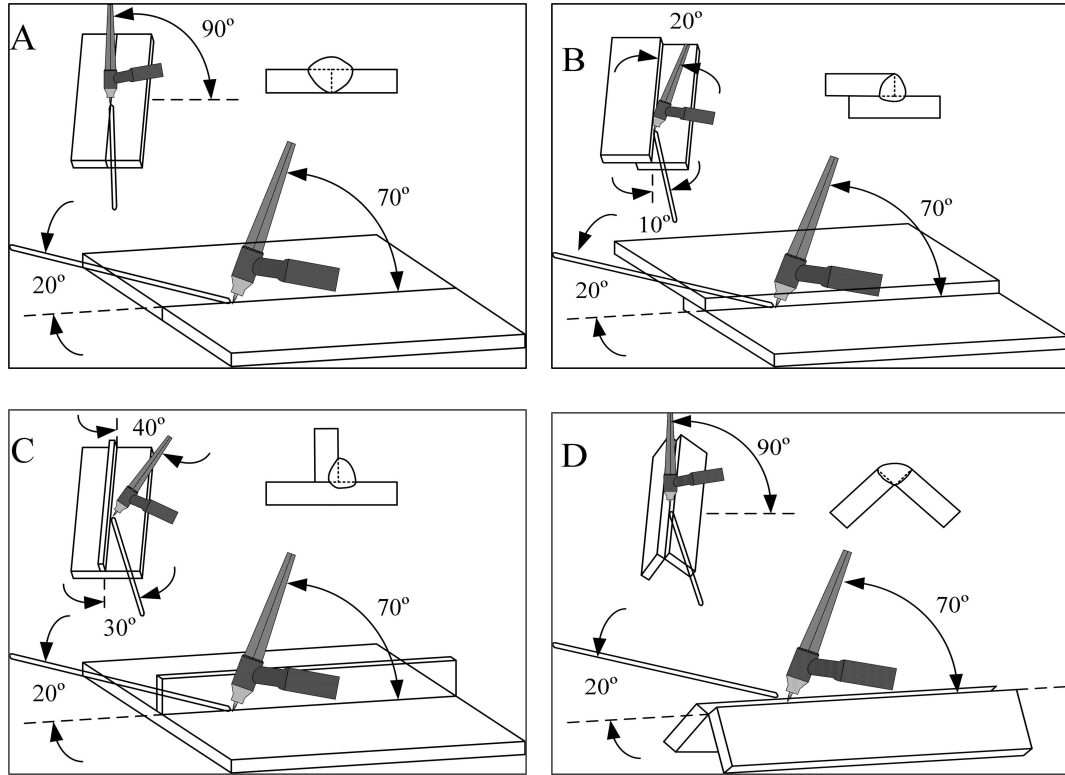


Figure 5.1: Torch orientations for different weld types in GTAW process: (A) butt welds; (B) lap joint; (C) T-joint; and (D) Corner joint.

Within the limit of the authors' searching capability, there is no literature found studying the welding torch orientation sensing in a manual arc welding process. A number of previous researchers focused on welding position sensing in robotic welding ([63]-[166]). However, those studies addressed the spatial position of the tungsten tip (in GTAW) or the wire tip (in GMAW) relative to visual reference (e.g., a laser marker) indicating the location of a weld seam. No torch orientation detection was involved, while this study concentrates on the 3-D orientation of the torch throughout a manual arc welding process. In [79], a speed and position sensor was proposed based on an accelerometer for a manual plasma pipe welding process in pulse current mode. Yet, the comparatively rigid assumptions on the torch movement pattern constrict its application in the other fit-ups (flat butt joint, T-type, etc) or power modes (constant current, constant voltage, etc).

The torch posture detection is essential in the welder training systems. However, those orientation detection technologies constrict themselves in certain working circumstances due to their own inherent constraints. For example, in the welding simulator, SimWelder from VRsim, Inc, the angular orientation of the welding torch is tracked using a tri-axial measurement gimbal at the attachment of the torch to the haptic device [44]. Yet, the hulking measurement device cannot be augmented to a torch in a real welding process. For the RealWeld Trainer, the torch posture is measured by detecting the spatial position of an infrared target amounted on the torch using three cameras augmented on the simulator stander [121]. The 2-D torch orientation was measured using a tri-axial accelerometer in the computer based welder training system in [126]. However, the variation of the torch

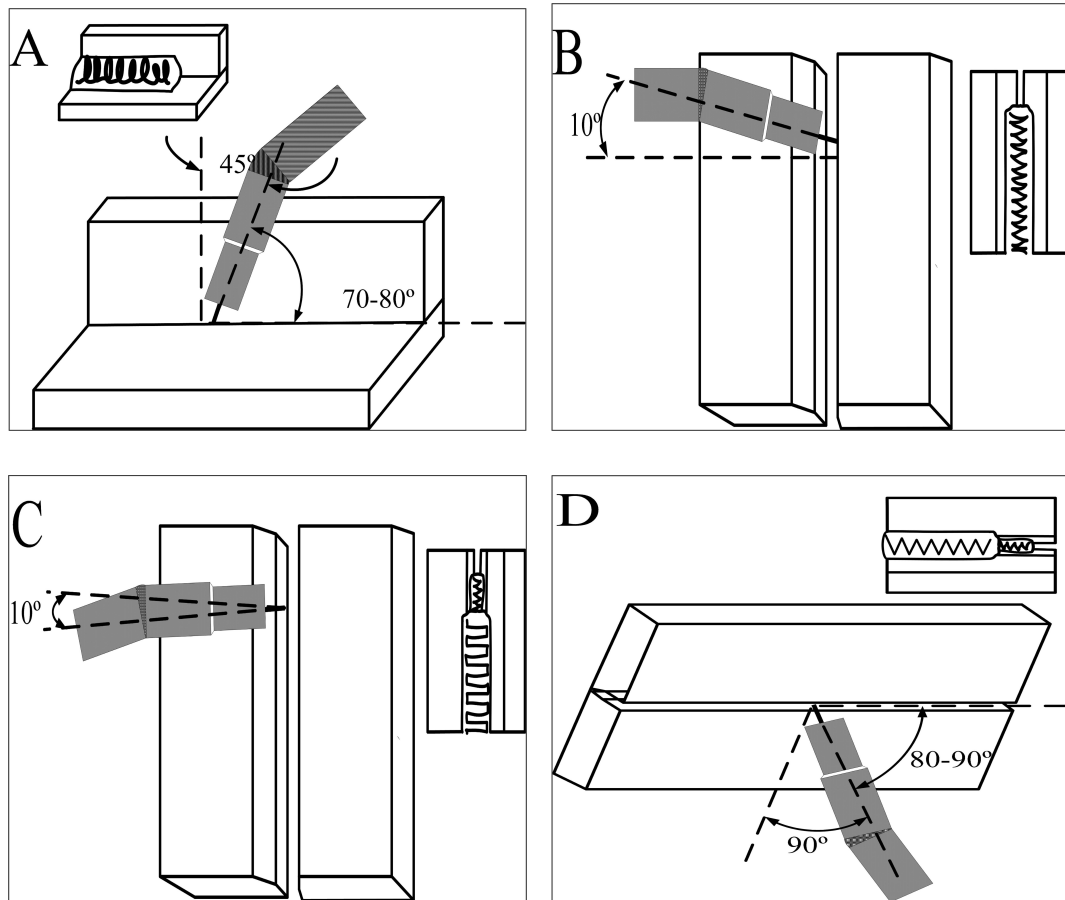


Figure 5.2: Torch orientations for different weld types in non and low alloyed steel GMAW process: (A) 2F/PB-horizontal-vertical fillet; (B) 3G \uparrow /PF-vertical up root pass and (C) fill passes; and (D) 4G/PE-overhead.

orientation in the gravitational direction can not be detected. There are also several virtual reality-based welder training systems augmented with 2-D torch postures measurements, the accuracy has been yet undisclosed ([40], [26]).

Accurate orientation measurements have been intensively investigated in a range of fields including avionics ([66], [36]), navigation ([20], [120]), human motion analysis ([135], [165]), and robotics [76]. Within a variety of technologies capable of orientation measurement, inertial sensing have the advantages of smaller, cheaper, being internally referenced and immune to constraints in any motion or specific environment ([131], [130]). An IMU (Inertial Measurement Unit) normally consists of an accelerometer and a gyroscope. It is capable of detecting the acceleration and the angular velocity of a rigid body on which the unit is attached. A tri-axial accelerometer can be used as an inclinometer when the magnitude of detected acceleration can be neglected with respect to the gravitational direction [82]. However, the accelerometer signal does not contain information for the rotation along the gravitational direction. Changes in orientation can be estimated by integrating the angular velocity measured by a gyroscope ([22], [61]). The problem is time-integrating the gyro signals superimposed with sensor drift and noise leads to unbounded estimation error.

Current researches have been carrying out to develop different filters using both the gyroscope and the accelerometer to estimate the orientation of a rigid body [104]. The orientation error resulting from the gyro output drift can be mitigated by additional sensors, the information from which is able to correct the orientation errors. The traditional use of linear Kalman filter (KF) and its extended version (EKF) for nonlinear models has been well established for the orientation estimation ([135], [82], [76], [68]) and the commercial inertial orientation sensors ([124]- [62]). Both the gyro data and acceleration data are applied in the KF or EKF based estimation algorithms.

For an accurate heading estimation, extra data from an additional magnetometer was incorporated in the Kalman filter based algorithms ([86], [109]). The adaptive EKF developed in [86] and [134] was embedded in an IMU incorporated with an magnetometer. The angular position was calculated mainly by the gyro data; the accelerometer was used to estimate the inclination; and the magnetometer was to estimate the heading angle. However, the use of the magnetometer could give large errors in the vicinity of a strong magnetic field, especially in places like the welding field where the welding machine and the welding arc are the sources of an extremely strong, time-varying, electromagnetic field [25]. Albeit a Kalman filter was proposed in [102] with a magnetic disturbance resistance to some extent, the designed magnetic disturbance, caused by an iron cylinder, was much smaller compared the disturbance caused by a welding machine/arc ([11], [21]). Thereby, the IMU in this study precludes the employment of an electromagnetic for torch orientation estimation. An auto-nulling algorithm is proposed to compensate the drift and measurement noise from the gyroscope, to ensure the accuracy of the heading estimation for the welding torch.

In addition, a quaternion was employed to represent the angular position since it requires less time complexity and avoid the singularity problems [31]. The attitude/orientation determination algorithm were developed in ([74]-[60]) based on the UKF instead of the traditional KF or the EKF, since the UKF is thought by many to be more accurate and less time complexity ([39], [75]).

This chapter aims to develop an accurate 3-D torch orientation measurement scheme which can be conveniently used in a real manual arc welding process or a welder training system. Based on a miniature IMU, the proposed scheme consists of a quaternion based UKF and an auto-nulling algorithm. The UKF is designed to estimate the 3-D orientation with the rotation quaternion included in its state vector. The innovative auto-nulling algorithm captures and compensates the gyro drift based on the gyro's own output, unlike the most other drift compensation algorithms which require extra information from an accelerometer. The proposed UKF incorporated with the auto-nulling algorithm provides a complete 3-D estimation with a reasonable accuracy, without the aiding of a magnetometer- a feature which is lacking in most orientation filter the authors are aware of. Moreover, the detection of human welders' torch manipulation is the foundation of studying their experienced behavior during the arc welding process which has been extensively studied by the authors ([146], [153],[154], [155]).

5.2 Representation of Torch Orientation

As shown in our proposed mobile sensing system in Figure 3.1, a torch for the GTAW process with the attached IMU is illustrated in Figure. 5.3. The IMU is mounted rigidly at the tail of

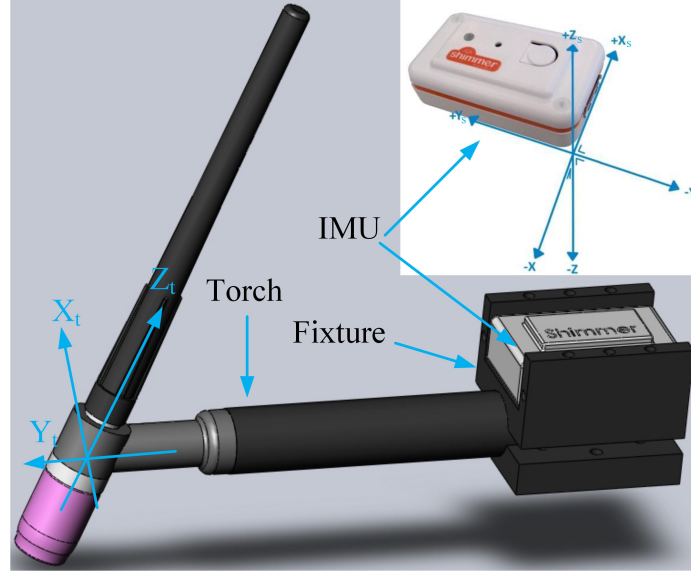


Figure 5.3: The illustration of torch and IMU which is rigidly amounted on the torch handle by a hard plastic fixture. ${}^t(XYZ)$ and ${}^s(XYZ)$ denote the 3-D Cartesian coordinate system for the torch and the WIMU, respectively.

the torch using a plastic fixture. The 3-D Cartesian coordinate frame, denoted as ${}^s(XYZ)$, in the IMU is its internal frame. It is worthy noting that during the assembly process, the torch was first hold still such that its handle was perpendicular to the gravitation direction, with aiding from external calibration tools, such as a gravimeter; the IMU was installed such that the gravitational acceleration direction coincided with the sZ axis. The coordinate frame ${}^t(XYZ)$ is the internal frame for the torch. It is defined in the following manner: axis tZ coincides with the torch head direction, axis tX coincides with axis sX . By doing this, frame ${}^t(XYZ)$ can be obtained by rotating frame ${}^s(XYZ)$ around sX axis for an angle, denoted as θ_{st} .

The orientation of the torch is determined when the axis orientation of the coordinate frame ${}^t(XYZ)$ is obtained with respect to an absolute 3-D Cartesian coordinate frame, denoted as frame ${}^E(XYZ)$. The negative direction of axis EZ is defined in coincidence with the local gravitational direction. The directions of the other two axes depend on the specific welding applications.

The torch orientation is presented by a quaternion denoted as ${}^s_E\tilde{q}$, where the sign $\tilde{\cdot}$ denotes a unit quaternion $\tilde{q} = [q_0, q_1, q_2, q_3]$, i.e.,¹

$$\|\tilde{q}\| = \sqrt{q_0^2 + q_1^2 + q_2^2 + q_3^2} = 1 \quad (5.1)$$

where q_0 is the scalar part and $[q_1, q_2, q_3]$ is the vectorial part of the quaternion.

The tri-axial gyroscope in the IMU measures the angular velocity of frame ${}^s(XYZ)$ relative to frame ${}^E(XYZ)$. The measurement (in rad/s) can be denoted by a 1-by-3 row vector

¹For the quaternion denotation, a leading subscript denotes the reference frame and a leading superscript indicates the frame being described.

shown in Equation. 5.2.

$${}^s\omega = [\omega_x, \omega_y, \omega_z] \quad (5.2)$$

The quaternion at instant $k + 1$ can be presented using the quaternion at k instant, angular measurement (${}^s\omega_k$), and the time interval denoted by T_s [31]:

$${}^s_E\tilde{q}_{k+1} = {}^s_E\tilde{q}_k \otimes \exp\left(\frac{T_s}{2}\omega_k\right) \quad (5.3)$$

where \otimes is the quaternion product, which is defined in Equation. 5.4. $\exp(\cdot)$ denotes the quaternion exponential, which is defined in Equation. 5.5, where $a = [a_1 \ a_2 \ a_3 \ a_4]$ and $b = [b_1 \ b_2 \ b_3 \ b_4]$.

$$a \otimes b = \begin{bmatrix} a_1b_1 - a_2b_2 - a_3b_3 - a_4b_4 \\ a_1b_2 + a_2b_1 + a_3b_4 - a_4b_3 \\ a_1b_3 - a_2b_4 + a_3b_1 + a_4b_2 \\ a_1b_4 + a_2b_3 - a_3b_2 + a_4b_1 \end{bmatrix}^T \quad (5.4)$$

$$\exp(v) \triangleq [\cos(\|v\|), \frac{v}{\|v\|} \sin(\|v\|)] \quad (5.5)$$

where v presents a 1-by-3 row vector. The torch orientation, ${}^t_E\tilde{q}$, can be calculated by Equation. 5.6.

$${}^t_E\tilde{q} = {}^s_E\tilde{q} \otimes \exp([\theta_{st}, 0, 0]) \quad (5.6)$$

5.3 Sensor Modeling

The gyroscope and the accelerometer in the IMU measure the angular velocity and the acceleration of the sensor, respectively. Besides the true values, ${}^s\omega_{true}$ and ${}^s a_{true}$, there are several main error sources affecting the IMU measurement including the bias, scale-factor instability, non-orthogonality of axes and the measurement noise. To this regard, the IMU measurements are expressed in Equation. 5.7 and Equation. 5.8.

$${}^s\omega = S_\omega {}^s\omega_{true} + T_\omega {}^s\omega_{true} + b_\omega + v_\omega \quad (5.7)$$

$${}^s a = S_a {}^s a_{true} + T_a {}^s a_{true} + b_a + v_a \quad (5.8)$$

where S_ω and S_a are the scale-factor matrices; T_ω and T_a are the non-orthogonality factor matrices; b_ω and b_a are the bias; and v_ω and v_a are the measurement noises. Please note this is a simplified sensor model. Some minor error sources are not considered, such as the cross-sensitivity and gravity-sensitivity.

Measurement noises v_ω and v_a are normally considered as uncorrelated white Gaussian noises, with a null mean and 3-by-3 covariance matrices ${}^R\sigma_\omega^2\mathbf{I}_{3\times 3}$ and ${}^R\sigma_a^2\mathbf{I}_{3\times 3}$, respectively. The covariance matrix of sensor model R is

$$R = \begin{bmatrix} {}^R\sigma_\omega^2\mathbf{I}_{3\times 3} & \mathbf{0} \\ \mathbf{0} & {}^R\sigma_a^2\mathbf{I}_{3\times 3} \end{bmatrix} \quad (5.9)$$

The true acceleration measurement includes two components: the sensor acceleration and the gravitation acceleration, as expressed by Equation. 5.10.

$${}^s a_{true} = {}^s a_{sensor} + {}^s g \quad (5.10)$$

where ${}^s g$ is the gravitational acceleration in the sensor frame, which can be obtained using Equation. 5.11.

$${}^s g = {}^s \tilde{q} \otimes [0, {}^E g] \otimes {}^s \tilde{q}^* \quad (5.11)$$

The torch should be moved smoothly along the weld bead with unnoticeable acceleration or deceleration throughout an arc welding process, given that the skilled welder is well motivated. Thereby, ${}^s a_{sensor}$ is insignificant compared with the gravitation acceleration and thus considered as a disturbance in our application. Henceforth, Equation. 5.10 can be expressed by Equation. 5.12.

$${}^s \tilde{a}_{true} \cong {}^s \tilde{g} \quad (5.12)$$

Using normalized gravity can eliminate the measurement error caused by localized gravity differences.

The bias and the scale factors, in Equation. 5.7 and Equation. 5.8, depend on the sensors' imperfections and the working field. The typical gyro bias is 0.017 – 0.17 rad/h and acceleration bias is about 100 – 1000 μg for tactical grade [93]. In particular, the ambient temperature significantly affects the gyro's bias. In this study, the IMU is employed near the welding arc which is a strong heat source. Hence, the gyro bias might not be constant throughout an arc welding process. To this regard, an auto-nulling algorithm is proposed to compensate the gyro's drift in-line to guard the effect of the drift variation over temperature to the estimation accuracy.

The influence of temperature on the accelerometer's bias is much less intense. The in-line calibration of an accelerometer usually requires the accelerometer remaining in a static or quasi-static condition for several different orientations [125]. However, in our application, the torch should be hold for one certain orientation, as shown in Figure. 5.1 and Figure. 5.2, throughout an arc welding process. Therefore, there will not be enough orientations for the in-line calibration. In this study, the accelerometer bias is assumed to be constant, and can be compensated by the calibration before use [45].

The scale factor drifts of IMU are known to affect the measurement accuracy to a much less extent than the bias drifts. The drift variation over temperature is also negligible [2]. Therefore, the scale factors can be considered subjected to small variations around their average values throughout the welding process. Their nominal values can be determined through the sensor calibration before using [45].

5.4 Auto-nulling Algorithm

The capture of the gyro drift usually requires keeping the gyro sensor from rotation. The basic principle is called zero attitude update (ZAU), also referred as auto-nulling, i.e., when no rotation occurs to the gyro sensor, its output can be considered as the drift caused by the bias and other error sources. The drift can be then periodically captured and compensated. A ZAU algorithm was proposed in [12] to detect human walk pace. The static status (i.e. no rotation) of the gyro sensor was detected by an accelerometer. However, that ZAU algorithm is only valid in two dimension applications since the accelerometer cannot detect the gyro's rotation in the gravitational direction. In [105], the authors compensated the gyro drift using an off-line ZAU algorithm in a gait pace detection application. The starting and ending time of a gait period were required before the gyro data recorded within the period was processed. Effective drift estimation was also accomplished by using an extra Kalman filter [54]. Yet, introducing an additional Kalman filter to estimate the gyro drift in our application is not computation efficient. Thereby, a new auto-nulling algorithm is proposed in this study in which the static status is detected using information from gyro's own output.

The mean and deviation of the gyro's output obtained in a small time interval when the IMU is set still can be used to determine the static status. The two variables are defined by

$$\mu_s = \sum_{k=1}^M {}^s\omega_k / M \quad (5.13)$$

and

$$\sigma_s = \sqrt{\frac{\sum_{k=1}^M ({}^s\omega_k - \mu_s) * ({}^s\omega_k - \mu_s)'}{M}} \quad (5.14)$$

where M is the number of samples. To record the data for calculating μ_s and σ_s , a static state experiment was conducted where the IMU was set still in a room temperature (about 23°C). Before recording valid gyro data, the IMU was allowed to power up for a few minutes till it reached a thermal stability.

For an arbitrary angular velocity ${}^s\omega_i$ recorded by the gyro sensor, the corresponding mean and deviation are defined in Equation. 5.15 and Equation. 5.16

$$\mu(i) = \sum_{k=i-N}^i {}^s\omega_k / N \quad (5.15)$$

$$\sigma(i) = \sqrt{\frac{\sum_{k=i-N}^i ({}^s\omega_k - \mu(i)) * ({}^s\omega_k - \mu(i))'}{N}} \quad (5.16)$$

where $i > N$, and N is the sampling number gathered in a small interval T_{au} right before ${}^s\omega_i$ is recorded. In this study, $T_{au} = 1$ s.

If the mean and the deviation of the gyro output within the interval T_{au} are close to μ_s and σ_s , then the torch/IMU is considered in the static state. According to the ZAU principle,

the mean value, $\mu(i)$, can be thus thought as a drift. In our application, the possible ambient temperature variation caused by the welding arc should be in a comparatively low rate due to the thermal latency. Therefore, the gyro data in the time vicinity of the static interval can be compensated using the drift obtained in the stationary interval. If the IMU is in a dynamic period ($\mu(i)$ or $\sigma(i)$ are much larger than μ_s and σ_s), then compensation can be accomplished by the mean value from the nearest static interval.

Furthermore, the drift of a gyro sensor is sensitive to temperature as discussed in the last section. Thereby, two thermal coefficients are included in the auto-nulling algorithm, ρ_μ and ρ_σ , accounting for the temperature difference between the environment where the torch/IMU is using and the one where static experiment are conducted. For the simulations in section 5.6, they were set 1 since the temperature at which the static experiment were conducted was about the same that the simulations were conducted. In the welding experiments, they were pre-set and given reasonable values based on estimation results. In practical applications, the two coefficients can be empirically chosen.

Hence, if there exist

$$\mu(i)^2 \leq \rho_\mu \mu_s^2 \quad \text{and} \quad \sigma(i) \leq \rho_\sigma \sigma_s \quad (5.17)$$

then torch/IMU is considered in stationary state, and $\mu(i)$ is referred as a valid drift.

Thereby, the proposed auto-nulling algorithm can be expressed by

$${}^s\omega_i = \begin{cases} {}^s\omega_i - \mu_s & i \leq N \\ {}^s\omega_i - \mu(i) & \text{WIMU is static, } i > N \\ {}^s\omega_i - \mu(\xi) & \text{WIMU is dynamic, } i > N \end{cases} \quad (5.18)$$

where $\mu(\xi)$ is the nearest valid drift for ${}^s\omega_i$, $\xi < i$.

Using the proposed auto-nulling algorithm, no data is required from some external sensors in order to compensate the effect of drift to the orientation estimation. The effectiveness of the algorithm will be evaluated in latter sections.

5.5 Unscent Kalman Filter (UKF) design

The state vector of the proposed UKF is composed of the torch orientation quaternion and the angular velocity.

$$x_k = [{}^s_E\tilde{q}_k, {}^s\omega_k] \quad (5.19)$$

Using the state vector, the sensor model (Equation. 5.7 and Equation. 5.8) can be rewritten as shown in Equation. 5.20.

$$z_{k+1} = h(x_k, v_k) \quad (5.20)$$

where $z_{k+1} = [{}^s\omega_{k+1}, {}^s a_{k+1}]$, and $v_k = [v_\omega, v_a]$.

The process model represented by the state vector is

$$x_{k+1} = f(x_k, w_k) = [{}^s_E\tilde{q}_k \otimes \exp(\omega_k) \otimes \exp(w_q), {}^s\omega_k + w_\omega] \quad (5.21)$$

where $w_k = [w_q, w_\omega]$ is the process noise with a covariance matrix denoted as Q_k , $exp(\omega_k)$ is the increment of rotation in k^{th} sampling period, and $exp(w_q)$ is the process uncertainty caused by w_q which is the quaternion component of the process noise.

In this study, the angular velocity is expected to be fairly small, since the torch is required to be maintained in a recommended orientation with small adjustments for possible disturbances. Thereby, the angular velocity can be modeled as a random walk in the process model.

Because of the nonlinear nature of the process model (Equation. 5.21) and the sensor model, the UKF approach is applied [39]. For the sake of readers' convenience, the UKF algorithm are summarized below.

Given the estimated state vector \hat{x}_{k-1} and its covariance P_{k-1} at instant $k-1$, an auxiliary vector set $\{\psi_i\}$ is defined by Equation. 5.22.

$$\psi_i = \begin{cases} \left(\sqrt{(n+\lambda) \cdot (P_{k-1} + Q)} \right)_i & i = 1, \dots, n \\ - \left(\sqrt{(n+\lambda) \cdot (P_{k-1} + Q)} \right)_{(i-n)} & i = n+1, \dots, 2n \end{cases} \quad (5.22)$$

where $\left(\sqrt{(n+\lambda) \cdot (P_{k-1} + Q)} \right)_i$ is the i^{th} row of the matrix square root, and $\lambda = \alpha^2(n + \kappa) - n$ in which α and κ are two scaling parameters. A subtle detail worthy noting is that the dimension of covariance P_{k-1} is 6-by-6, since the degree of freedom (DOF) of the state vector is 6 (unit quaternion constraint reduces one DOF). Therefore, ψ_i 's are 1-by-6 vectors.

UKF addresses the approximation of a nonlinear system by using a minimal set of sample points, i.e., sigma points, to capture the mean and covariance estimate. The sigma points set $\{(\chi_{k-1})_i\}$ is defined by

$$(\chi_{k-1})_i = \hat{x}_{k-1} = [{}^s_E \hat{q}_{k-1}, {}^s \hat{\omega}_{k-1}] \quad (5.23)$$

as $i = 0$, and

$$(\chi_{k-1})_i = \hat{x}_{k-1} + \psi_i = [{}^s_E \hat{q}_{k-1} \otimes exp(\psi_{i|q}), {}^s \hat{\omega}_{k-1} + \psi_{i|\omega}] \quad (5.24)$$

when $i = 1, \dots, 2n$, and $\psi_i = [\psi_{i|q}, \psi_{i|\omega}]$ in which $\psi_{i|q}$ is the first three elements of ψ_i corresponding to the quaternion part, and $\psi_{i|\omega}$ relates to the angular velocity. The length of state vector \hat{x}_{k-1} is 7 while ψ_i is a 6-element vector. Thereby, Equation. 5.24 performs a vector to quaternion conversion for $\psi_{i|q}$ using the quaternion exponential in Equation. 5.5.

After the sigma points $\{(\chi_{k-1})_i\}$ are obtained, the process model is used to project each point ahead in time. The propagation results are shown in Equation. 5.25, and *a priori* state estimate is thus obtained in Equation. 5.26.

$$(\chi_k)_i = f((\chi_{k-1})_i, 0, 0) \quad \text{for } i = 0, \dots, 2n \quad (5.25)$$

$$\hat{x}_k^- = \sum_{i=0}^{2n} W_i^{(m)} (\chi_k)_i \quad (5.26)$$

where weights $W_i^{(m)}$ are defined by

$$W_i^{(m)} = \begin{cases} \lambda/(n + \lambda) & i = 0 \\ \lambda/(2(n + \lambda)) & i = 1, \dots, 2n \end{cases} \quad (5.27)$$

The covariance of $(\chi_k)_i$ is

$$P_k^- = \sum_{i=0}^{2n} W_i^{(c)} [(\chi_k)_i - \hat{x}_k^-]^T [(\chi_k)_i - \hat{x}_k^-] \quad (5.28)$$

where weights $W_i^{(c)}$ are defined in Equation. 5.29, β is a scaling parameter used to incorporate prior knowledge about the distribution of state vector x . It should be noted that P_k^- is a 6-by-6 matrix, while $(\chi_k)_i$ and \hat{x}_k^- are 7-element vectors. Thereby, a conversion is performed to the right side of the equation to transform the quaternion parts into 3-element rotation vectors [74]. This quaternion-to-rotation conversion is a reverse procedure of Equation. 5.5.

$$W_i^{(c)} = \begin{cases} \lambda/(n + \lambda) + (1 - \alpha^2 + \beta) & i = 0 \\ \lambda/(2(n + \lambda)) & i = 1, \dots, 2n \end{cases} \quad (5.29)$$

The results for the projected set $\{(\chi_k)_i\}$ in the sensor model are expressed by

$$(\mathbf{y}_k)_i = h((\chi_k)_i, 0, 0) \quad \text{for } i = 0, \dots, 2n \quad (5.30)$$

The measurement estimate can thus be defined in Equation. 5.31.

$$\hat{z}_k^- = \sum_{i=0}^{2n} W_i^{(m)} (\mathbf{y}_k)_i \quad (5.31)$$

The *a posteriori* state estimate is computed using

$$\hat{x}_k = \hat{x}_k^- + K_k (z_k - \hat{z}_k^-) \quad (5.32)$$

where z_k is the measurement vector from WIMU, and K_k is the Kalman gain which is defined by

$$K_k = P_{\hat{x}_k \hat{z}_k} P_{\hat{z}_k \hat{z}_k}^{-1} \quad (5.33)$$

The cross correlation matrix $P_{\hat{x}_k \hat{z}_k}$ and measurement estimate covariance $P_{\hat{z}_k \hat{z}_k}$ are expressed in Equation. 5.34 and Equation. 5.35, respectively.

$$P_{\hat{x}_k \hat{z}_k} = \sum_{i=0}^{2n} W_i^{(c)} [(\chi_k)_i - \hat{x}_k^-]^T [(\mathbf{y}_k)_i - \hat{z}_k^-] \quad (5.34)$$

$$P_{\hat{z}_k \hat{z}_k} = \sum_{i=0}^{2n} W_i^{(c)} [(\mathbf{y}_k)_i - \hat{z}_k^-]^T [(\mathbf{y}_k)_i - \hat{z}_k^-] + R \quad (5.35)$$

A quaternion-to-rotation conversion is performed to the term in the second bracket of Equation. 5.34, to ensure a valid cross correlation matrix. The estimated state covariance is updated at instant k by

$$P_k = P_k^- - K_k P_{\hat{z}_k \hat{z}_k} K_k^T \quad (5.36)$$

For a successful UKF performance, the following parameters required to be determined first: Q_k , R , α , β , κ . Scaling parameters α , β , κ are empirically pre-set and given reasonable values based on filter tests results. ${}^R\sigma_\omega^2 \mathbf{I}_{3 \times 3}$ and ${}^R\sigma_a^2 \mathbf{I}_{3 \times 3}$ account for the spectral density of the sensor signal while the sensor is lying still.

Process noise covariance Q_k can be determined by

$$Q_k = \Phi_s \int_0^{T_s} \Phi(\tau) Q' \Phi^T(\tau) d\tau \quad (5.37)$$

where Φ_s is a scaling parameter, $\Phi(\tau)$ is an approximation to the fundamental matrix calculated by taking the Taylor-series expansion of the system dynamic matrix, and Q' is the continuous process noise matrix [142]. The covariance matrix Q' is expressed by

$$Q' = \begin{bmatrix} \Sigma_q & \mathbf{0} \\ \mathbf{0} & \Sigma_\omega \end{bmatrix} \quad (5.38)$$

where $\Sigma_q = {}^Q\sigma_q^2 \mathbf{I}_{3 \times 3}$ and $\Sigma_\omega = {}^Q\sigma_\omega^2 \mathbf{I}_{3 \times 3}$ are the covariance matrix of the quaternion part and angular velocity part of the process noise, respectively, which are assumed to be uncorrelated, zero-mean white noise.

5.6 Verifications Simulation and Experiments

5.6.1 Experimental equipment

The orientation estimation scheme was tested using the IMU illustrated in Figure. 5.3. Raw data was recorded, transmitted to a desktop, and processed by the proposed scheme. A welding robot (Universal Robot UR 5) was used to provide reference measurements of the torch orientation. To do so, either the torch (in welding experiments) or the IMU (in simulations) was rigidly amounted on the robot tool center, the center of the plane on the robot forearm [101]. The orientation of the tool center was calculated by the imported accompanying software using the feedback from the robot. The obtained reference orientation was filtered by a second-order low-pass Butterworth filter (cut-off frequency: 15 Hz). Initial calibration was conducted to determine the quaternion for converting the tool center orientation to the torch/IMU orientation. The performance of the proposed scheme was evaluated by comparing with the reference measurements.

The accuracy of the reference orientation delivered by the welding robots depends on the accuracy of the orientation measurement of the robot tool center and on the robot-IMU orientation calibration. The orientation measurement error of the robot can be estimated using the data supplied by the robot manufacturer [101]. The repeatability of the robot

is ± 0.1 mm. The robot’s shortest forearm around which the robot tool center rotates is about 89 mm. Hence, its maximum orientation error is about 0.06° , which is acceptable as a measurement reference.

5.6.2 Simulations procedure

A reference 3-D Cartesian coordinate frame $^E(XYZ)$ was defined to justify valid orientation measurements: the z -axis has been defined in section 5.2; x -axis and y -axis were arbitrarily defined by the right hand rule. The IMU was mounted on the robot tool center such that its internal coordinate frame $^s(XYZ)$ was identical to frame $^E(XYZ)$ at the initial position.

To simulate human hand’s behaviors, the welding robot was set in the teaching mode such that the robot tool center could be rotated manually and smoothly around the three axes of its internal frame. Four data sets were constructed in simulations denoted by D_i^s , where $i = 1, 2, 3, 4$. To evaluate the performance of the proposed scheme in the three dimensions separately, the IMU was rotated around one axis in each simulation by the leading author. Hence, for D_1^s to D_3^s , the robot tool center (and the IMU) was rotated around the x -axis, y -axis, and z -axis, respectively. The rotation sequence in the three data sets is identical, i.e., first rotate 90 degrees², back to initial position, then rotate -30 degrees, and back to initial position again. In each stage (at 90 degrees, -30 degrees and the initial positions), the robot tool center stayed still for a few seconds. It should be noted that the stationary phases might not exactly to be 90, -30 or 0 degrees since the robot tool center was manually rotated by the leading author. Yet, it does not affect the simulation procedure, or the estimation accuracy.

For D_4^s , the robot tool center was rotated around the three axes altogether with the aforementioned rotation sequence. The robot tool center was thought to be much steadier than a human hand due to human’s inherent neuro latency. To this regard, data set D_{4+n}^s was further artificially constructed by introducing two random Gaussian noises into the gyro and acceleration data in D_4^s , respectively, in order to simulate the unsteadiness of a human hand. The variances of the noises for gyro and acceleration data in D_4^s were $5e^{-2}$ and $5e^{-1}$.

Two UKF implementations were studied, henceforth called Method A, B. Method A incorporated the auto-nulling algorithm, while Method B did not. Besides, two additional trapezoidal numerical integration methods were included as comparison: Method C adopted the auto-nulling algorithm, while Method D did not. Four methods were tested at three different sampling rates: 256 Hz, 128 Hz, and 51.2 Hz. Six repeated tests were conducted for each condition including both methods and sampling rates.

The performance metric adopted in this study is the root-mean-square error (RMSE_θ) of the orientation in degree, which is defined by

$$\text{RMSE}_\theta = \sqrt{\frac{1}{n} \sum_{k=0}^{n-1} (\Delta\theta_k)^2} \quad (5.39)$$

²The positive direction indicates a clockwise rotation as viewing from the negative to the positive direction of one axis.

where n is the sample number of the data set being evaluated.

$$\Delta\theta_k = \frac{2 * 180}{\pi} \arccos((q_{t_k} \otimes q_{e_k}^*)_0) \quad (5.40)$$

where q_{t_k} and q_{e_k} are the truth-reference and estimated quaternion. Besides $RMSE_\theta$, RMSEs of rotated Euler angles in three axes were also adopted, denoted by $RMSE_x$, $MRSE_y$ and $RMSE_z$, respectively.

5.6.3 Experimental Validation

Two data sets of torch orientation used in this section, denoted by D_1^e and D_2^e , were obtained from welding experiments. Data set D_1^e was collected from the GTAW experiments containing four types of welding fit-ups sequentially corresponding to the configurations in Figure. 5.1, and data set D_2^e was obtained from the GMAW experiments including the welding types as shown in Figure. 5.2. Further, two more data sets D_{1+n}^e and D_{2+n}^e were artificially constructed by introducing the same noises mentioned in last section into D_1^e and D_2^e , respectively. The tested method was Method A which was the contest winner in the simulation trials. Six repeated trials were conducted for each welding type.

To construct the data sets, the IMU attached torch (as shown Figure. 5.3) was mounted on the tool center of the welding robot which was set in the teaching mode. The leading author (novice welder) was asked to hold the robot forearm and perform the aforementioned experiments. Each welding types lasted about 30 seconds. The welder took a break and set the torch to the initial posture between every two welding trials. The welding conditions for the GTAW experiments are listed in Table 5.1. No filler metal was used in the experiments. For the GMAW experiments, not only the torch orientations were required to maintain, but the specific torch swing patterns needed to be followed. In the experiments, the arc did not start due to the limited welding skill of the leading author, i.e., the torch was firmly hold above and smoothly dragged along the weld beam without the arc being established. The experimental data was transmitted to a host desktop, and processed off-line using Matlab R2011.

Table 5.1: Major Welding Conditions For the GTAW Experiments

Welding Parameter	Conditions
Welding Current (A)	60
Welding Speed [mm/s]	1 ~ 2 (varied by the welder)
Tungsten Tip-To-Work Distance (mm)	2 ~ 5 (varied by the welder)
Electrode Extension (mm)	3
Electrode Type	EWCe-2
Electrode Diameter (mm)	2.38
Electrode Tip Geometry [°]	30
Shielding Gas	Argon 100%
Flow rate of Shielding Gas [L/min]	11.8
Material	2 mm thick 304L sheet

A reference 3-D Cartesian coordinate frame ${}^E(XYZ)$ was defined for the experimental data. The negative direction of ${}^E Z$ coincided with the gravitational direction. The positive direction of ${}^E Y$ was the welding direction along the weld seam. Axis ${}^E X$ was then determined using the right hand rule. In the experiments, the spatial relation between the torch and the robot was carefully calibrated. In the initial posture, the torch head was set such that directions of the axis in ${}^E(XYZ)$ coincide with those in ${}^t(XYZ)$, respectively.

5.7 Results and discussion

5.7.1 Results

Simulation results

The initial parameters for the UKF is listed in Table 5.2. The mean and standard deviation of the gyro's output when the IMU is stationary in the room temperature ambient, μ_s and σ_s , were measured using Equation. 5.41 and Equation. 5.42. The coefficient ρ_μ , and ρ_σ were chosen to be 1.0 when conducting the simulations.

Table 5.2: Initializations of the UKF parameters for Method A and B

	Q_{σ_q}	Q_{σ_ω}	R_{σ_ω}	R_{σ_a}	α	β	κ
Method A	0.18	0.08	0.5	0.2	1.4	1.0	0
Method B	0.27	0.18	1.2	0.4	1.0	0	3.0

$$\mu_s = [8.50e^{-3} \quad 1.56e^{-2} \quad 4.70e^{-3}] \quad (5.41)$$

$$\sigma_s = [1.18e^{-4} \quad 1.47e^{-4} \quad 9.87e^{-5}] \quad (5.42)$$

The statistics of the resultant estimation $RMSE_\theta$ are listed in Table 5.3. In the table, the estimation performance of the proposed algorithm (Method A) is compared with the other three counterpart algorithms by the mean and the standard deviation of the $RMSE_\theta$.

The results of the orientation estimation for the three individual axes ($RMSE_s$ [$^\circ$]) are presented in Table 5.4. The evaluated data sets are D_1^s , D_2^s and D_3^s , respectively.

Figures 5.4-5.5 show the time functions of the Euler angles as they were measured in the simulation trials, and the reference measurements were from the welding robot. In particular, Figure. 5.4 shows the estimation of the orientation in x -axis, y -axis and z -axis using data set D_1^s , D_2^s and D_3^s , respectively. The 3-D orientation estimation is presented in Figure. 5.5 obtained using the four algorithms with data set D_4^s . Figure. 5.6 shows the quaternion time functions obtained by the proposed algorithm, i.e., Method A, using the data set corresponding to Figure. 5.5. It should be noted each of the figures only shows one of the estimation result of the six trials for the corresponding simulation conditions.

Table 5.3 and Table 5.4 show the estimation results of slow torch movement, in which the angular rate is about $3^\circ/s$. The orientation estimation results for the angular rate larger than $5^\circ/s$ of the torch movement are presented in Table 5.5.

Table 5.3: Orientation estimation (RMSE_θ), in the form of $\text{mean} \pm \text{standard deviation}$, obtained by the different estimation methods in the course of the monte carlo performance trials. Additional distance of gyro and acceleration were artificially introduced in data set D_{4+n}^s

	D_1^s	D_2^s	D_3^s	D_4^s	D_{4+n}^s
$f_s = 256 \text{ Hz}$					
A	0.53 ± 0.11	0.47 ± 0.14	0.91 ± 0.20	0.98 ± 0.25	1.35 ± 0.34
B	2.56 ± 0.17	2.74 ± 0.55	1.50 ± 0.48	2.67 ± 0.41	3.02 ± 0.58
C	4.91 ± 0.54	5.11 ± 1.36	6.43 ± 0.81	7.48 ± 0.67	7.85 ± 0.98
D	25.97 ± 2.58	19.18 ± 1.57	21.72 ± 2.27	30.14 ± 3.49	32.56 ± 3.98
$f_s = 128 \text{ Hz}$					
A	0.50 ± 0.13	0.40 ± 0.16	0.94 ± 0.29	1.01 ± 0.20	1.28 ± 0.32
B	3.52 ± 0.93	2.97 ± 0.73	2.25 ± 0.47	2.21 ± 0.35	2.45 ± 0.47
C	5.27 ± 1.18	6.12 ± 1.57	5.73 ± 0.36	7.14 ± 0.58	8.01 ± 0.79
D	28.39 ± 5.17	23.59 ± 4.18	29.42 ± 1.31	31.30 ± 4.78	41.44 ± 5.36
$f_s = 51.2 \text{ Hz}$					
A	0.67 ± 0.03	0.52 ± 0.08	1.57 ± 0.32	2.59 ± 0.24	2.81 ± 0.22
B	2.21 ± 0.28	3.74 ± 0.42	3.17 ± 0.52	3.75 ± 0.27	4.11 ± 0.31
C	5.45 ± 1.71	7.94 ± 3.84	8.49 ± 3.67	9.42 ± 3.65	9.84 ± 4.22
D	19.64 ± 3.82	18.12 ± 2.57	23.44 ± 5.12	25.14 ± 4.25	27.51 ± 4.44

Table 5.4: Orientation estimation ($\text{RMSEs} (\text{°})$), in the form of $\text{mean} \pm \text{standard deviation}$, obtained by the different estimation methods in course of six repeated trials for each simulation.

	D_1^s	D_2^s	D_3^s
$f_s = 256 \text{ Hz}$	RMSE_x	RMSE_y	RMSE_z
A	0.23 ± 0.01	0.16 ± 0.01	0.49 ± 0.04
B	0.26 ± 0.05	0.46 ± 0.29	1.14 ± 0.37
C	4.77 ± 0.58	4.60 ± 1.25	4.97 ± 0.71
D	12.86 ± 2.55	10.62 ± 1.30	13.42 ± 2.10
$f_s = 128 \text{ Hz}$			
A	0.32 ± 0.02	0.25 ± 0.02	0.76 ± 0.14
B	0.34 ± 0.02	0.70 ± 0.03	1.72 ± 0.31
C	4.69 ± 0.69	4.34 ± 0.94	5.16 ± 0.23
D	15.39 ± 2.58	10.86 ± 2.46	20.34 ± 1.51
$f_s = 51.2 \text{ Hz}$			
A	0.60 ± 0.02	0.46 ± 0.05	0.81 ± 0.18
B	0.62 ± 0.02	0.49 ± 0.05	2.24 ± 0.41
C	4.99 ± 1.39	6.68 ± 3.21	7.16 ± 2.33
D	10.97 ± 8.22	9.95 ± 1.64	24.79 ± 3.10

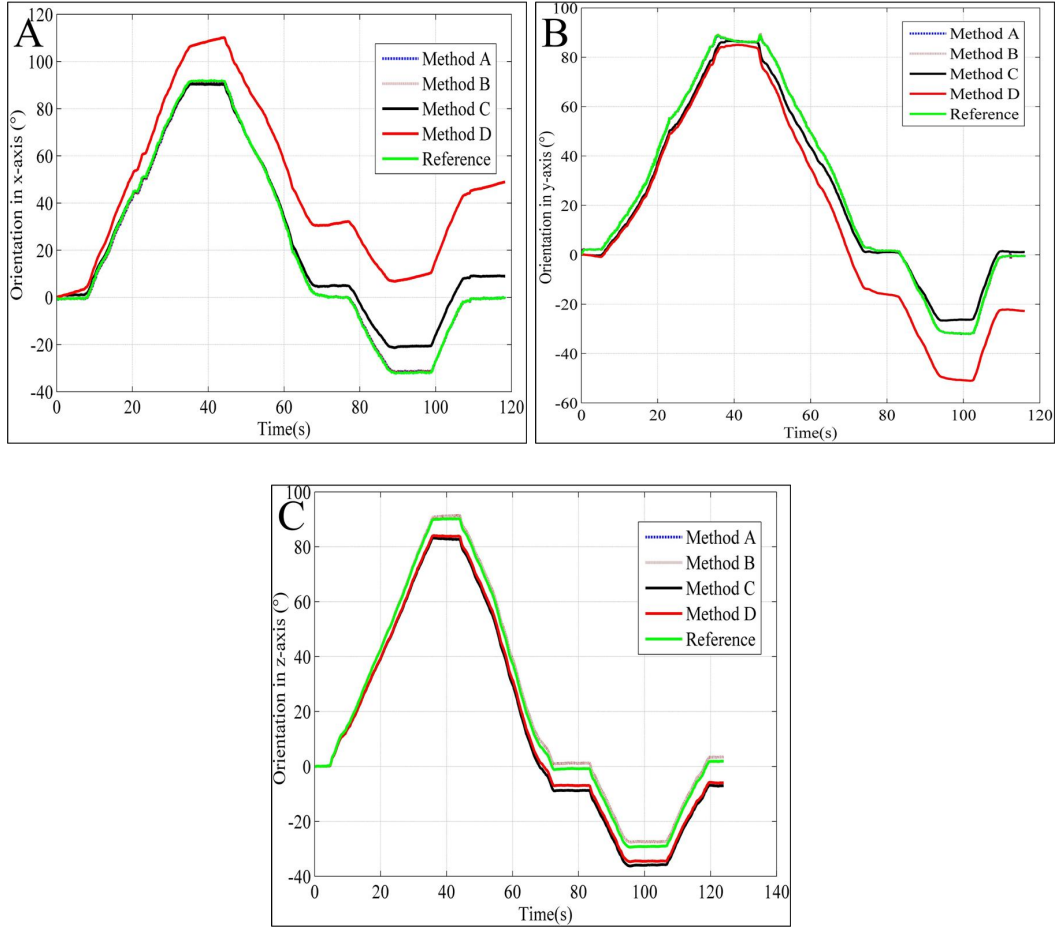


Figure 5.4: Estimated and reference orientation (in Euler angle) at sampling rate of $f_s = 128$ Hz for A) x -axis using data set D_1^s . B) y -axis using data set D_2^s , and C) z -axis using data set D_3^s .

Experimental results

One can find from the simulation results that the proposed algorithm (Method A) produce the best performance. The sampling rate chosen to conduct the experiments is 128 Hz since it is the best trade-off between estimation accuracy and computation load. Table 5.6 shows the mean and standard deviation of the estimation RMSE_θ obtained from the aforementioned experiments consisting of the two welding processes (GTAW and GMAW), each of which includes the four welding fit-ups. Since the welding experiments last only about 40 seconds on average, the ambient temperature is not significantly changed compared with that when the IMU were tested for the static drift. Therefore, thermal coefficient ρ_μ and ρ_σ were tuned in the range between 1.2 to 2.1 (they were set 1.0 in the GMAW experiments).

Figures 5.7-5.10 show the typical orientation estimation results in Euler angles. In particular, Figure. 5.7 shows the estimation results in one GTAW process with lap joint, corresponding the welding process shown in Figure. 5.1b. The initial posture of the torch should be 0° in all the three axes. According to the related welding type (Figure. 5.1b), the

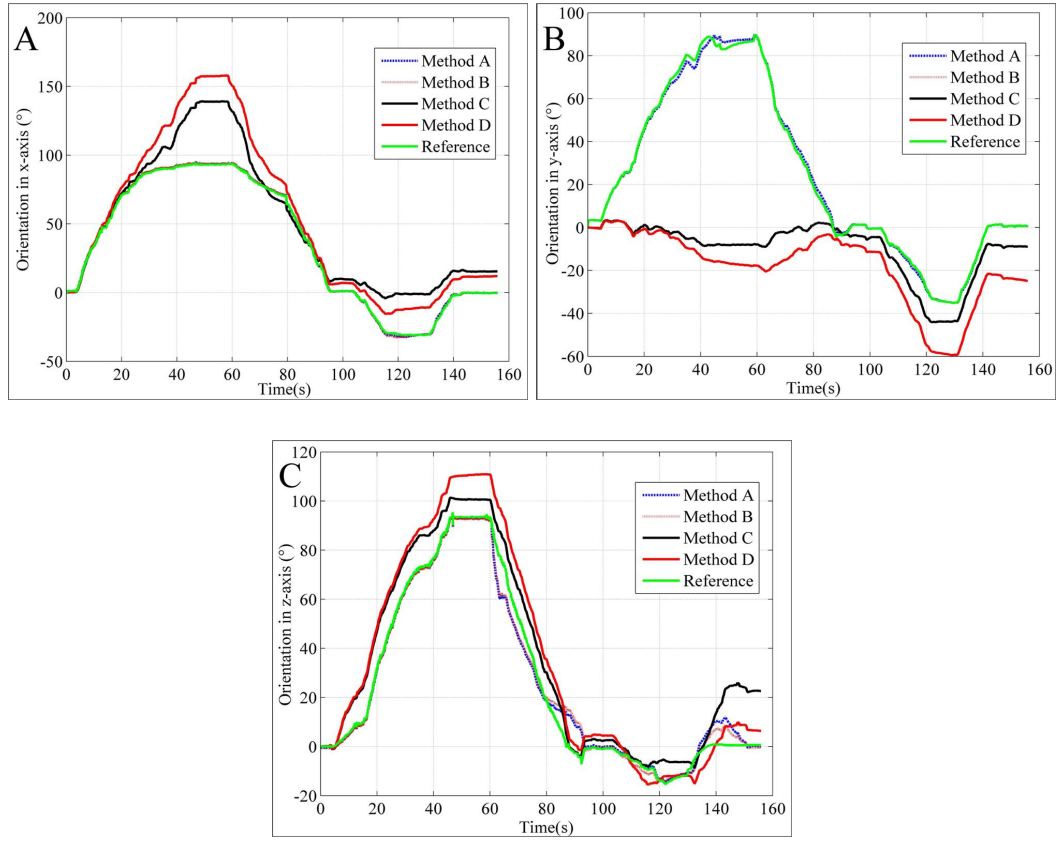


Figure 5.5: RMSEs of orientation in Euler angle at sample rate of $f_s = 51.2$ Hz for A) $RMSE_x$, B) $RMSE_y$, and C) $RMSE_z$ using data set D_4^s .

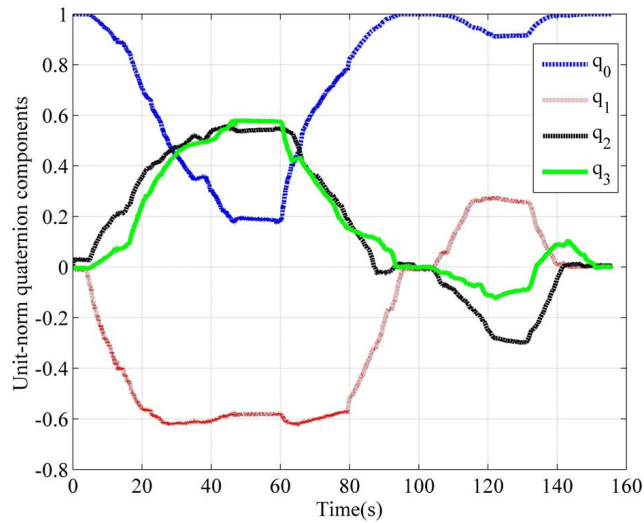


Figure 5.6: The obtained unit-norm quaternion of rotation from data set D_4^s using Method A at sampling rate $f_s = 51.2$ Hz. The quaternion components are dimensionless.

Table 5.5: Dynamic Orientation estimation $[\text{RMSE}_\theta](^\circ)$, in the form of mean \pm standard deviation, obtained by Method A. The angular rate is larger than 5°

	$f_s = 51.2$	$f_s = 128$	$f_s = 256$
D_1^s	1.40 ± 0.06	0.89 ± 0.18	0.61 ± 0.08
D_2^s	1.74 ± 0.07	0.91 ± 0.19	0.54 ± 0.11
D_3^s	1.89 ± 0.28	1.25 ± 0.35	1.10 ± 0.38
D_4^s	3.28 ± 0.29	1.62 ± 0.35	1.25 ± 0.26
D_{4+n}^s	3.56 ± 0.45	1.94 ± 0.41	1.55 ± 0.35

welder is expected to maintain the 3-D orientation of torch at $[20^\circ, -20^\circ, CR]$, where CR denotes 'custom-related', i.e., the orientation in that particular axis depends on the welder's individual operation custom. One can find in Figure. 5.7, the torch orientation deviated about 5° from the recommended torch posture as shown in Figure. 5.1b. This is normal since the welder, i.e., the leading author, is a novice welder who has not mastered the torch manipulation yet. The welding processes from which the results shown in Figure. 5.8- 5.10 are illustrated in Figure. 5.2a-5.2c, respectively. The recommended torch postures for the three welding types are $[10^\circ \sim 20^\circ, -45^\circ, CR]$, $[80^\circ, 0^\circ, 0^\circ]$, and $[100^\circ, 0^\circ, 0^\circ]$, respectively. Similarly, the orientation deviations from the corresponding recommendations are observed in the resultant figures. Nevertheless, those deviations don't affect the estimation accuracy of the proposed algorithm.

Table 5.6: Orientation estimation $[\text{RMSE}_\theta](^\circ)$, produced by different data sets using Method A with a sampling rate $f_s = 128$ Hz. The four types of welding account for those in Figure.5.1 (for data set D_1^e and D_{1+n}^e), and in Figure. 5.2(for data set D_2^e and D_{2+n}^e).

	Type A	Type B	Type C	Type D
D_1^e	2.59 ± 0.37	3.10 ± 0.44	2.67 ± 0.46	2.78 ± 0.42
D_2^e	2.37 ± 0.42	2.11 ± 0.59	2.14 ± 0.35	3.40 ± 0.54
D_{1+n}^e	3.74 ± 0.51	3.46 ± 0.45	3.44 ± 0.45	3.32 ± 0.48
D_{2+n}^e	4.04 ± 0.31	3.57 ± 0.41	3.84 ± 0.39	3.62 ± 0.51

5.7.2 Discussion

In the proposed measurement, i.e., Method A, the auto-nulling algorithm is incorporated in the effort to compensate the possible time-varying gyro drift during the simulations and the welding experiments; while for the in-line self-calibration of the accelerometer, multiple postures are required. However, the torch orientation is expected to be maintained to the recommended postures throughout the welding experiments. There are thus no enough postures in a single experiment for the accelerometer to conduct the calibration.

The UKF parameter initialization listed in Table 5.2 is found to work well after running an extensive number of simulations, experiments, even in presence of the incorporated noises. The IMU was calibrated well before use. In addition, the auto-nulling algorithm was also incorporated in Method A to compensate the gyro drift. Hence the covariances of the measurement noise and the process noise chosen for Method A are comparatively small;

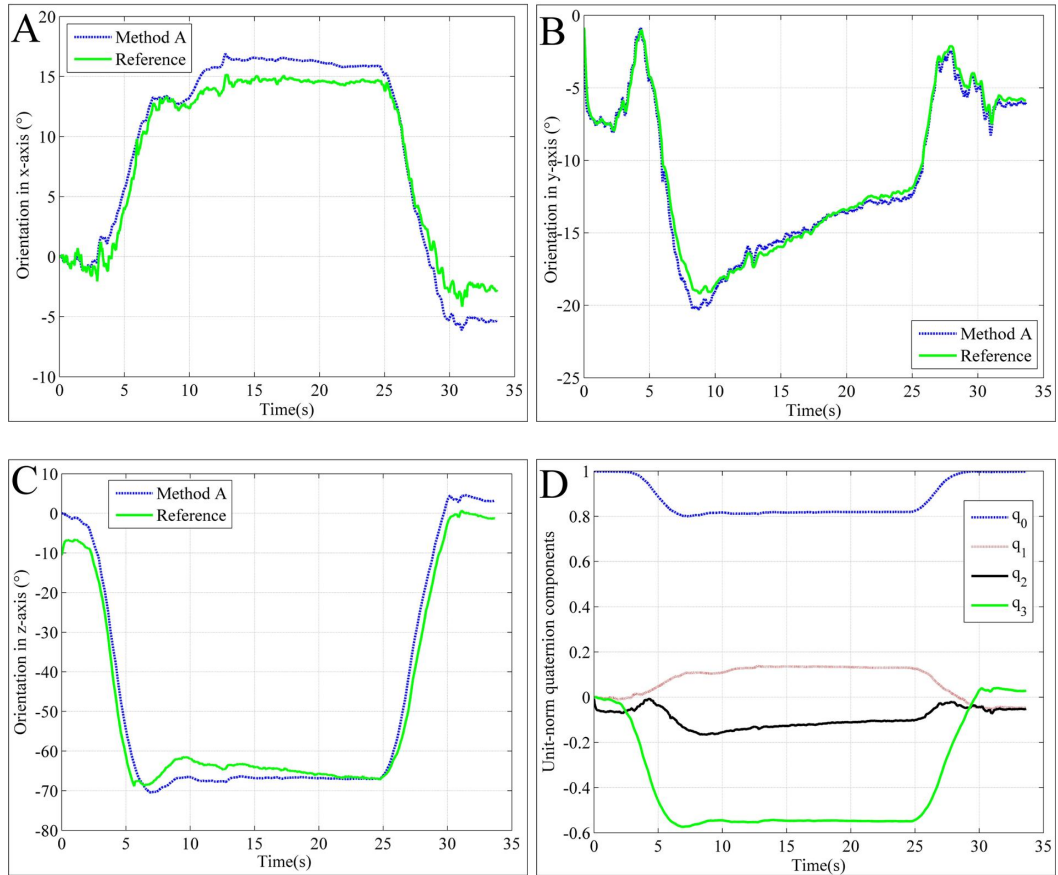


Figure 5.7: Orientation estimations in (A) x -axis, (B) y -axis and (C) z -axis, and D) the unit-norm quaternion components in a GTAW experiment using the proposed estimation algorithm, i.e., Method A. The used data set is D_1^e . The weld type is lap joint correspond to Figure. 5.1b

while the covariances in Method B are selected larger than those in A due to the absence of the auto-nulling algorithm. It is expected that increasing the process noise should be able to compensate the disturbance of the inaccurate modeling and to improve the tracking ability of the filter.

The results reported in Table 5.3 and Table 5.4 show that it is the combination of the UKF and the auto-nulling algorithm to give the best performance. Results for the x -axis and y -axis orientation estimations are comparable in accuracy. Yet, the z -axis estimation shows comparatively poor accuracy. It is arguable that because the accelerometer cannot provide the torch's orientation information in z -axis, estimations in UKF solely relies on the accuracy of the gyro outputs themselves. The performance is thus relatively poor without aiding from the acceleration data. Another interesting observation can be found in Table 5.4 by comparing the performance of Method A and Method B: the $RMSE_x$'s and $RMSE_y$'s yielded by the two methods are comparable, yet, the corresponding $RMSE_\theta$ obtained using Method A is significantly smaller. One can conclude from this observation: 1) the main source of $RMSE_\theta$ is from the estimation for the z -axis (heading); 2) significant improvement in estimation accuracy can be obtained as applying the proposed auto-nulling algorithm to

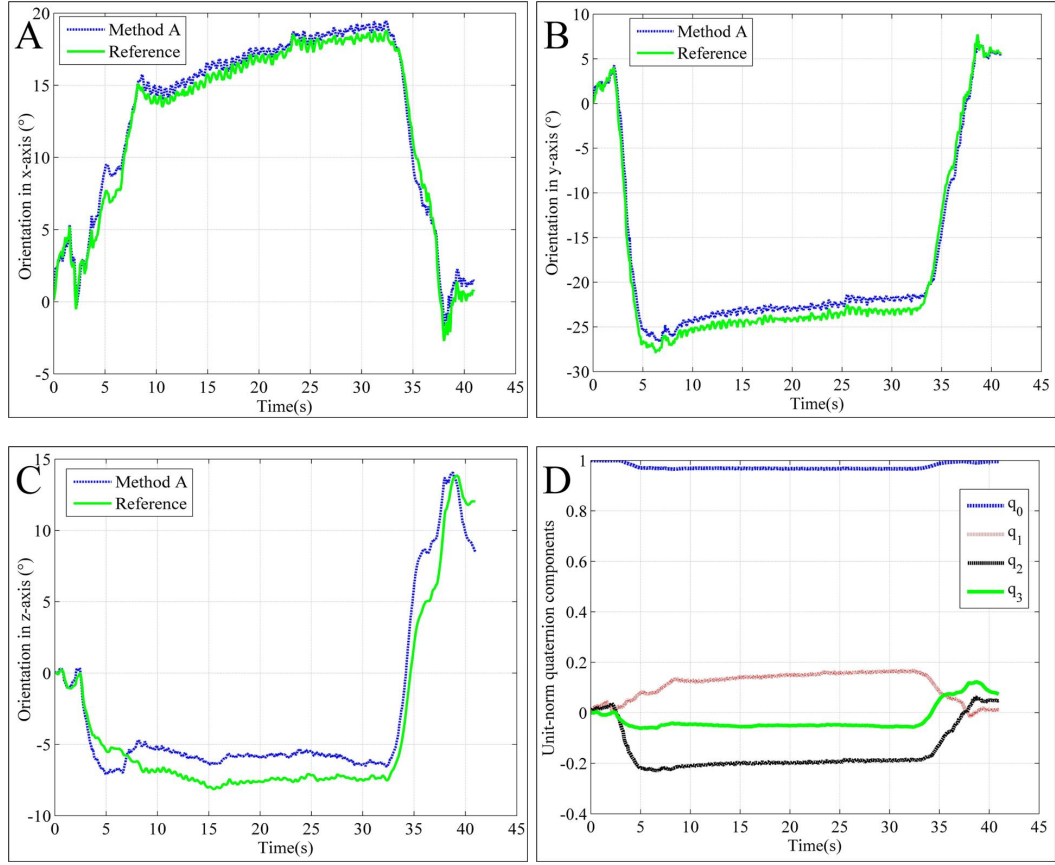


Figure 5.8: Orientation estimations in (A) x -axis, (B) y -axis and (C) z -axis, and D) the unit-norm quaternion components in a GMAW experiment using the proposed estimation algorithm, i.e., Method A. The used data set is D_2^e . The weld type is horizontal vertical fillet correspond to Figure. 5.2a

compensate the gyro drift.

The data from a magnetic sensor can be fused into the UKF to improve the estimation accuracy in z -axis. However, with the existence of the strong magnetic interference from the welding machine and welding arc, the accuracy of the orientation estimation may not be guaranteed. Thus, it might not be a good choice for applications in the welding fields. Fortunately, even without an extra magnetic sensor, the 3-D estimation errors reported in Table 5.3 and Table 5.6 are acceptable compared with state-of-art researches in other academic communities ([135], [82], [104]). Further, only accelerometers and gyroscopes are applied in the proposed method while other methods added magnetometers.

Degradations in estimation accuracy are observed in both Table 5.3 and Table 5.6 after injecting the noises into the gyro data and acceleration data. The auto-nulling algorithm should be able to compensate the noise in the gyro data. However, the contaminated acceleration data contains both gravitation and the fake acceleration induced by the injected noise, while the acceleration of the IMU is considered as a disturbance in the sensor model (Equation. 5.8). The sensor model thus tends to be inaccurate with the existence of the acceleration, and that leads to a degraded orientation estimation. Similar results can be

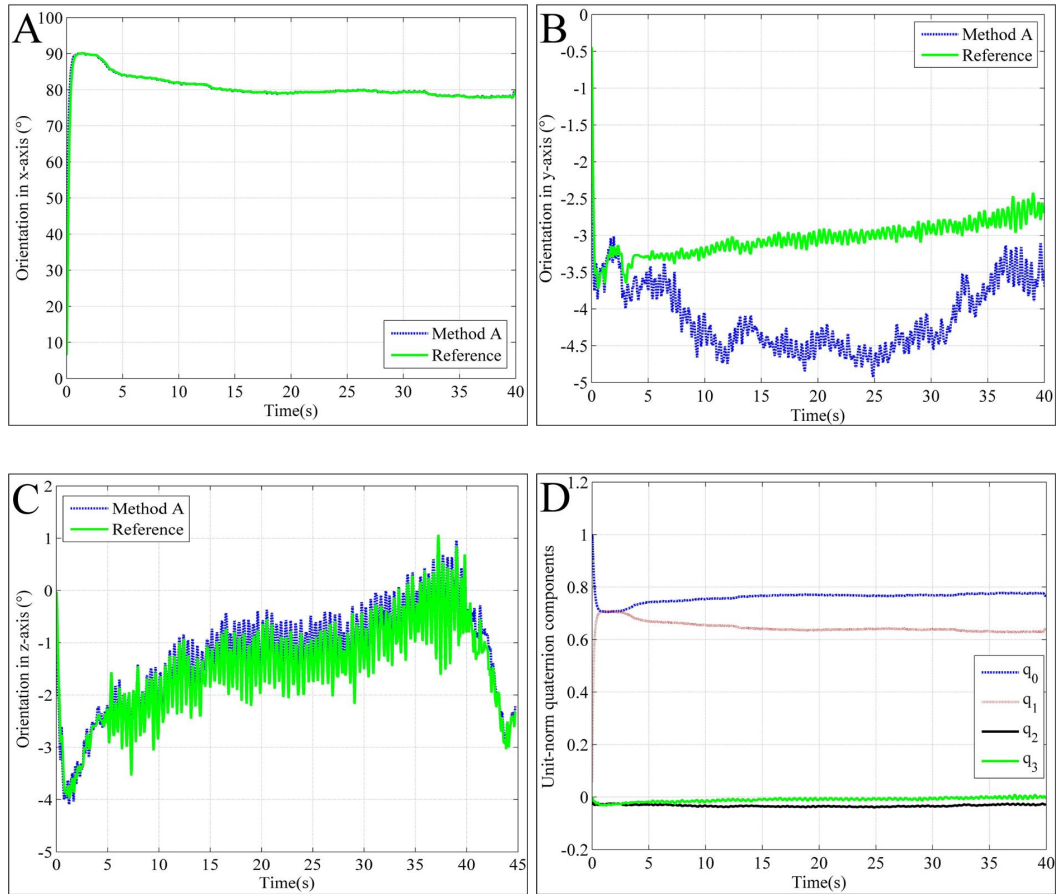


Figure 5.9: Orientation estimations in (A) x -axis, (B) y -axis and (C) z -axis, and D) the unit-norm quaternion components in one GMAW experiment using the proposed estimation algorithm, i.e., Method A. The used data set is D_2^c . The weld type is vertical up root pass correspond to Figure. 5.2b

found in Table 5.5. As the torch movement become faster, the accelerometer is more likely to detect the acceleration of the torch's movement. The estimation accuracy is thus degraded.

Within the limits of our analysis, increasing the sampling rate does improve the estimation accuracy, but its effect is not prominent. Unlike the EKF which usually requires a high sampling rate to avoid the possible filter instability, UKF has no such stability issue. Increasing sampling rate is a huge computation and energy assumption burden for the battery-powered IMU. Thereby, sampling rate was set at 128 Hz in the welding experiments.

One can find that some of the recommended torch orientations do not require specifications for the z -axis posture, such as those for the welding types in Figure. 5.1. It is because the torch posture in z -axis does not necessarily relate to weld quality in some welding processes. On the other hand, a proper z -axis torch posture is recommended weld types like those shown in Figure. 5.2 in order to perform the qualified weld. Further, in the applications as mentioned in Section ??, the total 3-D accurate orientation estimation might be highly appreciated.

The effect of the torch's swing motions to the torch orientation can be found by comparing

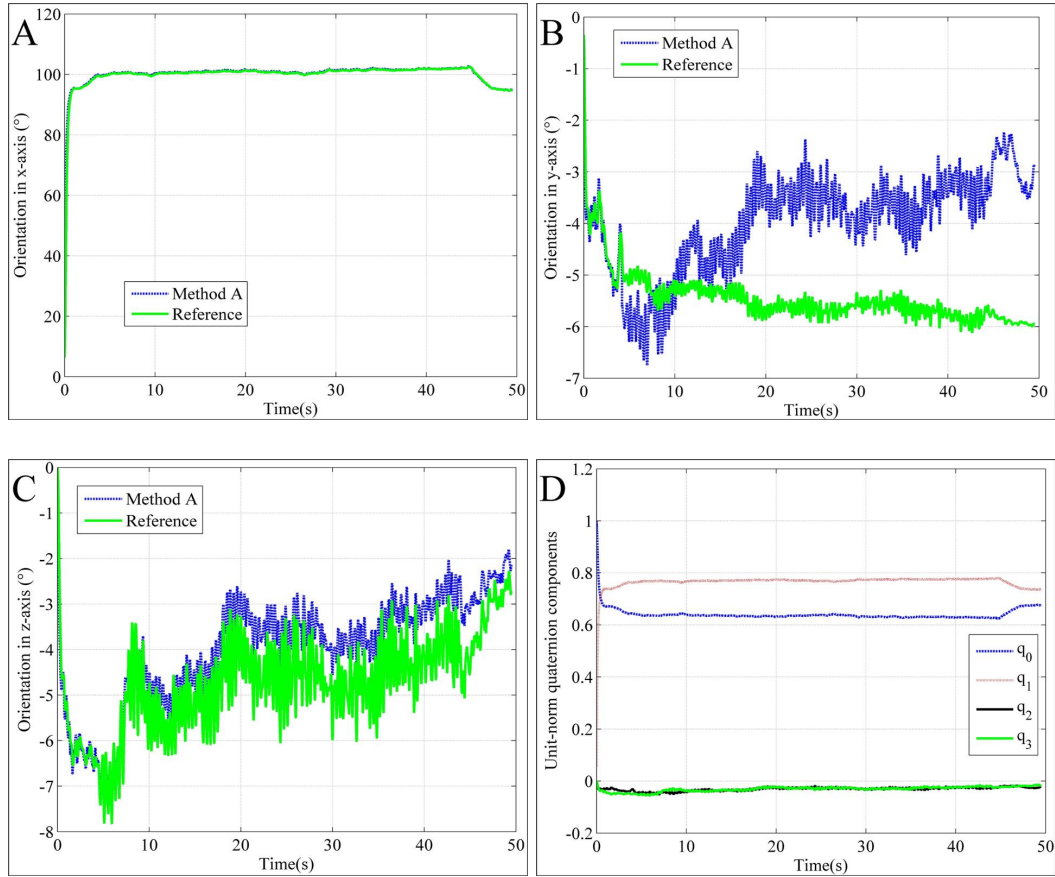


Figure 5.10: Orientation estimations in (A) x -axis, (B) y -axis and (C) z -axis, and D) the unit-norm quaternion components in a GMAW experiment using the proposed estimation algorithm, i.e., Method A. The used data set is D_2^e . The weld type is vertical up root pass correspond to Figure. 5.2c

Figure. 5.7 and Figure. 5.8-5.10: more ripples are observed in the torch orientation curves as torch swing motions are augmented. Yet, in this study no extra errors are observed to be yielded in the orientation estimation due to the swing motions.

5.8 Summary

An innovative measurement scheme for the 3-D welding torch orientation is developed in this chapter which can be conveniently adapted into a manual arc welding process or a welder training system. The proposed measurement scheme is composed of a quaternion based UKF incorporated by an auto-nulling algorithm. The UKF aims for the estimation of the 3-D welding torch orientation using a miniature WIMU endowed with a tri-axis gyro and one tri-axis accelerometer. The auto-nulling algorithm serves as an in-line calibration procedure to compensate the gyro drift, which has been verified to significantly improve the estimation accuracy in three-dimensional, especially in the heading estimation. It has been found that the proposed scheme is able to provide an accurate orientation estimation

without aiding from an extra magnetometer. The accuracy of the estimation using the proposed scheme has been validated by simulation and welding experiments. Statistics show that the estimation error in welding experiments is in the order of 3° .

In the rest of the dissertation, the WIMU is incorporated along with the proposed UKF in a manual welding process such that the welder's torch manipulations can be recorded, studied and modelled in relating to weld quality characters, such as the weld beam appearance and the weld penetration depth.

Chapter 6

Weld Pool Reconstruction Scheme

Accurate measurements of weld pool using proposed sensing system based on three prerequisites: 1) The qualified image of reflection pattern is captured; 2) and the reflection pattern is successful extracted through image processing; 3) the spatial geometric relation among the weld pool, torch and helmet is accurately estimated using the grid reflection pattern, and the data obtained from the two IMUs, i.e., A_1 and A_2 , as shown in Figure. 3.1. The first two issues are addressed in Chapter 3, 4, respectively. In this chapter, the third prerequisite, the spatial geometric relation of the sensing system, is addressed first. The weld pool surface reconstruction algorithm is formulated and demonstrated by an example. More reconstruction experiments are designed, conducted and analyzed to further verify the effectiveness and robustness of the proposed reconstruction algorithm.

6.1 Spatial Relations of the Sensing System

There are mainly four coordinate systems in the proposed sensing system (illustrated in Figure. 3.1) as shown in Figure. 6.1. Although the dimension of a weld pool surface is not subject to any coordinate systems, the weld pool in the moving coordinate system ($(xyz)|_w$) might present a more direct perspective. Hence, coordinate system $(xyz)|_w$ is selected where the spatial relations are formulated and the reconstruction algorithm is developed.

1. Transformation from universal coordinate system $(xyz)_U$ to moving coordinate system $(xyz)_w$

An arbitrary point/vector in $(xyz)_U$ can be transferred to $(xyz)_w$ using a rotation matrix ($R_{U \rightarrow w}$) and a translation matrix ($T_{U \rightarrow w}$). Denote $G_{A_1} = [g_{A_1}^x, g_{A_1}^y, g_{A_1}^z]$ the orientation of IMU A_1 , and θ_{tn} as the angle that the torch makes to the normal at the original of $(xyz)_w$, then the $R_{U \rightarrow w}$ and $T_{U \rightarrow w}$ can be written as:

$$R_{U \rightarrow w} = R^x(g_{A_1}^z - \theta_{tn}) \quad (6.1)$$

$$T_{U \rightarrow w} = T_{w \rightarrow center} R^x(-g_{A_1}^z - \theta_{tn}) T_{center \rightarrow w} \quad (6.2)$$

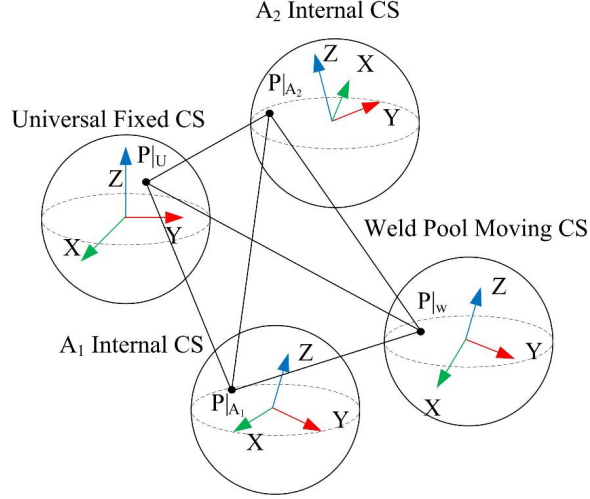


Figure 6.1: Illustration of coordinate systems (CS) : Universal fixed CS $((xyz)|_U)$, A_1 internal CS $((xyz)|_{A_1})$, A_2 internal CS $((xyz)|_{A_2})$, and weld pool moving CS $((xyz)|_w)$.

$$T_{w \rightarrow center} = \begin{bmatrix} 1 & 0 & 0 & 0 \\ 0 & 1 & 0 & 0 \\ 0 & 0 & 1 & 0 \\ 0 & 0 & L_p & 1 \end{bmatrix} \quad (6.3)$$

$$T_{center \rightarrow w} = \begin{bmatrix} 1 & 0 & 0 & 0 \\ 0 & 1 & 0 & 0 \\ 0 & 0 & 1 & 0 \\ 0 & 0 & -L_p & 1 \end{bmatrix} \quad (6.4)$$

2. The position of L_1 in $(xyz)_w$

The location of L_1 , $D_{L_1}|_w$, can be calculated using Equation. 6.5

$$D_{L_1}|_w = D_{A_1}|_w - d_1 \Psi_{Y_{A_1}}|_w \quad (6.5)$$

where $D_{A_1}|_w$ is the location of A_1 in $(xyz)_w$, and $\Psi_{Y_{A_1}}|_w$ is the direction vector of axis Y_{A_1} in $(xyz)_w$. They can be obtained using Equation. 6.6 and Equation. 6.7:

$$[\Psi_{Y_{A_1}}|_w, 1] = [0, 1, 0, 1] \mathbf{R}(G_{A_1}) R_{U \rightarrow w} \quad (6.6)$$

$$D_{A_1}|_w = d_{torch} \Psi_{Z_{A_1}}|_w \quad (6.7)$$

where

$$[\Psi_{Z_{A_1}}|_w, 1] = [0, 0, 1, 1] \mathbf{R}(G_{A_1}) R_{U \rightarrow w} \quad (6.8)$$

Given the position of L_1 , the incident ray functions of the projection matrix pattern in $(oxyz)_w$ are

$$[x, y, z] = D_{L_1}|_w + t\Psi_{p_{i,j}}|_w \quad (6.9)$$

where

$$[\Psi_{p_{i,j}}|_w, 1] = [\Psi_{p_{i,j}}|_{L_1}, 1]R^x(\pi + \theta_{TL_1})\mathbf{R}(G_{A_1})R_{U \rightarrow w} \quad (6.10)$$

in which $\Psi_{p_{i,j}}|_{L_1}$ can be calculated using Equation. 3.24.

3. The location of A_2 in $(oxyz)_w$

In coordinate system $(oxyz)_w$, the location of L_2 is

$$D_{L_2}|_w = D_{A_1}|_w - d_2\Psi_{YA_1}|_w \quad (6.11)$$

An auxiliary coordinate system $(oxyz)_{L_2}$ is generated in two steps: 1) move $(oxyz)_w$ to L_2 , i.e., translate origin O_{A_2} to L_2 ; 2) rotate $(oxyz)_{L_2}$ around its three axes till the projection vector $\Psi_{L_2}|_{L_2}=[0, 0, 1]$ with rotation matrix $R_{w \rightarrow L_2}$. That are:

$$[0, 0, 1, 1] = [\Psi_{L_2}|_w, 1]R_{w \rightarrow L_2} \quad (6.12)$$

where

$$[\Psi_{L_2}|_w, 1] = [\Psi_{L_2}|_{initial}, 1]\mathbf{R}(G_{A_1})R_{U \rightarrow w} \quad (6.13)$$

$$R_{w \rightarrow L_2} = R^x(g_{A_1}^z + \theta_{tn})\mathbf{R}(-G_{A_1})R^x(\theta_{TL_2}) \quad (6.14)$$

Figure 6.2 illustrates the shield glass plane in coordinate system $(oxyz)_{L_2}$. Plane P_{shield}^{xoy} shows the interception pattern 2 if the shield glass plane is parallel with plane $(xoy)_{L_2}$. The laser lines $f'h'$ and $g'i'$ are parallel with y_{L_2} -axis and x_{L_2} -axis, respectively, and the center point (e') is in z_{L_2} -axis.

The shield glass plane function in coordinate system $(oxyz)_{L_2}$ can be written as:

$$\Psi_{P_s}|_{L_2} ([x, y, z] - [0, 0, z_e])^T = 0 \quad (6.15)$$

where $[0, 0, z_e]$ is the coordinate of point e in Figure. 6.2, Ψ_{P_s} is the normal of the shield glass plane, and

$$[\Psi_{P_s}|_{L_2}, 1] = [0, 1, 0, 1]\mathbf{R}(G_{A_2})R_{U \rightarrow w}R_{w \rightarrow L_2} \quad (6.16)$$

In Equation. 6.15, only z_e is the unknown variable.

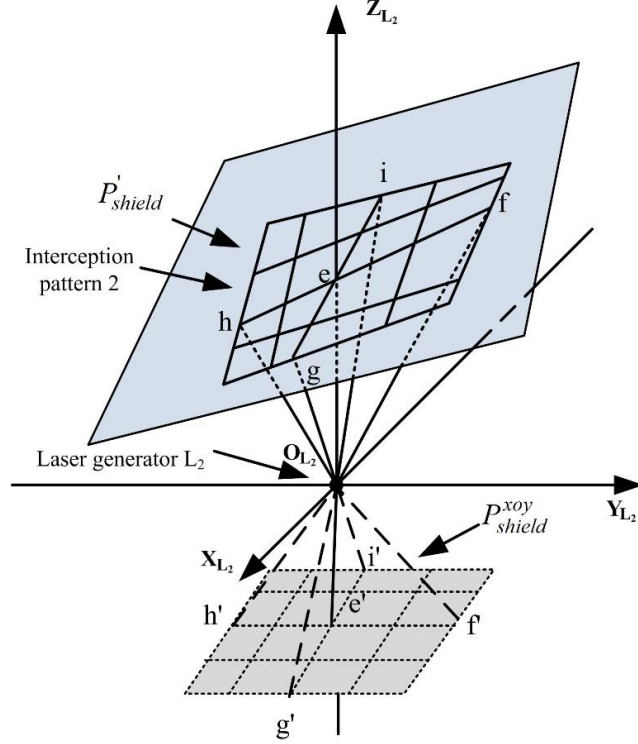


Figure 6.2: Illustration of the shield glass plane in the auxiliary coordinate system. Grid patten is imaged in the plane.

Assuming the coordinate for point f in $(oxyz)_{L_2}$ is $[0, y_f, z_f]$, then the line function for fO_{L_2} is

$$[x, y, z] = t\Psi_f|_{L_2} \quad (6.17)$$

where

$$\Psi_f|_{L_2} = [0, \sin(2\theta_{in_2}), \cos(2\theta_{in_2})] \quad (6.18)$$

Using Equation. 6.15 and Equation. 6.17, point f 's coordinate can be obtained which is subject to variable z_e :

$$[0, y_f, z_f] = \frac{\Psi_{P_s}|_{L_2}[0, 0, z_e]^T}{\Psi_{P_s}|_{L_2}\Psi_f|_{L_2}^T}\Psi_f|_{L_2} \quad (6.19)$$

The grid pattern can be extracted through image processing during welding process. Hence, the length of any line segments in P'_{shield} , for instance, the line segment L_{fe} can be calculated which can be written:

$$\|[0, y_f, z_f] - [0, 0, z_e]\|_2 = L_{fe} \quad (6.20)$$

then z_e can be obtained from Equation. 6.20, which is the length of eO_{L_2} , denoted as d_{eL_2} . Since d_{eL_2} is not subject to any coordinate system, the distance from point e to L_2 in $(xyz)_w$ is d_{eL_2} .

The location of point e in $(xyz)_w$ is

$$D_e|_w = D_{L_2}|_w + d_{eL_2}\Psi_{L_2}|_w \quad (6.21)$$

The coordinate of point e in $(xyz)_{A_2}$, $D_e|_{A_2}$ is obtained through image processing. The position of A_2 in $(xyz)_w$, $D_{A_2}|_w$, thus can be obtained by Equation. 6.22.

$$[D_{A_2}|_w, 0] = [D_e|_w, 1] - [D_e|_{A_2}, 1]\mathbf{R}(G_{A_2})R_{U \rightarrow w} \quad (6.22)$$

Given the obtained position of A_2 ($D_{A_2}|_w = [d_{A_2}^x|_w, d_{A_2}^y|_w, d_{A_2}^z|_w]$), the translation matrix ($T_{A_2 \rightarrow w}$) and the rotation matrix ($R_{A_2 \rightarrow w}$) can thus be obtained to transfer an arbitrary point from coordinate system $(xyz)_{A_2}$ to $(xyz)_w$:

$$T_{A_2 \rightarrow w} = \begin{bmatrix} 1 & 0 & 0 & 0 \\ 0 & 1 & 0 & 0 \\ 0 & 0 & 1 & 0 \\ d_{A_2}^x|_w & d_{A_2}^y|_w & d_{A_2}^z|_w & 1 \end{bmatrix} \quad (6.23)$$

$$R_{A_2 \rightarrow w} = \mathbf{R}(G_{A_2})R_{U \rightarrow w} \quad (6.24)$$

6.2 3D Weld Pool Surface Reconstruction

6.2.1 Modeling of 2D weld pool boundary

Before the 3D surface is reconstructed, the boundary of the weld pool should be determined first. The model used to fit the boundary of the weld pool is from literature [157] and demonstrated in Figure 6.3:

$$y_r = \pm ax_r^b(1 - x_r) \quad (6.25)$$

where $x_r = x/L, y_r = y/L$, and L is the length of the weld pool, which is the distance from the head to the tail of the weld pool. The width of the weld pool can be calculated using parameter a, b and L .

$$w = w_r \times L = 2aL \left[\frac{b}{1+b} \right]^b \left(\frac{1}{1+b} \right) \quad (6.26)$$

It can be seen that the 2D parametric model of the weld pool boundary is a transcendental equation in which normally only numerical or approximate solution exists. Hereby, when solving the equation in real-time, reasonable ranges for the parameters are predefined. In particular, since the moderate current and speed are applied in the experiments in this study, the weld pool dimension should be in a medium size. Thus, the range for the length of the weld pool is considered from 0 mm to 10 mm. The width's range is from 0 mm to 12 mm.

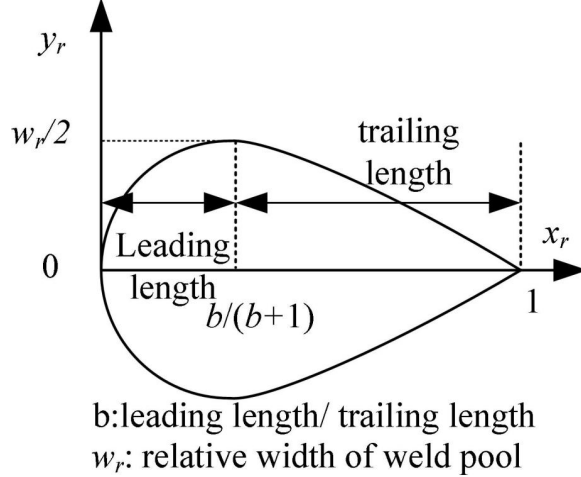


Figure 6.3: Illustration of the weld pool boundary model

6.2.2 3D weld pool reconstruction

The projection and reflection patterns are illustrated in Figure. 6.4. The projection laser dots are specularly reflected by the weld pool surface, and imaged on the helmet shield glass. To this end, the weld pool reconstruction is to find the positions, i.e., the 3D coordinates, of the projection dots on the surface where the specular reflection law holds, i.e., 1) The incident ray, the reflected ray and the normal to the reflection surface at the point of the incidence lie in the same plane; 2) The angle which the incident ray makes with the normal is equal to the angle which the reflected ray makes to the same normal; 3) The reflected ray and the incident ray are on the opposite sides of the normal.

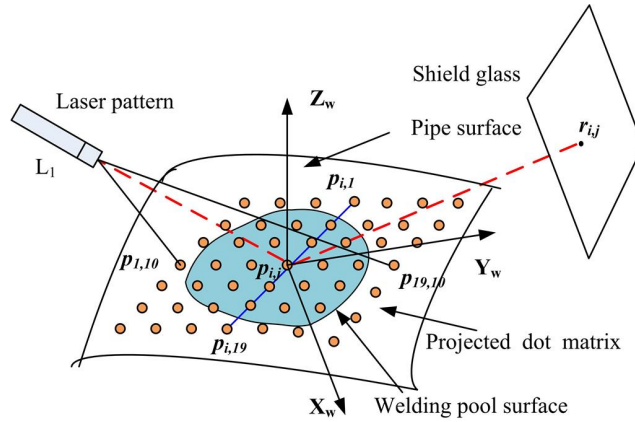


Figure 6.4: Illustration of the projection and reflection dot matrix patterns

Considering the work piece surface as the initial estimation of the weld pool surface $s_w^{(0)}$, the projection laser dots, $D_{p_{i,j}}^{(0)}|_w$ are the intersection points of the projection rays (Equation. 6.9) and the pipe function (Equation. 6.27).

$$(z_w + L_p)^2 + y_w^2 = L_p^2 \quad (6.27)$$

$$D_{p_{i,j}}^{(0)}|_w = D_{L_1}|_w + t^{(0)}\Psi_{p_{i,j}}|_w \quad (6.28)$$

where

$$t^{(0)} = \frac{M_{t^{(0)}}^{(1)} - M_{t^{(0)}}^{(3)}}{M_{t^{(0)}}^{(2)}} \quad (6.29)$$

$$M_{t^{(0)}}^{(1)} = -2(d_{L_1}^y|_w\psi_{p_{i,j}}^y|_w + d_{L_1}^z|_w\psi_{p_{i,j}}^z|_w + L_p\psi_{p_{i,j}}^z|_w) \quad (6.30)$$

$$M_{t^{(0)}}^{(2)} = 2((\psi_{p_{i,j}}^y|_w)^2 + (\psi_{p_{i,j}}^z|_w)^2) \quad (6.31)$$

$$M_{t^{(0)}}^{(3)} = \sqrt{(M_{t^{(0)}}^{(1)})^2 - 2M_{t^{(0)}}^{(2)}M_{t^{(0)}}^{(4)}} \quad (6.32)$$

$$M_{t^{(0)}}^{(4)} = (d_{L_1}^y|_w)^2 + (d_{L_1}^z|_w)^2 + 2d_{L_1}^z|_wL_p \quad (6.33)$$

The reflection pattern on shield glass $D_{r_{i,j}}|_{A_2}$ can be obtained through image processing, those dots in $(xyz)_w$ can be calculated using Equation. 6.34.

$$[D_{r_{i,j}}|_w, 1] = [D_{r_{i,j}}|_{A_2}, 1]T_{A_2 \rightarrow w}R_{A_2 \rightarrow w} \quad (6.34)$$

The reflection vector for the j^{th} dot in the arbitrary ζ^{th} row are:

$$\Psi_{rp_{\zeta,j}}^{(0)}|_w = \frac{D_{rp_{\zeta,j}}|_w - D_{p_{\zeta,j}}^{(0)}|_w}{\|D_{rp_{\zeta,j}}|_w - D_{p_{\zeta,j}}^{(0)}|_w\|_2} \quad (6.35)$$

where $j = 1, 2, \dots, m$, m is the number of dots in ζ^{th} row that are reflected by the weld pool. Since the projection vector $\Psi_{p_{\zeta,j}}|_w$ has been obtained in Equation. 6.10, the normal vector for the reflection at $D_{p_{\zeta,j}}^{(0)}|_w$ is

$$\Psi_{np_{\zeta,j}}^{(0)}|_w = \frac{\Psi_{rp_{\zeta,j}}^{(0)}|_w - \Psi_{p_{\zeta,j}}|_w}{\|\Psi_{rp_{\zeta,j}}^{(0)}|_w - \Psi_{p_{\zeta,j}}|_w\|_2} \quad (6.36)$$

An auxiliary coordinate system $(xyz)_{p_\zeta}$ is built based on $(xyz)_w$: 1) translate origin O_w to $D_{p_{\zeta,9}}^{(0)}|_w$; 2) rotate the coordinate system till $\Psi_{p_{\zeta,9}}|_w = [0, 0, -1]$. The two corresponding transformation matrices, $T_{w \rightarrow p_\zeta}$ and $R_{w \rightarrow p_\zeta}$, can be written as:

$$T_{w \rightarrow p_\zeta} = \begin{bmatrix} 1 & 0 & 0 & 0 \\ 0 & 1 & 0 & 0 \\ 0 & 0 & 1 & 0 \\ -d_{p_{\zeta,9}}^{(0)x}|_w & -d_{p_{\zeta,9}}^{(0)y}|_w & -d_{p_{\zeta,9}}^{(0)z}|_w & 1 \end{bmatrix} \quad (6.37)$$

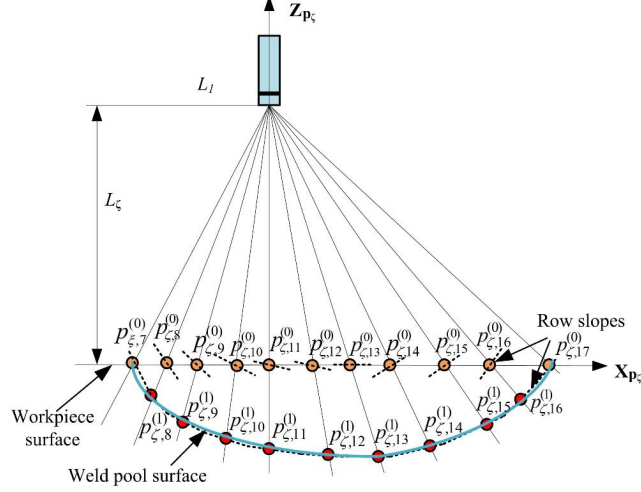


Figure 6.5: Illustration of the projected laser dot in ζ^{th} row (an arbitrary row) of pattern L_1 . Along the x_{p_ζ} -axis, the short dash lines are the row slopes at the dots projected on the pipe surface. The dash curve below the axis is the desired curve of the row that satisfies the row slopes at each new dot along the curve.

$$R_{w \rightarrow p_\zeta} = R^x(g_{A_1}^z + \theta_{tn}) \mathbf{R}(-G_1) R^x(-\theta_{TL_1} + (9 - \zeta)\theta_{in_1}) \quad (6.38)$$

The laser dots in ζ^{th} row that projected in the weld pool are illustrated in Figure. 6.5. It can be found from the figure, the weld pool surface at this row can be interpolated by the laser dots. Since only those dot positions on the surface can be accurately calculated, the weld pool surface can be measured row by row.

It should be noted that the weld pool surface does not have to be concave as shown in Figure. 6.5. It could be either concave or convex based on the welding conditions.

Transforming $\Psi_{np_{\zeta,j}}^{(0)}|_w$ to $(oxyz)_{p_\zeta}$ that is

$$\Psi_{np_{\zeta,j}}^{(0)}|_{p_\zeta} = \Psi_{np_{\zeta,j}}^{(0)}|_w R_{w \rightarrow p_\zeta} \quad (6.39)$$

and the row slopes at reflection dots in ζ^{th} row, $S_{\zeta,j}^{(0)}|_{p_\zeta}$, as shown in Figure. 6.5, can be written as:

$$S_{\zeta,j}^{(0)}|_{p_\zeta} = -\frac{\psi_{np_{\zeta,j}}^{(0)x}|_{p_\zeta}}{\psi_{np_{\zeta,j}}^{(0)z}|_{p_\zeta}} \quad (6.40)$$

where

$$\Psi_{np_{\zeta,j}}^{(0)}|_{p_\zeta} = [\psi_{np_{\zeta,j}}^{(0)x}|_{p_\zeta}, \psi_{np_{\zeta,j}}^{(0)y}|_{p_\zeta}, \psi_{np_{\zeta,j}}^{(0)z}|_{p_\zeta}] \quad (6.41)$$

The weld pool surface can be considered as a smooth liquid surface. The curve of ζ^{th} row as shown in Figure. 6.5 can thus be described by a n^{th} order polynomial:

$$d_{p_{\zeta,j}}^{(1)z}|p_{\zeta} = a_n^{(1)}(d_{p_{\zeta,j}}^{(1)x}|p_{\zeta})^n + \dots + a_1^{(1)}d_{p_{\zeta,j}}^{(1)x}|p_{\zeta} + a_0^{(1)} \quad (6.42)$$

where $D_{p_{\zeta,j}}^{(1)}|p_{\zeta} = [d_{p_{\zeta,j}}^{(1)x}|p_{\zeta}, d_{p_{\zeta,j}}^{(1)y}|p_{\zeta}, d_{p_{\zeta,j}}^{(1)z}|p_{\zeta}]$, $a_n^{(1)}, \dots, a_1^{(1)}$ and $a_0^{(1)}$ are the coefficients of the row curve $r_{\zeta}^{(1)}$, and $n < m + 3$.

The slopes of the incident laser rays for the laser dots, $k_{\zeta,j}$, can be obtained from the inter-beam angle of the pattern. The coordinate for the laser generator is:

$$[0, 0, L_{\zeta}, 1] = [D_{L_1}|w, 1]T_{w \rightarrow p_{\zeta}}R_{w \rightarrow p_{\zeta}} \quad (6.43)$$

where

At an arbitrary dot $p_{\zeta,j}^{(1)}$ in the row curve $r_{\zeta}^{(1)}$, the following equations can be obtained:

$$\begin{bmatrix} d_{p_{\zeta,j}}^{(1)z}|p_{\zeta} \\ d_{p_{\zeta,j}}^{(1)z}|p_{\zeta} \\ \left(d_{p_{\zeta,j}}^{(1)z}|p_{\zeta}\right)' \end{bmatrix} = \begin{bmatrix} a_n^{(1)} & \dots & a_1^{(1)} & a_0^{(1)} \\ 0 & \dots & k_{\zeta,j} & L_{\zeta} \\ 0 & na_n^{(1)} & \dots & a_1^{(1)} \end{bmatrix} \begin{bmatrix} \left(d_{p_{\zeta,j}}^{(1)x}|p_{\zeta}\right)^n \\ \vdots \\ d_{p_{\zeta,j}}^{(1)x}|p_{\zeta} \\ 1 \end{bmatrix} \quad (6.44)$$

In Equation. 6.44, $\left(d_{p_{\zeta,j}}^{(1)z}|p_{\zeta}\right)'$ is the slopes of row curve $r_{\zeta}^{(1)}$ at each $D_{p_{\zeta,j}}^{(1)}|p_{\zeta}$. They are required to solve row curve function (Equation. 6.42), yet they can not be accurately calculated without knowing the row curve equation. In order to solve this chicken-egg paradox, $S_{\zeta,j}^{(0)}|p_{\zeta}$ is applied to estimate $\left(d_{p_{\zeta,j}}^{(1)z}|p_{\zeta}\right)'$:

$$\left(d_{p_{\zeta,j}}^{(1)z}|p_{\zeta}\right)' = S_{\zeta,j}^{(0)}|p_{\zeta} \quad (6.45)$$

It can be observed the edge dots ($p_{\zeta,7}^{(0)}$ and $p_{\zeta,17}^{(0)}$ in Figure. 6.5) are in the weld pool boundary. They can be considered the intersection points between the projection matrix pattern and the work piece surface. Therefore their $z_{p_{\zeta}}$ -coordinates can be assumed to be zero. This can be applied to solve the Equation. 6.44 and 6.45, then $a_n^{(1)}, \dots, a_1^{(1)}$ and $a_0^{(1)}$ can be obtained, as well as the $D_{p_{\zeta,j}}^{(1)}|p_{\zeta}$. After an inverse transformation, the projection dots on the row curve $r_{\zeta}^{(1)}$ in $(oxyz)|w$, $D_{p_{\zeta,j}}^{(1)}|w$, can be calculated:

$$[D_{p_{\zeta,j}}^{(1)}|w, 1] = [D_{p_{\zeta,j}}^{(1)}|p_{\zeta}, 1]R_{w \rightarrow p_{\zeta}}^{-1}T_{w \rightarrow p_{\zeta}}^{-1} \quad (6.46)$$

Using the aforementioned procedure, all the projection dots on the weld pool surface can be obtained which leads to a complete reconstruction of the surface $s_w^{(1)}$.

During welding experiments, it is practically impossible to compare $s_w^{(1)}$ and the real weld pool surface to verify the reconstruction accuracy. However, with the knowledge of the spatial relations in the sensing system, the virtual reflection laser dots, $D_{rp_{i,j}}^{(1)}|w$, reflected by $s_w^{(1)}$

can be calculated. The reconstruction accuracy then can be evaluated by matching $D_{rp_{i,j}}^{(1)}|_w$ with their corresponding dots in the real reflection pattern, $D_{rp_{i,j}}|_w$ which are identified from captured images. A match coefficient M_c is defined to quantify the reconstruction accuracy:

$$M_c^{(1)} = \frac{\frac{1}{N} \sum \|D_{rp_{i,j}}^{(1)}|_w - D_{rp_{i,j}}|_w\|_2}{L_{ws}} \quad (6.47)$$

where N is the number of dots in the reflection patterns, L_{ws} is the distance from the O_w to the shield glass.

$$L_{ws} = \|\Psi_{P_s}|_w([0, 0, 0] - D_{A_2}|_w)^T\|_2 \quad (6.48)$$

$$[\Psi_{P_s}|_w, 1] = [0, 1, 0, 1]\mathbf{R}(G_{A_2})R_{U \rightarrow w} \quad (6.49)$$

If $M_c^{(1)}$ is larger than a pre-defined value (1.6% in this study), the reconstructed weld pool surface is recursively updated to $s_w^{(*)}$ till $M_c^{(*)} < 1.6\%$. Then $s_w^{(*)}$ can be considered close enough in shape to the real weld pool surface. To this end, the reconstruction process is illustrated in Fig. 6.6.

6.3 Reconstruction Example

Figure 4.14a is taken as an example in this subsection to demonstrate the proposed reconstruction algorithm.

In order to verify the accuracy of the proposed reconstruction algorithm, the results in this study are compared with the previous work in ([114, 106]). High reconstruction accuracy is acquired through detailed quantitative analysis in the two studies. In addition, two measurement metrics in [114] are adopted here, i.e., average reflection error (ARE) and maximum reflection error (MRE):

$$ARE = \frac{1}{N} \sum_{k=1}^N E_k \quad (6.50)$$

$$MRE = \max(E_k), k = 1, \dots, N \quad (6.51)$$

where

$$E_k = \sqrt{\left[\left(x_k^{(e)} - x_k^{(c)} \right) \frac{W_p}{W_r} \right]^2 + \left[\left(y_k^{(e)} - y_k^{(c)} \right) \frac{L_p}{L_r} \right]^2} \quad (6.52)$$

Coordinate pairs $(x_k^{(e)}, y_k^{(e)})$ present the reflection pattern extracted from image processing, while $(x_k^{(c)}, y_k^{(c)})$ is dot matrix pattern reflected by calculated weld pool surface, i.e., the

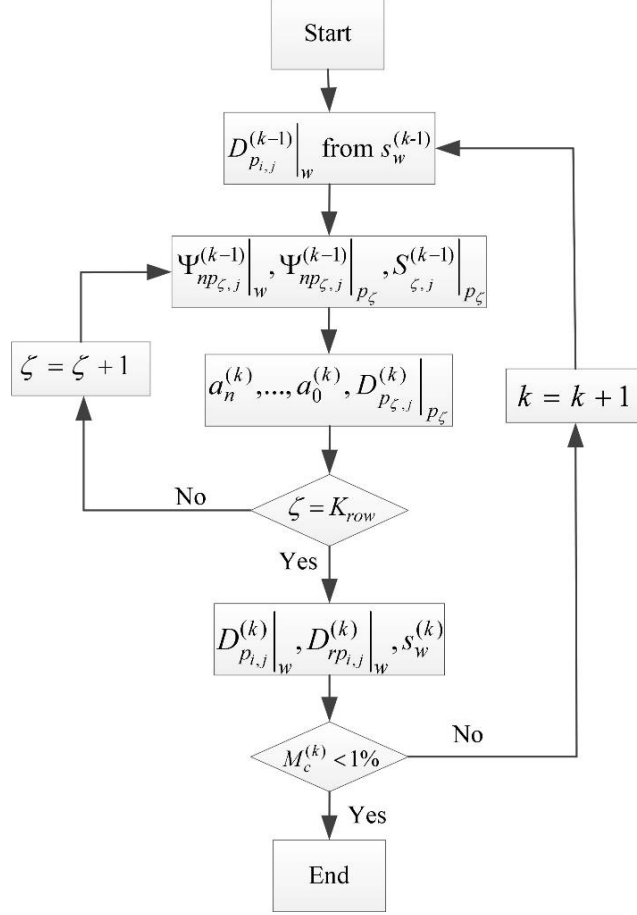


Figure 6.6: Flowchart of the reconstruction algorithm. K_{row} is the number of the rows in the matrix pattern reflected by the weld pool surface.

mirror in subsection. W_r and L_r are the horizontal and vertical ranges of the actual reflected dots extracted from image processing, respectively and W_p and L_p represent the horizontal (x axis) and vertical (y axis) ranges of the corresponding projected dots on the work piece, which are the width and length of the weld pool boundary, i.e., the mirror boundary in subsection.

The results of the image processing, as shown in Figure. 4.14, and the corresponding torch/helmet position and orientation information are both utilized in the reconstruction procedure, and the results of the 3D weld pool reconstruction are shown in Figure. 6.7: A) The calculated coordinates of all the projected laser dots; B) Interpolated weld pool surface; C) the height errors between the actual and reconstructed mirror row by row. Row 1 is defined as the most left dot row in Fig. 6.7a; D) The boundary/edge of the reconstructed mirror; E) The comparison of the extracted and calculated reflection dot matrix pattern. The crosses indicate the dots in extracted reflection pattern; the stars show the dots in the pattern calculated from the reconstructed surface; F) The distances/errors between corresponding laser dots in the two reflection patterns.

The 3D coordinates of all the laser dots projected on the mirror are calculated by the proposed reconstruction algorithm are shown in Figure. 6.7a. Using these coordinates, the

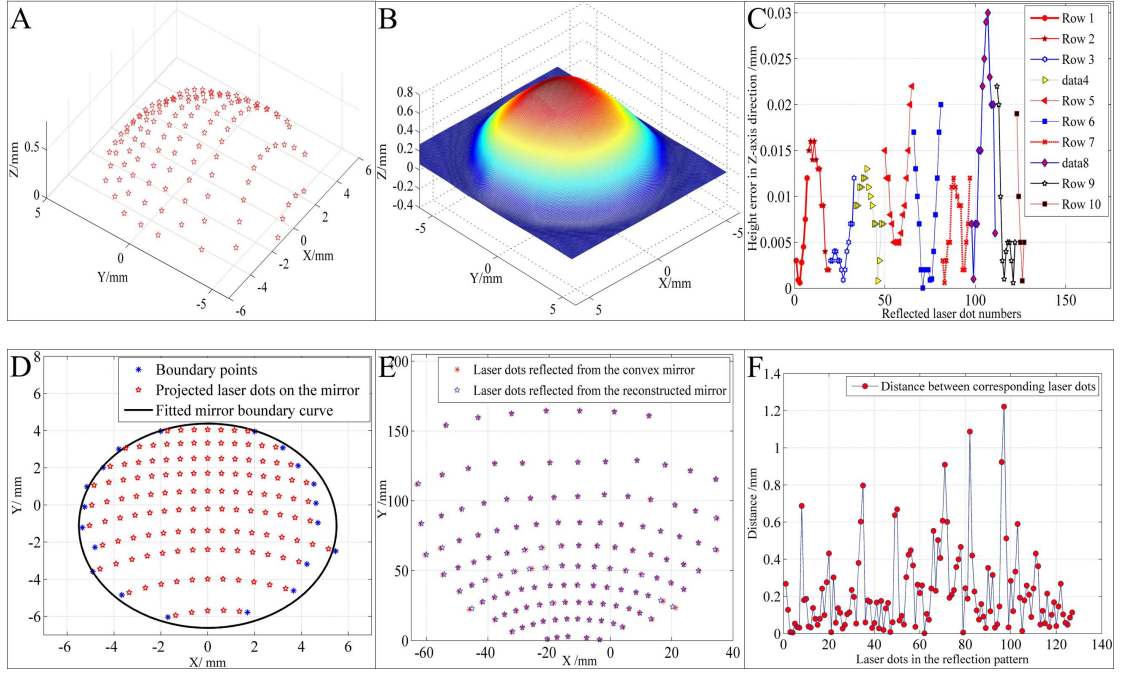


Figure 6.7: Results of weld pool reconstruction

convex mirror surface can be easily interpolated, as shown in Figure. 6.7b.

With the known geometry of the convex spherical mirror, the actual height, i.e., z-axis coordinates, at all the (x,y) coordinate of the projected laser dots on the mirror can be easily obtained. The height errors of the reconstruction obtained for all the projected laser dots are shown in Figure. 6.7c. The maximum height error is 0.03 mm at 10th point of Row 8. The minimum height error is 2×10^{-5} mm at 5th point of Row 6. At the two positions, the heights of the mirror are 0.58 mm and 0.61 mm, which lead to the relative height error 19%, and 0.03%, respectively. The convex mirror reaches the maximal height, i.e., 0.74 mm at 8th point of Row 6, and the height error is 9×10^{-5} mm, which is 0.12%. Compared with the result in [106], 0.16% of height error, the accuracy of the proposed algorithm is comparable.

With the reflected dots obtained, the boundary of the mirror can be least-square fitted by a circle, as shown in Figure. 6.7d. The resultant circle 10.98 mm is diameter, which is 1.9% relative reconstruction error in diameter of the convex mirror. It should be noted that in practical welding processing, the boundary of a weld pool is shaped as Figure. 6.3. Therefore, boundary modeling for weld pools obtained in welding process uses the method addressed in Section 6.2.1. In simulations using spherical convex mirror, boundary fitting using a circle is considered reasonable.

Figure 6.7e shows the comparison between the laser dots (the crosses) reflected by the actual mirror and those reflected dots (the stars) by the virtual reconstructed mirror. The two reflection patterns generally match well with each other. The distance deviations between corresponding dots in the two patterns are shown in Figure. 6.7f. The maximum deviation is 1.22 mm, and the average deviation is 0.23 mm. The distance between the mirror and the shield glass is 125 mm. The match coefficient, according to Equation. 6.47, then is

0.18%, which is smaller than 1%, the pre-defined threshold. That means the proposed reconstruction procedure only needs to iterate once to reconstruct a accuracy-acceptable 3D convex mirror.

Furthermore, using the data from Figure. 6.7d and Figure. 6.7e, ARE and MRE can be calculated, 0.12 mm and 0.02 mm, respectively. Compared with the minimal ARE and MRE obtained in [114], 0.22 mm and 0.08 mm, the reconstruction accuracy using the proposed algorithm increases 78% in ARE and 45% in MRE.

6.4 Simulation and results analysis

A series of experiments are performed to verify 1) the feasibility of the proposed sensing system, 2) robustness and accuracy of the proposed reconstruction algorithm. The experiment configuration used in this section is shown in Figure. 3.16, which are detailed in Chapter 3. The geometry setup for the configuration is listed in Table 3.1. The convex spherical mirror (Edmund optics NT64-057) shown in Figure. 3.11 is used in the experiments as a weld pool simulation.

The effectiveness and robustness of the proposed sensing system can be evaluated by the accurate reconstruction of the convex mirror while the position and orientation of torch and shield glass vary within the range obtained in Chapter 3. The initial setups of the torch and helmet are the same as they are in Chapter 3, i.e., $\Theta_{mh} = [0^\circ, 0^\circ, 0^\circ]$, $D_{A_2}|_{initial} = [0, 125\text{mm}, 20\text{mm}]$, and $\Theta_{mt} = [0^\circ, 0^\circ, 0^\circ]$. The images captured during the translation of the helmet has no significant difference except for the coverage of the laser reflection in the imaging plane, which does not affect the image processing and weld pool reconstruction procedure. Because of that, the experiments performed in this section can be sorted into two categories: A) the rotation of the helmet only while the torch is initial position, and B) the rotation of the torch only while the helmet is in initial position. For example, in category A, the torch is set stationary in its initial position, while the helmet, i.e., the whole tripod along with the shield glass, is manually rotated from its initial position (Fig 3.16) to the corresponding movement boundary position (Fig 3.18).

The images of the two reflection patterns are captured consecutively as the torch/helmet rotates from the initial positions to the boundary positions and processed in real-time with the rate at 30 fps (frame per second). During the rotations, the orientation of the torch and helmet at corresponding instants are calculated using the data from the two IMUs. Using the obtained reflection patterns and the orientations, the mirror surface is reconstructed in real-time. The matching coefficient M_c , measurement metrics ARE and MRE are used to verify the accuracy of the reconstruction algorithm.

In order to verify the effectiveness of orientation algorithm in the experiments, a commercial orientation algorithm imported from the WIMU company (Shimmer) is used as a reference, as shown in Fig 6.10 and Fig 6.14.

6.4.1 Helmet rotation-category A

The results of the real-time image processing and weld pool reconstruction for the helmet orientation are shown in Figure. 6.8 to Figure. 6.11.

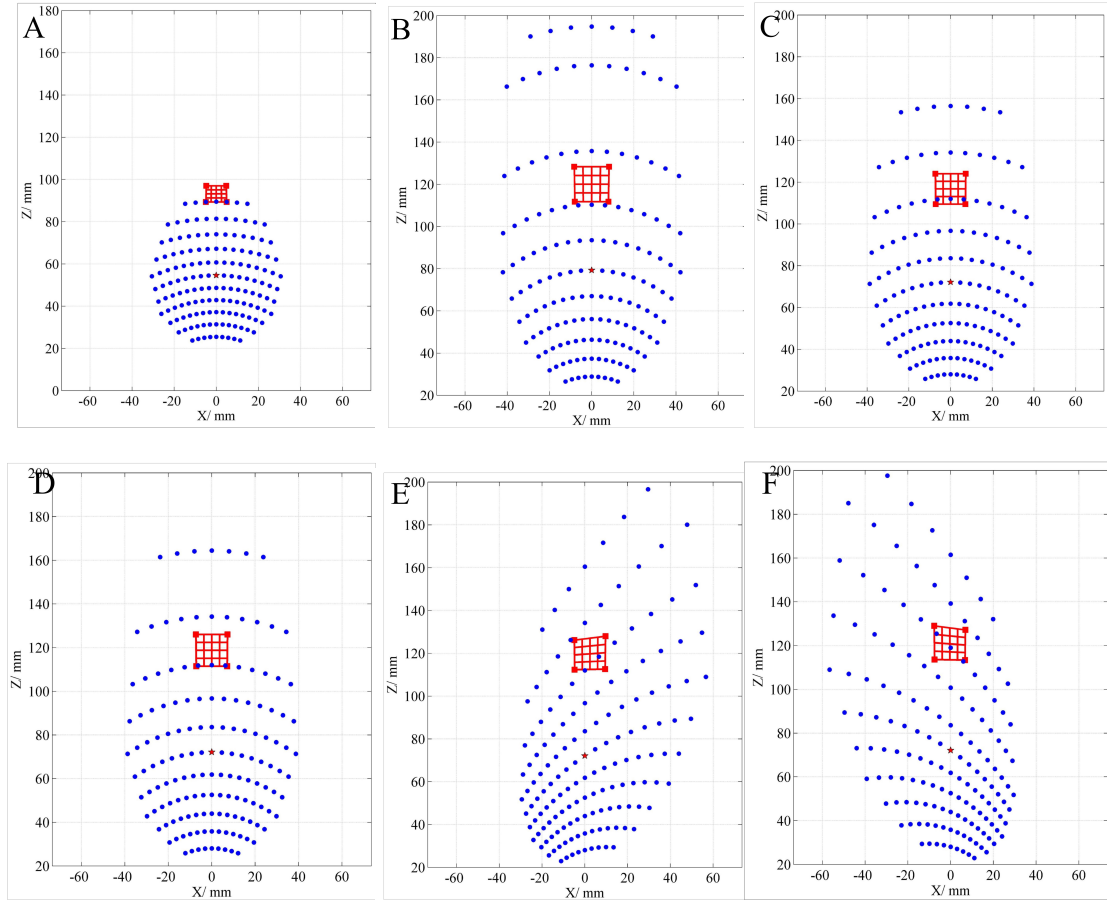


Figure 6.8: Corresponding results of image processing for images where helmet rotates to the boundary positions of: A) Positive x-axis direction; B) Negative x-axis direction; C) Positive y-axis direction; D) Negative y-axis direction; E) Positive z-axis direction; and F) Negative z-axis direction.

6.4.2 Torch rotation-category B

The results of the real-time image processing and weld pool reconstruction for the helmet orientation are shown in Figure. 6.12 to Figure. 6.15.

Comparing images in Fig. 6.8 and Fig. 6.12 with corresponding images Fig. 3.18 and Fig. 3.19, one can find that proposed image processing algorithm can successfully identify the dot matrix and grid laser reflections from captured raw images at the boundary positions. Furthermore, comparing Fig. 6.8 and Fig. 6.12 with Fig. 3.14 and Fig. 3.15, one should be note that there exit a few deviations in terms of the shape patterns between the processed reflections from experiment and those from numerical simulations. Due to the inevitable minor misalignment in mechanics, assembly errors, and etc, the captured raw images are a slightly different than the one obtained in numerical simulations, which leads to those deviations. Using the proposed reconstruction algorithm, the 3D weld pool surface at the boundary positions of the torch/helmet rotation are rebuilt as shown in Fig. 6.9 and Fig. 6.13. The rotation angles are real-time estimated with acceptable accuracy compared to the

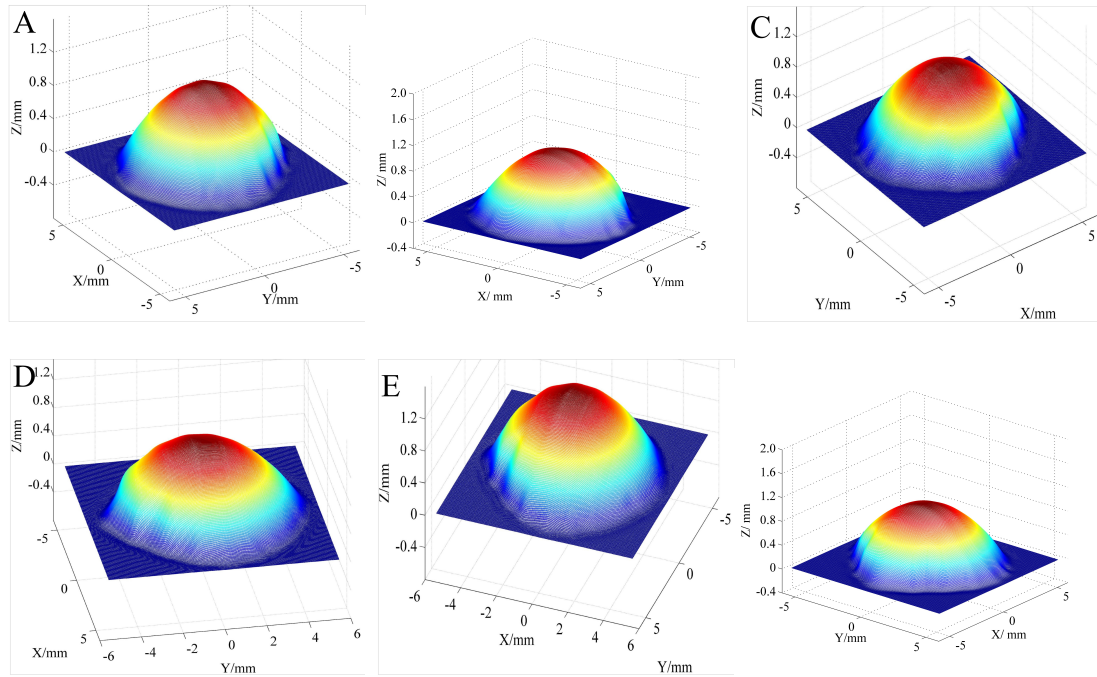


Figure 6.9: The reconstruction results of the spherical convex mirror as the helmet rotates from the initial positions to the boundary points along: A) Positive x-axis direction; B) Negative x-axis direction; C) Positive y-axis direction; D) Negative y-axis direction; E) Positive z-axis direction; and F) Negative z-axis direction.

reference, as shown in Fig. 6.10 and Fig. 6.14, where Method A is the proposed orientation estimation algorithm in Chapter 5. It should be noted that angles the torch/helmet rotates, as shown in the Figures, are not exact angles as calculated in numerical simulations in Chapter 3, mainly because that the torch/helmet were manual rotated. It however does not affects the accuracy of the orientation accuracy, in which as can be found that there is only around 0.5 degree of maximum deviation from the reference orientation.

It should be noted that the reconstruction duration and the orientation monitoring time are different. There is because the reconstruction process and orientation monitoring procedure are manually switched on and off. In situations that the rotations of the torch/helmet stop before the reconstruction procedure, the last sampled orientations are used for the reconstruction algorithm.

Further, it is noted that although one reconstruction algorithm has been proposed [115], its error-based recursive algorithm using the slope filed cannot be claimed as a real-time scheme for the reconstruction of the weld pool surface in GTAW. On the other hand, the proposed reconstruction algorithm in this paper provides an analytic solution for 3D weld pool surface reconstruction. Since it does not need iterative computation, the time cost is significantly reduced.

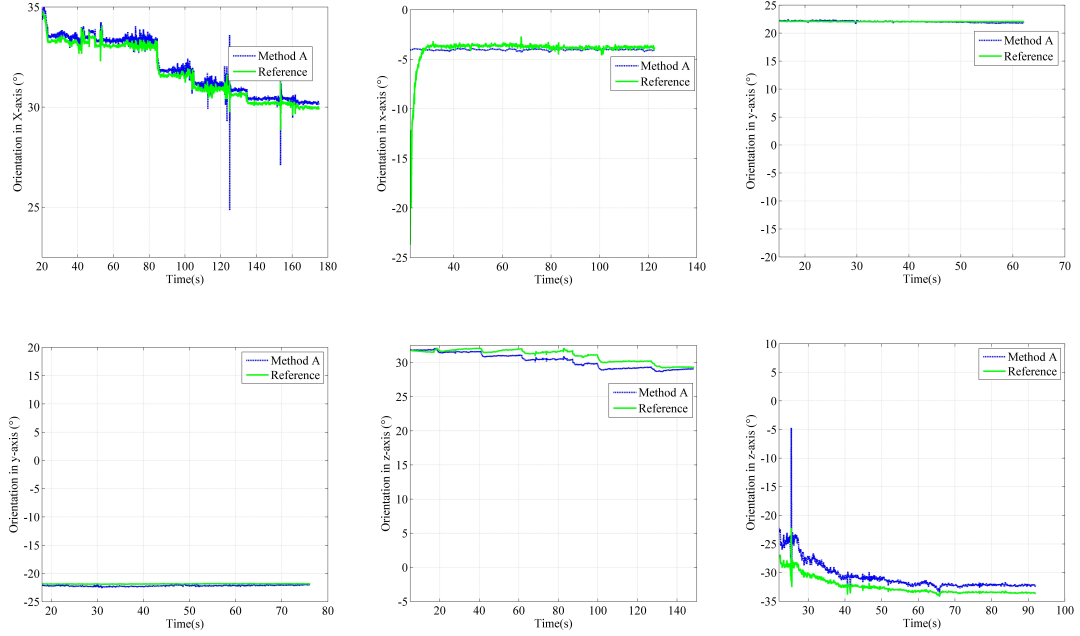


Figure 6.10: Orientation of the helmet where helmet rotates from the initial positions to the boundary positions of: A) Positive x-axis direction; B) Negative x-axis direction; C) Positive y-axis direction; D) Negative y-axis direction; E) Positive z-axis direction; and F) Negative z-axis direction.

6.5 Summary

The monitoring and measurement of three-dimensional weld pool surface provides the foundation for a possible advanced control for the welding process. An analytic reconstruction algorithm based on the slope field of the reflected laser pattern is proposed in this paper to measure the 3D weld pool surface in real-time. The reconstruction is mathematically formulated. The virtual spherical convex surface and the real convex mirror, considered as similar in shape of a weld pool surface which cannot be precisely measured by any existing methods, were used to test the effectiveness and accuracy of the proposed algorithm. A real-time experiment was conducted to verify the robustness of the proposed algorithm. The following are concluded:

1. The proposed algorithm can effectively reconstruct the weld pool surface. Reconstruction procedure only needs to iterate once since the matching coefficient after first iteration is smaller than the accuracy control threshold 1% for the both simulation and experiments.
2. Reconstruction accuracy is improved. The boundary reconstruction error in the simulation of the bench mark is 0.11%; the height reconstruction error at the maximum height is 0.024 %. The two reconstruction error parameters ARE (average reconstruction error) and MRE (average reconstruction error) are 0.06 mm and 0.21 mm. The boundary and height error in the convex mirror reconstruction experiment are 2.2 % and 0.13 %. ARE and MRE obtained are 0.03 mm and 0.13 mm. Compared with the previous works, the reconstruction accuracy is significantly improved.

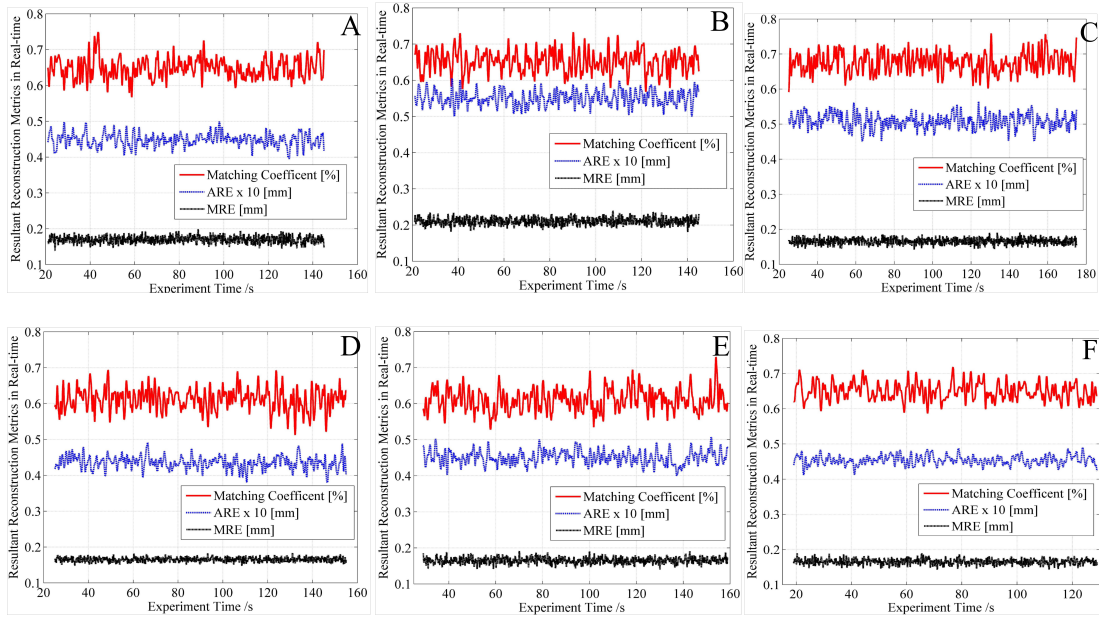


Figure 6.11: M_c , ARE and MRE of weld pool reconstruction as the helmet rotates to the boundary points along: A) Positive x-axis direction; B) Negative x-axis direction; C) Positive y-axis direction; D) Negative y-axis direction; E) Positive z-axis direction; and F) Negative z-axis direction.

3. The time cost for the reconstruction algorithm is 3.04 ms on average in the simulation and 3.22 ms on average obtained in the real-time welding experiment. The proposed algorithm is thus considered to be real-time for GTAW application.

4. The matching coefficient in the experiment varies from 0.45 % to 0.89%. The variation margin of ARE is 0.03 mm to 0.06 mm. Resultant MRE varies from 0.17 mm to 0.2 mm. The robustness of the proposed reconstruction algorithm is thus verified.

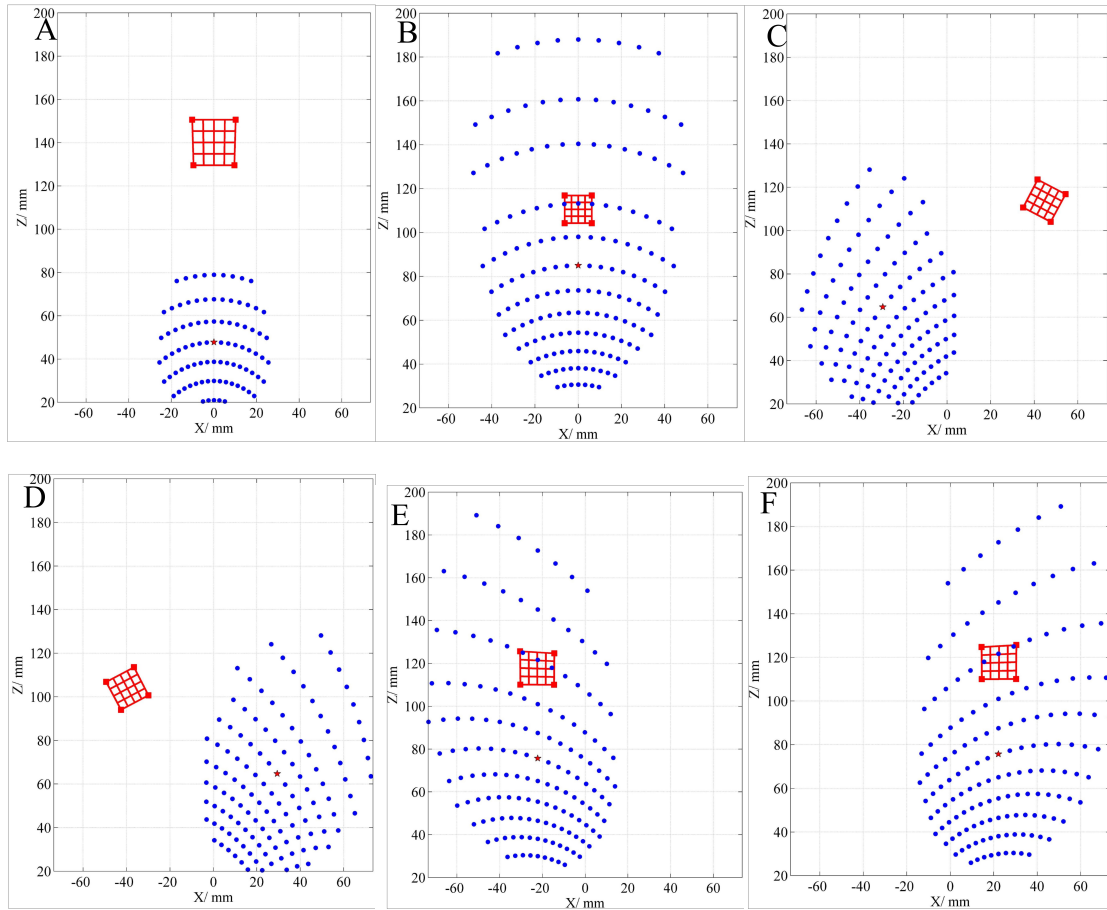


Figure 6.12: Corresponding results of image processing for images where torch rotates to the boundary positions of: A) Positive x-axis direction; B) Negative x-axis direction; C) Positive y-axis direction; D) Negative y-axis direction; E) Positive z-axis direction; and F) Negative z-axis direction.

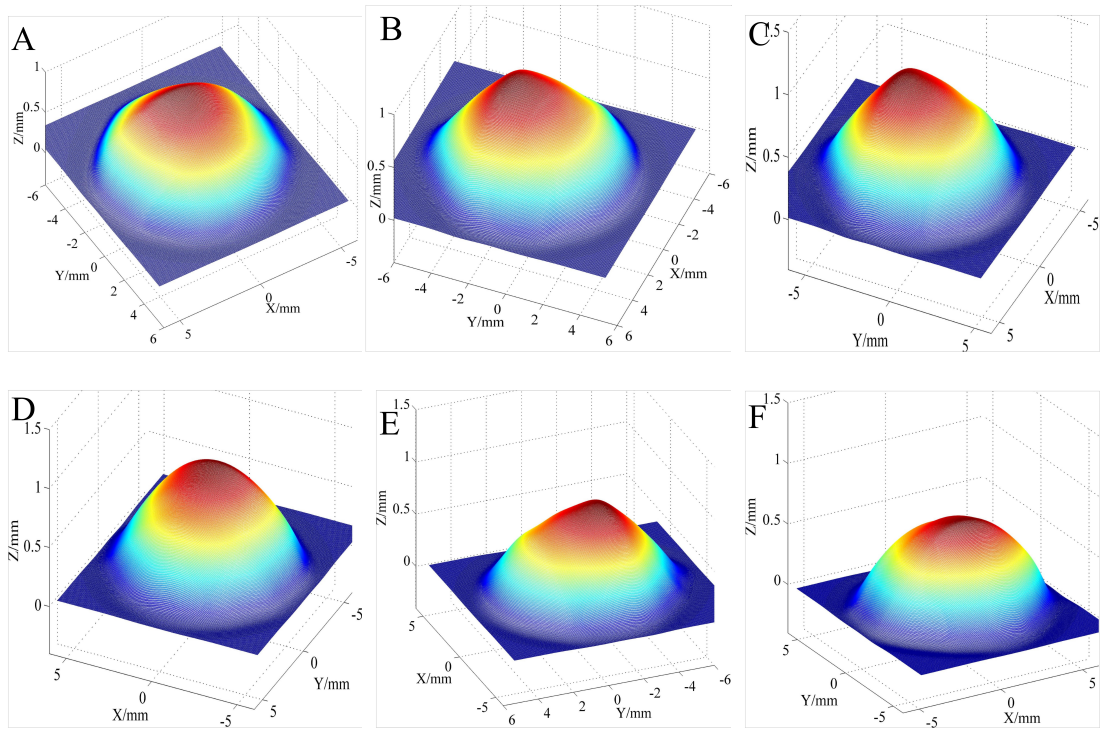


Figure 6.13: The reconstruction results of the spherical convex mirror as the torch rotates from the initial positions to the boundary points along: A) Positive x-axis direction; B) Negative x-axis direction; C) Positive y-axis direction; D) Negative y-axis direction; E) Positive z-axis direction; and F) Negative z-axis direction.

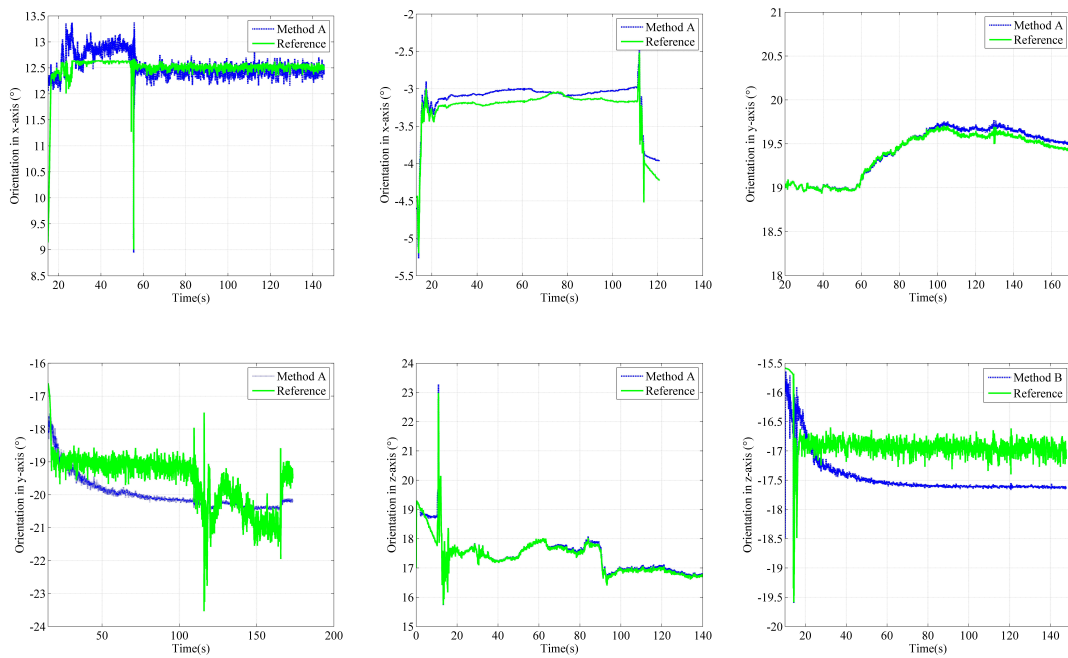


Figure 6.14: Orientation of the helmet where torch rotates from the initial positions to the boundary positions of: A) Positive x-axis direction; B) Negative x-axis direction; C) Positive y-axis direction; D) Negative y-axis direction; E) Positive z-axis direction; and F) Negative z-axis direction.

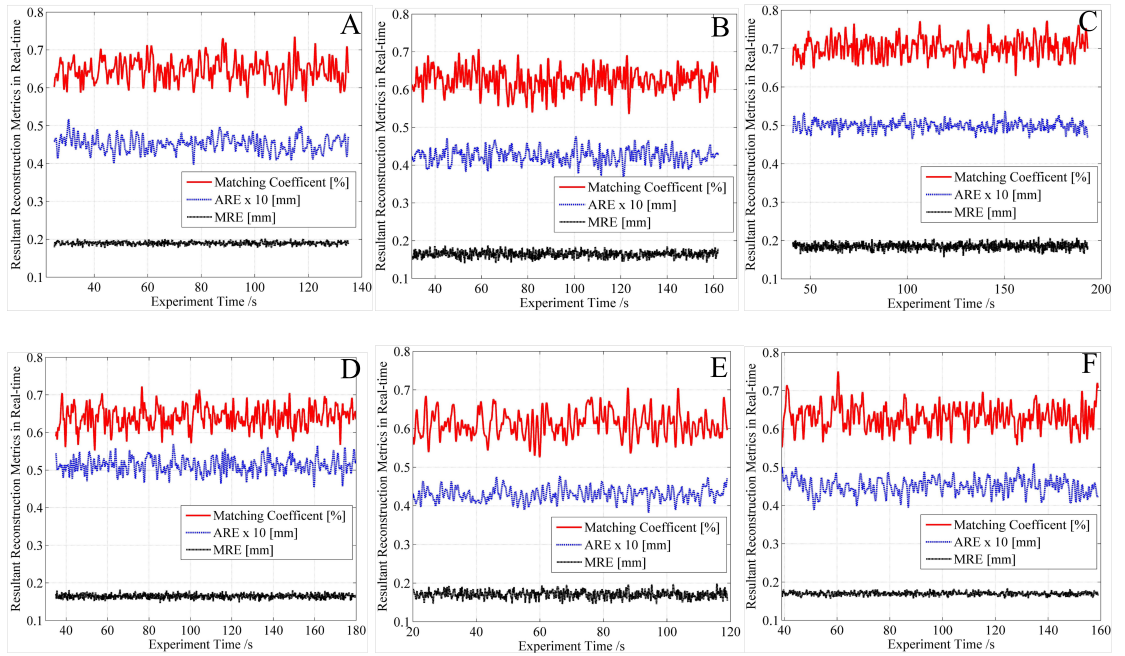


Figure 6.15: M_C , ARE and MRE of weld pool reconstruction as the torch rotates to the boundary points along: A) Positive x-axis direction; B) Negative x-axis direction; C) Positive y-axis direction; D) Negative y-axis direction; E) Positive z-axis direction; and F) Negative z-axis direction.

Chapter 7

Modeling of Human Welder Behavior

In modern manufacturing industry automated welding tends to be the mainstream, while manual welding is still irreplaceable in applications where human welders' experience and skills are critical for the services. Exploring the mechanism of welders' intelligent weld behavior would have broad and significant impacts in weld training, education, and the development of intelligent welding robots. As the first effort to study welders' behavior mechanism, the chapter focuses on two essential questions: 1) what information welders acquire through their observation of weld pool; 2) how human welders intelligently respond, i.e., adjust welding parameter(s), to the sensory information they obtain. In particular, the principle of welders' behavior is analyzed from modeling's point of view. To answer the first question, the weld pool surface is characterized to find the information which is able to indicate the weld status. It has been found that the length, width and convexity of weld pool surface provide an optimal estimation of the weld penetration. For the second question, the mechanism of a welder's behavior/adjustment on welding current as a response to the characteristic parameters is mathematically formulated. The dynamic models of the welder's behavior are obtained and analyzed.

7.1 Background and Purpose

In manual welding, skilled welders can appraise the penetration status through their observation of the weld pool and intelligently adjust the welding parameters (e.g., welding current, welding speed, arc length and torch orientation) accordingly in order to maintain a desired penetration. Because of the visual sensing capabilities and experience-based behavior, they are preferred over mechanized welding control systems in many manufacturing applications.

Training a welder to be qualified for critical operations (e.g., full penetration, vertical-up or overhead welds) typically require years of practice through acquired rule-of-thumb techniques. However, the manufacturing industry has been suffering from welder shortage for a long time ([129], [8]). Research on the mechanism of welders' experience-based weld behavior can be utilized to accelerate the welders' training. Exploring the mechanism

would be of a great help to reveal why the experienced welders can perform better weld than the inexperienced welders. That would definitely facilitate the welding education and verification of welders' qualifications in weld performance.

Human welders have physical limitations although their experience and skills are crucial in producing quality welds. Critical operations require them consistently concentrate on the welding process to react rapidly and accurately. Then fatigue and stress build up dramatically which would not only degrade their capabilities in daily operations but also cause long-term health risks. Further, inconsistent concentration during weld might adversely affect the assurance of the weld quality and the production cycle.

On the other hand, welding robots don't have the physical limitations. However, they are pre-programmed actuators lack of intelligence and adaption to different working environments. As a result, they are primarily used in well-controlled environments such as assembly lines for mass production. Given that manufacturing is moving towards more customized productions, intelligent welding robots that possess intelligence comparable to skilled welders but less physical restrictions will thus be one of the keys to maintaining a competitive manufacturing industry despite relatively high labor costs/wages. Therefore, the human welders' behavior should be interpreted, mechanized and transferred into welding robots. Using those intelligent robots to assist inexperienced welders, they could perform as well as those skilled welders. Furthermore, those robots could release human welders working on critical applications in harsh/health-risk welding environments, such as the commercial nuclear plants explored in the 2011 Japan earthquake[112].

Mathematically formulating welders' behavior is so far still a challenging task. This is mainly because a human welder, as an intelligent welding controller, makes decisions primarily based on past learned experience which might not involve a fundamental understanding of the laws of physics. Further, explaining this knowledge involving precise visual cues to others is also difficult. Studying welders' experience-based behavior involves two fundamental questions: 1) *What is the information acquired by welders from weld pool capable of estimating weld status?* 2) *How do welders intelligently respond to the obtained information by adjusting the welding parameters such that a desired weld status can be achieved/maintained?*

Numerous studies have been conducted with different sensing techniques including pool oscillation([70], [97], [141]), ultrasound ([50, 57]), infrared sensing([29], [91], [18], [33]). Various types of information about weld pool have been extracted and interpreted to describe the welding process. Yet, the first fundamental question has not been explicitly answered. The weld pool geometry is believed to provide valuable insights into the welding status. Important information such as weld defects and penetration are contained in the surface deformation of the weld pool([80, 103]). It also has been studied in ([158], [71], [73], [164], [16]) as a means of measuring and controlling the weld joint penetration. A recent study has suggested the 3D weld pool geometry can estimate weld penetration measured by the backside weld bead width with an acceptable accuracy[146].

In order to answer the second question, the mechanism of welders' behavior should be modeled. The modeling of human controller dynamics has been extensively studied since 1940s. Great progresses had been achieved in the 1960s and 1970s ([48], [87], [67]). Nonlinear methods were introduced to model human operators by neural networks, neuro-fuzzy and adaptive models ([28], [128], [64], [35], [41]). However, instead of taking real industrial processes, most of the literature took bench marks, such as the pendulum, joystick, as control

objects. Further, those models tend to be too complex to be applied to the practical manufacturing. Therefore, exploring welders' behavior remains challenging. A human welder's adjustment of welding current in response to the 3D weld pool geometry has been dynamically modeled and analyzed([149, 150]), and the resultant model has been further used in a robotic GTAW as a controller for a consistent full penetration[148]. Other than those work, there is no literature published in this particular area.

7.2 Principle of Human Welder Behavior

In this section, the principle of human welders' behavior in weld operations is mathematically formulated. The diagram of human welders' behavior is shown in Figure. 7.1. In the figure, I is the welding input, $r(\cdot)$ is the welding process, Ω is the direct information acquired by welders, w and v are the disturbance, Ψ is the indirect information of weld pool, Φ , $\hat{\Phi}$ and Φ^* are the current, next instant and desired status of the weld process. Ξ is the welding requirement and ΔI is the adjustment of welding parameters. $\eta(\cdot)$, $v(\cdot)$, and $\omega(\cdot)$ are mapping processes.

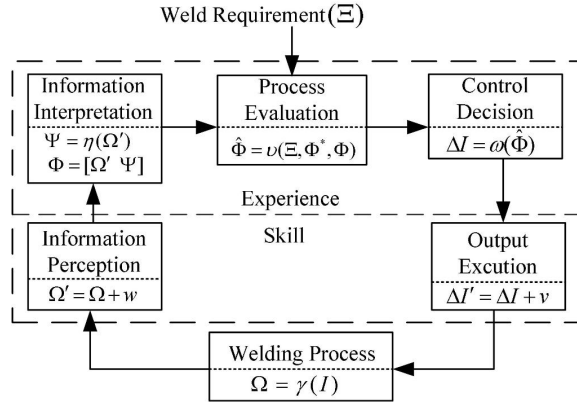


Figure 7.1: Illustration of an interpretation of human welders' behavior

Given a certain weld requirement, e.g., full penetration, a welder starts weld with an estimated initial input I including welding current, speed, etc. It is generated based on the welder's experience. If well trained, the welder may generate a better guess of weld input which might exactly correspond to the required full penetration.

1. Information Perception After the initial input, the welder perceives necessary direct information Ω' from the weld pool. This sensing process is however perturbed, in a sense of mathematical modeling, by a noise w , e.g., an independent white noise. The noise represents the randomness of the welder. The accuracy of the sensing process as measured by w reflects the welder's perception skill. Ω is the actual direct information.

2. Information Interpretation The welder may derive some indirect information (Ψ) from the direct information. The deriving process $\eta(\cdot)$ is task-oriented and experience based which may involve taking the derivative, the integral of the direct information or the prediction of the information in the future [41]. The instant weld status of Φ obtained by the welder might contain both the direct and indirect information.

3. Process evaluation The process evaluation is the decision-making process where the welder first maps/correlates the weld requirement (Ξ) to the desired weld status (Φ^*), then compares Φ^* with the current weld status Φ , and finally decides the next weld status $\hat{\Phi}$. A welder is believed to make an optimal or a semi-optimal adjustment in weld parameters to minimize the error between the current and the desired weld status, provided that he/she is well motivated. Therefore, $\hat{\Phi}$ can be considered the optimal status for the next instant through evaluation process, $v(\cdot)$ in terms of the welder's capability and experience.

4. Control Decision The welder correlates $\hat{\Phi}$ to the weld input adjustment ΔI such that the next weld status can be achieved by the weld input $I + \Delta I$.

5. Output execution The output execution may be considered to be perturbed by a white noise v , which reflects the welder's maneuver skill.

It should be noted that the human welders' behavior depends on their skills and experiences. For the five elements of welders' behavior in both skill and experience levels in Figure. 7.1, there might be difference in each individual element in various extents for different welders. However, it is believed that their behavior has an identical result for the combination of the five elements based on the fact that for the one welding process, different skilled welders can produce almost the same weld which meets the same weld requirements. Therefore, there exists a unified correlation $F(\cdot)$ connecting the direct information Ω with the welder's adjustment ΔI :

$$\Delta I = F(\Omega) \tag{7.1}$$

This study focuses the mechanism how a human welder produces the adjustment of welding parameter (ΔI) based on the extracted information Ω for a consistent full penetration. It is known a skilled welder can assure the desired full penetration by adjusting welding input based on the observation of weld pool. As mentioned in last section, the weld pool geometry is thought by many as the major source to indicate the status of the welding process. Moreover, it also couples with almost all the other sensory signals of welding process, such as arc length (voltage), arc light intensity, temperature, etc. A human welder can easily acquire the geometric information of weld pool. Therefore, it is reasonably believed that a human welder can acquire adequate information from the geometry of weld pool surface to control the weld penetration.

7.3 Weld Pool Characterization

The objective of this section is to answer the first question in Section 7.1: *What information the welder acquires from the weld pool to estimate the weld status.* Although even the welder cannot tell what she/he is seeing, it is reasonable to believe the information acquired by the welder should be a set of parameters of the weld pool surface which can provide an optimal estimation of the weld penetration. To this end, five candidates parameters are proposed to predict the penetration measured by the backside weld bead width, i.e., the weld pool length (L), width (W), area (A), interception area (I) and convexity (C). The definitions of the parameters are detailed as following:

1. The weld pool length The description of the weld pool boundary adopted in this study is from literature [157]. The corresponding parametric model is given below:

$$y_r = \pm ax_r^b(1 - x_r) \quad (7.2)$$

where a and b are the model parameters, (x_r, y_r) are the coordinates of the pool boundary in the normalized coordinate system as shown in Figure. 7.2. The x, y coordinates are calculated as: $x_r = x/L, y_r = y/L$, L is the length of the weld pool, which is the distance from the head to the tail of the weld pool.

2. The weld pool width The width of the weld pool can be calculated as shown in Equation. 7.3.

$$w = w_r \times L = 2aL \left[\frac{b}{1+b} \right]^b \left(\frac{b}{1+b} \right) \quad (7.3)$$

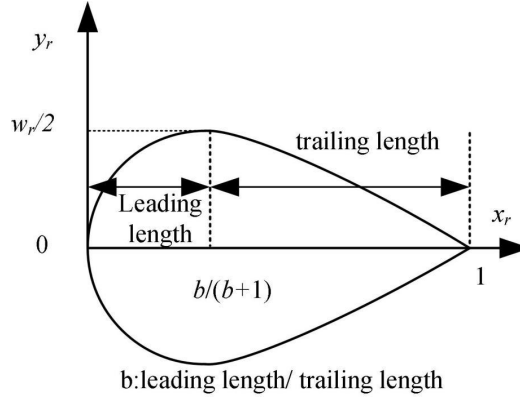


Figure 7.2: Illustration of the weld pool boundary model

3. The weld pool area The weld pool area A is the area of weld pool in the oxy plane:

$$A = 2L^2 \int_0^1 ax_r^b(1 - x_r)dx_r \quad (7.4)$$

4. The weld pool interception area The interception area I is the cross section area of weld pool in the oyz plane, shown in Figure. 7.3:

$$I = \int_{y_0}^{L+y_0} (z(y) - z_0) dy \quad (7.5)$$

where y_0 is the y coordinate of the weld pool front edge and z_0 is the z coordinate of the work-piece surface.

5. The weld pool convexity The of the weld pool surface is defined as the average height of the weld pool surface above the work piece along x -axis:

$$C = I/L \quad (7.6)$$

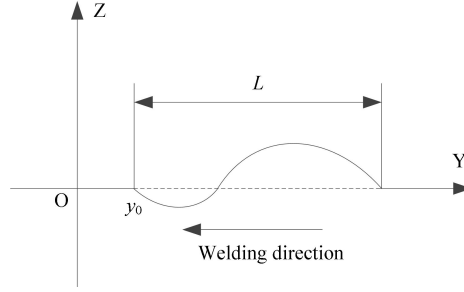


Figure 7.3: Schematic of the cross section of weld pool in the oyz plane

7.3.1 Estimation of weld penetration with characteristic parameters

This subsection concentrates on the relationship of the backside bead width, the primary measurement of the weld penetration, with the proposed candidate characteristic parameters in steady state. Since it is nearly impossible to exactly obtain this relationship theoretically due to the complexity of the problem, statistical approaches are adopted here.

Figure. 7.4 shows the 3D weld pool surface parameters measured from all 36 experiments conducted in this subsection with the welding parameters detailed in Table 4.3. Since the 3D weld pool surface has been real-time reconstructed in Chapter 6, those candidate parameters can also be calculated during the welding experiments. The backside bead width w_b is measured after the parameters from the cross section of the weld bead as shown in Figure. 7.5.

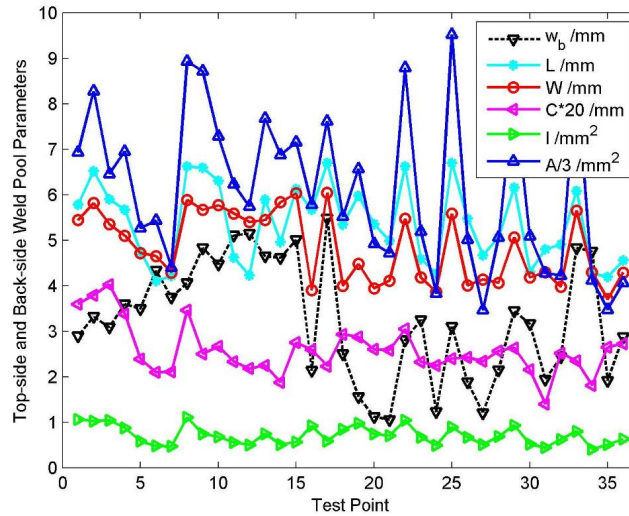


Figure 7.4: Measured 3D weld pool surface parameters from 36 experiments. The values of the convexity and area have been adjusted for illustration purpose

One may notice that all the intercepted area and convexity are positive. While they could be negative under a greater arc pressure and greater penetration, the moderate current/arc pressure and penetration in this study resulted in the weld pool surface convex rather than concave. Hence, the two variables describing the overall shape of the weld pool surface are both positive.



Figure 7.5: Cross-section of full-penetration weld, the current is 56 A, arc length is 4 mm, and welding speed is 1 mm/s

Least-squares method is widely used for the model parameter estimation [14]. Consider the following linear model:

$$\hat{w}_b(k) = \alpha_0 + \sum_{j=1}^n \alpha_j \chi_j(k) \quad (7.7)$$

where $\hat{w}_b(k)$ is estimation of the measured backside weld bead width $w_b(k)$ at the k th experiment, $\alpha_j (j = 0, 1, \dots, n)$ are the model parameters to be estimated, and $\chi_j(k)$ are the regressive factors, which consist of the possible candidate characteristic parameters. The structure determination, i.e., how to choose the regressive factors χ_j , is based on the F-test [98].

The estimation using 1 parameter to predict the backside weld bead width is first performed using the model in Equation. 7.7. Then 2 candidate parameters are utilized as the regression factors in the model. Finally the estimation using 3 candidate parameters is conducted. Then F-test is performed to find a trade-off between the accuracy and the complexity of the model. The estimation results of the 5 candidate parameters are presented in Table 7.1.

Estimation variance $\hat{\sigma}^2$ are used here to evaluate the accuracy of the estimation models:

$$\hat{\sigma}^2 = \frac{RSS}{N} = \frac{\sum_{k=1}^N (\hat{w}_b(k) - w_b(k))^2}{N} \quad (7.8)$$

where RSS is the residual sum of squares, N is the number of the test points, $\hat{\sigma}$ is the estimation deviation.

Although the width (W) provides the best model to estimate w_b in all the 1-parameter models in terms to the large r and small $\hat{\sigma}^2$, the width itself cannot provide sufficient information about the weld penetration. It has been found in [156] that the pool width is often not very sensitive to variations in welding conditions or changes in welding parameters, which may significantly alter the weld penetration.

The estimation using I is similar with that using C in terms to the nearly identical $\hat{\sigma}^2$ and r . I is also coupled with L according to its definition. To this end, C is be used instead of I

Table 7.1: Characteristic parameters estimation results

Parameters ^a	$\hat{\sigma}^2$	r^b	$e_{average}^c$	e_{max}^d	Estimation model
W	0.73	0.75	0.70	2.19	$w_b = 1.27W - 2.88$
A	1.24	0.51	0.95	2.27	$w_b = 0.13A + 0.90$
L	1.60	0.21	1.09	2.25	$w_b = 0.31L + 1.57$
I	1.64	0.13	1.07	2.22	$w_b = -0.82I + 3.83$
C	1.64	0.12	1.08	2.20	$w_b = -5.98C + 4.02$
$W + L$	0.49	0.84	0.57	1.66	$w_b = 1.83W - 0.77L - 1.51$
$W + C$	0.53	0.82	0.59	1.62	$w_b = 1.44W - 17.26C - 1.47$
$A + C$	1.04	0.61	0.84	1.98	$w_b = 0.16A - 17.85C + 2.55$
$W + L + C$	0.43	0.86	0.52	1.44	$w_b = 1.79W - 0.57L - 10.81C - 0.99$

^aWidth: W , Area: A , Length: L , Interception area: I , Convexity: C

^bCorrelation coefficient r measures the strength and the direction of a linear relationship between input and output variables. A large r indicates high estimation accuracy.

^c $e_{average}$ is the average estimation error in the experiments.

^d e_{max} is the maximum estimation error in the experiments.

in the 2 and 3 parameters estimation. Therefore, the following possible 2-parameter model are proposed: width and length, width and convexity, as well as area and convexity. Here the width and area, length and area are not considered, because of the coupling of area and width / length, and only the combination of the length, width and convexity is considered in 3-parameter characterization.

It can be found the estimation using the width, length, and convexity, as shown in Table 7.1, is better than all the 1-parameter and 2-parameter models in estimating w_b . The estimation result at each experiment is presented Figure. 7.6.

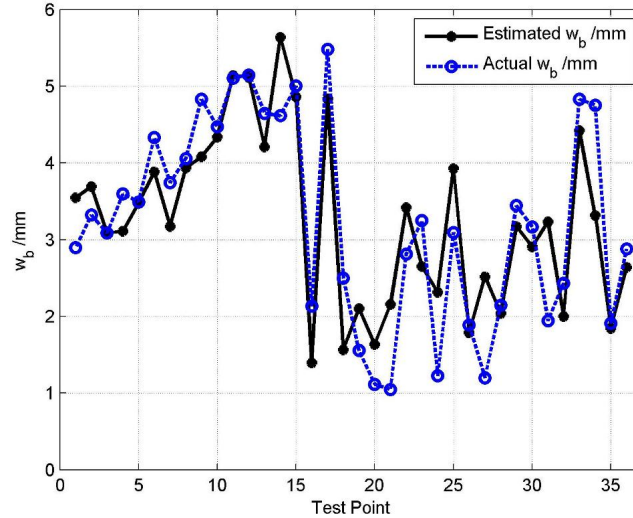


Figure 7.6: 3-parameter model estimation of backside weld bead using the width, length, and convexity

In the 3-parameter model, the backside bead width (w_b) will increase by 1.79 mm when the weld pool width (W) increases by 1 mm. The coefficient of the width larger than 1 is because the full penetration is not established until W reaches a certain value but w_b would approach W when a burn-through is being reached. The difference in magnitude of

coefficients for the width (1.79) and length (−0.57) indicates that the width has a stronger effect on the backside bead width than length. This effect difference is understandable because when the welding current increases, the length and width of the weld pool should both increase but the length would increase faster than the width due to the heat transfer in the transverse direction is faster than that along the longitudinal direction.

While the positive effect of the width is easily understood, the negative effect of the length needs an explanation. To this end, one may imagine what happens if the welding speed increases while keeping the heat input unchanged by increasing the current. Because the arc pressure increases with the square of the current, the weld joint penetration and the weld pool width would not tend to reduce despite the increase in the welding speed. On the other hand, the weld pool would tend to elongate because of the increased welding speed. Hence, the effect of the length on the weld joint penetration should be negative when the heat input is unchanged. In case the heat input increases under the same speed, the weld pool would increase in all directions. Since the magnitude of the coefficient for the width is approximately three times that for the length, the net effects from the increases in the width and length would thus be positive, i.e., to increase the weld joint penetration.

From Figure. 7.4, the range of the convexity in the experimental is from 0.05 mm to 0.2 mm, and the magnitude of the coefficient for the convexity is 10.81 in Table 7.1. Thus the contribution of the convexity on the variation of w_b is about 1.65 mm. The coefficient is negative, indicating when the convexity is smaller the back-side bead width is greater. This is understandable because a wider backside weld pool allows more liquid metal to move toward the back side such that the convexity reduces.

All three weld pool surface parameters are significant in characterizing the weld pool surface for their capability in estimating the weld penetration. However, as one can observe in Table 7.1, the estimation accuracy of the 2-parameter model using the width and length is close to that of the 3-parameter model. To this end, F-test is utilized here to verify if the increase in accuracy is significant enough to choose the complex model, the 3-parameter model, over the simpler model. F-value is given by

$$F = \left(\frac{RSS_1 - RSS_2}{P_2 - P_1} \right) / \left(\frac{RSS_2}{N - P_2} \right) \quad (7.9)$$

where RSS_i and P_i the residual sum of squares and number of regression factors/parameters of model i ($i = 1, 2$); N is the number of the samples that is 36 in this study. For a confidence level of 5%, the critical value of F distribution is 4.17. If the F value calculated using Equation. 7.9 is larger than 4.17, the reduction in the modeling error due to the increase in the model parameters is significant such that the complex model is selected over the simpler model.

The calculated F value for the comparison between the 2-parameter model and the 3-parameter model is 4.60, larger than the critical value 4.17. That means the 3-parameter model provides an optimal estimation of the backside weld bead width.

As mentioned in last section, gaining welding experience needs countless hours of practice while explaining it to others with clear visual cue is also difficult. The 3-parameter models presents a quantitative relation between front-side weld pool dimension and the weld penetration. This is a significant advantage that can be utilized in welding training/education.

Different welders may evaluate penetration using different weld pool information. The information might not be exact the length, width and convexity of the weld pool. However, there should be a certain correlation ($g(\cdot)$) between the acquired information (Ω) and the three characteristic parameters given that both of them can be used to estimate the weld penetration:

$$\Omega = g(W, L, C) \quad (7.10)$$

The human welder's behavior (Equation. 7.1) can be rewritten in a modeling point of view as:

$$\Delta I = F(\Omega) = F(g(W, L, C)) = H(W, L, C) \quad (7.11)$$

Therefore, modeling human welders' behavior is to develop a dynamic model correlates the adjustments of the welding parameters (ΔI) to the three characteristic parameters (W, L, C).

7.4 Modeling Experiments

The section focus on exploring the mechanism of the human welder's behavior such that the second questioned, *how a human welder responds to the characteristic parameters*, can be answered. It has been well established in the last section that, from modeling's point of view, human welders can be considered to acquire the weld pool's length, width and convexity to control the weld penetration. To this end, dynamic models of a novice human welder's adjustment on the welding current in response to the observed 3D weld pool surface during the full penetration process are developed in this section.

The models' output is the adjustment of the welding current, the primary parameter used by welding robots to control the welding process. Such models which present the mechanized welder's wisdom are convenient to be applied in robotic welding process. Modeling welder's adjustments of other parameters, such as the arc length, welding speed and torch orientation according to the weld pool surface is the authors' future work and is beyond the scope of this first study of this kind. A novice welder is studied first because the authors intend to study and follow the development of welder skills and responses.

7.4.1 Experiment set-up

In this first study on human welder behavior, the human welder only adjusts the welding current based on his observation on the 3D weld pool surface. Other parameters including the welding speed, arc length, torch orientation that may be adjusted in typical manual welding processes are not considered. To this end, an experiment set-up illustrated in Figure. 7.7 is proposed. The structured light laser pattern, Lasiris SNF-519 \times 0.77-685-50, projects a 19×19 laser dot matrix onto the area under the torch electrode and covers the whole possible weld pool region. During GTAW, the liquid weld pool with a mirror-like specular surface reflects the incident laser pattern. Since the surface of the solid base metal is not specular, only the portion of the laser pattern projected on the weld pool is reflected.

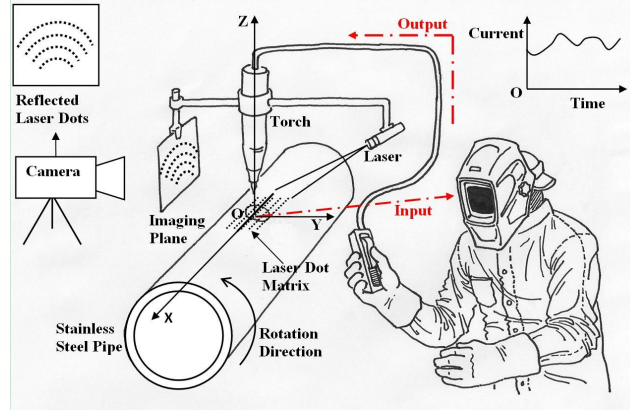


Figure 7.7: Demonstration of a manual control system of GTAW process

An imaging plane, made by a sheet of glass attached with a piece of paper, is installed with a distance of 100 mm approximately from the electrode. The reflected dots are intercepted by the imaging plane, forming an image of the reflection pattern. In order to capture the reflection pattern, a camera (Pointgrey Flea 3 FL3-FW-03S1C-C) is located behind the imaging plane. The captured image is 8-bit monochrome with a 640×480 resolution. A band-pass filter of 20 nm band-width centered at a wavelength of 685 nm is installed in the camera to block the majority of the arc radiation. A computer connects with the camera using a 9-pin 1394b interface.

The pipe rotates during welding while the torch orientation, imaging plane, laser projector, and camera are stationary. The rotation speed and the distance from the tungsten tip to the pipe surface are controlled by the computer.

Based on the reflection of the dot matrix pattern, a 3D weld pool surface can be reconstructed using the proposed image processing and reconstruction algorithms detailed in Chapter 4 and Chapter 6. The characteristic parameters of the weld pool surface can thus be obtained.

The human welder observes the weld pool and adjusts the welding current accordingly using an amperage remote control installed on the torch for a desired penetration status. The use of the current remote controller shown in the figure is for demonstration purposes. The actual controller is a thumb turn knob on the torch which adjusts the current setting for the power supply.

7.4.2 Dynamic experiment design

The vision-based sensing system in Figure. 7.7 is capable of measuring the weld pool surface and calculating the characteristic parameters in real-time. Further, the responses the human welder made to the weld pool surface also can be recorded simultaneously. A model can be established to correlate the responses to the characteristic parameters. However, a successful identification of a meaningful model requires appropriate preparations.

1. Time interval and delay of the dynamic experiment The response of the human welder is expected to be a dynamic process. That is, the welder may make the adjustments

on the welding parameters not only based on the weld pool surface he just observed but also those he observed earlier. Further, it is unlikely that the welder may respond to the change in the weld pool surface immediately. There must be a time delay in his response. As a result, the time intervals should be determined within which the characteristic parameters should be included in the model to test their significance for their effect on the response. It has been found that the average time interval obtained from the conducted step response experiments is 8.7seconds, and the delay of the welder response varies from 1 to 3 seconds[149].

2. Sampling frequency Human welders always scan weld pool with a certain frequency during the welding process. Thus, it is reasonable to apply a discrete model to identify the human welder's behavior. To determine the data acquisition frequency, the scan frequency of human welder can be considered as a reference. In this study, the data acquisition frequency is 2 Hz.

3. Identification experiment In order to model the dynamics of the welder's behavior, the weld pool surface should be designed to vary with enough magnitude and frequency span. Ideally, the characteristic parameters should be random signals with sufficient large values and high orders. However the variation of a weld pool cannot be generated in a designed random form. Instead, the random signals of the welding speed are applied to the process in this study, and the weld pool geometry is expected to vary in a random manner. Therefore, for identifying the welder's behavior, dynamic experiments are designed with random welding speed variations in which 5 welding speeds are used: 1 mm/s, 1.25 mm/s, 1.5 mm/s, 1.75 mm/s and 2.0 mm/s. Hence, for each experiment, the welding speed is randomly changed among the 5 welding speeds. The average transition time is 8.7 seconds including the time delay of the welder, the welder's response time and the settling time of the weld pool. In this sense, the speed change interval should be shorter than the transition time, since it is not necessary for each speed to last till the weld pool fully resumes its steady state. Therefore, the time interval for each change is set to be 6 seconds.

Each dynamic experiment has two periods: the constant speed period and random speed period, which use a constant and a randomly changing welding speed respectively. The purpose of the constant speed period is to allow the human welder to bring the welding process to the desired full penetration and the random speed period is to produce the dynamic weld pool for the human welder to respond. The duration of the constant speed period is set at 18 seconds. The duration for the random speed period is 120 seconds. The arc length is set at the same constant in each experiment in [2mm, 5mm], i.e., 2 mm, 3 mm, 4 mm and 5 mm.

4. Model structure Two discrete model structures are proposed:

First, according to the principle of human welder's behavior in Section 7.2, a welder is believed to control the weld penetration such that the characteristic parameters ($[w, l, c]^l$) approaches the desired ones ($[w^*, l^*, c^*]$). Generally, a human welder should make the adjustment on welding current (Δi) based on not only the newest observation but also the previous observations. Moreover, there should be a certain time period of delay for the welder to respond. Therefore, the model of the welder's behavior should be:

$$\Delta i_k = \sum_{j=1}^M (g_j^w (w_{k-d-j} - w^*) + g_j^l (l_{k-d-j} - l^*) + g_j^c (c_{k-d-j} - c^*)) \quad (7.12)$$

Δi_k is the current difference, i.e., $\Delta i_k = i_k - i_{k-1}$ at k instant, g_j^w, g_j^l, g_j^c ($j = 1, 2, \dots, M$), are the coefficients corresponding to the three characteristic parameters, M is the order of the model, and d is the delay. Since w^*, l^* , and c^* are constants, model Equation. 7.12 can be rewritten as:

$$\Delta i_k = \sum_{j=1}^M \left(g_j^w w_{k-d-j} + g_j^l l_{k-d-j} + g_j^c c_{k-d-j} \right) + \Gamma \quad (7.13)$$

where $\Gamma = -\sum_{j=1}^M \left(g_j^w w^* + g_j^l l^* + g_j^c c^* \right)$

Second, the human welder's behavior model can also be written as:

$$\Delta i_k = \sum_{h=1}^{M_1} a_h \Delta i_{k-h} + \sum_{j=1}^{M_2} \left(b_j^w w_{k-d-j} + b_j^l l_{k-d-j} + b_j^c c_{k-d-j} \right) \quad (7.14)$$

The inclusion of $\Delta i_{k-1}, \dots, \Delta i_{k-M_1}$ into the model basically introduces the welder's previous actions. If this inclusion can better predict the welder's adjustments on the welding current, it would suggest that the welder not only depends on the weld pool surface but also on his previous actions to adjust the welding current.

7.5 Experimental Results and Analysis

7.5.1 Dynamic experiments and modeling results

The identification experiments designed in the last subsection are conducted. The data including the length, width, and convexity of the weld pool and the welder's current adjustment is recorded simultaneously at a sampling frequency of 2 Hz. The recorded data from one of the experiments is used to model the welder's behavior. The data from all other experiments are applied to verify the accuracy of the identified model.

The recorded data from the identification experiment is shown in Figure. 7.8. From the figure, it can be observed that the weld pool dimension varied severely which indicates the welder did not adjust the current fast and accurately enough to compensate for the effect of the welding speed on the weld penetration. It needs to point out that this is of course not required because no any skilled welders may control the penetration consistent under the designed substantial welding speed changes. The variation of the weld pool geometry is produced on purpose in order to identify how the welder responds to the dynamic weld pool surface.

To model the welder's behavior/adjustment, Least-square method is applied to decide the coefficients in the model, i.e., g_j^w, g_j^l, g_j^c and Γ in Equation. 7.13, $a(h)$ and b_j^w, b_j^l, b_j^c in Equation. 7.14. The F-test is used to decide the complexity of the model, i.e., to determine the value of M in Equation. 7.13, M_1 and M_2 in Equation. 7.14. Based on the two model structures in the last subsection, two corresponding dynamic models are obtained. The estimation deviation ($\hat{\sigma}$) in Equation. 7.8, and correlation coefficient (r) are the two criteria to evaluate the accuracy of the two models. The resultant models are listed in

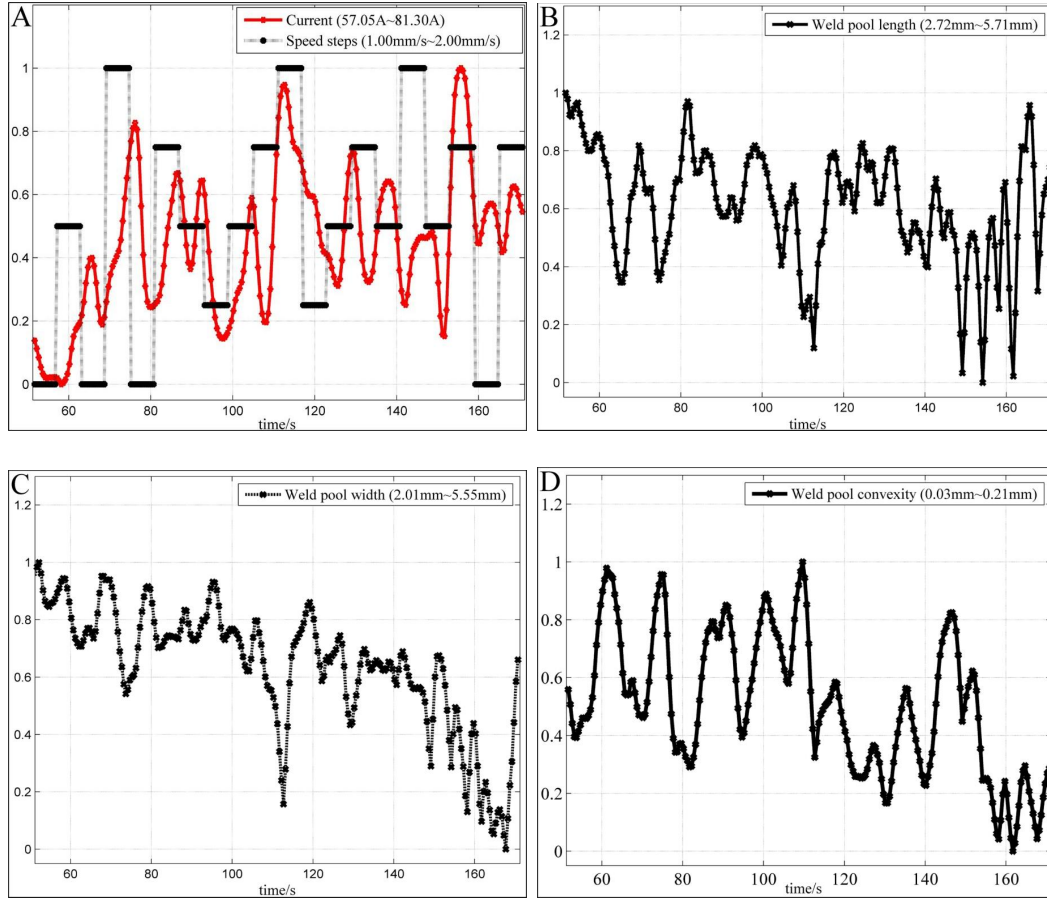


Figure 7.8: The random speed period in the identification experiment. (a) current and speed; (b) length; (c) width; (d) convexity. The range for each variable is given in each plot and corresponds to $[0, 1]$ in the normalized scale.

Table 7.2. The estimations of the welding current using the two models are shown in Figure. 7.9. Since the sampling frequency is 2 Hz, Model 1 shows that human welder has 0.5 second delay, and Model 2 indicates the delay is 1 second. Both of the models contain the characteristic parameter at instant $k - 6$. That means the human welder is capable of extracting the characteristics from the weld pool surfaces in the previous 3 second period. Model 2 indicates that the human welder's current adjustment also relates the previous adjustments in the last 1 second period.

It can be observed in Figure. 7.9, that Model 2 predicts the human welder's response well than Model 1. One can found in Table 7.2, Model 2 obtains lower standard deviation ($\hat{\sigma}$) and higher correlation coefficient (r) than Model 1. That indicates the human welder adjusts the current based on both the previous weld pool surfaces and his previous actions.

However, it is can be observed in Figure. 7.9 that Model 2 does not estimate the current adjustment well in a few steps which contains the welder's actions in high frequency. Since the experiment is conducted by a newly trained welder who may frequently over-reacts/under-reacts during the operation, it is understandable that the steep current adjustments cannot, and should not, be fit well using the model. A model can possibly estimate better a skilled

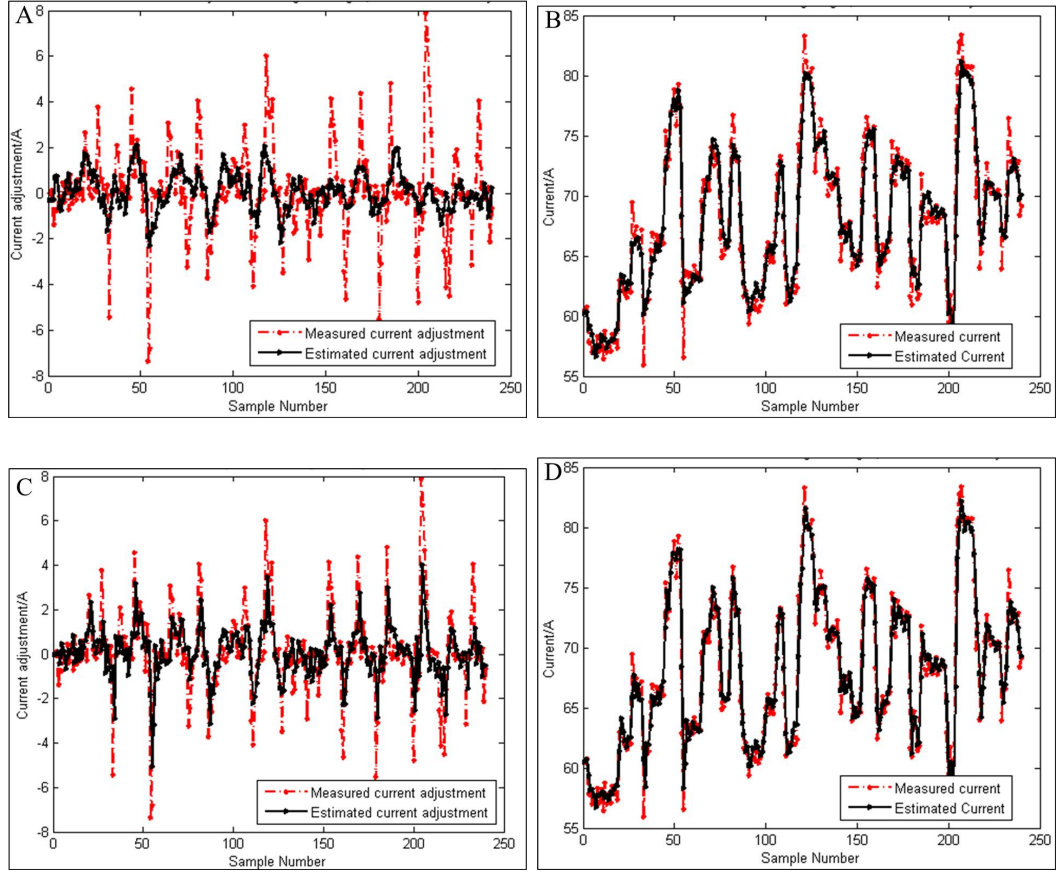


Figure 7.9: Comparison of estimated current and current adjustment using the two models in Table 7.2. (a) and (b) shows the estimation results using the Model 1, and the estimation results of Model 2 are shown in (c) and (d).

human welder's behavior with less sudden current changes in the welding process.

Model 2 can be further analyzed by exploring the following properties:

1. **Steady state equation** The steady state equation of Model 2 is:

$$\Delta I = -0.025W - 0.007L + 1.717C \quad (7.15)$$

where ΔI is the current adjustment Δi in steady state, and W , L , and C are the width, length and convexity of the weld pool in steady state. Ideally, the desired penetration is achieved such that ΔI is 0, and the W , L , and C are the desired characteristic parameters.

According to Equation. 7.15, the welder tends to reduce the current as the length or width grows, and increases the current as the convexity of the weld pool rises in steady state. Growth of length width means the growth of the weld pool, while increase in convexity indicates decrease of the weld pool size. The human welder intends to maintain a consistent/desired size of the weld pool such that a desired full penetration (w_b^*) can be achieved, therefore he reduces or increases the current to prevent the weld pool bigger or smaller than the desired weld pool dimension($[W, L, C]$).

Table 7.2: Resultant dynamic models of human welder's behavior

Model ID	$\hat{\sigma}$	r	Model
Model 1	1.71	0.45	$\Delta i_k = -0.89w_{k-3} + 0.97w_{k-4} + 0.54w_{k-5} - 0.63w_{k-6}$ $- 1.31l_{k-2} + 2.47l_{k-3} - 3.17l_{k-4} + 1.89l_{k-5} + 55.24c_{k-2}$ $- 63.44c_{k-3} + 90.9c_{k-4} - 96.15c_{k-5} + 17.56c_{k-6} + 0.21$
Model 2	1.57	0.57	$\Delta i_k - 0.47\Delta i_{k-1} + 0.14\Delta i_{k-2} = -1.27w_{k-3} + 1.77w_{k-4}$ $+ 0.09w_{k-5} - 0.61w_{k-6} + 0.61l_{k-3} - 2.23l_{k-4} + 1.61l_{k-5}$ $+ 30.37c_{k-3} + 19.64c_{k-4} - 67.64c_{k-5} + 18.78c_{k-6}$

2. **Step response** A step response simulation in which one of the three characteristic parameters suddenly increases 1 mm while other two remain constant shows how the human welder adjusts the current in response to the suddenly increase. Figure. 7.10 shows the results of the simulations.

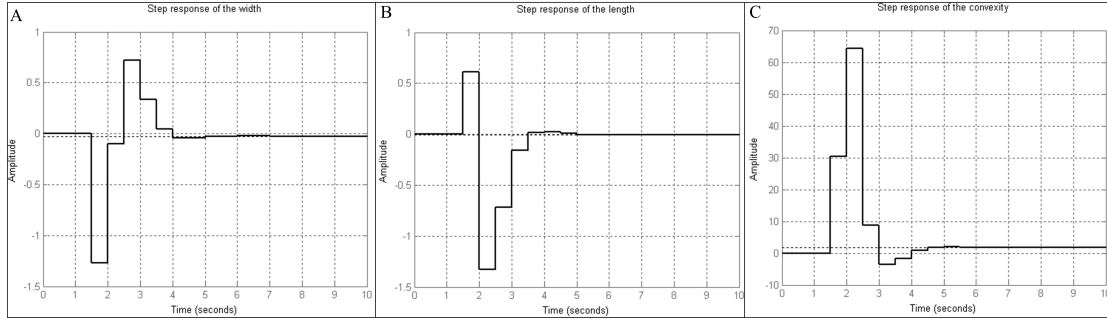


Figure 7.10: Step responses of the human welder model which are step responses for (a) the width, (b) the length and (c) the convexity

Large adjustment oscillations are shown in the three step responses. This is because, as discussed in the steady state equation part, the welder is newly trained who might not be able to handle well, i.e., adjust welding current accordingly and appropriately, to a sudden change of weld pool geometry. It is suspected that the model for a skilled/experienced welder would exhibit much less significant oscillations.

Because the model output is Δi , all the step responses settle down back to zero approximately. The integration of the step response gives the net change in the welding current due to the step change in one of the characteristic parameters. In the figure, the integration of the length and width are negative, and it is positive for the convexity. That implies that the welder reduces the current as a response to an increased weld pool length and width or a reduced convexity, which coincide with the analysis for the steady state equation.

7.5.2 Model verification

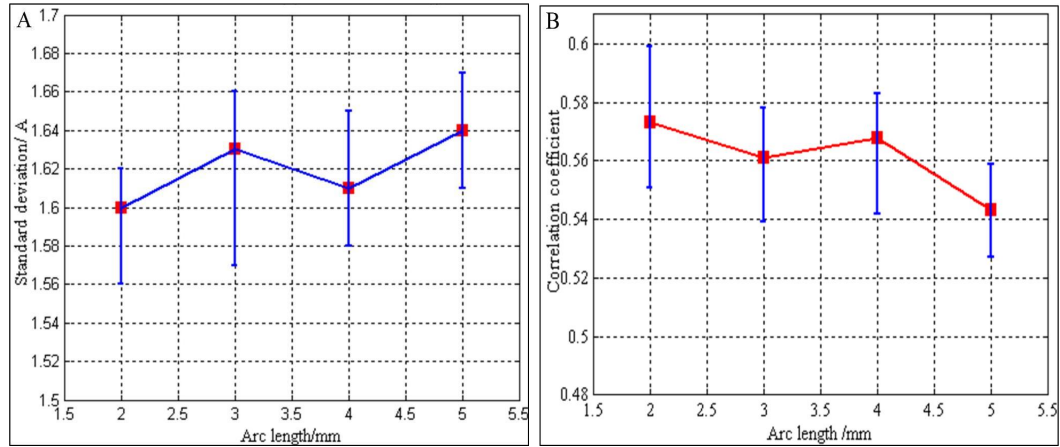


Figure 7.11: Results of the verification experiments at different arc length, (a) Standard deviation; (b) Correlation coefficients. The square and error bar for the experiments at each arc length are the average value and the range of the two values from the verification experiments conducted at this particular arc length.

Due to the consistency of the human welder's performance, the obtained model is expected to have a similar performance to predict the current in other dynamic experiments. The obtained model of the welder's behavior is verified by estimating the welding current adjustment in the dynamic experiments. The standard deviation and correlation coefficient are used to evaluate the performance of the model. All results are shown in Figure 7.11. It can be observed that the model shows a consistent performance in predicting the human welder's behavior on the adjustment of the current in the verification experiments.

7.6 Summary

Understanding and modeling of welder response to 3D weld pool surface may help develop intelligent welding robotic systems and train welders faster. In this first effort on modeling human welder behaviors, a welder's adjustment on the welding current as a response to the 3D weld pool surface as characterized by its width, length, and convexity is studied. A unique innovative machine vision system that can real-time measure the specular 3D weld pool surface under strong arc in GTAW is used to record the weld pool surface the welder observes. Experiments are designed to produce random changes in the welding speed. The changing weld pool surface and welder's adjustment on the welding current are recorded. Through the least squares algorithm various models with different structures are identified to correlate the current adjustment to the 3D weld pool surface. It is found that the human welder's behavior is not only related to the 3D weld pool geometry but also relies on the welder's previous adjustment. In this sense, an ARX (auto-regressive with exogenous terms) model with the optimal estimation is selected to model human welder's responses to the 3D weld pool surface. This model has been evaluated and verified by further experiments. The consistent performance of this model in predicting the welder's behavior in different experiments verified its effectiveness.

Copyright© WeiJie Zhang, 2014.

Chapter 8

Human Machine Cooperative Welding Process

8.1 Automatic GTAW Process Using Human Welder Behavior Model

The model of human welders' behavior has board impacts in welding education/training, qualification and manufacturing industry. By comparing a model of an experienced welder's behavior with that of the performance from a unskilled welder, it is easy to understand specifically in quantity why the unskilled welder does not weld well as the skilled welder. Further, the unskilled welder's performance can be quickly tuned/trained to be as good as an experience welder. The model of one weld expert behavior can be set as a standard for the weld qualification test. Further, since the welder's behavior has been mathematically formulated, it is easy to transferred into robotic welding machine. Such weld robots can perform high-speed and high-precision weld while allowing more variations of the work piece and environments. Having those robots to assist a manual welding, an inexperienced welder could weld as good as a skilled welder.

As a demonstration of the application for the model of the welder's behavior, it is implemented in automated GTAW to control process for a consistent penetration. The effectiveness and robustness of the model based control are evaluated.

8.1.1 Experiment configuration and approach

The configuration of the experimental system is shown in Fig. 8.1. A computer connected to the camera is responsible for processing the captured image, reconstructing the weld pool surface and extracting the characteristic parameters. Based on the obtained characteristic parameters, the adjustment needed for the welding current is thus calculated by the human welder behavior model.

Experiments are conducted starting with different welding conditions (joint gap, arc length) and initial current. Specifically, the initial current is in [50A, 62A], the arc length varies within [2 mm, 5 mm] and the joint gap changes from 0 mm to 5 mm. In manual arc

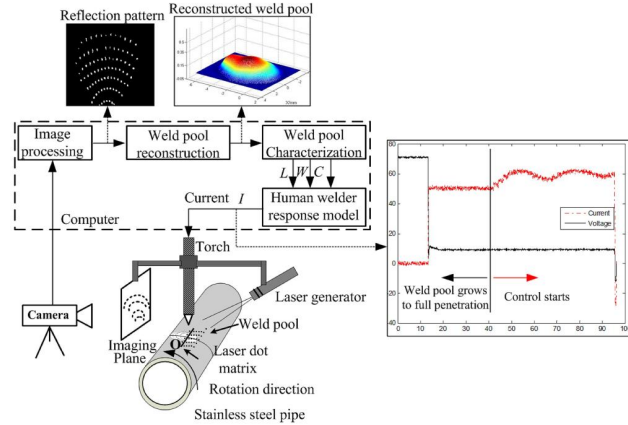


Figure 8.1: Demonstration of experimental set-up.

welding where sometimes welding current is the major parameter controlled by the welder, the welding speed does not change much, although it might vary within a small range. Thus, the welding speed is constant (1 mm/s).

At the beginning in each experiment, the weld pool grows freely to full penetration with specific welding conditions and initial current. The dimension of the weld pool at full penetration in each experiment is expected to be different. Then the experiment is manually switched to control mode, that is, to apply the human welder response model to control the process. Specifically, the model adjusts the welding current based on the characteristic parameters to obtain a desired penetration which is evaluated by backside weld bead width.

Data including current, voltage and characteristic parameters, except the backside weld bead width, are recorded in real-time in the experiments. The backside weld bead width is used as the measurement for the weld penetration. The backside bead width is measured with one sample per second interval off-line. The bead width measurement can be matched with the time scale for other data.

8.1.2 human welder response model control

In this section, the results from the experiments with initial current are presented and analyzed. Major welding parameters used in the experiments are listed in Table 8.1; the rest is the same as in Table 4.3. Results from the two experiments including the current, backside bead appearance and its width are presented in Figure. 8.2 and Figure. 8.3, respectively. The red vertical lines in the two figures indicate the time instant when the process is switched to the model based control mode, i.e., the human welder response model is applied to adjust the current based on the 3D weld pool surface.

Table 8.1: Welding parameters in experiments with different initial currents

Welding current / A	50, 54
Arc length / mm	3

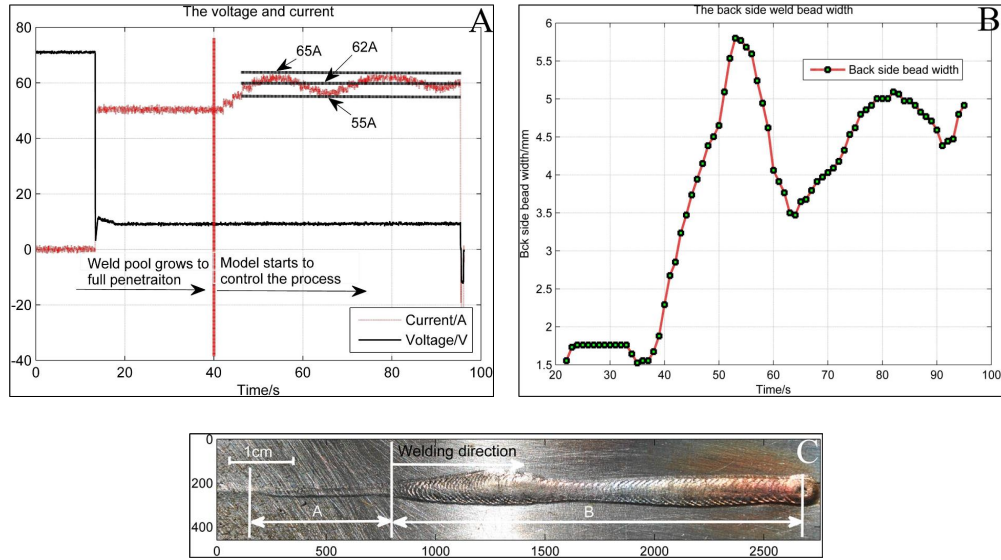


Figure 8.2: Results from experiment with initial current 50 A. a) the current and voltage; b) the backside weld bead width; c) the backside weld bead (the unit of x and y axis is pixel)

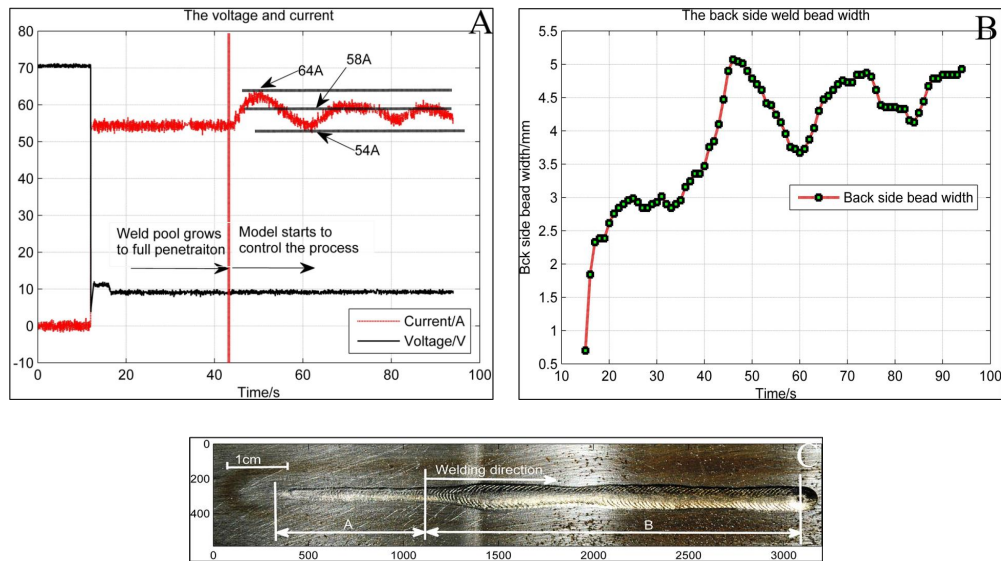


Figure 8.3: Results from experiment with initial current 54 A. a) the current and voltage b) the backside weld bead width c) the backside weld bead (the unit of x and y axis is pixel)

Each of the weld beads in the two experiments is divided into two zones as shown in Figure. 8.2c and Figure. 8.3c. In zone A, the backside bead width is determined by the welding conditions and the initial current. It can be observed that since the difference in initial current, the backside bead in the second experiment (54A) is wider than that in the first one (50A). Difference in the widths indicates the different characteristic parameters are obtained in zone A. Despite the difference, the welding processes in the two experiments

controlled by the human welder response model reach a nearly identical penetration such that the average backside bead widths are 4.8 mm and 4.7 mm in zone B.

It can be found there are current fluctuations during the control period in both two experiments, although the current is settled down within a certain amount of time. That leads to distinctive variation of the backside bead width such that it changes from about 5.8 mm to 3.5 mm in the first experiment, and 5.2 mm to 3.7 mm in the second one. The oscillation of the backside bead width indicates the model is able to adjust the current quickly but not skilled enough to reduce the backside width ripples. The fluctuation of the current adjusted by the model is understandable since the model is developed using the data from behavior of a novice welder with limited skills. It is believed that an unskilled welder might not predict the process quickly and accurately so that he/she would frequently overestimate or underestimate the weld penetration. A seasoned welder can easily avoid the fluctuation by smoothing the behavior on the current adjustment.

8.1.3 Improvement of human welder response model

As discussed in the Section 7.5.1, the model presents the average performance of a novice welder with limited skill. As a result, it has been found that the model has large current oscillations when the weld pool geometry changes. The corresponding variation of the weld bead width is expected to be large in robotic welding directly using the model. It is known that a skilled welder can avoid the current ripple with smooth current adjustment. In this sense, to smooth the model's adjustment is to filter out the high frequency part of the calculated current adjustment. A simple method is to adopt a digital low-pass filter after the model in the control system as shown in Figure. 8.4.

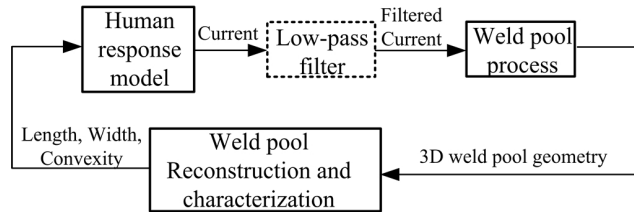


Figure 8.4: Diagram of control system of the human welder response model with additional low-pass filter

The low-pass filter used in this study can be written:

$$\Delta i'_k = \alpha \Delta i'_{k-1} + (1 - \alpha) \Delta i_k \quad (8.1)$$

where $\Delta i'_k$ and $\Delta i'_{k-1}$ the filtered current adjustment at time instant k and $k-1$ respectively, and Δi_k is the current adjustment calculated by the welder response model at time instant k . Coefficient α control the frequency bandwidth of the filter. A greater α gives a wider band width. In this study, α is selected to be 0.5.

Since the filter blocks high-frequency components in the current output, its function would be pronounced during the transition period. However, when the current approaches steady state, the high-frequency components become insignificant. The steady-state value of the current is thus not affected by the filter. Moreover, since the current adjustment is smoothed

by the filter, the current ripple is expected to be minimized. The backside weld bead width is expected to be more consistent. Moreover, since the welder’s behavior has been formulated to be a mathematically model, the inconsistent/randomness of the welder performance have been diminished. If the current is smoothly and quickly adjusted by the model in one circumstance, the model will keep adjusting the welding with the same mechanism. In this sense, adapting a low-pass filter to the human welder response model makes the model function like a skilled welder.

8.1.4 Robustness experiment results and analysis

The human weld response model based control is now improved simply by adding a low-pass filter . To confirm its effectiveness in controlling the process to achieve the desired weld penetration, various experiments have been designed and conducted under different welding conditions and initial welding currents.

1. Robustness with respect to initial current Initial currents in Table 8.2) are used in order to examine the system’s robustness against the initial current used. The results are shown in Figure. 8.5 to Figure. 8.7.

Table 8.2: Welding parameters for initial current robustness experiments

Welding current / A	50, 54, 58, 62
Arc length / mm	3

With different initial currents the obtained weld beads have different backside widths in zone A. The steady-state current corresponding to the penetration obtained by the human welder response model varies from 59.5 A to 61.5 A, as shown in Figure. 8.5. The steady-state width of the obtained weld beads, shown in Figure. 8.7, converges within the range from 5.0 mm to 5.3 mm in zone B. Therefore, despite the different backside width obtained at the beginning of those experiments, a consistent penetration with only 0.3 mm width variation is achieved using the model based control. A 0.3 mm deviation in backside bead width is considered acceptable. It is known that the weld pool is dynamic and vibrating through the welding process. Even a constant welding input might cause the backside bead width varies within a small range.

The settling time (set the error margin 5%) [123] for the process to achieve the steady state is in the range from 3.5 seconds to 4.5 seconds. For the experiment with initial current 62 A, the steady-state current is only about 0.5 A less than the initial current. The transition period is negligible from Figure. 8.5d.

2. Robustness with respect to arc length Arc length is another variation whose effect on the control system needs to be examined. Hence, experiments with different arc length are conducted. The initial current, arc length are listed in Table 8.3. The resultant current, backside weld bead and backside width measurements are presented in Fig. 8.8, Fig. 8.9 and Fig. 8.10 respectively.

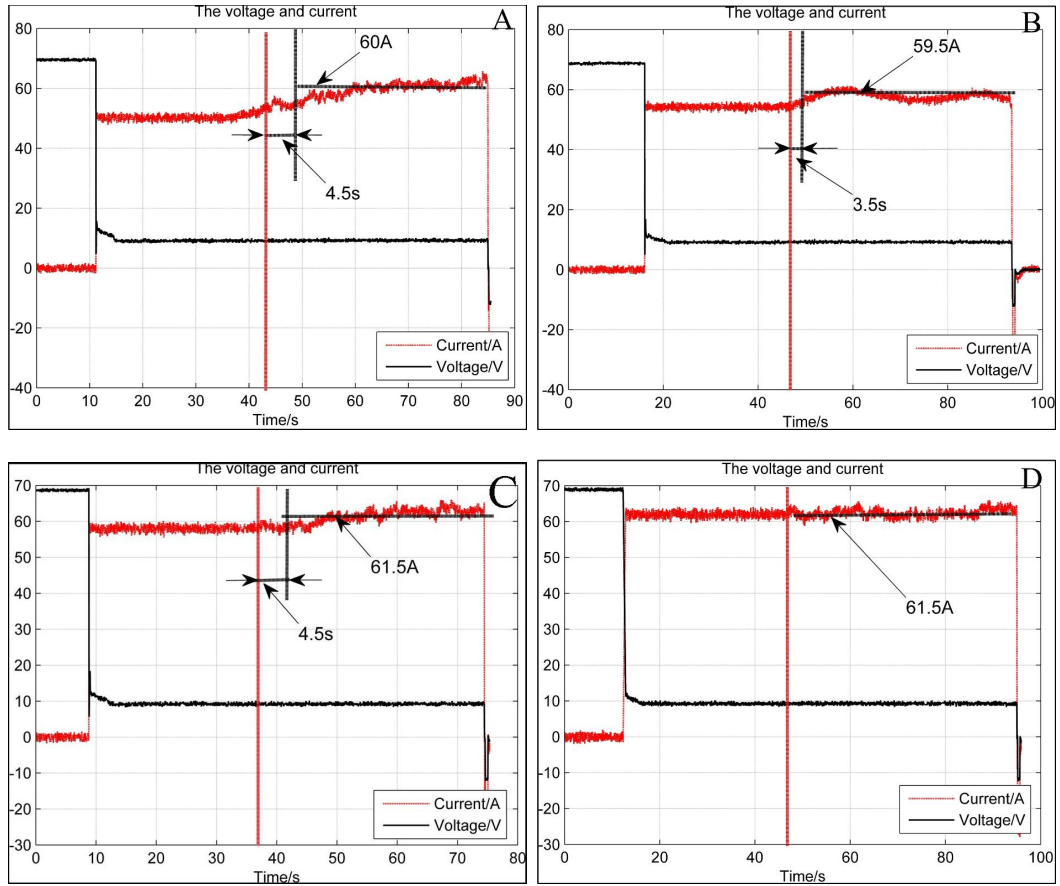


Figure 8.5: Current and voltage of the experiments with initial current (a) 50 A, (b) 54 A, (c) 58 A and (d) 62 A

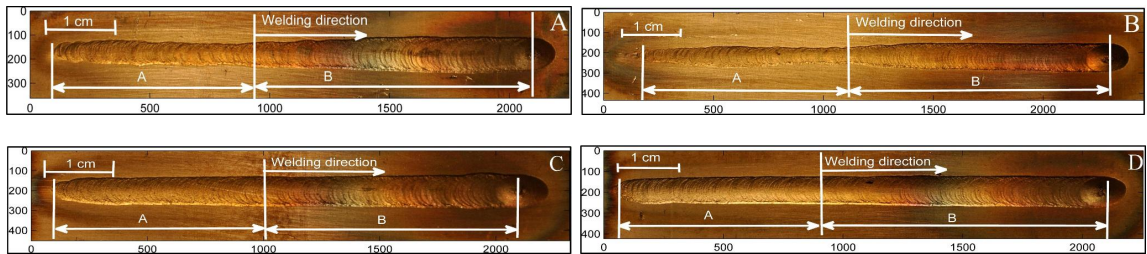


Figure 8.6: The backside appearance of the weld bead with initial current (a) 50 A, (b) 54 A, (c) 58 A and (d) 62 A

Table 8.3: Welding parameters for arc length robustness experiments

Welding current / A	54
Arc length / mm	2, 3, 4, 5

With an increase in the arc length, the arc distribution becomes broader and the arc energy

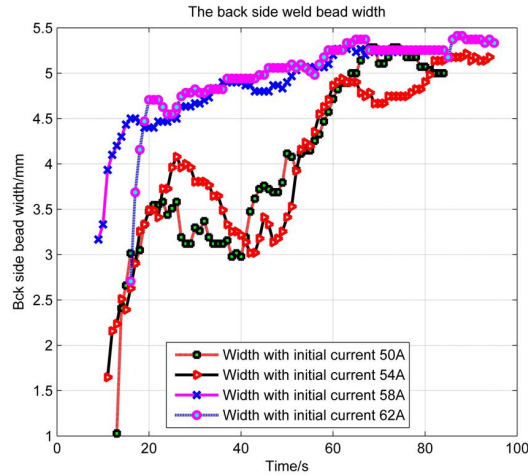


Figure 8.7: The backside width of weld beads with different initial current

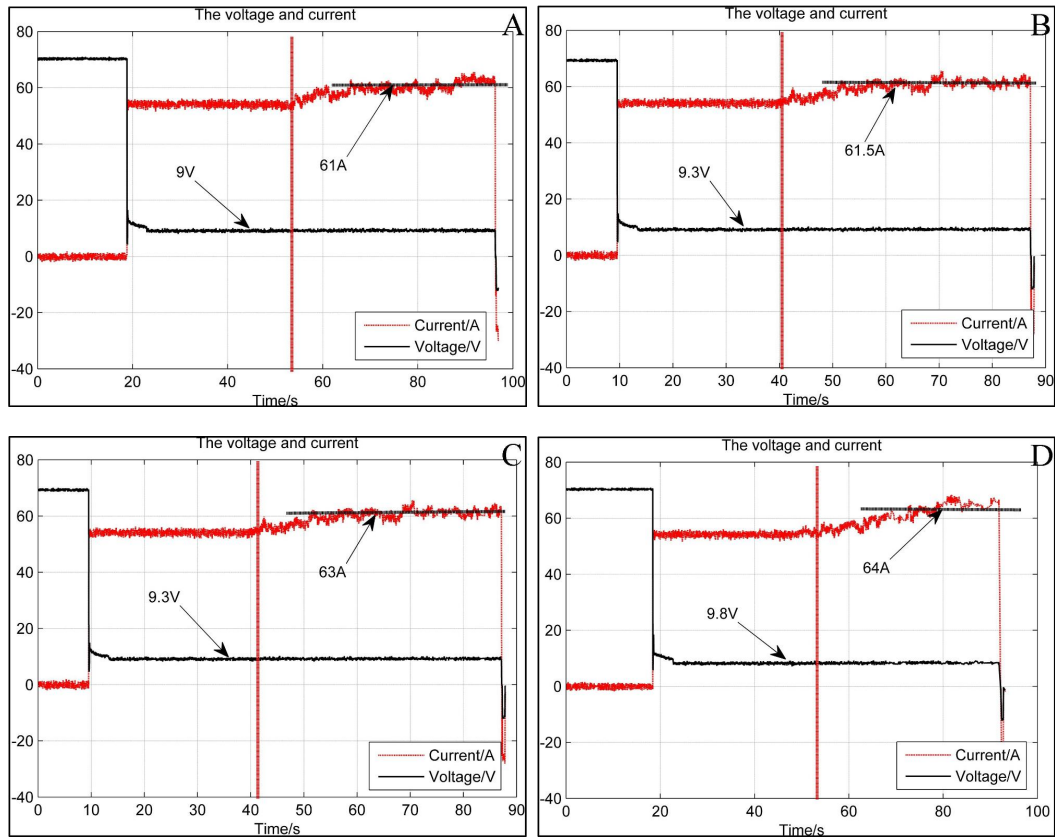


Figure 8.8: Current and voltage from arc length robustness experiments with arc length (a) 2 mm, (b) 3 mm, (c) 4 mm, and (d) 5 mm.

intensity decreases. The penetration capability thus reduces. It can be observed in Figure 8.10, the width of the four weld beads in zone A reduces down from 3.7 mm to 2.5 mm. In order to obtain a consistent penetration, the model based control increases the steady-state current from 61 A to 64 A in the experiments with the arc length changing from 2 mm to

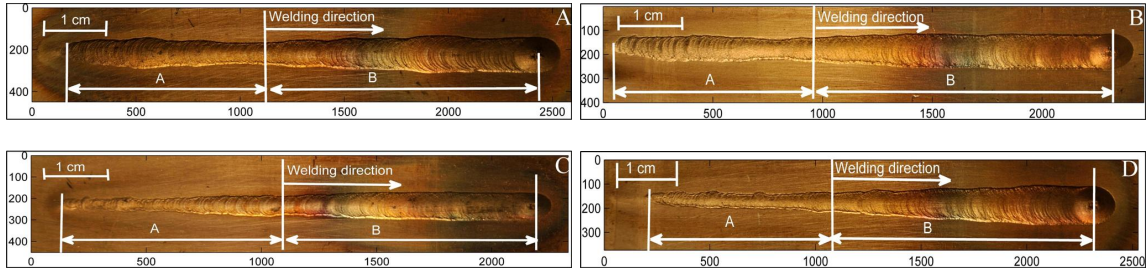


Figure 8.9: The backside weld beads from arc length robustness experiments with arc length (a) 2 mm, (b) 3 mm, (c) 4 mm, and (d) 5 mm.

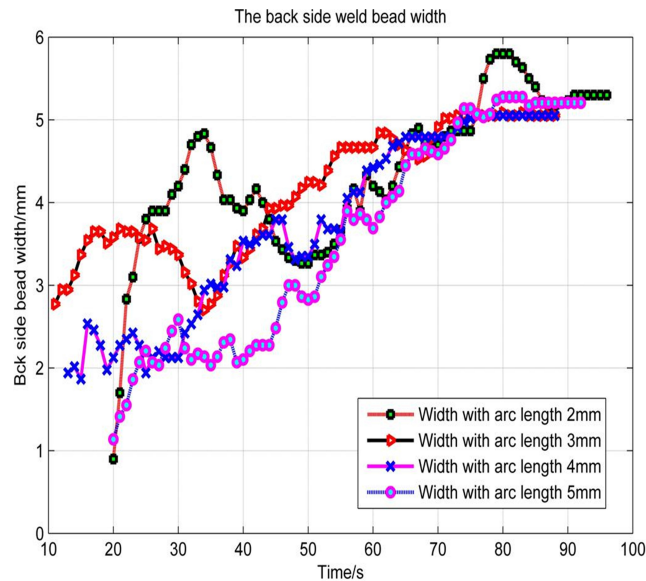


Figure 8.10: The backside width of weld beads from arc length robustness experiments

5 mm.

From Figure. 8.9, the backside width of the weld bead in the four experiments converges to about 5.2 mm in zone B. Among the four weld beads, the one with 2 mm arc length reaches largest steady-state width (5.4 mm), and the weld beads with 3 mm and 4 mm arc length have smallest steady-state width which is about 5.0 mm. From Figure. 8.9 and Figure. 8.7, one can find that a nearly identical backside width which is about 5.2 mm with 0.4 mm variation margin is obtained. The model is able to maintain a consistent penetration despite the different arc length and initial current.

3. Joint gap robustness Joint gap is difficult to be precisely controlled in production. The effectiveness of the human welder response model based control needs to be examined under varying/different gaps. In this subsection, experiments with different joint gap conditions/variations are conducted. The joint gap, arc length and welding speed are listed in Table 8.4. The joint gap conditions in the three experiments are shown in Figure. 8.11. The results are shown in Figure. 8.12 to Figure. 8.14.

Table 8.4: Welding parameters for arc length robustness experiments

Welding parameters	Experiments		
	1	2	3
Joint gap / mm	0	2	[0, 5]
Arc length / mm	3		
Initial Current / A	54	58	54

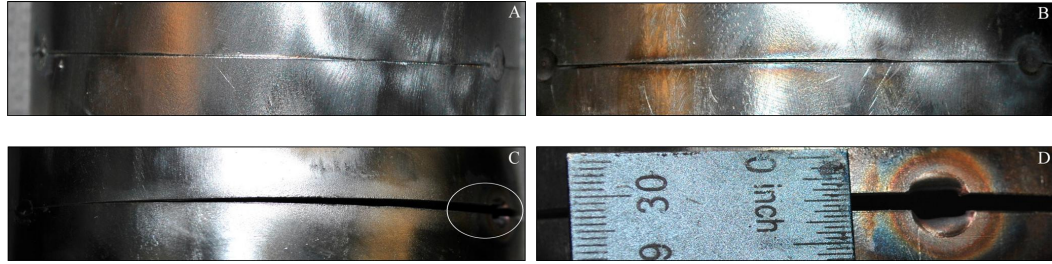


Figure 8.11: Front side of the weld joint before experiment for joint gap robustness experiments. (a) 0 nominal joint gap; (b) 2 mm nominal joint gap; (c) nominal joint gap increases from 0 to 5 mm (0.21 inch); (d) close review of the wide gap for marked area in (c).

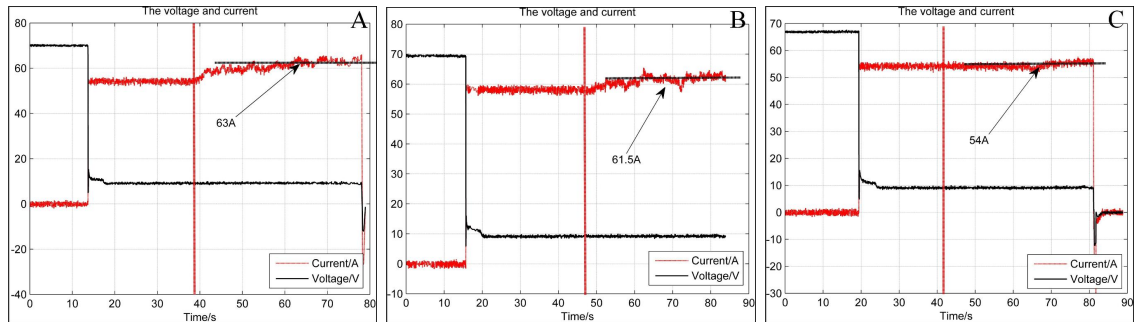


Figure 8.12: Current and voltage from joint gap robustness experiments. (a) 0 nominal joint gap; (b) 2 mm nominal joint gap; (c) nominal joint gap increases from 0 mm to 5 mm.

The steady-state current differs in these three experiments. The joint gap is close to zero in the first experiment in which the welding process is close to those without gap. Therefore, the steady-state current (63 A) is close to the resultant steady-state current obtained in the last two subsections. However, as the joint gap increases, the weld pool surface tends to be more concave which means the convexity of the weld pool is smaller. The current adjustment controlled by the human welder response model (in Table 7.2) tends to be smaller accordingly. The penetration capability of the arc also increases with the gap. Therefore, less heat input is required to produce the same penetration as the gap increases. The steady-state current for the second and third experiment are thus reduced to 61.5 A and 54 A respectively. The obtained backside widths of the weld beads in these three experiments are about 5.2 mm, 5.5 mm and 5.6 mm, which are considered consistent with a reasonably small variation margin.

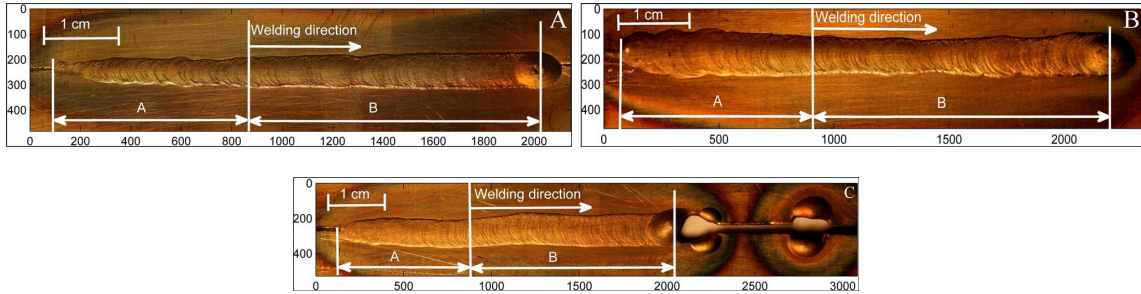


Figure 8.13: The backside appearance of the weld beads from joint gap robustness experiments. (a) 0 nominal joint gap; (b) 2 mm nominal joint gap; (c) nominal joint gap increases from 0 mm to 5 mm.

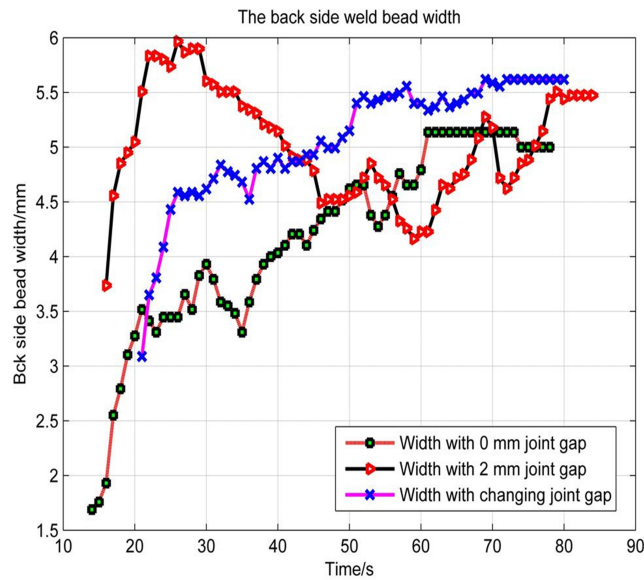


Figure 8.14: The backside width of weld beads from joint gap robustness experiments.

It needs to be mentioned that the welding process stops at the position where the joint gap is about 4 mm in the third experiment. The experimental results in experiment 3 thus only claims that the human welder response model based control can control the welding process to maintain the consistent penetration for a joint gap 4 mm or smaller.

8.2 Manual GTAW Process Using Human Welder Behavior Model

The using welder behavior model is further applied in manual GTAW experiments in this section. The experiment configuration and approach is detailed in section 8.2.1. Section 8.2.2 presents the experiments results.

8.2.1 Experiment configuration and approach

The configuration of the experimental system is shown in Fig. 8.15. A computer connected to the camera is used to process captured images, calculate the translation, rotation of the torch and the helmet, based on which the weld pool surfaces is reconstructed. And the characteristic parameters are extracted, based on which human welder response model can render a current for the manual process to maintain a persistent weld penetration.

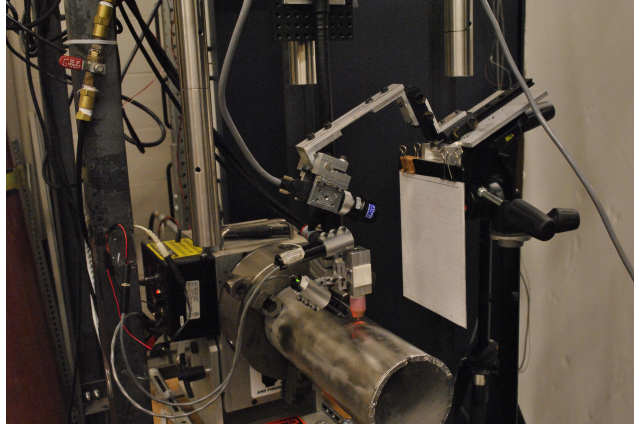


Figure 8.15: The experimental setup for manual GTAW process

The major parameters for the manual welding are presented in Table 3.1. The initial settings are thus: $\Theta_{mh} = [0^\circ, 0^\circ, 0^\circ]$, $\Theta_{mt} = [0^\circ, 0^\circ, 0^\circ]$ and $D_{A_2}|_{initial} = [0, 125\text{mm}, 20\text{mm}]$.

The main object of this section is to verify the effectiveness of human welder response model along with the mobile sensing system in manual GTAW process, i.e., a consistent full penetration is maintained by the control of the human welder response model with the assistance of the mobile sensing system. Therefore, there types of experiments, e.g., manual welding while A) the helmet is in translation, in B) rotation, and C) the torch is in rotation. The experiments starts at a low current (55A, not enough for full penetration) while the welder response model is not in control. Then the response model is manual turned on to control the process for full penetration while the torch/helmet are translating/rotating.

8.2.2 Experiment results

There are total 9 experiments are conducted, i.e., three helmet translation experiments, three rotation experiments for both the torch and the helmet. The real-time measurement metrics the matching coefficient (M_c), ARE and MRE are applied to evaluate the effectiveness of the human-machine cooperative control system. In the meantime, the backside weld bead width for each experiments are measured.

The results are show in Fig. 8.16 to Fig. 8.18, and Fig. 8.19.

One can find from Fig. 8.16 to Fig. 8.18 that the M_c , ARE and MRE are around 1.2%, 0.08 mm and 0.3 mm respectively. Although they are within the pre-defined tolerance, they are larger than the results obtained in the experiments in Chapter 6, in which the arc interference and errors from the sensing system might be less severe. The back side bead

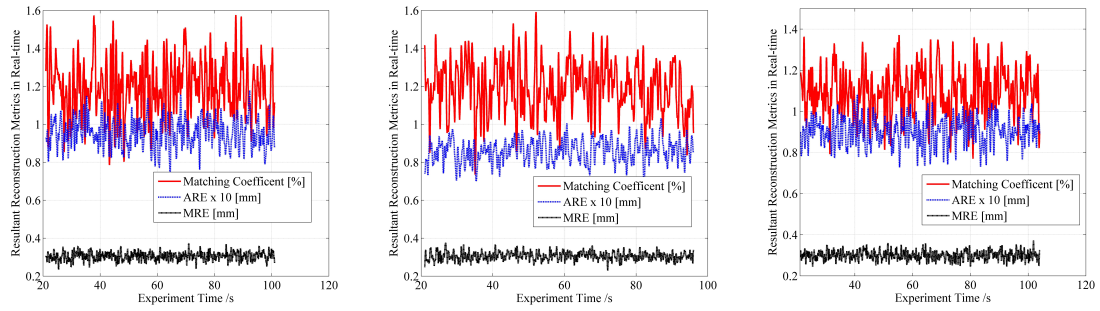


Figure 8.16: M_c , ARE and MRE of weld pool reconstruction as the helmet translates to the boundary points along: A) x-axis; B) y-axis; C) z-axis

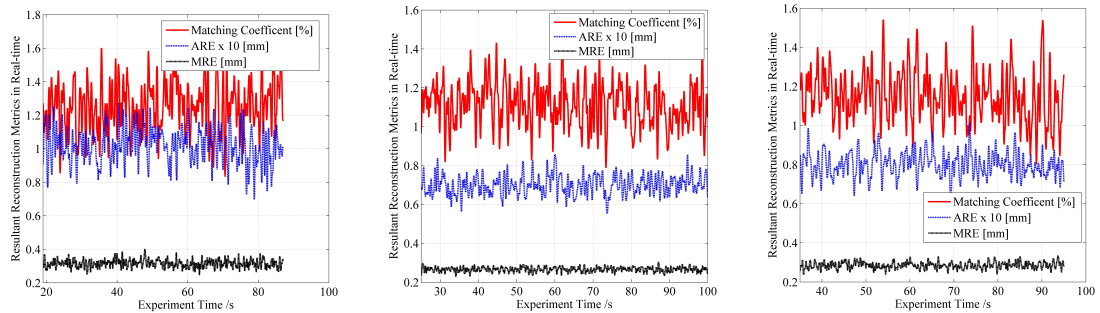


Figure 8.17: M_c , ARE and MRE of weld pool reconstruction as the helmet rotates to the boundary points along: A) x-axis; B) y-axis; C) z-axis

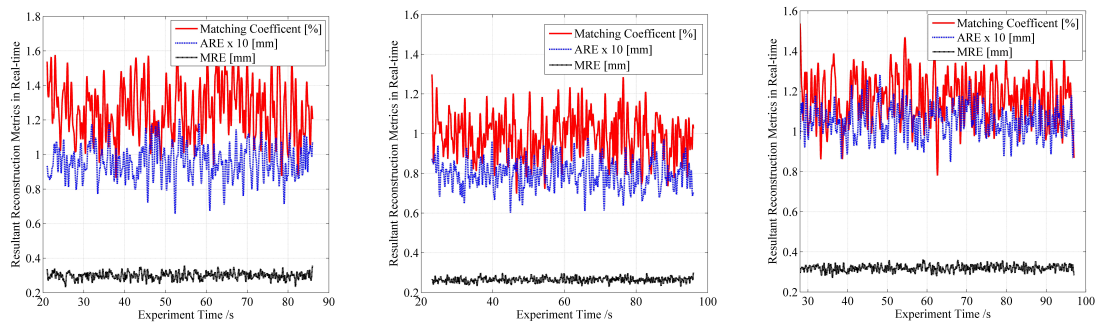


Figure 8.18: M_c , ARE and MRE of weld pool reconstruction as the torch rotates to the boundary points along: A) x-axis; B) y-axis; C) z-axis

width in all the experiments converges to around 5.2 mm with about 0.2 mm deviation. The measurement metrics results and the back side weld bead width verify the effectiveness of the human-machine cooperative control system in manual GTAW process.

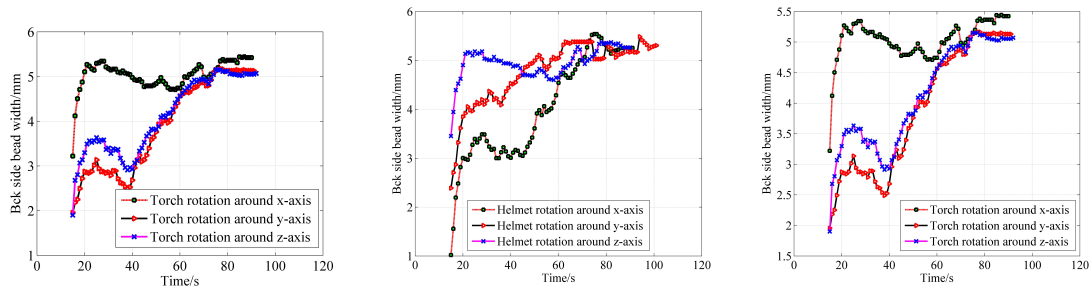


Figure 8.19: The backside weld bead width for the 9 experiments for human-machine cooperative control in A) helmet translation; B) helmet rotation; and C) torch rotation

8.3 Summary

In modern welding industry where automated welding tends to be the mainstream, manual welding is still not replaceable when human experience and skills are critical in producing quality welds. Yet the mechanization and transformation of human welder's intelligence into robotic welding have not been explored. In the last chapter of modeling for human welder's behavior, welder's adjustments on welding current are modeled as response to characteristic parameters of the three-dimensional weld pool surface. In this chapter, this response model is implemented to feedback control the GTAW process to maintain a consistent full penetration. Experiments have been designed to start welding with different welding conditions (arc length, welding speed and the joint gap) and initial current. After the initial open-loop control period, the welding current is adjusted by the controller that uses the welder's response model to determine how to adjust the welding current based on measured weld pool surface characteristic parameters. The resultant current waveform and its backside weld bead width were recorded/measured and analyzed. It is found that the human welder response model can adjust the current appropriately to control the welding process to a desired penetration level despite the difference in the welding conditions and initial current.

Chapter 9

Conclusion and Future Work

9.1 Conclusion

Manual welding processes are widely used in many manufacturing areas, such as automotive, aerospace and shipbuilding industries. In the meantime, welding is a labor intensive and skill required operation, while lacking of skilled welders is the critical problem facing by the whole industry areas. Since both robotic and manual welding processes have their advantages and limits, this study proposes an innovative approach to assist the manual welder in weld performance by taking advantages of both human and robots. In this dissertation, a new mobile sensing and control system is developed to monitor and control a manual welding process. The main work in the thesis includes three parts: establishment of a mobile sensing system, including the design of the system (Chapter 3), processing of acquired reflected images (Chapter 4), orientation estimation of the sensing system (Chapter 5) and reconstruction of three-dimensional weld pool surface based on achieved information (Chapter 6); modeling of human welder behavior based on characteristic parameters obtained from reconstructed weld pool surface(Chapter.7); and control of robot/manual welding process using both the sensing system and behavior model together (Chapter 8). The three procedures can be briefly described as Acquisition, Modeling and Implementation process. By using the developed system, the 3D profile of weld pool front surface can be computed on-line, the characteristic parameters can be obtained based on the surface, and model of human welder's behavior of adjusting the current in response to the 3D weld pool surface dimensional variations. This research is not only important for development of machine vision for welding robots, but also the first of this kind to study human welder's weld behavior in manual GTAW, both of which are critical puzzle for next generation intelligent welding process. The main achievements and contributions in this dissertation can be summarized as follow:

- Proposed a new approach to effectively observe and measure weld pool surface in manual welding. Compact sensors are installed on the torch and helmet with no interference for manual welding. The mobile sensing system also takes advantages of movement of a welder's head/helmet to intercept the laser reflection far away from the arc radiation interference. That results in comparatively clear images of laser reflection, which takes advantage of the specular surface and the difference between propagation in an illumination laser and arc plasma.

- Established the orientation estimation procedure for helmet and torch. In the phase of implementation, real-time detection of the orientations of the helmet and the torch is in manual welding is accomplished by Kalman-based orientation estimation algorithm. Through experiments with different conditions, acceptable orientation accuracy and robustness have been achieved.
- Developed robust image processing algorithms to effectively analyze the acquired reflected images. The usefully information, i.e., the two laser reflections (the dot matrix and the grid pattern), have been successfully extracted. For the dot matrix reflection pattern, the reflected dots' coordinates and row/column positions can be extracted.
- Proposed a real-time reconstruction procedure to reconstruct three-dimensional weld pool surface. This research provides an innovative and effective way for the proposed sensing system to reconstruct the weld pool surface in-line for a manual GTAW process. The reconstruction results verified the accuracy of the mobile sensing system.
- Modeled human welder's behavior of adjusting current in response to weld pool surface dimension variations. This study shows that the welder adjusts the current based on the weld pool length, width and convexity. In full penetration status, the welder increases the current if the length or width decrease or convexity increases. Further, welder makes adjustments not only based on the weld pool dimension at current instant but the dimensions within 3 5 seconds ago.
- Implemented the mobile sensing system in a robotic/manual GTAW process along with the human welder response model which acts as a control in the process. Results from a series of experiments conducted under different welding conditions show that the proposed sensing system and control algorithm can effectively and robustly maintain the welding process in a consistent full penetration status despite of the various disturbances.

9.2 Future Work

The proposed system used in this dissertation is intended for laboratory experiments and realized only for designed GTAW process. To make the system more practical and be used in next generation intelligent welding machines, more future work can be done in different aspects to improve the design of the mobile sensing system and the human welder response, which include:

- Simplify and refine the design and make the mobile sensing system compact The simply the system design, the two laser generators on the torch should be replace by smaller and lighter one. The design of the powering system for the current generator contributes the most body volume and weight. Therefore, finding a smaller, lighter batter for the corresponding laser generator could be the key to make the project torch compact. The camera mounted on the helmet should be replaced by a battery-powered camera with wireless communication capability. In this case, the cable for the camera in the current design of the sensory helmet can be eliminated. Furthermore, the sensory helmet used in the experiments is only for laboratory demonstration. To

further possible commercial purpose, the sensory helmet needs to be redesigned, in terms of the imaging plane/shield glass, and position of the camera.

- Improve the projected laser pattern and power It can be seen in the analysis in this study that denser laser dot matrix, for example, replacing the 19×19 dot matrix by a 38×38 dot matrix, the accuracy of the weld pool reconstruction would be greatly improved. Thus if possible denser commercial available laser pattern should be applied to improve the sensing system. Further, the power of continuous laser is only 20 mW in the experiments in this study. In order to improve the contrast of the reflected images and ease the image processing algorithm, the laser diode with larger power should be used. It is also necessary in the applications by using large welding current.
- Further modeling of human welder's behavior In this study, only current is considered as an adjusting parameter in the human welder response model. Practically, a welder might adjust the speed, arc length and torch orientation as well in weld performance. More complex model is required to study the human welder's behavior in response to the weld pool dimension variations.

Bibliography

- [1] Ansi/asme standard 36.19m.
- [2] imu and nimu temperature dependant bias, scale factor and cross sensitivity correction performance revision 1. Technical report, MEMSense.
- [3] Joint tracking robot system transforms companys welding production. *Welding Journal*, 73(3):68–69, 1994.
- [4] Lincolns mig welding guidance. LINCOLN ELECTRIC, 22801 St. Clair Avenue, Cleveland, Ohio 44117-1199 USA, 1997.
- [5] Aws c5.5/c5.5m recommended practices for gas tungsten arc welding, 2003.
- [6] Guidelines to gas tungsten arc welding (gtaw). MILLER ELECTRIC, 2003.
- [7] Aws c5.6 recommended practices for gas metal arc welding, 2004.
- [8] Welding shortage fact sheet, 2007.
- [9] R. Adams and L. Bischof. Seeded region growing. *IEEE Transactions on Pattern Analysis and Machine Intelligence*, 16:641–647, 1994.
- [10] X. P. Ai, N. S. Liu, Y. Q. Wei, X. Hu, and X. R. Liu S. Wei. Study on image acquisition in 3-d sensor system of arc welding pool surface shape using grating projection. *Proceedings of SPIE*, 7506 750628, 2009.
- [11] T.R. Anderson. Control of electromagnetic interference from arc and electron beam welding by controlling the physical parameters in arc or electron beam theoretical model. In *IEEE International Symposium o Electromagnetic Compatibility*, volume 2, pages 695–698, Washington, DC, Au 2000.
- [12] R. Williamson B.J. Andrews. Detecting absolute human knee angle and angular velocity using accelerometer and rate gyroscope. *Medical & Biological Engineering & Computing*, 39:294–302, 2001.
- [13] A. J. R. Anedenroomer and G. den Ouden. Weld pool oscillation as a tool for penetration sensing during pulsed gta welding. *Welding Journal*, 77(5):181–187, 1998.
- [14] K. J. Astrom and B. Wittenmark. *Adaptive Control*. Addison-Wesley, 1995.
- [15] K.Y. Baea, T.H. Leea, and K.C. Ahnb. An optical sensing system for seam tracking and weld pool control in gas metal arc welding of steel pipe. *Journal of Materials Processing Technology*, 120:458–465, 2002.

- [16] C. Balfour, J.S. Smith, and A.I Al-Shamma. A novel edge feature correlation algorithm for real-time computer vision-based molten weld pool measurements. *Welding Journal*, 85(1):1s–8s., 2006.
- [17] J. Balzer and S. Werling. Principles of shape from specular reflection. *Measurement*, 43(10):1305–1317, 2010.
- [18] P. Banerjee and et al. Infrared sensing for on-line weld shape monitoring and control. *ASME Journal of Engineering for Industry*, 117:323–330, 1995.
- [19] M. Bao and I. C. Ume. Real-time weld penetration depth monitoring with laser ultrasonic sensing system. *Transactions of the ASME*, 28:280–286, 2006.
- [20] S. Beauregard. Omnidirectional pedestrian navigation for first responders. In *Proceeding 4th Workshop on Positioning, Navigation and Communication WPNC*, pages 33–36, March 2007.
- [21] Nuri Bhieh, Esmail Elshghier, Marai Ali Khalifa, and Mohammed Salem Elamari. Controlling arc welding risk to persons with pacemaker. *International Journal of Sciences and Techniques of Automatic control & computer engineering*, 1:213–225, 2007.
- [22] J.E. Bortz. A new mathematical formulation for strapdown inertial navigation. *IEEE Aerospace and Electronic Systems*, 7(1):61 – 66, 1971.
- [23] Duane C. Brown. Close-range camera calibration. *PHOTOGRAMMETRIC ENGINEERING*, 37:855–866, 1971.
- [24] B. Butler. Joint tracking automation triples propane cylinder production. *Welding Journal*, 71(8):61–63, 1992.
- [25] M.J. Caruso. Applications of magnetic sensors for low cost compass systems. In *IEEE Position Location and Navigation Symposium*, 2000.
- [26] Terrence L. Chambers, Amit Aglawe, Dirk Reiners, Steven White, Christoph W. Borst, Mores Prachyabrued, and Abhishek Bajpayee. Real-time simulation for a virtual reality-based mig welding training system. *Virtual Reality*, 16(1):45–55, 2012.
- [27] Mahesh S. Chavan, Nikos Mastorakis, Manjusha N. Chavan, and M. S. Gaikwad. Implementation of symlet wavelets to removal of gaussian additive noise from speech signal. In *NEHIPISIC'11 Proceeding of 10th WSEAS international conference on electronics, hardware, wireless and optical communications, and 10th WSEAS international conference on signal processing, robotics and automation, and 3rd WSEAS international conference on nanotechnology, and 2nd WSEAS international conference on Plasma-fusion-nuclear physics*, 2011.
- [28] L. K. Chen and A. G. Ulsoy. Identification of a nonlinear driver model via narmax modeling. *Proceedings of American Control Conference*, pages 2533–2537, 2000.
- [29] W. Chen and B.A. Chin. Monitoring joint penetration using infrared sensing techniques. *Welding Journal*, 69(4):181s–185s, 1990.

- [30] D. Y. Choong and J Lee. 3-d measurement of weld pool using biprism stereo vision sensor. [Http://joining1.kaist.ac.kr/research/vision.htm](http://joining1.kaist.ac.kr/research/vision.htm), *Seoul National University*, 2004.
- [31] J.C.K. Chou. Quaternion kinematic and dynamic differential equations. *IEEE Transactions on Robotics and Automation*, 8(1):53–64, 1992.
- [32] Miller Electric Mfg Co. Tig welding tips, 2013.
- [33] H. C.Wikle, R. H. Zee, and B.A. Chin. Sensing system for weld process control. *Journal of Materials Processing Technology*, 89-90:254–259, 1999.
- [34] I. Daubechies. *Ten lectures on Wavelets*. Philadelphia: Society for Industrial and applied Mathematics, 1992.
- [35] I. I. Delice and S. Ertugrul. Intelligent modeling of human driver: A survey. *2007 IEEE Intelligent Vehicles Symposium*, pages 648 –651, 2007.
- [36] Jung Dongwon and Tsiotras Panagiotis. Inertial attitude and position reference system development for a small uav. In *In Proceeding of the American Institute of Aeronautics and Astronautics Technical Conference*, Rohnert Park, CA, May 7-10 2007.
- [37] D. L. Donoho and I. M. Johnstone. Ideal spatial adaptation by wavelet shrinkage. *Biometrika*, 81:425–455, 1994.
- [38] Q. Y. Du, S. B. Chen, and T. Lin. Reconstruction of weld pool surface based on shape from shading. *Journal of Mechanical Engineering*, 19(2):168–171, 2006.
- [39] E.A.Wan and R. Van der Merwe. The unscented kalman filter for nonlinear estimation. In *IEEE Adaptive Systems for Signal Processing, Communications, and Control Symposium*, pages 153 – 158, 2000.
- [40] Lincoln Electric. *VRTEX 360*. Lincoln Electric, Cleveland, Ohio 44117-1199 U.S.A, im10046-e edition, October 2012.
- [41] S. Ertugrul. Predictive modeling of human operators using parametric and neuro-fuzzy models by means of computer-based identification experiment. *Engineering Applications of Artificial Intelligence*, 21:259–268, 2008.
- [42] ESAB, P.O. Box 100545, 411 South Ebenezer Road, Florence, SC 29501-0545. *Welder Guide Book*, 2011.
- [43] C.L. Fan, F. Lv, and S. Chen. Visual sensing and penetration control in aluminum alloy pulsed gta welding. *The International Journal of Advanced Manufacturing Technology*, 42(1):126–137, 2009.
- [44] K Fast, T Gifford T, and R Yancey. Virtual training for welding. In *Proceedings of the third IEEE and ACM international symposium on mixed and augmented reality*, page 298299, Washington, DC, 2004.
- [45] F. Ferraris, U. Grimaldi, and M. Pavis. Procedure for effortless in-field. calibration of three-axis rate gyros and accelerometers. *Sensors and Materials*, 7:311–330, 1995.

- [46] J.G. Fryer and D.C. Brown. Lens distortion for close-range photogrammetry. *Photogrammetric Engineering and Remote Sensing*, 52:51–58, 1986.
- [47] K. Fukunage. *Introduction to Statistical Pattern Recognition*. New York Academic, 1972.
- [48] B Gaines. Linear and nonlinear models of the human controller. *International Journal of Man-Machine Studies*, pages 1333–360, 1969.
- [49] Rafael C. Gonzalez and Richard E. Woods. *Digital Image Processing (3rd Edition)*. Prentice Hall, 2007.
- [50] G.M. Graham and I.C. Ume. Automated system for laser ultrasonic sensing of weld penetration. *Mechatronics*, 7(8):711–721, 1997.
- [51] R. A. Groenwald, T. A. Mathieson, C. T. Kedzior, and I.N.C Gaid. Acoustic emission weld monitor system data acquisition and investigation. Technical report, US Army Tank-Automotive Research and Development Command Report ADA085-518, 1979.
- [52] S. Gupta, L. Kaur, R.C. Chauhan, and S.C. Saxena. A wavelet based statistical approach for speckle reduction in medical ultrasound images. In *Conference on Convergent Technologies for the Asia-Pacific Region*, 2009.
- [53] S. C. We H. B. Ma. Binocular vision system for both weld pool and root gap in robot welding process. *Sensor Review*, 30(2):116–123, 2010.
- [54] Yanling Hao, Hongwei Mu, and Xintao Liu. On-line calibration technology for sin-s/cns based on mpf-kf. In *International Conference on Mechatronics and Automation (ICMA)*, 2012.
- [55] D.A. Hartman, D.R. DeLapp, G.E. Cook, and R.J. Barnett. Intelligent control in arc welding. In *ANNIE '99: Smart Engineering System Design Conference St. Louis, Missouri November 7-10, 1999*, 1999.
- [56] Janne Heikkil and Olli Silv. A four-step camera calibration procedure with implicit image correction. In *Proceedings of IEEE Computer Society Conference on Computer Vision and Pattern Recognition*, 1997.
- [57] S.N. Hopko and I.C. Ume. Laser generated ultrasound by material ablation using fiber optic delivery. *Ultrasonics*, 37(1):1–7, 1999.
- [58] P. V. C. Hough. Method and means for recognizing complex patterns, 1962.
- [59] L. Huang, C. S. Ng, and A. K. Asundi. Dynamic three-dimensional sensing for specular surface with monoscopic fringe reflectometry. *Optics Express*, 19(13):12809–12814, 2011.
- [60] B. Huyghe, J. Doutrelaigne, and J. Vanfleteren. 3d orientation tracking based on unscented kalman filtering of accelerometer and magnetometer data. In *IEEE Sensors Applications Symposium*, pages 148 – 152, 2009.
- [61] M.B. Ignagni. Optimal strapdown attitude integration algorithms. *Journal of Guidance, Control and Dynamics*, 13:363–369, 1990.

- [62] InterSense Inc., 36 Crosby Drive, Suite 150, Bedford, MA, 01730 USA. *InertialCube2+ Manual*, 1.0 edition, 2008.
- [63] Thien Phuc Iran, Tan Lam Chung, Hak Kyeong Kim, Sang Bong Kim, and Myung Suk Oh. Trajectory tracking of mobile manipulator for welding task using sliding mode control. In *Industrial Electronics Society, 2004. IECON 2004. 30th Annual Conference of IEEE*, volume 1, pages 407–412, 2004.
- [64] E. Itoh and S Suzuki. Nonlinear approach for human internal models: Feed forward and feedback roles in pilot maneuver. *Systems. Man and Cybernetics. 2005 IEEE International Conference.*, 3:2455–2462, .2005.
- [65] Yang Bae Jeon, Byoung Oh Kam, Soon Sil Park, and Sang Bong Kim. Seam tracking and welding speed control of mobile robot for lattice type welding. In *IEEE International Symposium on Industrial Electronics (ISIE)*, volume 2, pages 857–862, 2001.
- [66] Derek B. Kingston and Randal W. Beard. Real-time attitude and position estimation for small uavs using low-cost sensors. In *In Proceeding of the 3rd American Institute of Aeronautics and Astronautics Technical Conference*, pages 20–23, Chicago, IL, USA, 2004.
- [67] D. L. Kleiman, S. Baron, and W. H Levison. An optimal model of human response, part 1. theory and validation. *Automatica*, 6:357–369, 1970.
- [68] H.G. Kortier, H.M. Schepers, V.I. Sluiter, and P.H. Veltink. Estimation of hand and finger kinematics using inertial sensors. In *In: 4th Dutch Bio-Medical Engineering Conference*, Egmond aan Zee, Netherlands., Jan 2013.
- [69] Poolsak Koseeyaporn, G.E. Cook, and Alvin M. Strauss. Adaptive voltage control in fusion arc welding. *IEEE Transactions on Industry Applications*, 36(5):1300–1307, 2000.
- [70] D. J. Kotecki, D.L. Cheever, and D.G. Howden. Mechanism of ripple formation during weld solidification. *Welding Journal*, 51(8):386s–391s, 1972.
- [71] R. Kovacevic and Y. M. Zhang. Sensing free surface of arc weld pool using specular reflection: principle and analysis. *Proceedings of the Institution of Mechanical Engineers, Part B, Journal of Engineering Manufacturing*, 210(6):553–564, 1996.
- [72] R Kovacevic, Y. M. Y. M. Zhang, and S. Ruan. Sensing and control of weld pool geometry for automated gta welding. *ASME Journal of Engineering for Industry*, 117(2):210–222, 1995.
- [73] R. Kovacevic and Y.M.. Zhang. Monitoring of weld joint penetration based on weld pool geometrical appearance. *Welding Journal*, 75(10):317329, 1996.
- [74] E. Kraft. A quaternion-based unscented kalman filter for orientation tracking. In *Proceedings of the Sixth International Conference of Information Fusion*, 2003.
- [75] Joseph J. LaViola. A comparison of unscented and extended kalman filtering for estimating quaternion motion. In *Proceeding of the American Control Conference*, pages 2435–2440, 2003.

- [76] Hyung-Jik Lee and Seul Jung. Gyro sensor drift compensation by kalman filter to control a mobile inverted pendulum robot system. In *Industrial Technology, 2009. ICIT 2009. IEEE International Conference on*, pages 1–6, 2009.
- [77] Jong-Sen Lee. Speckle analysis and smoothing of synthetic aperture radar images. *Computer Graphics and Image Processing*, 17:24–32, 1981.
- [78] L. P. Li, X. Q. Yang, F. Y. Zhang, and T. Lin. Research on surface recover of aluminum alloy pgtaw pool based on sfs. *Robotic Welding, Intelligence and Automation, Lecture Notes in Electrical Engineering.*, 88:307–314, 2011.
- [79] Xiang Rong Li, Yi Lu, and Yu Ming Zhang. Accelerometer-based position and speed sensing for manual pipe welding process. *The International Journal of Advanced Manufacturing Technology*, 2013.
- [80] M.L. Lin and T.W. Eagar. Influence of arc pressure on weld pool geometry. *Welding Journal*, 64(6):163–169, 1985.
- [81] Mingji Lou. Computation of weld pool surface from specular reflection and optical flow. Master’s thesis, University of Kentucky, 2004.
- [82] H.J. Luinge and P.H. Veltink. Inclination measurement of human movement using a 3-d accelerometer with autocalibration. *IEEE Transactions on Neural Systems and Rehabilitation Engineering*, 12(1):112 – 121, 2004.
- [83] X. J. Ma and Y. M. Zhang. Gas metal arc weld pool surface imaging: Modeling and processing. *Welding Journal*, 90(5):85s–94s, 2011.
- [84] R.B. Madigan. Ways to keep torches in seams. *Welding Design and Fabrication*, pages 48–50, 1987.
- [85] S.G. Mallat. *A Wavelet Tour of Signal Processing*. Academic Press, 1999.
- [86] J.L. Marins, X. Yun, E.R. Bachmann, R.B. McGhee, and M.J. Zyda. An extended kalman filter for quaternion-based orientation estimation using marg sensors. In *IEEE/RSJ International Conference on Intelligent Robots and System*, volume 4, pages 2003–2011, 2001.
- [87] D. McRuer, D. Graham, E. Krendel, and W. Reisener. Human pilot dynamics in compensatory systems. Technical report, Air Force Flight Dynamics Laboratory, Wright-Patterson AFB. Ohio., 1965.
- [88] MicroStrain Inc., 459 Hurricane Lane, Suite 102, Williston, VT 05495 USA. *3DM-GX3-25 miniature attitude heading reference sensor*, 2009.
- [89] C. Mnich, F. Al-Bayat, C. Debrunner, and et al. In situ weld pool measurement using stereovision. *Proceedings of 2004 Japan-USA Symposium on Flexible Automation, ASME*, pages 1–2, 2004.
- [90] Preto Moreno. *Welding Defects (1st ed.)*. Aracne, 2013.
- [91] S. Nagarajan, P. Banerjee, W.H. Chen, and B.A. Chin. Control of the welding process using infrared sensors. *IEEE Transactions on Robotics and Automation*, 8(1):86–93, 1992.

- [92] R.L. O'Brien, editor. *Welding Handbook, 8th Edition VOL. 2 - Welding Processes*. AWS, 1998.
- [93] Giorgio De Pasquale and Aurelio Soma. Reliability testing procedure for mems imus applied to vibrating environments. *Sneosr*, 10:456–474, 2010.
- [94] S.H. Pourtakdoust and H. Ghanbarpour Asl. An adaptive unscented kalman filter for quaternion-based orientation estimation in low-cost ahrs. *Aircraft Engineering and Aerospace Technology*, 79(5):485 – 493, 2007.
- [95] Baldev Raj, T. Jayakumar, and M. Thavasimuthu. *Practical non-destructive testing*. Woodhead Publishing, 2002.
- [96] Hoobasar Rampaul. *Pipe welding procedures (2nd ed.)*. Industrial Press, 2003.
- [97] R.J. Renwick and R.W. Richardson. Experimental investigation of gta weld pool oscillations. *Welding Journal*, 62(2):29s–35s, 1983.
- [98] G. L. Richard. *Statistical Concepts: A Second Course, Third Edition*. Routledge Academic., 2007.
- [99] R. W. Richardson. Coaxial arc weld pool viewing for process monitoring and control. *Welding Journal*, 63(3):43–50, 1984.
- [100] R.Kovacevic and Y. M. Zhang. Real-time image processing for monitoring of free weld pool surface. *Journal of Manufacturing Science and Engineering*, 119:161–169, 1997.
- [101] Universal Robots. Online, 2013.
- [102] Daniel Roetenberg, Henk J. Luinge, Chris T. M. Baten, and Peter H. Veltink. Compensation of magnetic disturbances improves inertial and magnetic sensing of human body segment orientation. *IEEE Transactions on Neural Systems and Rehabilitation Engineering*, 12:395–405, 2005.
- [103] S.I. Rokhlin and A.C. Guu. A study of arc force, pool depression, and weld penetration during gas tungsten arc welding. *Welding Journal*, 72(8):381–390, 1993.
- [104] Angelo M. Sabatini. *Computational Intelligence for Movement Sciences: Neural Networks and Other Emerging Techniques*, chapter Inertial Sensing in Biomechanics: A Survey of Computational Techniques Bridging Motion Analysis and Personal Navigation, pages 70–100. Idea Group Publishing, 2006.
- [105] Angelo M. Sabatini, Chiara Martelloni, Sergio Scapellato, and Filippo Cavallo. Assessment of walking features from foot inertial sensing. *IEEE Transactions on Biomedical Engineering*, 52(3):486–494, 2005.
- [106] G. Saeed, M. J. Lou, and Y. M. Zhang. Computation of 3d weld pool surface from the slope field and point tracking of laser beams. *Measurement Science and Technology*, 15(2):389–403, 2004.
- [107] G. Saeed and Y. M. Zhang. Mathematical formulation and simulation of specular reflection based measurement system for gas tungsten arc weld pool surface. *Measurement Science and Technology*, 14(8):1671–1682, 2003.

- [108] Gohar Saeed. Vision-based sensing of the welding process: a survey. *International Journal of Modeling, Identification and Control*, 2005.
- [109] H. Martin Schepers, Daniel Roetenberg, and Peter H. Veltink. Ambulatory human motion tracking by fusion of inertial and magnetic sensing with adaptive actuation. *Medical & Biological Engineering & Computing*, 48(1):27–37, 2010.
- [110] Hongyuan Shen, Tao Lin, Shanben Chen, and Laiping Li. Real-time seam tracking technology of welding robot with visual sensing. *Journal of Intelligent & Robotic Systems*, 59:283–298, 2010.
- [111] M. Shiwa, A. Yamaguchi, M. Sato, S. Murao, and M. Nagai. Acoustic emission waveform analysis from weld defects in steel ring samples. *Journal of Pressure Vessel Technology*, 121(1):77–83, 1999.
- [112] Simon Shuster. Fire at fourth reactor: Is worse yet to come in the fukushima nuclear disaster?, May 2011.
- [113] E. Siores. *Development of a Realtime Ultrasonic Sensing System for Automated and Robotic Welding*. PhD thesis, Brunel University, 1988.
- [114] H. S. Song and Y. M. Zhang. Three-dimensional reconstruction of specular surface for gas tungsten arc weld pool. *Measurement Science and Technology*, 18:3751–3767, 2007.
- [115] H.S. Song. machine vision recognition of three-dimensional specular surface for gas tungsten arc weld pool. *Ph.D. dissertation, University of Kentucky*, 2007.
- [116] C. Sorensen and T. Eagar. Measurement of oscillations in partially penetrated weld pools through spectral analysis. *Journal of Dynamic Systems, Measurement, and Control*, 112:463–468, 1990.
- [117] J. Steele, C. Mnich, C. Debrunner, T. Vincent, and S. Liu. Development of closed-loop control of robotic welding processes. *Industrial Robot: An International Journal*, 32(4):350–355, 2005.
- [118] Peter F. Sturm and Stephen J. Maybank. On plane-based camera calibration: a general algorithm, singularities, applications. In *IEEE Computer Society Conference on Computer Vision and Pattern Recognition*, 1999.
- [119] W. Swaim. Gas tungsten arc welding made easy. *Welding Journal*, 77(9):51–52, 1998.
- [120] Z. F. Syed, P. Aggarwl, C. Goodall, W. Niu, and N. El-Sheimi. A new multi-position calibration method for mems inertial navigation systems. *Measurement of Science and Technology*, 18:1897–1907, 2007.
- [121] RealWeld System, 2013.
- [122] Y. Tang, X. Su, F. Wu, and Y. Liu. A novel phase measuring deflectometry for aspheric mirror test. *Optic Express*, 17(22):19778–19784, 2009.
- [123] T.T. Tay, I. Mareels, and J. B. Moore. *High performance control*. Birkhuser, 1997.

- [124] Xsens Technology. *MTi and MTx user manual and technical documentation*. Xsens Technology B.V., pantheon 6a, 7521 PR Enschede the netherlands, May 2009.
- [125] Kian Sek Tee, Mohammed Awad, Abbas Dehghani, David Moser, and Saeed Zahedi, editors. *Triaxial Accelerometer Static Calibration*, volume III, London, UK, July 2011. Proceedings of the World Congress on Engineering.
- [126] Sakol Teeravarunyou and Bovornchok Poopatb. Computer based welding training system. *International Journal of Industrial Engineering*, 16(2):116–125, 2009.
- [127] Brandt Tso and Paul Mather. *Classification Methods for Remotely Sensed Data (2nd ed.)*. CRC Press, 2009.
- [128] T. Tsuji and Y. Tanaka. Tracking control properties of human-robotic systems based on impedance control. *IEEE Transactions on Systems, Man, and Cybernetics- Part A: Systems and Humans.*, 35(4):523–535, 2005.
- [129] G. D. Uttrachi. Welder shortage requires new thinking. *Welding Journal*, 86(1):6, 2007.
- [130] Henne van Heeren, Jeremie Bouchaud, Richard Dixon, and Patric Salomon. Rewards and risks of moving into new applications case study accelerometers. *MST News*, 1:35–39, 2007.
- [131] C. Verplaetse. Inertial proprioceptive devices: self-motion-sensing toys and tools. *IBM Systems Journal*, 35:639–650, 1996.
- [132] J. F. Wang, W. Y. Wang, and S. B. Chen. Extraction of welding pool shape using linear approximation. *Transactions of the China Welding Institution*, 28(8):54–56, 2007.
- [133] J.F. Wang, W.Y. Wang, and S.B. Chen. Inspection of welding pool height from shading in pulsed gtaw with wire filler. *Industrial Robot: An International Journal*, 36 (3):270–276, 2009.
- [134] Mei Wang, Yunchun Yang, R.R. Hatch, and Yanhua Zhang. Adaptive filter for a miniature mems based attitude and heading reference system. In *Position Location and Navigation Symposium*, pages 193–200, 2004.
- [135] D. Weenk, B.J.F. van Beijnum, C.T.M. Baten, H.J. Hermens, and P.H. Veltink. Automatic identification of inertial sensor placement on human body segments during walking. *Journal of NeuroEngineering and Rehabilitation*, 10(31):1–9, 2013.
- [136] Y. Q. Wei, N. S. Liu, X. Hu, and X.P. Ai. Phase-correction algorithm of deformed grating images in the depth measurement of weld pool surface in gas tungsten arc welding. *Optical Engineering*, 50:5, 2011.
- [137] Klas Weman. *Welding processes handbook*. New York, NY: CRC Press., 2003.
- [138] H. C. Winkle, R. H. Zee, and B. Chin. Sensing system for weld process control. *Journal of Materials Processing Technology*, 80-90:254–259, 1999.

- [139] Z. H. Yan, G. J. Zhang, and L. Wu. Simulation and controlling for weld shape process in p-gmaw based on fuzzy logic. *Proceedings of the 2011 IEEE International Conference on Mechatronics and Automation*, pages 2078–2082, 2011.
- [140] Xiao Y.H. and G. den Ouden. Weld pool oscillation during gta welding of mild steel. *Welding Journal*, 72(8):428s–434s, 1993.
- [141] M. Zacksenhouse and D.E. Hardt. Weld pool impedance identification for size measurement and control. *ASME Journal of Dynamic Systems, Measurement, and Control*, 105(3):179–184, 1984.
- [142] Paul Zarchan and Howard Musoff. *Fundamentals of Kalman Filtering:: A Practical Approach*. American Institute of Aeronautics and Astronautics, 2009.
- [143] G. J. Zhang, Z. H. Yan, and L. Lin. Reconstructing a three- dimensional p-gmaw weld pool shape from a two-dimensional visual image. *Measurement Science and Technology*, 17(7):1877–1882, 2006.
- [144] S. Zhang. Recent progresses on real-time 3d shape measurement using digital fringe projection techniques. *Optic Lasers Engineering*, 48(2):149–158, 2010.
- [145] S. Zhang and P. S. Huang. High-resolution, real-time three-dimensional shape measurement. *Optic Engeering*, 45(12):123601., 2006.
- [146] W. J. Zhang, Y. Liu, and Y. M. Zhang. Characterization of three-dimensional weld pool surface in gtaw. *Welding Journal*, 91(7):195s–203s, 2012.
- [147] W. J. Zhang and Y. M. Zhang. Automated three-dimensional reconstruction of weld pool surface in gtaw process. *IEEE Transactions on Automation Science and Engineering*, *in review*, 2012.
- [148] W. J. Zhang and Y. M. Zhang. Dynamic control of gtaw process using human welder response model. *Welding Journal (accepted for publication)*, 2012.
- [149] W. J. Zhang and Y. M. Zhang. Modeling of human welder response to 3d weld pool surface: Part 1- principles. *Welding Journal (accepted for publication)*, 2012.
- [150] W. J. Zhang and Y. M. Zhang. Modeling of human welder response to 3d weld pool surface: Part 2-results and analysis. *Welding Journal (accepted for publication)*, 2012.
- [151] W. J. Zhang and Y. M. Zhang. Real-time measurement of the weld pool surface in gtaw process. In *Trends in Welding Research Proceedings of the 9th International Conference*, 2012.
- [152] Wei Jie Zhang, Jun Xiao, and Yu Ming Zhang. Measurement of three-dimensional welding torch orientation for manual arc welding process. *Measurement Science and Technology (accepted for publication)*, 2013.
- [153] Wei Jie Zhang and Yu Ming Zhang. Modeling of human welder response to 3d weld pool surface: Part i- principles. *Welding Journal*, 91:310s318s, 2012.
- [154] Wei Jie Zhang and Yu Ming Zhang. Modeling of human welder response to 3d weld pool surface: Part ii- results and analysis. *Welding Journal*, 329s353s:2012, 2012.

- [155] Wei Jie Zhang and Yu Ming Zhang. Dynamic control of gtaw process using human welder response model. *Welding Journal*, 92:154s–166s, 2013.
- [156] Y. M. Zhang, R. Kovacevic, and L. Wu. Sensitivity of torch-side weld geometry in representing the full penetration. *Proceedings of institution in Mechanics and Engineering, Part B: Journal of Engineering Manufacture*, 206(3):191–197, 1992.
- [157] Y. M. Zhang and L. Li. Dynamic estimation of full penetration using geometry of adjacent weld pools. *Journal of Manufacturing Science and Engineering*, 19:631–644, 1997.
- [158] Y. M. Zhang, L. Li, and R Kovacevic. Monitoring of weld pool appearance for penetration control. *Proceedings of the 4th International Conference*, page 683688., 1995.
- [159] Zhengyou Zhang. Flexible camera calibration by viewing a plane from unknown orientations. In *The Proceedings of the 7th IEEE International Conference on Computer Vision*, 1999.
- [160] Zhengyou Zhang. A flexible new technique for camera calibration. In *IEEE Transactions on Pattern Analysis and Machine Intelligence*, volume 22, pages 1330–1334, 2000.
- [161] C. X. Zhao, I. M. Richardson, S. Kenjeres, C. R. Kleijn, and Z. Saldi. A stereo vision method for tracking particle flow on the weld pool surface. *Journal of Applied Physics*, 105(12): 123104, 2009.
- [162] D.B. Zhao, J. Q. Yi, S.B. Chen, L. Wu, and Q. Chen. Extraction of three-dimensional parameters for weld pool surface in pulsed gtaw with wire filler. *Journal of Manufacturing Science and Engineering*, 125:493–503, 2003.
- [163] W. Zhao, X. Su, Y. Liu, and Q. Zhang. Testing an aspheric mirror based on phase measuring deflectometry. *Optic Engineering*, 48(10): 103603, 2009.
- [164] B. Wang Zheng, Wang H.J., Q.I., and R. Kovacevic. Control for weld penetration in vppaw of aluminum alloys using the front weld pool image signal. *Welding Journal*, pages 363s–370s., 2000.
- [165] Huiyu Zhou and Huosheng Hu. Human motion tracking for rehabilitation survey. *Biomedical Signal Processing and Control*, 3(1):1–18, 2008.
- [166] L. Zhou, J. F. Wang, T. Lin, and S. B. Chen. Planning the torch orientation of planar lap joint in robotic welding. *Robotic Welding, Intelligence and Automation*, 362:145–151, 2007.
- [167] Xuli Zong, Andrew F. Laine, and Edward A. Geiser. Speckle reduction and contrast enhancement of echocardiograms via multiscale nonlinear processing. *IEEE Transactions on Medical Imaging*, 17:532–540, 1998.

Vita

WeiJie Zhang was born on in HaiMen, JiangSu, China.

Education

M.S. in Electrical Engineering, Harbin Institute of Technology, Harbin, China, July, 2007.

B.S. in Electrical Engineering, Harbin Institute of Technology, Harbin, China, July, 2005.

Recent Award

Henry Granjon Prize (2013) International Institute of Welding(IIW)

Charles H. Jennings Memorial Award (2012) American Welding Society(AWS)

Publications

Journal Papers

1. W.J. Zhang, Y. K. Liu, X. Wang, Y.M. Zhang, “Characterization of Three-dimensional Weld Pool Surface in Gas Tungsten Arc Welding”, *Welding Journal*, vol. 91, pp. 195s-203s, 2012.
2. W. J. Zhang and Y. M. Zhang, “Modelling of Human Welder Response to 3D Weld Pool Surface: Part I- Principles”, *Welding Journal*, vol. 91(11), pp. 310-318s, 2012.
3. W. J. Zhang and Y. M. Zhang, “Modelling of Human Welder Response to 3D Weld Pool Surface: Part II-Results and Analysis”, *Welding Journal*, vol. 91(12), pp. 329s-337s, 2012.
4. W. J. Zhang and Y. M. Zhang, “Dynamic Control of GTAW Process Using Human Welder Response Model”, *Welding Journal*, vol. 92(5):154s-163s, 2013.
5. W. J. Zhang, X. Zhang, Y. M. Zhang, “Robust Pattern Recognition for Measurement of Three Dimensional Weld Pool Surface in GTAW”, *Journal of Intelligent Manufacturing*, (accepted for publication), 2013.

6. W. J. Zhang, Y. M. Zhang, "Analytical real-time measurement of three-dimensional specular weld pool surface", *Measurement Science and Technology*, (accepted for publication), 2013.
7. W. J. Zhang, J. Xiao, Y. M. Zhang, "Measurement of Three-dimensional Welding Torch Orientation for Manual Arc Welding Process", *Measurement Science and Technology*, (accepted for publication), 2013.
8. J. Xiao, G.J. Zhang, W.J Zhang, Y.M. Zhang. "Active metal transfer control by using enhanced droplet oscillation Part 1-Experimental study". *Welding Journal*. (accepted for publication), 2013.
9. J. Xiao, G.J. Zhang, W.J Zhang, Y.M. Zhang. "Active metal transfer control by using enhanced droplet oscillation Part 2-Modeling and analysis". *Welding Journal*. (accepted for publication), 2013.
10. Y. K. Liu, W.J. Zhang, Y.M. Zhang, "Estimation of Weld Joint Penetration Under Varying GTA Pools", *Welding Journal*. (accepted for publication), 2013.
11. Y. K. Liu, W.J. Zhang, Y.M. Zhang, "Adaptive Neuro-Fuzzy Inference System (ANFIS) Modeling of Human Welder's Response to 3D Weld Pool Surface in GTAW", *Journal of Manufacturing Science and Engineering-Transactions of the ASME*, vol. 135, pp. 0210101-02101011, 2013.
12. Y. K. Liu, W.J. Zhang, Y.M. Zhang, "A Tutorial on Learning Human Welder's Behavior: Sensing, Modeling, and Control", *Journal of Manufacturing Processes (Elsevier)*, (accepted for publication), 2013.
13. Y. K. Liu, W.J. Zhang, Y.M. Zhang, "Dynamic Neuro-fuzzy Based Human Intelligence Modeling and Control in GTAW", *IEEE Transactions on Automation Science and Engineering*. (accepted for publication), 2013.
14. W. J. Zhang, Y. M. Zhang, "Flexible Mobile System for Measurement of Three-Dimensional Weld Pool Surface", *IEEE Transactions on Automation Science and Engineering*. (submitted for review), 2014.
15. W. J. Zhang, Y. M. Zhang, "A Flexible Mobile Sensing System for Manual Gas Tungsten Arc Welding Process", *IEEE Transactions on Automation Science and Engineering*. (submitted for review), 2014.

Conference Papers

1. W. J. Zhang and Y. M. Zhang, "Real-time Measurement of the Weld Pool Surface in GTAW Process" *Trends in Welding Research Proceedings of the 9th International Conference*, 2012.
2. W.J. Zhang, Y. K. Liu, Y.M. Zhang, "Robust Pattern Recognition of Three Dimensional Weld Pool Surface in Gas Tungsten Arc Welding" *IEEE International Instrumentation and Measurement Technology Conference*, 2013.

3. W. J. Zhang and Y. M. Zhang, "Real-time Measurement of the Weld Pool Surface in GTAW Process", IEEE International Conference on Automation Science and Engineering, 2012.
4. Y. K. Liu, W.J. Zhang, Y.M. Zhang, "Nonlinear Dynamic Estimation of the Weld Penetration in Gas Tungsten Arc Welding", IEEE International Instrumentation and Measurement Technology Conference, 2013.
5. Y. K. Liu, S. J. Chen, Zhang, W.J. Zhang, Y.M. Zhang, "Nonlinear Dynamic Modeling of Weld Penetration in Gas Tungsten Arc Welding Process", AASRI Conference on Modeling, Identification and Control, 2012.
6. Y. K. Liu, W.J. Zhang, Y.M. Zhang, "Neuro-fuzzy Modeling of Human Welders Response to 3D Weld Pool Surface in GTAW", in Proc. of 21th IEEE International Symposium on Industrial Electronics (IEEE-ISIE 2012), Hangzhou, China, May 28-31, 2012.
7. X. Wang, Y. K. Liu, W.J. Zhang, Y.M. Zhang, "Estimation of Weld Penetration Using Parameterized Three-Dimensional Weld Pool Surface in GTAW" in Proc. of 21th IEEE International Symposium on Industrial Electronics (IEEE-ISIE 2012), Hangzhou, China, May 28-31, 2012.

Book Chapter

1. W.J. Zhang, Y. K. Liu, Y.M. Zhang, "Real-time Measurement of Three Dimensional Weld Pool Surface in GTAW" in book "Welding Process" ISBN 979-953-307-1089-4. 2012.